

US-APWR Fuel System Design Evaluation

Non-Proprietary Version

February 2008

**© 2008 Mitsubishi Heavy Industries, Ltd.
All Rights Reserved**

Revision History

| Revision | Page | Description |
|----------|------|-----------------|
| 0 | All | Original issued |

© 2008
MITSUBISHI HEAVY INDUSTRIES, LTD.
All Rights Reserved

This document has been prepared by Mitsubishi Heavy Industries, Ltd. (MHI) in connection with the U.S. Nuclear Regulatory Commission ("NRC") licensing review of the US-APWR nuclear power plant design. No right to disclose, use or copy any of the information in this document, other than that by the NRC and its contractors in support of the licensing review of the US-APWR, is authorized without the express written permission of MHI.

This document contains MHI's technology information and intellectual property relating to the US-APWR and it is delivered to the NRC on the express condition that it not be disclosed, copied or reproduced in whole or in part, or used for the benefit of anyone other than MHI without the express written permission of MHI, except as set forth in the previous paragraph. This document is protected by the laws of Japan, U.S. copyright law, international treaties and conventions, and the applicable laws of any country where it is being used.

Mitsubishi Heavy Industries, Ltd.
16-5, Konan 2-chome, Minato-ku
Tokyo 108-8215 Japan

Abstract

The US-APWR fuel system design is based on the significant experience with and demonstrated high reliability performance of Mitsubishi fuel in Japan.

The US-APWR fuel incorporates the latest design features, such as corrosion resistant cladding, 97 % theoretical density pellets, 10 wt% gadolinia doped fuel and features to reduce or eliminate debris fretting, grid fretting and incomplete rod insertion.

The fuel rod and fuel assembly design criteria and methodology applied to the US-APWR fuel design is described in the topical report, "Mitsubishi Fuel Design Criteria and Methodology"(MUAP-07008-P/-NP), which includes the detailed description and the validation of the FINE fuel rod design code which is used in the US-APWR fuel rod design evaluation.

Results of the application of the fuel rod and fuel assembly design criteria and methodology, described in the topical report (MUAP-07008-P/-NP), to the US-APWR fuel are given in this report:

- evaluation results for the fuel rod internal pressure, cladding stresses, fuel-cladding mechanical interaction, cladding strain, chemical reaction, cladding fatigue, creep collapse, and fuel temperature, which confirm that their respective design criteria are satisfied, and
- evaluation results for the loads during normal operation and AOOs, loads in shipping and handling, fuel assembly dimensional changes, such as fuel rod bowing, fuel assembly growth, fuel rod growth and fuel assembly bowing, irradiation behavior of the grid spacers, fuel cladding fretting wear, and fuel assembly liftoff, which are shown to meet their respective design criteria.

The design bases and criteria for the US-APWR in-core control components, the control rods, burnable absorber rods and neutron source rods, are defined, and design evaluation results for temperatures, insertability, material requirements, cladding stresses, cladding fatigue, and cladding wear, are given, which confirm that their respective design criteria are satisfied.

Table of Contents

| | |
|---|------|
| List of Tables..... | iv |
| List of Figures..... | vi |
| List of Acronyms..... | viii |
| | |
| 1.0 INTRODUCTION..... | 1-1 |
| | |
| 2.0 US-APWR FUEL SYSTEM DESIGN DESCRIPTION..... | 2-1 |
| 2.1 Fuel Rod..... | 2-1 |
| 2.2 Fuel Assembly Structure..... | 2-2 |
| 2.3 In-Core Control Components..... | 2-5 |
| 2.4 References..... | 2-8 |
| | |
| 3.0 FUEL ROD DESIGN EVALUATION..... | 3-1 |
| 3.1 General..... | 3-2 |
| 3.2 Design Interface Data..... | 3-11 |
| 3.3 Fuel Rod Internal Pressure..... | 3-15 |
| 3.4 Cladding Stresses..... | 3-22 |
| 3.5 Chemical Reaction..... | 3-29 |
| 3.6 Cladding Fatigue..... | 3-32 |
| 3.7 Creep Collapse..... | 3-35 |
| 3.8 Cladding Strain..... | 3-36 |
| 3.9 Fuel Temperature..... | 3-38 |
| 3.10 Fuel-Cladding Mechanical Interaction..... | 3-44 |
| 3.11 References..... | 3-45 |
| | |
| 4.0 FUEL ASSEMBLY DESIGN EVALUATION..... | 4-1 |
| 4.1 Loads under Normal Operation and AOOs..... | 4-1 |
| 4.2 Loads in Fuel Shipping and Handling..... | 4-8 |
| 4.3 Fuel Assembly Dimensional Changes..... | 4-13 |
| 4.4 Grid Spacer Irradiation Behavior..... | 4-22 |
| 4.5 Fuel Cladding Fretting Wear..... | 4-29 |
| 4.6 Fuel Assembly Liftoff..... | 4-34 |
| 4.7 References..... | 4-40 |
| | |
| 5.0 IN-CORE CONTROL COMPONENTS DESIGN EVALUATION..... | 5-1 |
| 5.1 Rod Cluster Control Assembly..... | 5-1 |
| 5.2 Burnable Absorber Assembly..... | 5-7 |
| 5.3 Neutron Source Assembly..... | 5-11 |

5.4 Thimble Plug Rods and Assembly 5-15
5.5 References 5-16

6.0 CONCLUSION 6-1

Appendix A NUCLEAR DESIGN (24-MONTH EQUILIBRIUM CORE)

Appendix B FUEL ASSEMBLY AND ICCM MATERIAL PROPERTIES

Appendix C FUEL ROD FRETTING WEAR EVALUATION METHODOLOGY

Appendix D FUEL CLADDING COLLAPSE EVALUATION

List of Tables

| | | |
|-------------------|--|------|
| Table 2.0-1 (1/2) | The US-APWR Fuel System Design Parameters (Fuel Assembly) | 2-9 |
| Table 2.0-1 (2/2) | The US-APWR Fuel System Design Parameters (Fuel Assembly) | 2-10 |
| Table 2.0-2 (1/2) | The US-APWR Fuel System Design Parameters (Fuel Rod)..... | 2-11 |
| Table 2.0-2 (2/2) | The US-APWR Fuel System Design Parameters (Fuel Rod)..... | 2-12 |
| Table 2.0-3 (1/2) | The US-APWR Fuel System Design Parameters (In-Core Control Components) | 2-13 |
| Table 2.0-3 (2/2) | The US-APWR Fuel System Design Parameters (In-Core Control Components) | 2-14 |
| Table 3.1-1 (1/2) | Fuel Design Uncertainty Assessment Items | 3-5 |
| Table 3.1-1 (2/2) | Fuel Design Uncertainty Assessment Items | 3-6 |
| Table 3.1-2 | Fuel Performance Model Uncertainty Parameters | 3-7 |
| Table 3.1-3 | Fuel Manufacturing Uncertainty Parameters | 3-8 |
| Table 3.2-1 | US-APWR Thermal-Hydraulic Conditions..... | 3-13 |
| Table 3.3-1 | Rod Internal Pressure Evaluation Results | 3-19 |
| Table 3.3-2 | Evaluation of DNB Propagation in AOO | 3-20 |
| Table 3.3-3 | Parametric Survey of DNB Propagation for Postulated Accidents..... | 3-21 |
| Table 3.4-1 | Stress Categories..... | 3-27 |
| Table 3.4-2 | Stress Intensity Limits..... | 3-27 |
| Table 3.4-3 | Cladding Stresses Evaluation Results | 3-28 |
| Table 3.5-1 | Chemical Reaction Evaluation Results..... | 3-31 |
| Table 3.6-1 | Cladding Fatigue Evaluation Results..... | 3-34 |
| Table 3.8-1 | Cladding Strain during AOOs Evaluation Results | 3-37 |
| Table 3.9-1 | Fuel Centerline Temperature Uncertainty Evaluation (UO ₂ Fuel) | 3-40 |
| Table 4.1-1 | Stress Evaluation Results for the Fuel Assembly Components during NO and AOOs..... | 4-5 |
| Table 4.2-1 | Strength Evaluation for Shipping and Handling Loads..... | 4-11 |
| Table 4.5-1 | US-APWR EOL Wear Depth Evaluation Results | 4-32 |
| Table 4.6-1 | Holddown Spring Evaluation at Cold and Hot Conditions | 4-37 |
| Table 4.6-2 | Holddown Spring Evaluation at Pump-over-speed Condition..... | 4-37 |
| Table 5.1-1 | Stress Limits..... | 5-5 |
| Table 5.1-2 | Typical Loads Applied to the Control Rods under Normal Operation and AOOs..... | 5-5 |
| Table 5.1-3 | Summary of the Evaluation during Normal Operation and AOOs | 5-5 |
| Table 5.2-1 | Stress Limits..... | 5-10 |
| Table 5.2-2 | Typical Loads Applied to the Absorber Rods under Normal Operation and AOOs..... | 5-10 |
| Table 5.2-3 | Summary of the Evaluation during Normal Operation and AOOs | 5-10 |
| Table 5.3-1 | Stress Limits..... | 5-14 |
| Table 5.3-2 | Typical Loads Applied to the Neutron Source Rods under Normal Operation and AOOs | 5-14 |

Table 5.3-3 Summary of the Evaluation during Normal Operation and AOOs 5-14

List of Figures

| | | |
|--------------|---|------|
| Figure 2.0-1 | Fuel Assembly Schematic View..... | 2-15 |
| Figure 2.0-2 | Fuel Assembly Array Cross Section | 2-16 |
| Figure 2.1-1 | Fuel Rod Schematic View | 2-17 |
| Figure 2.1-2 | Fuel Pellet Schematic View | 2-18 |
| Figure 2.2-1 | Fuel Assembly Full-Length Schematic View (1/3)..... | 2-19 |
| Figure 2.2-1 | Fuel Assembly Full-Length Schematic View (2/3)..... | 2-20 |
| Figure 2.2-1 | Fuel Assembly Full-Length Schematic View (3/3)..... | 2-21 |
| Figure 2.2-2 | Bottom Nozzle Schematic View | 2-22 |
| Figure 2.2-3 | Control Rod Guide Thimble to Bottom Nozzle Joint..... | 2-23 |
| Figure 2.2-4 | Top Nozzle Schematic View | 2-24 |
| Figure 2.2-5 | Control Rod Guide Thimble to Top Nozzle Joint | 2-25 |
| Figure 2.2-6 | Control Rod Guide Thimble to Intermediate Grid Spacer Joint | 2-26 |
| Figure 2.2-7 | High Performance Grid Spacer (Z3 Type) Schematic View | 2-27 |
| Figure 2.3-1 | Rod Cluster Control Assembly Schematic View | 2-28 |
| Figure 2.3-2 | Burnable Absorber Assembly Schematic View | 2-29 |
| Figure 2.3-3 | Primary Source Assembly Schematic View | 2-30 |
| Figure 2.3-4 | Secondary Source Assembly Schematic View | 2-31 |
| Figure 3.1-1 | Examples of UO ₂ Rod Power Histories based on the US-APWR Equilibrium Core..... | 3-9 |
| Figure 3.1-2 | Examples of (U,Gd)O ₂ Rod Power Histories based on the US-APWR Equilibrium Core..... | 3-10 |
| Figure 3.2-1 | Typical Axial Power Distributions..... | 3-14 |
| Figure 3.9-1 | Fuel Centerline Temperature versus Local Linear Heat Rate(UO ₂ Fuel) .. | 3-41 |
| Figure 3.9-2 | Fuel Temperature Design Limit versus Burnup (UO ₂ Fuel)..... | 3-42 |
| Figure 3.9-3 | Local Linear Power Limit versus Burnup (UO ₂ Fuel) | 3-43 |
| Figure 4.1-1 | Sample Analytical Model, Top Nozzle FEM Analysis..... | 4-6 |
| Figure 4.1-2 | Analytical Model for Assembly Axial Mechanical Behavior..... | 4-7 |
| Figure 4.2-1 | Fuel Rod and Control Rod Guide Thimble Load Distribution | 4-12 |
| Figure 4.3-1 | Rod Bowing of Mitsubishi 17×17 Fuel Assemblies..... | 4-15 |
| Figure 4.3-2 | Mitsubishi 17x17 Fuel Assembly Growth Data with Inconel Grid Spacers | 4-17 |
| Figure 4.3-3 | Total Gap Change of Mitsubishi 17×17 Fuel Assemblies | 4-19 |
| Figure 4.3-4 | Fuel Assembly Bowing of Mitsubishi 17×17 Fuel Assemblies | 4-21 |
| Figure 4.4-1 | Load-Deflection Curve of the Inner Grid Spring (at Room Temperature). 4-24 | |
| Figure 4.4-2 | Grid Spacer Spring Relaxation Rate (US Reactor Data) | 4-24 |
| Figure 4.4-3 | Grid Spacer Spring Relaxation Rate (Japanese Reactor Data)..... | 4-25 |
| Figure 4.4-4 | Grid Spring Fatigue Properties | 4-25 |
| Figure 4.4-5 | Burnup Dependence of Outer Size Increase in Zircaloy-4 Grid Spacer .. | 4-28 |

| | | |
|--------------|---|------|
| Figure 4.5-1 | Zircaloy-4 Grid Relative Restraint Force after 2 Cycles of Irradiation..... | 4-33 |
| Figure 4.5-2 | Corrosion Thickness Axial Distribution | 4-33 |
| Figure 4.6-1 | Holddown Spring Deformation..... | 4-38 |
| Figure 4.6-2 | Spring Characteristics and the Holddown Force of Top Nozzle Spring.... | 4-39 |
| Figure 5.1-1 | Summary of the ICCG Content Temperature Calculation..... | 5-6 |

Lists of Acronyms

| | |
|--------|--|
| AOOs | Anticipated Operating Occurrences |
| A.O. | Axial Offset |
| APWR | Advanced Pressurized Water Reactor |
| ARI | All Control Rods In |
| ARO | All Control Rods Out |
| BA | Burnable Absorber |
| BOC | Beginning of Cycle |
| CAOC | Constant Axial Offset Control |
| DNB | Departure from Nucleate Boiling |
| DNBR | Departure from Nucleate Boiling Ratio |
| EOC | End of Cycle |
| EFPM | Effective Full-Power Months |
| EFPH | Effective Full-Power Hours |
| EOC | End of Cycle |
| EOL | End of Life |
| FEM | Finite Element Method |
| FINE | Fuel rod INtegrity Evaluation |
| HFP | Hot Full Power |
| HZP | Hot Zero Power |
| ICCC | In-Core Control Component |
| IRI | Incomplete Rod Insertion |
| LOCA | Loss of Coolant Accident |
| LLLP | Low-Leakage Loading Pattern |
| L.P.L. | Local Power Limit |
| MOC | Middle of Cycle |
| NO | Normal Operation |
| NRC | Nuclear Regulatory Commission |
| MDF | Mechanical Design Flow |
| OBE | Operating Basis Earthquake |
| PA | Postulated Accident |
| PCI | Pellet Cladding Interaction |
| PCMI | Pellet Cladding Mechanical Interaction |

| | |
|-------|---|
| RCC | Rod Cluster Control |
| RCCA | Rod Cluster Control Assembly |
| RIA | Reactivity Initiated Accident |
| RIA | Rod Insertion Allowance |
| RIL | Rod Insertion Limits |
| SAFDL | Specified Acceptance Fuel Design Limits |
| SRSS | Square Root of the Sum of the Squares |
| SSE | Safe Shutdown Earthquake |
| TD | Theoretical Density |
| TDF | Thermal Design Flow |
| UTS | Ultimate Tensile Strength |

1.0 INTRODUCTION

Mitsubishi Heavy Industries, Ltd. (Mitsubishi) has substantial experience in the nuclear industry in Japan, having supplied approximately 18,000 nuclear fuel assemblies to Japanese PWR utilities since 1969. The irradiation experience accumulated for Mitsubishi fuel assemblies has demonstrated excellent performance and high reliability.

The fuel design, fabrication, the associated analysis methods and criteria that have led to high reliability performance of Mitsubishi fuel in Japan will be applied to the design and manufacture of US-APWR fuel, consistent with NRC regulations and standards.

The US-APWR fuel incorporates the latest fuel design features, such as corrosion resistant cladding, 97 % theoretical density (TD) pellets, 10 wt% gadolinia doped fuel and the features to reduce or eliminate debris fretting, grid fretting and incomplete rod insertion.

The fuel rod and fuel assembly design criteria and methodology applied to the US-APWR fuel design are described in the topical report, "Mitsubishi Fuel Design Criteria and Methodology" (MUAP-07008-P/-NP), which includes Mitsubishi fuel experience, the detailed description and the validation of the FINE fuel rod design code which is used in the US-APWR fuel rod design.

This report contains:

1. A description of the design features, materials, specification of the fuel rod, and fuel assembly structure components and the in-core control components such as control rods, burnable absorber rods and neutron source rods, used in the US-APWR (Chapter 2),
2. Evaluation results obtained from the application of the fuel rod and fuel assembly design criteria and methodology, specified in the topical report (MUAP-07008-P/-NP) to the US-APWR fuel,
 - Design interface data used in fuel rod design, and the evaluation results for the fuel rod internal pressure, cladding stresses, fuel-cladding mechanical interaction, cladding strain, chemical reaction, cladding fatigue, creep collapse, and fuel temperature (Chapter 3),
 - Design evaluation results for the loads during normal operation and AOOs, loads in shipping and handling, fuel assembly dimensional changes, such as fuel rod bowing, fuel assembly growth, fuel rod growth and fuel assembly bowing, irradiation behavior of grid spacer, fuel cladding fretting wear, and fuel assembly liftoff (Chapter 4).
3. Design bases, criteria, and evaluation results for temperatures, insertability, material requirements, cladding stresses, cladding fatigue, and cladding wear, of the in-core control components (Chapter 5).

Evaluation of the structural response to seismic and LOCA loads is described in separate reports.

2.0 US-APWR FUEL SYSTEM DESIGN DESCRIPTION

The US-APWR fuel system design specifications are given in Tables 2.0-1 to 2.0-3.

A fuel assembly consists of 264 fuel rods arranged in a 17x17 square array, together with 24 control rod guide thimbles, an in-core instrumentation guide tube, 11 grid spacers, a top nozzle and a bottom nozzle. The control rod guide thimbles guide the in-core control components, such as the control rods, the burnable absorber rods, the neutron source rods and the thimble plug rods, into the fuel assembly. The in-core instrumentation tube directs the movable neutron detector into the fuel assembly from the center hole of the top nozzle adapter plate. The in-core instrumentation guide tube is located at the center of the square array, whereas the control rod guide thimbles are symmetrically arrayed according to arrangement of the control rods in the rod cluster control assembly. The fuel assembly full length schematic view is shown in Figure 2.0-1. The cross section of the fuel assembly array is shown in Figure 2.0-2.

To preclude contact between the fuel rod and the nozzles, the fuel rods are loaded into the fuel assembly with an initial clearance between the fuel rod ends and the top and bottom nozzles. The fuel rods are supported by 11 grid spacers. The top and bottom grid spacers are made of Inconel 718, and the intermediate grid spacers are fabricated from Zircaloy-4.

The fuel assembly is loaded into the core barrel and supported by the lower core support plate. The upper core plate is installed over the fuel assemblies after their loading. Fuel assembly alignment is provided by engagement between alignment holes in the fuel assembly top and bottom nozzles and guide pins attached to the lower core support plate and the upper core plate. The upper core plate compresses the holddown spring of the fuel assembly to fix the axial location of the fuel assembly.

2.1 Fuel Rod

The fuel rod and pellet schematic view are shown in Figures 2.1-1 and 2.1-2, respectively. The fuel rods consist of cold-worked and stress relieved ZIRLO™* fuel cladding (referred to simply as "cladding" below) loaded with sintered uranium dioxide pellets and/or sintered gadolinia-uranium dioxide pellets, a coil spring (called the "plenum spring") in the upper plenum, a lower plenum spacer, and end plugs welded at the top and bottom ends to seal the rod, as shown in Figure 2.1-1. ZIRLO is a zirconium based alloy with improved corrosion resistance compared with Zircaloy-4. The sintered uranium dioxide pellets and sintered gadolinia-uranium dioxide pellets are produced by compression molding powdered uranium dioxide, or a mixture of powdered uranium dioxide and gadolinia, respectively, and then sintered in an atmosphere of hydrogen or a hydrogen/nitrogen mixture. The pellets are cylindrical with a hollow (called a "dish") at the center of each end surface and with chamfered edges of the end surfaces, as shown in Figure 2.1-2. The dishes accommodate the axial swelling and thermal expansion of the pellet during irradiation. The chamfer acts to strengthen the pellet ends to reduce the incidence of small defects close to the pellet surface and to suppress deformation of the end surfaces when the pellets expand.

Between the pellet stack and both end plugs, there are an upper and a lower plenum to accommodate the increase in the internal gas content due to the release of gaseous fission products with irradiation. The plenum spring placed in the upper plenum prevents the pellets from moving during shipping and handling of fuel assemblies. The US-APWR fuel rod design

* ZIRLO™ is the trademark of the Westinghouse Electric Corporation.

includes a lower plenum. A stainless steel spacer in the lower plenum supports the fuel stack and provides additional cladding support. The cladding wall thickness and the radial gap between the pellets and cladding are determined so that the integrity of the fuel rod is fully maintained during normal operation including AOOs, where the thermal expansion of the pellet exceeds that of the cladding. The axial clearance between the fuel rod and the top nozzle and between the fuel rod and the bottom nozzle are determined to allow for the difference between the fuel rod and assembly axial dimensional changes due to irradiation growth and thermal expansion during normal operation.

To reduce pellet-cladding interaction and prevent collapse during normal operation, the fuel rods are pressurized with helium through a pressurization hole provided in the top end plug, which is then closed off by welding to yield a sealed structure.

2.2 Fuel Assembly Structure

As shown in Figure 2.2-1, the fuel assembly structure consists of the bottom nozzle, the top nozzle, the fuel rods, the control rod guide thimbles, the in-core instrumentation guide tube and the grid spacers.

2.2.1 Bottom Nozzle

A schematic view of the bottom nozzle is shown in Figure 2.2-2. The bottom nozzle has the following functions:

- Positioning the fuel assemblies properly inside the core barrel
- Introducing the primary coolant into the fuel assembly
- Receiving dropped fuel rods during irradiation and accidents
- Acting as a filter for debris
- Bearing the axial loads of the fuel assembly, including its weight

The bottom nozzle consists of a top plate, four legs and side panels between the legs. The top plate and side panels are called the “adapter plate” and “skirt”, respectively. All of these parts are made of stainless steel. The bottom nozzle is connected to the control rod guide thimbles by thimble screws that pass through the insert and into the thimble end plug, as shown in Figure 2.2-3.

In addition to guiding the primary coolant into the fuel assembly, the flow holes in the adapter plate are designed in both their position and their diameter, to prevent dropped fuel rods from passing through the flow holes and going out of the fuel assembly during operation.

An anti-debris bottom nozzle with a built-in debris filter is used in the US-APWR fuel assembly, as shown in Figure 2.2-2. Thin plates are placed and welded in grooved slits in the adapter plate, providing a filter for debris passing through the flow holes. The thin plates, made of Inconel 718, are called “blades”. This type of debris filter can trap smaller debris than the conventional debris filter bottom nozzle. The bottom nozzle skirt also catches debris that flows out from the bottom of the adapter plate into gaps between the fuel assemblies. Fuel

assemblies with this type of bottom nozzle have been installed into some of the Japanese plants.

Axial loads on the fuel assembly are transmitted through the bottom nozzle from the lower core support plate. Alignment holes in two diagonally opposite legs of the bottom nozzle properly position the fuel assembly in the core by engaging with guide pins on the lower core support plate. Lateral loads on the fuel assembly are transmitted through the guide pins from the lower core support plate.

2.2.2 Top Nozzle

The top nozzle is the uppermost structural component of the fuel assembly. The parts of the top nozzle are the holddown springs, a top plate, an enclosure, clamps and the adapter plate, as shown in Figure 2.2-4. The holddown spring is made of Inconel 718, and the other parts of the top nozzle are made of type 304 stainless steel.

The top nozzle has the following functions and mechanisms:

- Housing for the in-core control components,
- Fixing the holddown springs to prevent liftoff of the fuel assembly due to the hydraulic force of the primary coolant,
- Removing the heat generated in the fuel assembly by guiding the primary coolant flow out of the assembly,
- Preventing ejection of the fuel rods upward from the fuel assembly during accidents,
- Allowing for assembly re-constitution so that fuel rods can be replaced if there is fuel leakage.

The in-core control components are positioned in the space formed by the top plate, enclosure and the adapter plate.

The top nozzle has four sets of holddown springs, attached to the top nozzle by two diagonally opposite clamps. Each set of holddown springs is attached to the clamp by means of a spring screw.

There are alignment holes in the two diagonally opposite corners of the top nozzle that do not have the holddown spring clamps. The alignment holes engage with the guide pins attached to the upper core plate. The indexing hole in one corner of the top plate assures that the fuel assembly is loaded in the proper position in the core. The identification number engraved on the opposite corner clamp is used for visual confirmation of correct assembly loading.

The nozzle sleeves are mechanically connected to holes for the control rod guide thimble holes in the adapter plate, as shown in Figure 2.2-5. This enables removal and replacement of the top nozzles for replacing leaking fuel rods. To remove the top nozzle, a tool is inserted into the holes for the control rod guide thimbles to rotate the lock parts at the holes. After removing the top nozzle, any fuel rod in the assembly can be gripped and withdrawn for examination or replacement. The re-construction of the top nozzle is completed by setting the top nozzle on the top nozzle sleeves and rotating the lock parts.

The positions of the flow holes in the adapter plate are designed to prevent upward rod ejection during irradiation and accidents.

2.2.3 Control Rod Guide Thimble and In-Core Instrumentation Guide Tube

The control rod guide thimble is a structural member of the fuel assembly and has the function of guiding the in-core control components, such as the control rods, the burnable absorber rods or the neutron source rods, when they are inserted into the fuel assembly, and then holding them in place. The control rod guide thimble is fabricated from Zircaloy-4. The lower part of the control rod guide thimble has a reduced diameter and small holes to provide a buffer effect when the control rods are dropped. This configuration reduces the impact force on the top nozzle when the RCCA drops. The bottom end of the control rod guide thimble is welded to an end plug which has a small flow hole to avoid the stagnation of the primary coolant in the control rod guide thimble during operation.

The bottom grid spacer is spot-welded to an insert tube which is made of type 304 stainless steel. As shown in Figure 2.2-3, the control rod guide thimbles are positioned within the insert and connected with the bottom nozzle adapter plate by thimble screws.

The top nozzle sleeve for the re-constructible top nozzle is linked to the top of the control rod guide thimble by three bulge joints, as shown in Figure 2.2-5.

Mechanical testing of the locking and unlocking mechanism to connect the top nozzle with the control rod guide thimble has been carried out to verify that these designs satisfy the design requirements.

The grid spacers, except for the bottom grid spacer, are connected to the control rod guide thimbles by bulge joints. The schematic view of the connection is shown in Figure 2.2-6.

The in-core instrumentation guide tube has a uniform diameter and has the function of guiding the in-core neutron detector which is inserted from the top nozzle into the fuel assembly. The instrumentation tube is also made of Zircaloy-4 and both ends are inserted into the top and bottom nozzles. The instrumentation tube is connected to the top grid spacer and the intermediate grid spacers by a single-stage bulge joint identical to that used to attach the control rod guide thimbles to the grid spacers.

2.2.4 Grid Spacer

As shown in Figures 2.0-1 and 2.2-1, the fuel rods are supported by the grid spacers. The grid spacers have a 17x17 lattice structures, and are made by interlocking thin straps made of Inconel 718 or Zircaloy-4. The grid spacer holds the fuel rod by means of two grid spacer springs and four dimples as shown in Figure 2.2-6. It also has the function of maintaining the clearance between the fuel rods, the control rod guide thimbles and the in-core instrumentation guide tube to maintain the nuclear and thermal-hydraulic performance.

The top and bottom grid spacers are fabricated from Inconel 718 to provide a restraint force on the fuel rod. The restraint force is designed to prevent grid fretting wear of the fuel rod cladding and fuel rod bowing during the assembly lifetime.

The nine intermediate grid spacers are fabricated from Zircaloy-4 to improve neutron economy. The intermediate grid spacers hold the fuel rods by the grid spacer springs and dimples in the

same manner as the top and bottom grid spacers. The grid spacer straps of the Inconel 718 and Zircaloy-4 grid spacers are respectively brazed or welded together.

The intermediate grid spacers have mixing vanes on the top of inner straps to increase the mixing of the primary coolant and increase the heat removal efficiency. The top and bottom grid spacers do not have mixing vanes.

A grid spacer design called the "I-type grid spacer" (Z2 type) is used in Mitsubishi conventional fuel assemblies in Japan. A feature of the I-type grid spacer spring design is good stability of the spring force even after excessive displacement due to fuel rod vibration or decreased spring deflection due to the creep-down of the outer diameter of the fuel rod cladding.

The design of the I-type grid spacer improves the resistance to grid fretting, and there has been no evidence of fuel leakage due to grid fretting during approximately 16 years of experience with over 3,500 assemblies using the Mitsubishi I-type grid spacer design ⁽²⁻¹⁾.

A high performance grid spacer, called Z3 type, is used in the US-APWR fuel. The Z3 type high performance grid spacer retains the performance features of the I-type grid spacer, with:

- Improved DNB performance and reduced pressure-drop due to mixing vane design improvements.
- Improved seismic performance due to grid spacer strap design improvements. The improved design uses an improved spring shape to reduce the stresses at the spring.

Figure 2.2-7 shows the high performance grid spacer. The results of the hydraulic testing, the DNB testing and impact testing confirmed good performance of the Z3 type grid ^{(2-1),(2-2)}.

The outermost straps of all grid spacers are provided with guide vanes and guide tabs to avoid interference with adjacent fuel assemblies and the neutron reflector during loading and unloading of the fuel assemblies.

2.3 In-Core Control Components

The in-core control component specifications are given in Table 2.0-3. Except for their length, the geometry and materials of the US-APWR in-core control components are the same as those of the current Mitsubishi in-core control components.

2.3.1 Control Rods and Rod Cluster Control Assemblies

As shown in Figure 2.3-1, the rod cluster control assembly consists of the spider assembly and the control rods attached to the spider assembly. The rod cluster control assemblies are inserted into the control rod guide thimbles of the fuel assemblies in specific positions in the reactor.

The control rod contains a neutron absorbing alloy composed of 80 % silver, 15 % indium and 5 % cadmium, and a coil spring made of type 302 stainless steel in a cladding made of type 304 stainless steel.

Both ends of the control rod are plugged by end plugs and welded. To prevent excessive loads on the cladding, the diametrical clearance between the cladding and the absorber is

determined to accommodate the difference in thermal expansion between the cladding and the absorber. The bottom end plug, which is made of type 308 stainless steel, has a bullet tip shape to reduce water resistance and expedite smooth control rod insertion during scrams. The top end plug is made of the same material as the bottom end plug. The top end plug consists of two structurally different sections: a section with a screw for connecting to the spider assembly, and a section with a smaller diameter that provides flexibility at the root of the control rod attachment point.

The spider assembly consists of a spider body, a spring, a spring retainer and a bolt for attaching the spring to the spider body. The spider body is a single-piece machined structure, with vanes extended from the center of the body in a radial pattern. A control rod is hung at the tip of each vane. A groove is machined in the upper part of the spider body for connection with the handling tool and CRDM. A coil spring is contained and axially fixed by the bolt and the spring retainer inside the spider body. The retainer can move toward the inside of the spider body so that energy can be absorbed when the rod cluster control assembly impacts on the adapter plate of the top nozzle. The components of the spider assembly, except for the spring retainer and the coil spring, are made of type 304 stainless steel. The spring retainer and the coil spring are made of type 630 stainless steel and Inconel 718, respectively.

All of the rod cluster control assemblies are withdrawn from the fuel stack during normal operation. Reactor scram is achieved by gravitational drop of the rod cluster control assemblies together with the drive rods.

The design lifetime of the control rod and cluster control assembly is 15 years.

2.3.2 Burnable Absorber Rods and Assemblies

As shown in Figure 2.3-2, the burnable absorber assembly consists of the burnable absorber rods, thimble plug rods and the holddown assembly for attaching the burnable absorber rods.

The burnable absorber contains an annular tube made of borosilicate glass in a cladding made of type 304 stainless steel. The neutron absorption of the borosilicate glass gradually depletes with irradiation. This characteristic of the absorber allows its use for long term reactivity control and operational flexibility. The annular glass tube is axially supported on the inside by a thin spacer tube made of type 304 stainless steel.

Both ends of the cladding are plugged by end plugs and welded. Both end plugs are made of type 308 stainless steel. As with the control rod top end plug, the burnable absorber top end plug has two structurally different sections, one of which is screw-shaped, to connect the burnable absorber rod to the holddown assembly and the other of which has a reduced diameter.

The holddown assembly is composed of a base plate, a spring guide, a holddown spring and a holddown bar. The holddown assembly is located between the adapter plate of the top nozzle and the upper core plate in the reactor. Components of the holddown assembly other than the holddown spring are made of type 304 stainless steel. The holddown spring is made of Inconel 718. The base plate has holes with female screws to fix the burnable absorber and the thimble plug rods, and flow holes for the coolant. The spring guide supports the holddown spring and prevents the holddown bar from rotating. In order to prevent the burnable absorber assembly from lifting due to the hydraulic force of the coolant, the holddown spring provides a

compression force via the holddown bar, which is compressed downward by the upper core plate. Both ends of the holddown bar are bent so as to not interfere with the top nozzle.

2.3.3 Neutron Source Rods and Assemblies

As shown in Figure 2.3-3, the primary source assembly consists of a primary source rod, thimble plug rods and the same holddown assembly as the burnable absorber assembly. The primary source assembly is used for supplying neutrons at reactor startup and for sub-criticality monitoring during the first fuel loading.

A duplex structure consisting of an outer cladding and a capsule is used in the primary neutron source rods. The outer cladding of the primary neutron source rod encases a capsule that contains californium as the neutron source, and a spacer tube for positioning the capsule. The outer cladding, the capsule and the spacer tube are made of type 304 stainless steel.

Each end of the outer cladding is plugged by an end plug and welded. Both end plugs are made of type 308 stainless steel.

While californium undergoes α decay with emission of an α particle, its spontaneous fission also radiates neutrons. Although helium gas is released due to the α decay, the internal pressure of the outer cladding is not increased, since the source is contained in the capsule.

As shown in Figure 2.3-4, the secondary source assembly consists of four secondary source rods, thimble plug rods and the same holddown assembly as the burnable absorber and primary source assemblies. The secondary neutron source assembly is used for supplying neutrons at reactor startup and for sub-criticality monitoring during fuel loading.

While the primary neutron source is radioactive from the beginning, the secondary neutron source becomes radioactive during reactor operation and then is able to function as the neutron supplier during reactor startup. The secondary neutron source assembly is used instead of the primary source assembly after the initial reactor startup.

The secondary neutron source rod also has a duplex structure composed of an outer cladding and a capsule containing the secondary neutron source. The capsule is made of type 304 stainless steel and contains mixed antimony and beryllium pellets, a spring clip made of type 401 stainless steel and a spacer tube made of type 304 stainless steel. The capsule is inserted into the outer cladding made of type 304 stainless steel. The outer cladding is plugged by the end plugs and welded. The antimony and beryllium in the secondary neutron source pellets are mixed with volume ratio of 50 % each.

2.3.4 Thimble Plug Rods and Assemblies

The thimble plug assembly can be installed into fuel assemblies that are not equipped with other in-core control components such as the rod cluster control, burnable absorber and neutron source assemblies. The thimble plug assembly has a structure in which thimble plug rods are fixed to the same holddown assembly as other holddown type of in-core control components. The thimble plug rods are also used in other in-core control assemblies than the thimble plug assembly for plugging the control rod guide thimbles where the burnable absorber rods and neutron source rods are not installed. Thimble plug rods are solid rod structure made of type 304 stainless steel.

2.4 References

- (2-1) "Mitsubishi Fuel Design Criteria and Methodology", MUAP-07008-P (Proprietary) and MUAP-07008-NP (Non-Proprietary), May 2007
- (2-2) "Thermal Design Methodology", MUAP-07009-P (Proprietary) and MUAP-07009-NP (Non-Proprietary), May 2007

**Table 2.0-1 (1/2) The US-APWR Fuel System Design Parameters
(Fuel Assembly)**

| | Nominal | Note |
|---|--|----------------|
| Fuel Assembly | | |
| Fuel rod array | 17 x 17 | |
| Number of fuel rods | 264 | |
| Number of control rod guide thimbles | 24 | |
| Number of in-core instrumentation guide tube | 1 | |
| Number of grid spacers | 11 | |
| Measure for trapping debris | Anti-debris bottom nozzle with built-in filter | |
| Materials | | |
| Top/Bottom nozzle | Type 304 Stainless Steel | |
| Top nozzle holddown spring | Inconel -718 * | |
| Top/Bottom grid spacer | Inconel -718 * | |
| Intermediate grid spacer | Zircaloy-4 | Recrystallized |
| Control rod guide thimble | Zircaloy-4 | Recrystallized |
| In-core instrumentation guide tube | Zircaloy-4 | Recrystallized |
| Sleeve between top nozzle and top grid spacer | Type 304 Stainless Steel | |
| Sleeve for intermediate grid spacers | Zircaloy-4 | |

* Inconel 718 is nickel-chromium-iron Alloy 718.

Table 2.0-1 (2/2) The US-APWR Fuel System Design Parameters (Fuel Assembly)

| | Nominal | Tolerances | Note |
|---|---------------------|------------|------|
| Geometry | | | |
| Overall fuel assembly length | [] | [] | |
| Maximum fuel assembly width | 8.426 in.(214.02mm) | | |
| Fuel rod pitch | 0.496 in.(12.6mm) | | |
| Equivalent hydraulic diameter | 0.464 in.(11.78mm) | | |
| Control rod guide thimble outer diameter (upper part) | 0.482 in.(12.24mm) | | |
| Control rod guide thimble inner diameter (upper part) | 0.450 in.(11.43mm) | | |
| Control rod guide thimble outer diameter (lower part) | 0.429 in.(10.9mm) | | |
| Control rod guide thimble inner diameter (lower part) | 0.397 in.(10.08mm) | | |
| In-core instrumentation guide tube outer diameter | 0.482 in.(12.24mm) | | |
| In-core instrumentation guide tube inner diameter | 0.450 in.(11.43mm) | | |

* These values indicate the fuel assembly length excluding the top nozzle clamp height.

Table 2.0-2 (1/2) The US-APWR Fuel System Design Parameters (Fuel Rod)

| Fuel Rod | Nominal | Tolerances | Note | |
|------------------------------------|--|------------|--------------|---------------|
| Overall rod length | 181.5 in.(4610mm) | | | |
| Upper plenum length | 6.77 in.(172mm) | | | |
| Lower plenum length | [] | | | |
| Rod internal void volume | [] | | | |
| Fill gas type and pressure | [He gas] | | | |
| Sorbed gas composition and content | - | | | |
| Active fuel length | 165.4 in. (4,200mm) | | | |
| Outer diameter | 0.374 in. (9.50mm) | | | |
| Rod design burnup | 62,000 MWD/MTU | | | |
| Pellet | | | | |
| Material | Sintered uranium dioxide(UO ₂) Sintered gadolinia-uranium dioxide((U, Gd)O ₂) | | | |
| Fissile enrichment (wt%U-235) | 2.05/3.55/4.15 | | Region 1/2/3 | |
| Pellet diameter | 0.322 in. (8.19 mm) | | | |
| Pellet length | 0.453 in.(11.5mm) | | | |
| Pellet dish dimensions | [] | | Figure 2.1-2 | |
| Pellet chamfer dimensions | [] | | | |
| Pellet roughness | - | | | |
| Pellet density | 97%TD | | | |
| Pellet resintering data | [] | | | Typical value |
| Pellet grain size | - | | [] | Typical value |
| Open porosity | [] | | | Typical value |
| Burnable absorber (Gd) content | Max10wt% | [] | | |

Table 2.0-2 (2/2) The US-APWR Fuel System Design Parameters (Fuel Rod)

| | Nominal | Tolerances | Note |
|--|---------------------------|------------|------|
| Cladding | | | |
| Material of cladding | ZIRLO | | |
| Type and metallurgical state of the cladding | Cold Work Stress relieved | | |
| Cladding outer diameter | 0.374 in. (9.50mm) | | |
| Cladding inner diameter | 0.329 in. (8.36mm) | | |
| Cladding thickness | — | | |
| Cladding inside roughness | — | | |
| Pellet spring and endplugs | | | |
| Upper plenum spring | | | |
| Lower plenum spacer volume | | — | |
| Length of upper endplug | | — | |
| Length of lower endplug | | — | |

**Table 2.0-3 (1/2) The US-APWR Fuel System Design Parameters
(In-Core Control Components)**

| | Nominal | Tolerances | Note |
|--------------------------------------|---------------------------|------------|------|
| Rod Cluster Control Assembly | | | |
| Number of control rods per assembly | 24 | | |
| Absorber material | Ag (80%)-In (15%)-Cd (5%) | | |
| Upper absorber length | 151.3 in.(3843mm) | [] | |
| Lower absorber length | [] | | |
| Upper absorber outer diameter | 0.341 in.(8.66mm) | | |
| Lower absorber outer diameter | [] | | |
| Cladding material | Type 304 Stainless Steel | | |
| Cladding outer diameter | 0.381 in.(9.68mm) | [] | |
| Cladding inner diameter | 0.344 in.(8.74mm) | | |
| Cladding thickness | - | | |
| Design lifetime | 15 years | | |
| Burnable Absorber Assembly | | | |
| Number of absorber rods per assembly | Max. 24 | | |
| Absorber material | Borosilicate-Glass | | |
| Absorber length | 159.4 in.(4050mm) | [] | |
| Cladding material | Type 304 Stainless Steel | | |
| Cladding outer diameter | 0.381 in.(9.68mm) | [] | |
| Cladding inner diameter | 0.344 in.(8.74mm) | | |
| Cladding thickness | - | | |

**Table 2.0-3 (2/2) The US-APWR Fuel System Design Parameters
(In-Core Control Components)**

| | Nominal | Tolerances | Note |
|--|--------------------------|------------|------|
| Neutron Source Assembly (Primary Neutron Source Assembly) | | | |
| Number of source rods per assembly | 1 | | |
| Neutron source material | Californium 252 | | |
| Neutron source outer diameter | 0.330 in.(8.38mm) | [] | |
| Neutron source length | 1.5 in.(38mm) | [] | |
| Cladding material | Type 304 Stainless Steel | | |
| Cladding outer diameter | 0.381 in.(9.68mm) | [] | |
| Cladding inner diameter | 0.344 in.(8.74mm) | [] | |
| Cladding thickness | – | [] | |
| Neutron Source Assembly (Secondary Neutron Source Assembly) | | | |
| Number of source rods per assembly | 4 | | |
| Neutron source material | Antimony–Beryllium | | |
| Neutron source outer diameter | 0.292 in. (7.42mm) | [] | |
| Neutron source length | 88.0 in.(2235.2mm) | – | |
| Cladding material | Type 304 Stainless Steel | | |
| Cladding outer diameter | 0.381 in.(9.68mm) | [] | |
| Cladding inner diameter | 0.344 in.(8.74mm) | [] | |
| Cladding thickness | – | [] | |

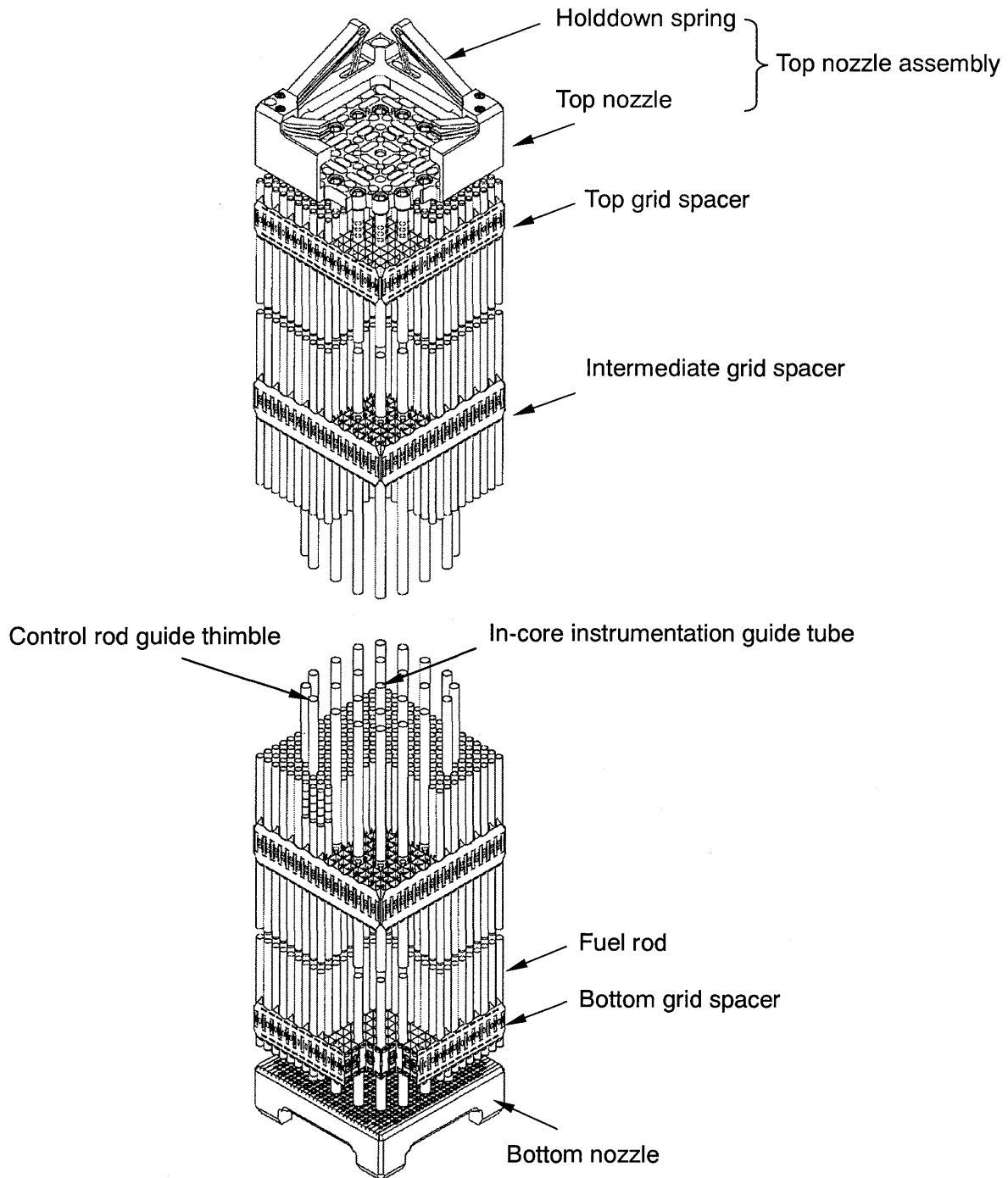
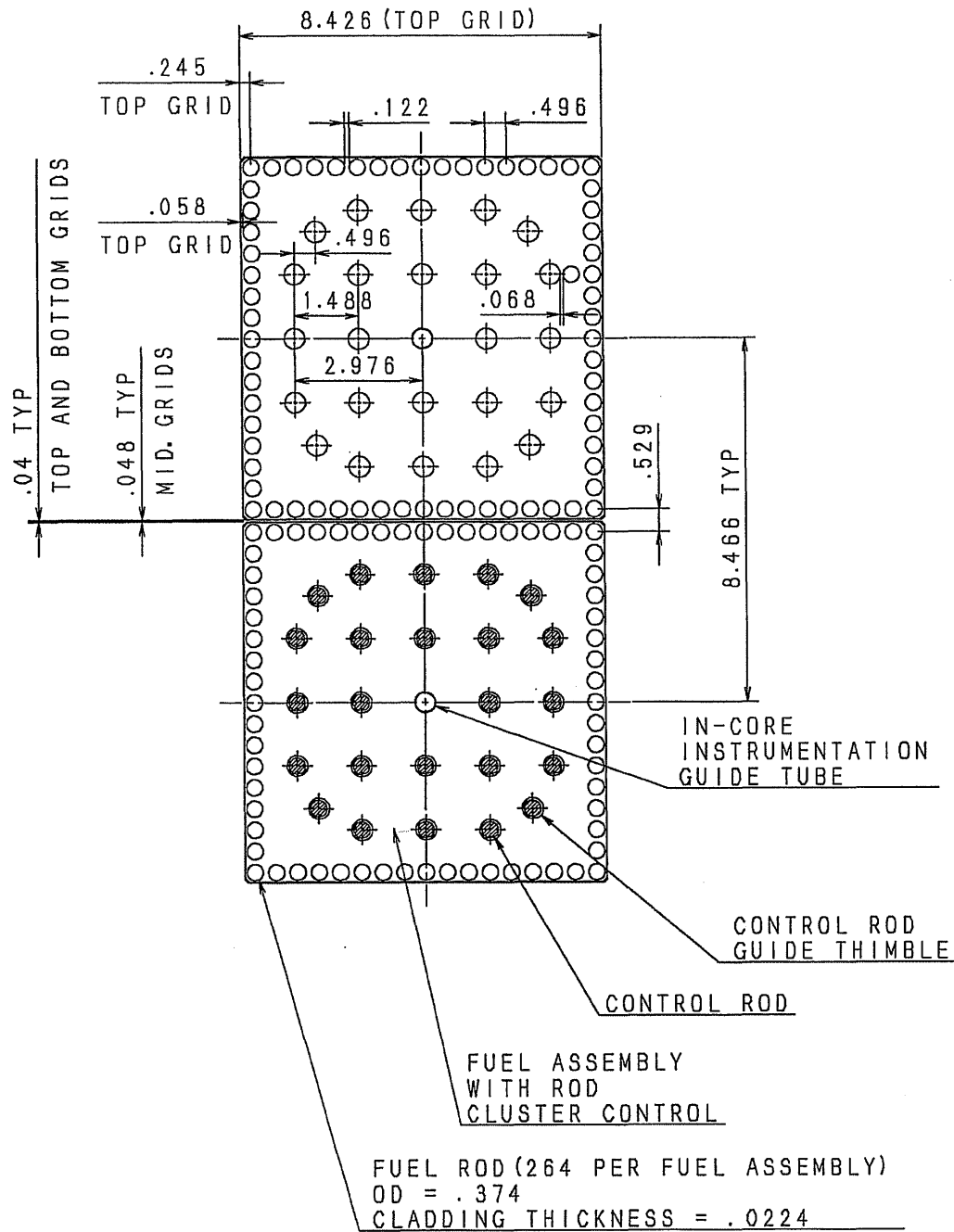
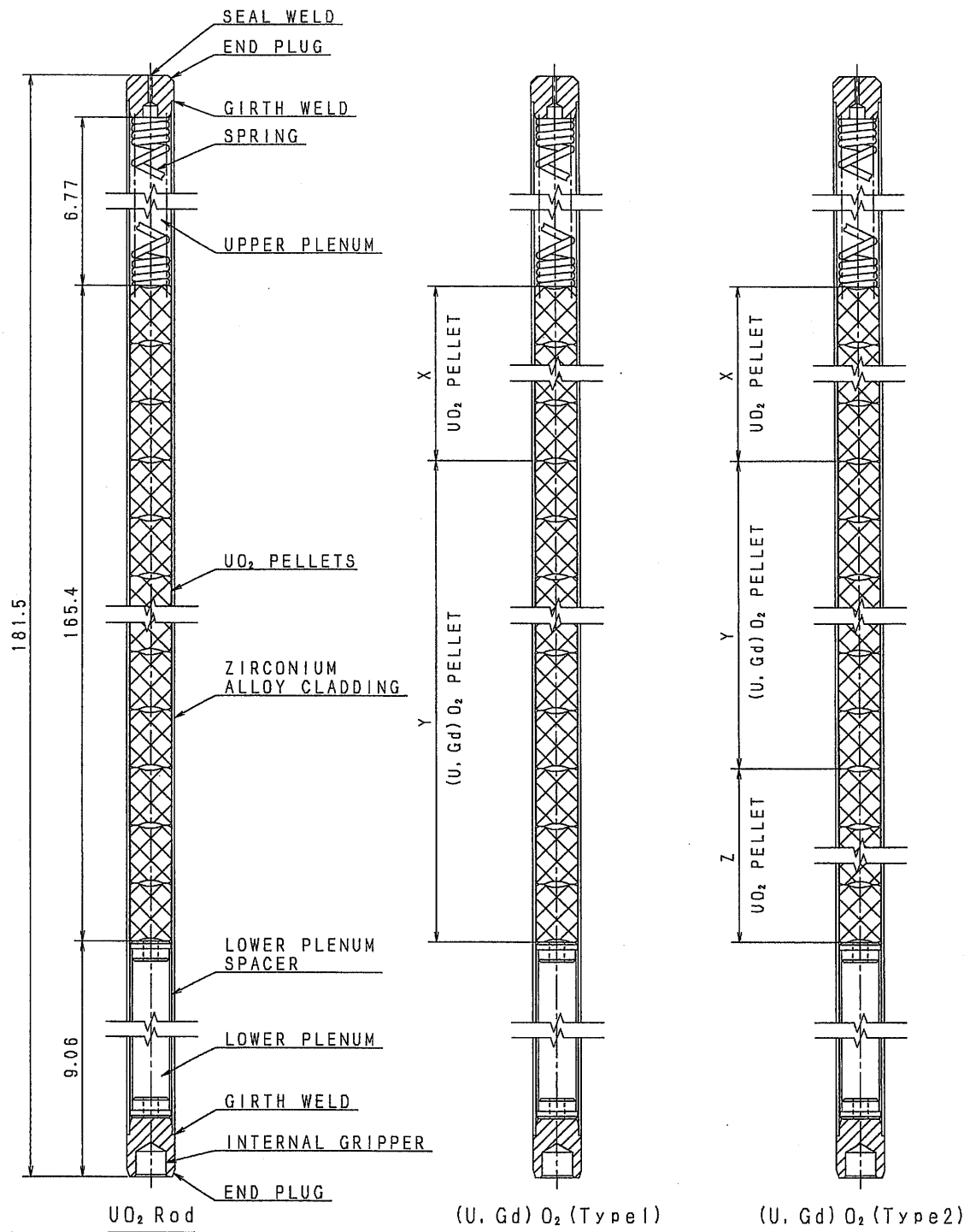


Figure 2.0-1 Fuel Assembly Schematic View



DIMENSIONS ARE IN INCHES (NOMINAL)

Figure 2.0-2 Fuel Assembly Array Cross Section



X,Y,Z dimensions depend on core design.
Dimensions are in inches.

Figure 2.1-1 Fuel Rod Schematic View

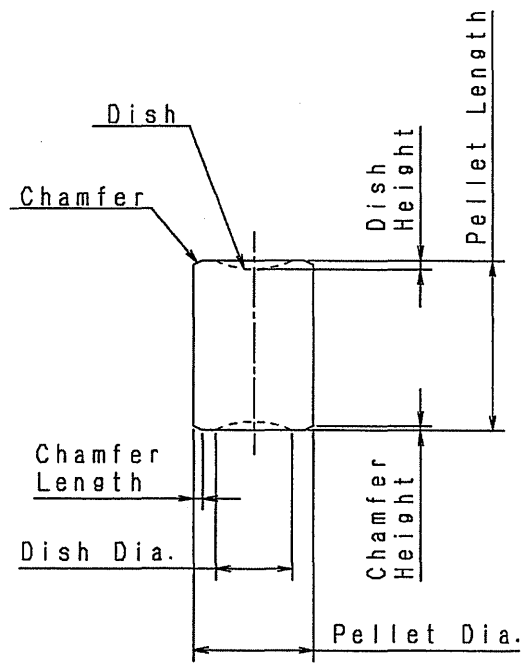


Figure 2.1-2 Fuel Pellet Schematic View

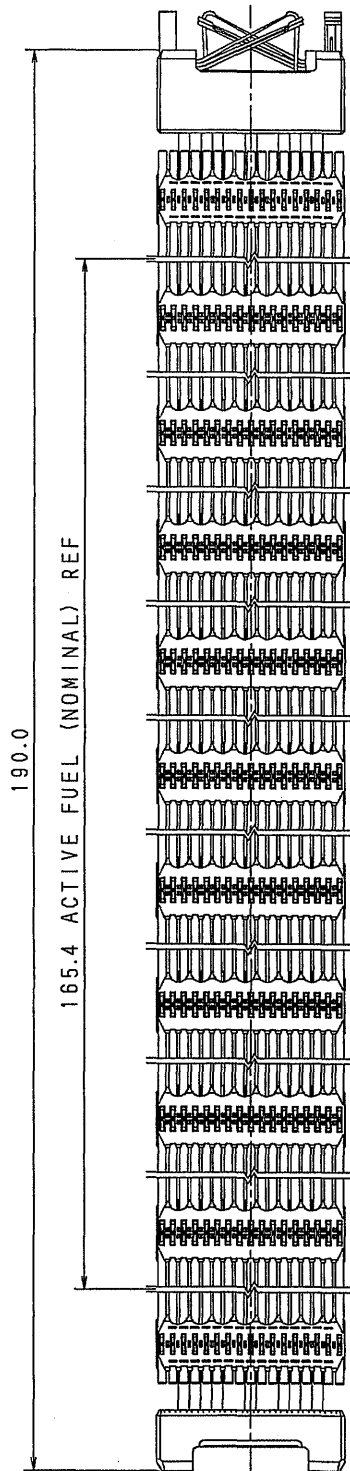
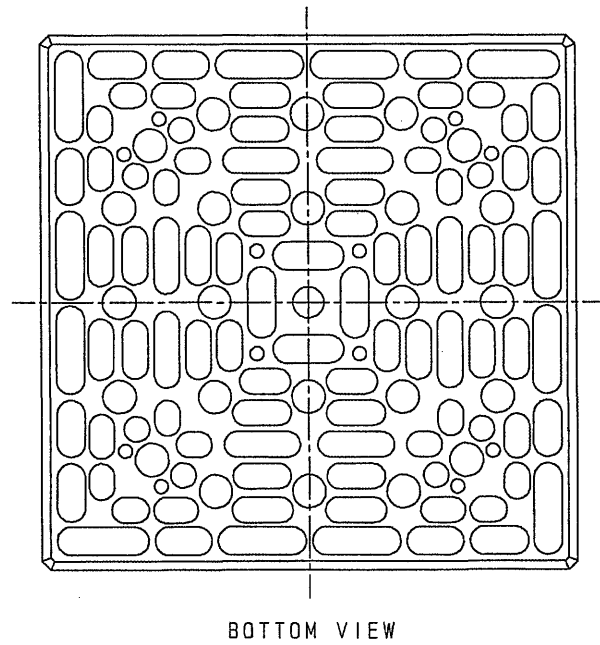
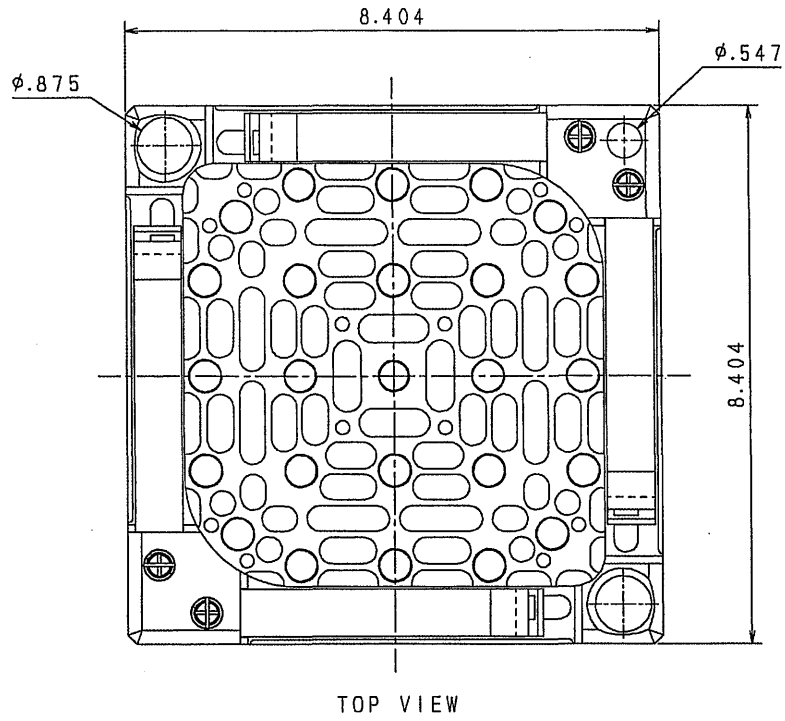
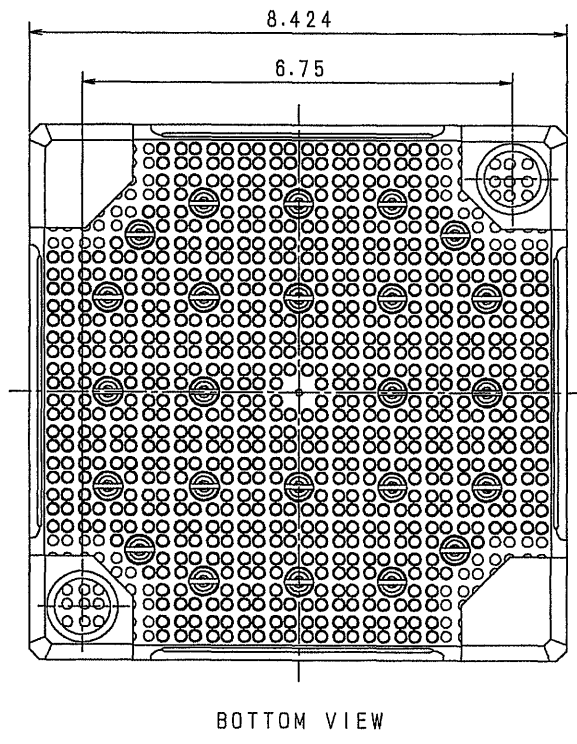
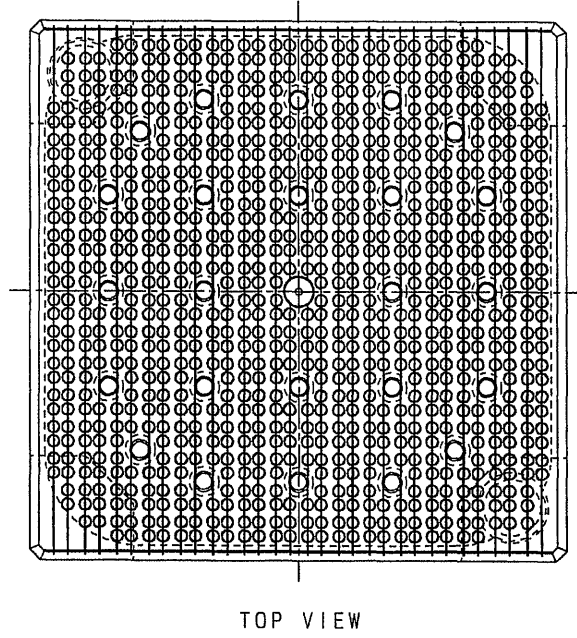


Figure 2.2-1 Fuel Assembly Full-Length Schematic View (1/3)



Top Nozzle

Figure 2.2-1 Fuel Assembly Full-Length Schematic View (2/3)



Bottom Nozzle

Figure 2.2-1 Fuel Assembly Full-Length Schematic View (3/3)

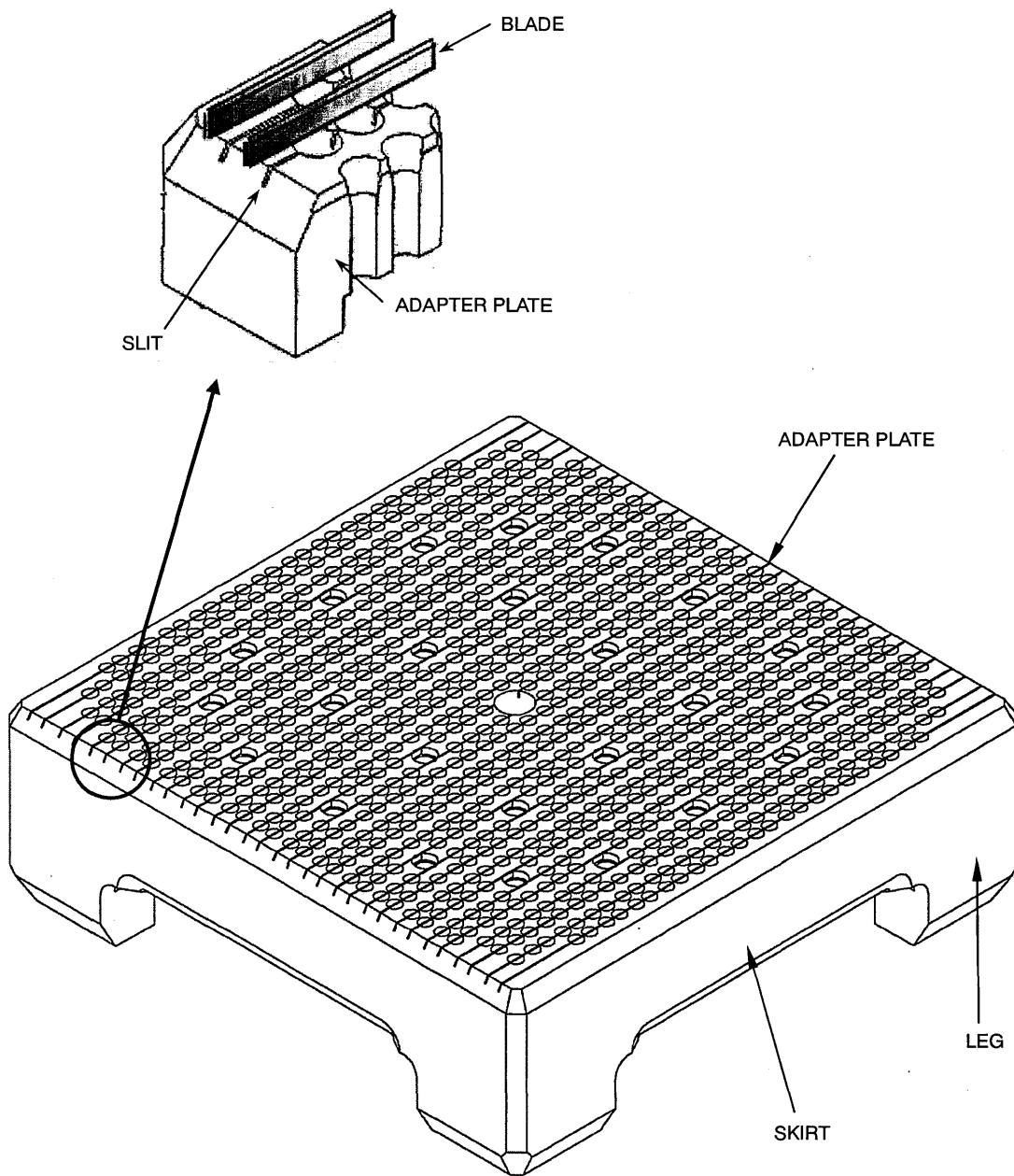


Figure 2.2-2 Bottom Nozzle Schematic View

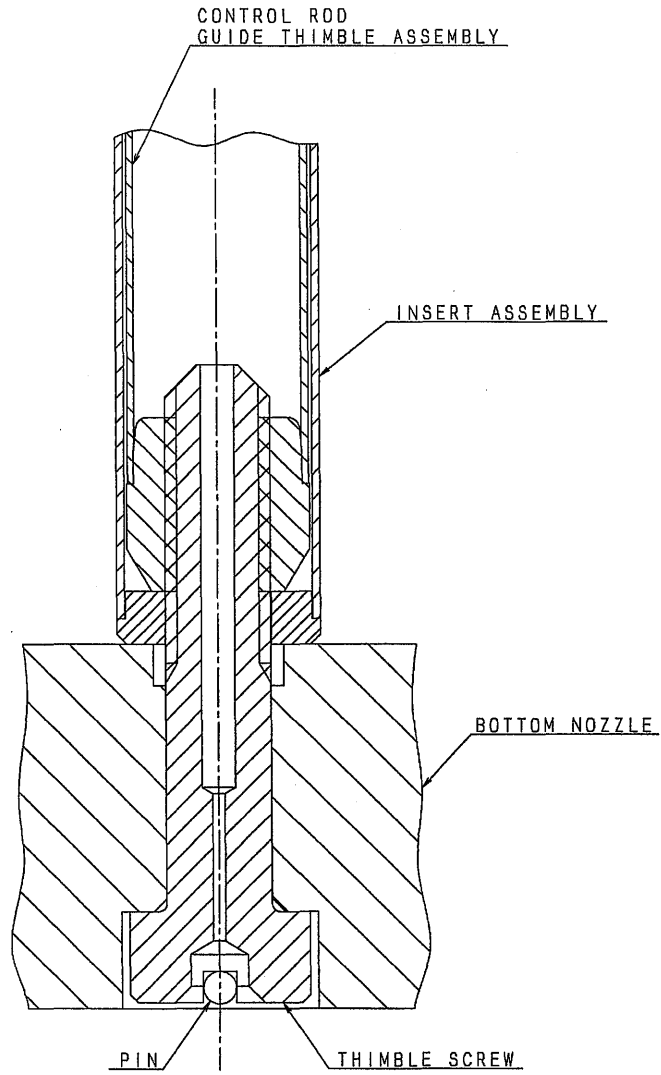


Figure 2.2-3 Control Rod Guide Thimble to Bottom Nozzle Joint

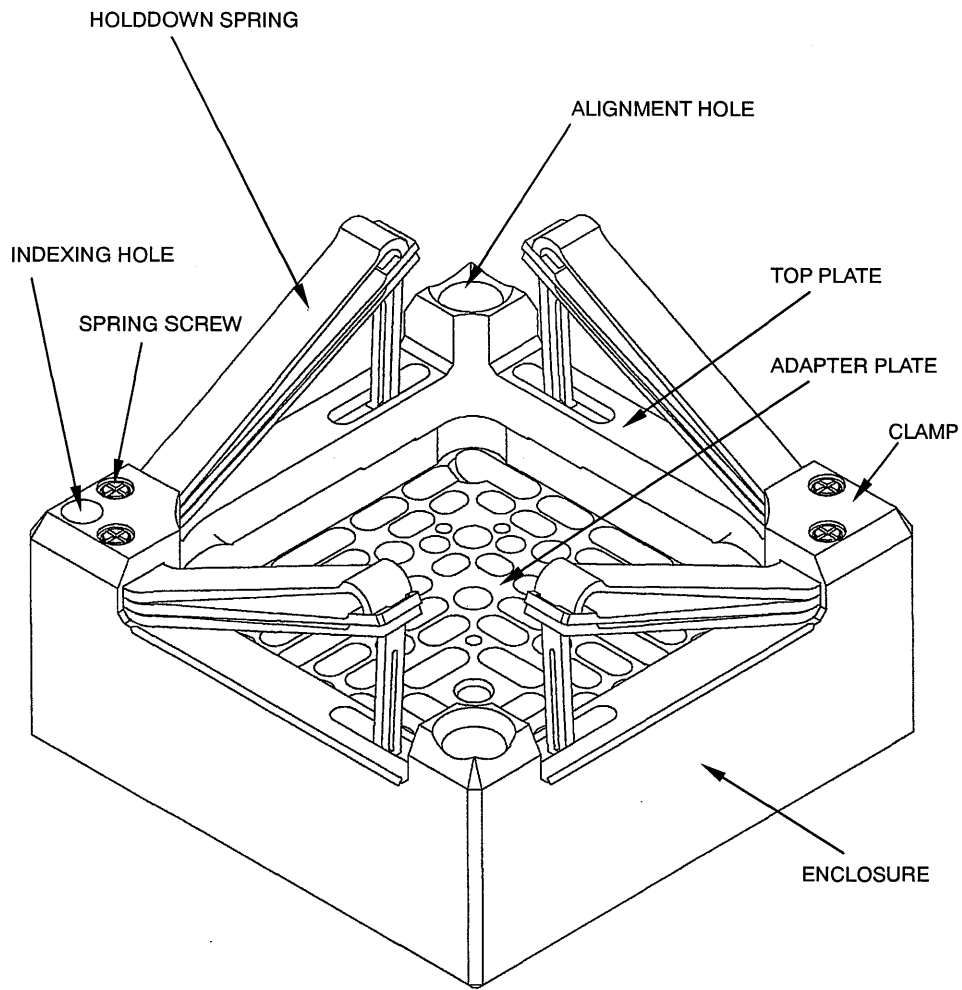


Figure 2.2-4 Top Nozzle Schematic View

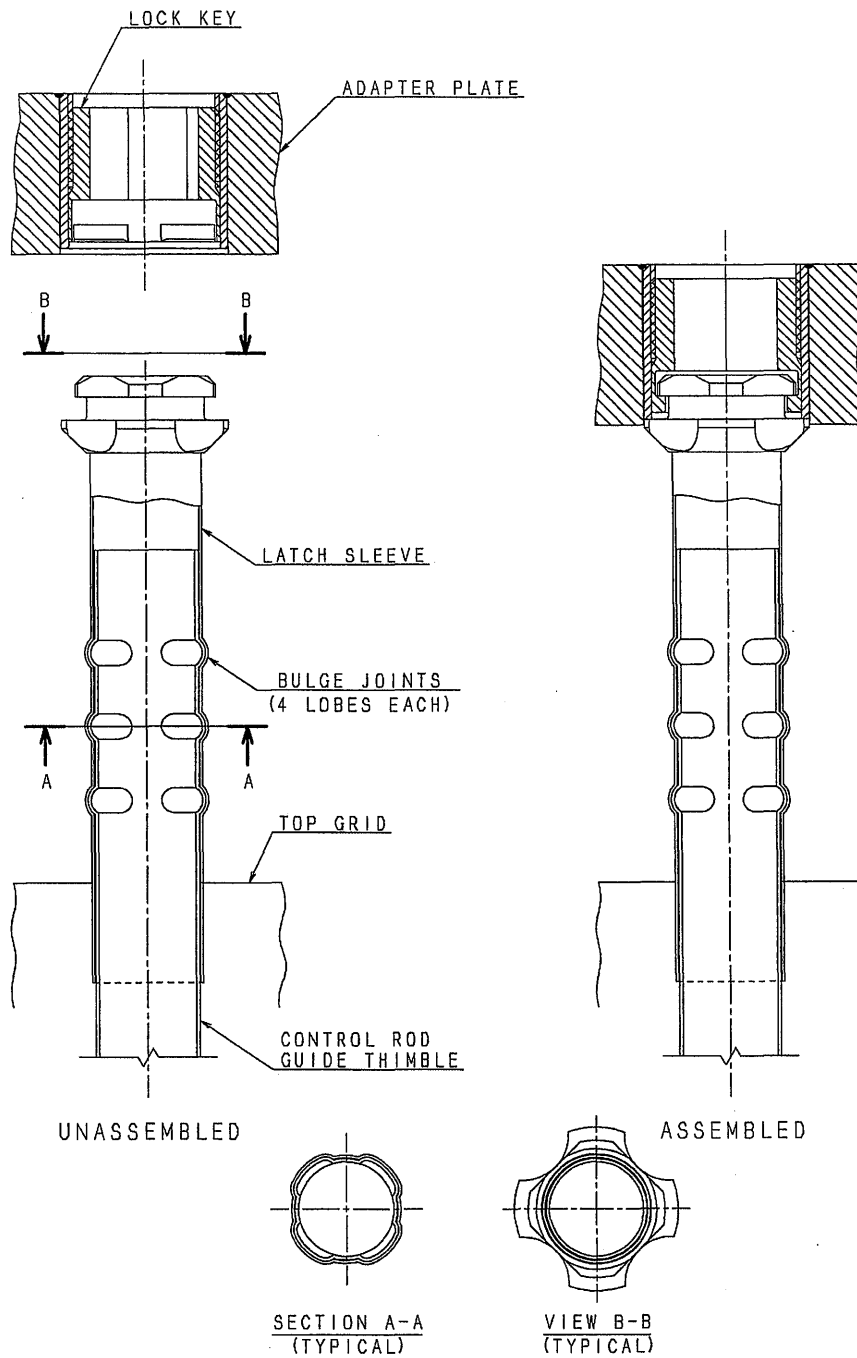
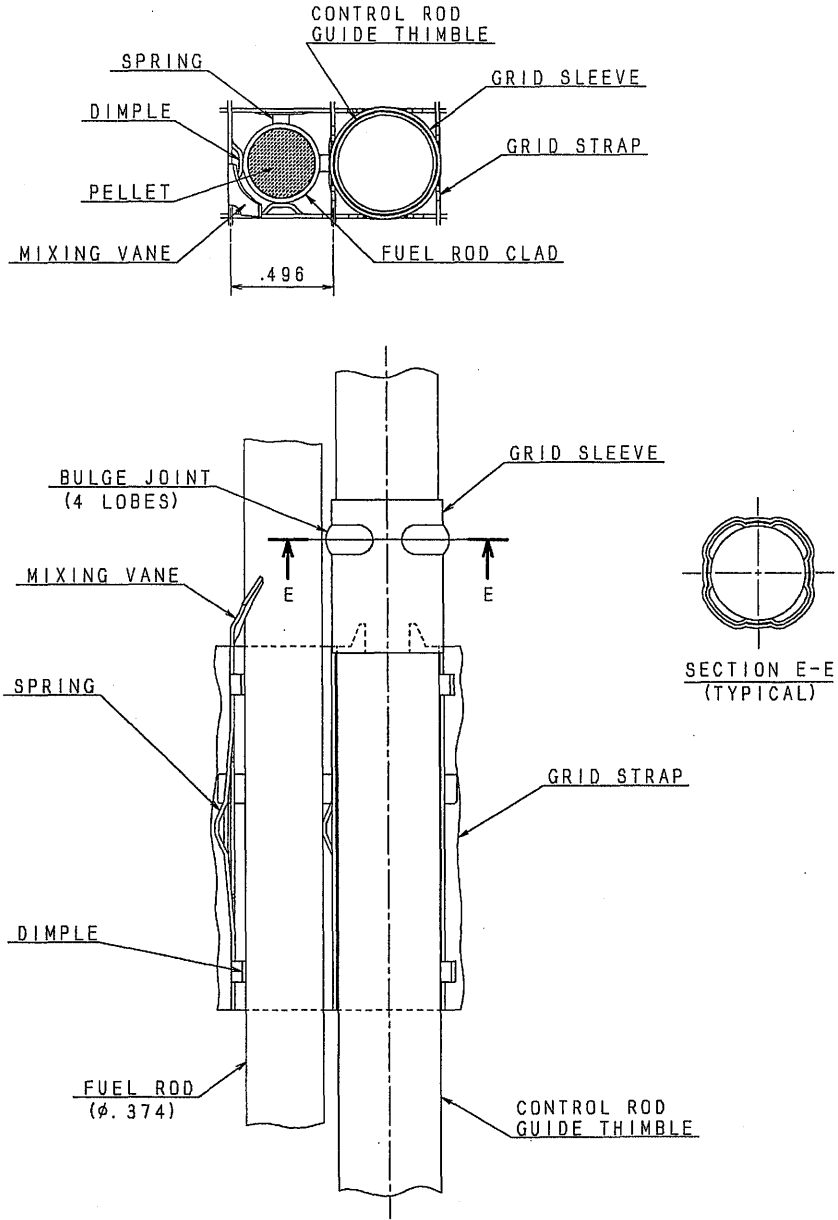
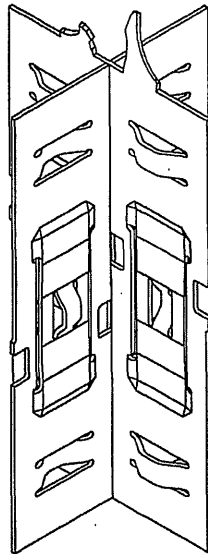


Figure 2.2-5 Control Rod Guide Thimble to Top Nozzle Joint



DIMENSIONS ARE IN INCHES (NOMINAL)

Figure 2.2-6 Control Rod Guide Thimble to Intermediate Grid Spacer Joint



Mitsubishi Conventional Grid Spacer (I-type Design: Z2 Type)

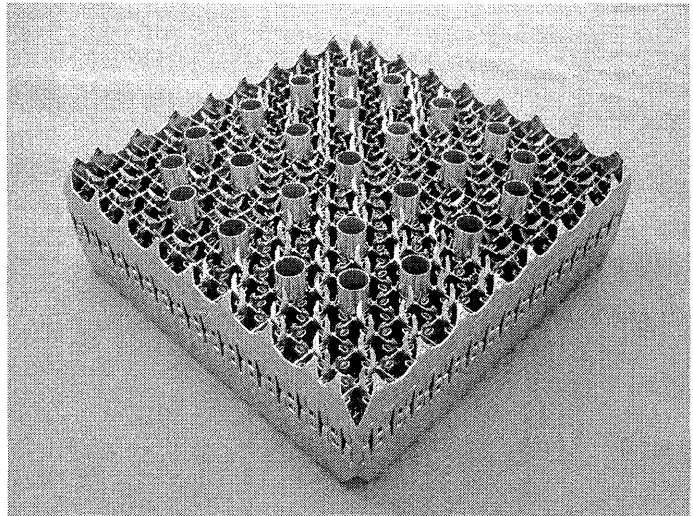
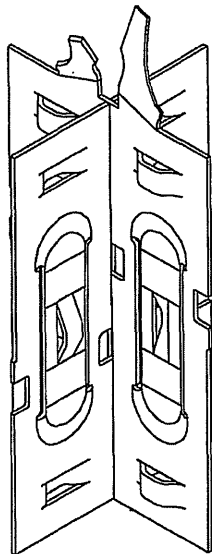


Figure 2.2-7 High Performance Grid Spacer (Z3 Type) Schematic View

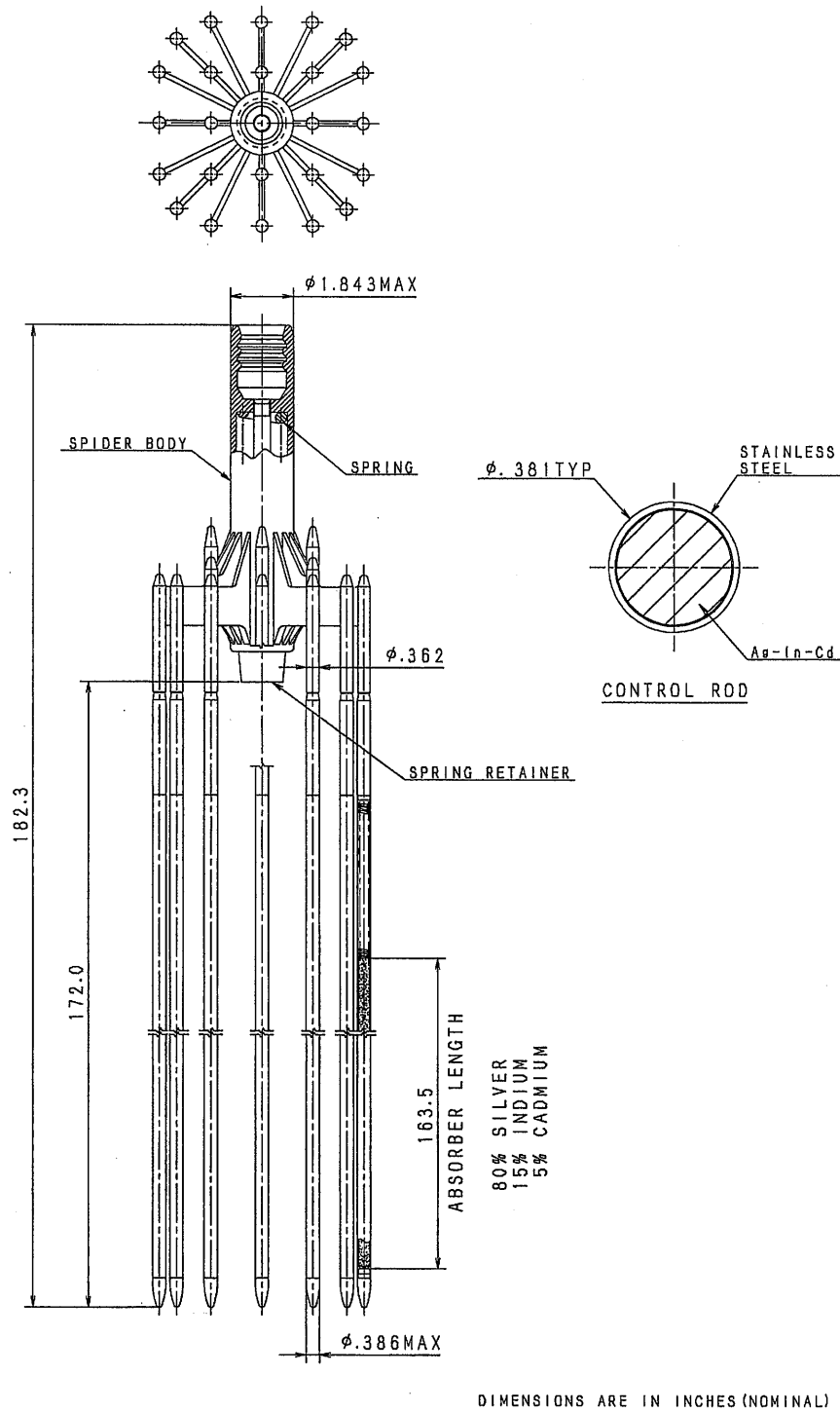
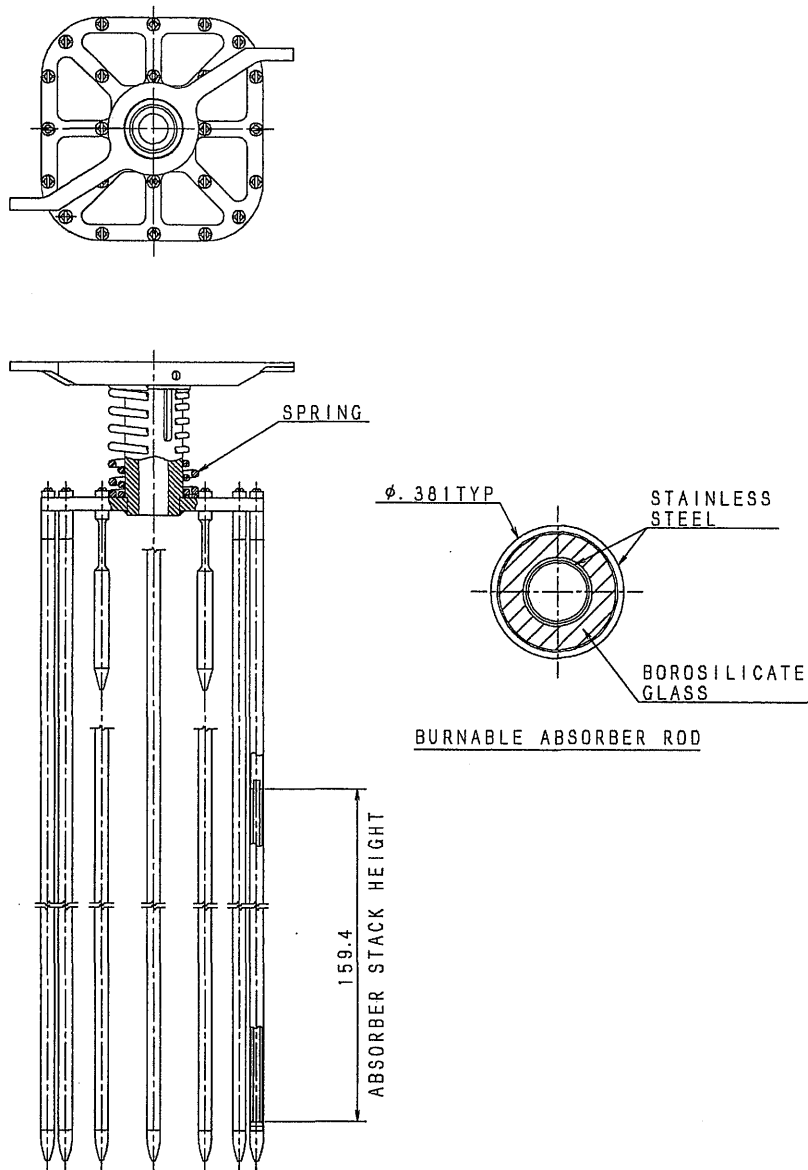
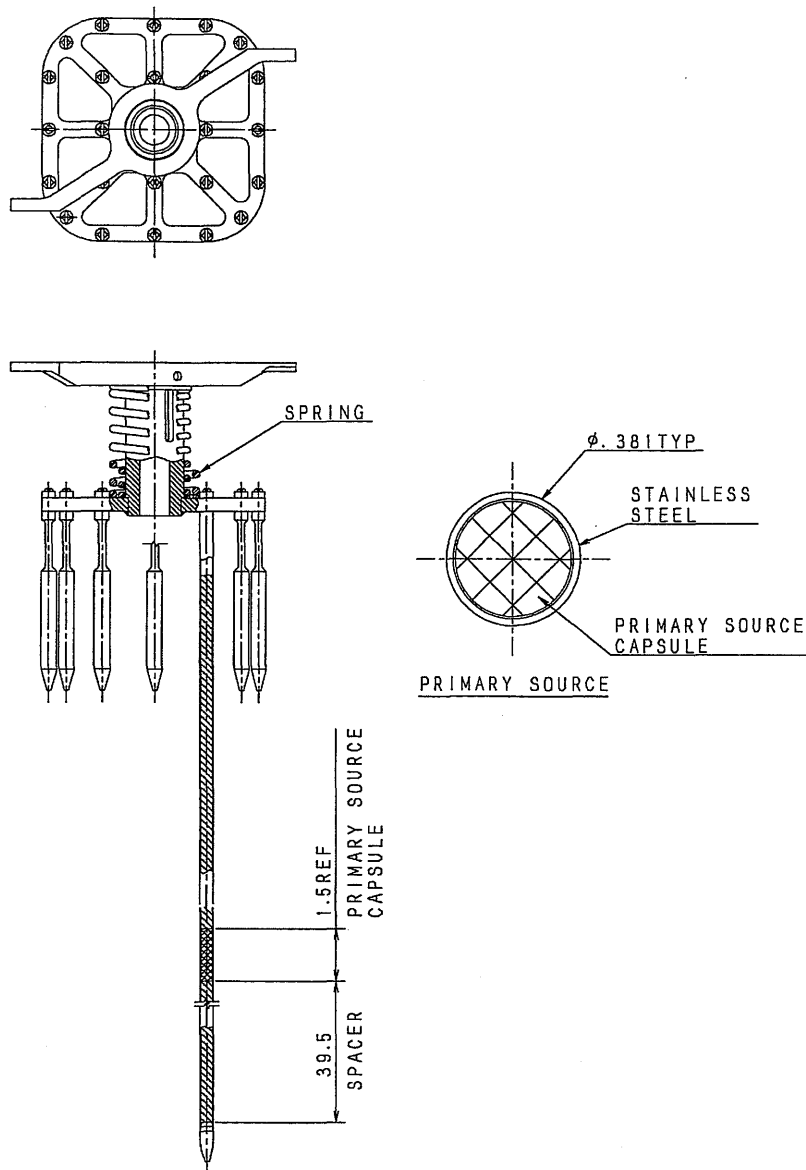


Figure 2.3-1 Rod Cluster Control Assembly Schematic View



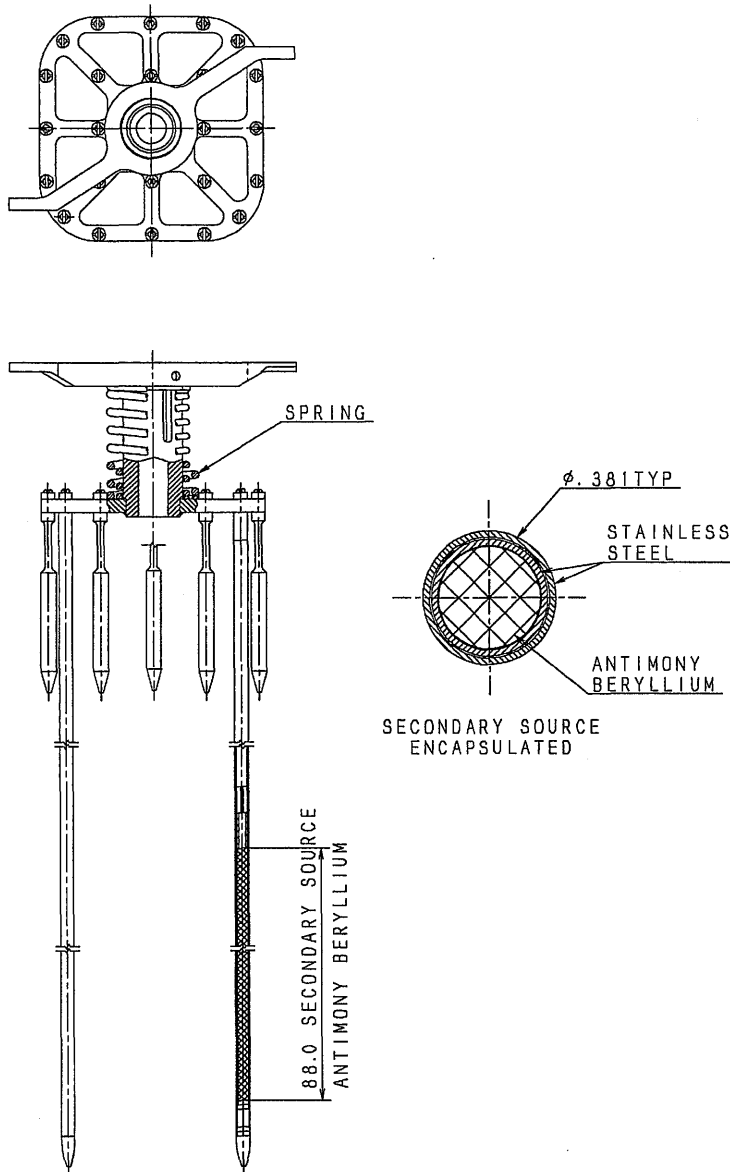
DIMENSIONS ARE IN INCHES (NOMINAL)

Figure 2.3-2 Burnable Absorber Assembly Schematic View



DIMENSIONS ARE IN INCHES (NOMINAL)

Figure 2.3-3 Primary Source Assembly Schematic View



DIMENSIONS ARE IN INCHES (NOMINAL)

Figure 2.3-4 Secondary Source Assembly Schematic View

3.0 FUEL ROD DESIGN EVALUATION

This section describes the Mitsubishi fuel rod design evaluation process for the following fuel rod design criteria evaluations.

- Fuel Rod Internal Pressure
- Cladding Stresses
- Chemical Reaction
- Cladding Fatigue
- Creep Collapse
- Cladding Strain
- Fuel Temperature
- Fuel-Cladding Mechanical Interaction

3.1 General

Mitsubishi has developed the FINE code ⁽³⁻¹⁾ for fuel rod design evaluations. The FINE code is applicable for US-APWR fuel rod design as described in subsection 3.1.1.

The US-APWR fuel rod specifications are given in Chapter 2 of this report. The most sensitive and important parameter for the fuel rod design evaluation is the rod power distribution. Power histories based on reactor core analysis are the primary interface data obtained from the core design. Since each fuel rod in the core has its own specific power history in actual operation and there are large numbers of fuel rods in the reactor core, it is necessary to treat power histories as described in subsection 3.1.2.

To ensure fuel rod integrity as part of the design process, the fuel rod design must be evaluated with consideration of the impact of uncertainties. The uncertainties that must be accounted for in the design evaluations include manufacturing uncertainties, performance model uncertainties, and operational uncertainties as described in subsection 3.1.3.

The material properties of each component of the fuel rod ⁽³⁻¹⁾ are used in the fuel rod design.

3.1.1 FINE Code

The FINE Code is used for fuel rod licensing evaluations, and the details of its models are given in "Mitsubishi Fuel System Design Criteria and Methodology," MUAP-07008-P/-NP ⁽³⁻¹⁾. The FINE code is applicable for US-APWR fuel rod design as follows:

Fuel : UO₂, (U,Gd)O₂ (Gadolinia content is up to 10wt%)
Cladding : ZIRLO
Burnup : up to 62GWD/MTU at fuel rod average burnup

3.1.2 Fuel Rod Power History

The fuel rod powers are time dependent, and are the primary data obtained from the interface between fuel rod design and core analysis, as described in Appendix A of this report.

The fuel rod design considers all events expected during normal operation and AOOs. The fuel rod power as a function of the irradiation time, i.e., the fuel rod power history, is an important parameter in the assessment of fuel rod behavior. Some characteristic power histories are known to be most limiting with respect to margin to the fuel rod design limits. These limiting histories may be the highest or lowest power rods in a cycle or the highest burnup fuel rods in a cycle, depending on the fuel rod design criterion to be assessed. In general, a single fuel rod power history is not limiting for all fuel criteria, so a set of limiting characteristic power histories are typically assessed in the fuel rod design. These power histories bracket the range of fuel rod power histories for the fuel region, and provide the basis for assessing fuel rod performance relative to the established specified acceptable fuel design limits (SAFDLs).

General trends for the influence of the power history on the evaluations of specific design criteria, such as fuel rod internal pressure, cladding stresses, chemical reaction, cladding fatigue, cladding strain and fuel temperature, are:

- Fuel rod internal pressure

[]

- Cladding stresses

[]

- Chemical Reaction

[]

- Cladding Fatigue

[]

- Cladding strain

[]

- Fuel temperature

[]

Based on the above Mitsubishi fuel rod design evaluation experience, the following power history types at each fuel types are selected and assessed as part of the process for defining the limiting rods for each criterion.

[]

The time-dependant power histories based on the reactor core analysis are the interface information from the core design. The US-APWR fuel rod design evaluations given in this report use the core conditions, such as a 24 months cycle length and the equilibrium core described in Appendix A, to define the typical operating conditions for the US-APWR. Figure 3.1-1 and Figure 3.1-2 show maximum and minimum burnup power histories for UO_2 and $(\text{U,Gd})\text{O}_2$ fuel that are based on Appendix A.

3.1.3 Evaluation of Uncertainties

The manufacturing tolerances and the other uncertainties considered in the uncertainty assessment of the fuel design are summarized in Table 3.1-1. Specific values are shown in Table 3.1-2⁽³⁻¹⁾ and Table 3.1-3 as described in Chapter 2 of this report. The basis for the fuel rod performance model uncertainties is given in Chapter 4 of "Mitsubishi Fuel System Design Criteria and Methodology," MUAP-07008-P/-NP⁽³⁻¹⁾.

The effect of a specific uncertainty is evaluated by replacing the nominal or best estimate value of that input parameter for the fuel rod design evaluation with the value of the parameter including uncertainties. The effect of the uncertainty is given by the difference between the design result using the uncertainty and the design result with all best estimate or nominal inputs. These uncertainty effects are calculated separately for each uncertainty parameter. They are each considered to be statistically independent, and the total uncertainty in the design parameter is calculated by the SRSS (Square Root of the Sum of the Squares) method, where the difference from the best estimate value of the design parameter is considered to be at a 95% probability with a 95% confidence level if the input tolerances and uncertainties are each at least at a 95% probability with a 95% confidence level.

The uncertainty parameters selected for consideration for each criterion are based on the evaluation of which parameters have a significant effect on the design evaluation for that criterion. Tables 3.1-1, 3.1-2 and 3.1-3 identify the significant uncertainties for the fuel rod design criteria, based on the fuel rod design evaluations for US-APWR equilibrium core.

Table 3.1-1 (1/2) Fuel Design Uncertainty Assessment Items

| Item | Uncertainty Category | Criterion | | |
|------|----------------------|------------------|----------------------------|-----------------|
| | | Fuel Temperature | Fuel Rod Internal Pressure | Cladding Stress |
| | | | | |

Table 3.1-1 (2/2) Fuel Design Uncertainty Assessment Items

| Item | Uncertainty Category | Criterion | | | |
|------|----------------------|-----------------|------------------|-----------|----------|
| | | Cladding Strain | Cladding Fatigue | Oxidation | Hydrogen |
| | | | | | |

Table 3.1-2 Fuel Performance Model Uncertainty Parameters

| Model | Parameter |
|-------|-----------|
| | |

Table 3.1-3 Fuel Manufacturing Uncertainty Parameters

| Geometry | Parameter |
|----------|-----------|
| | |

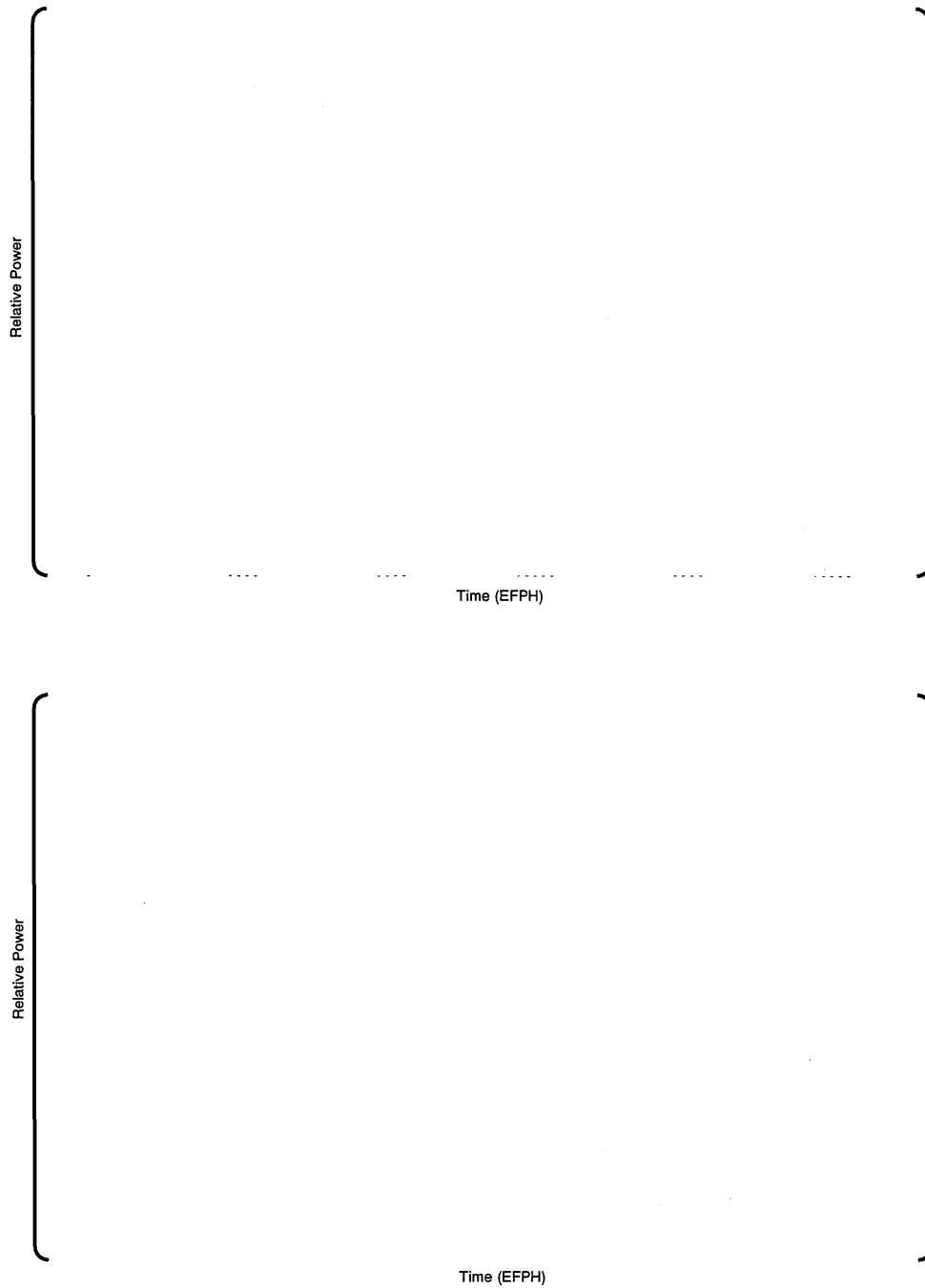


Figure 3.1-1 Examples of UO₂ Rod Power Histories Based on the US-APWR Equilibrium Core

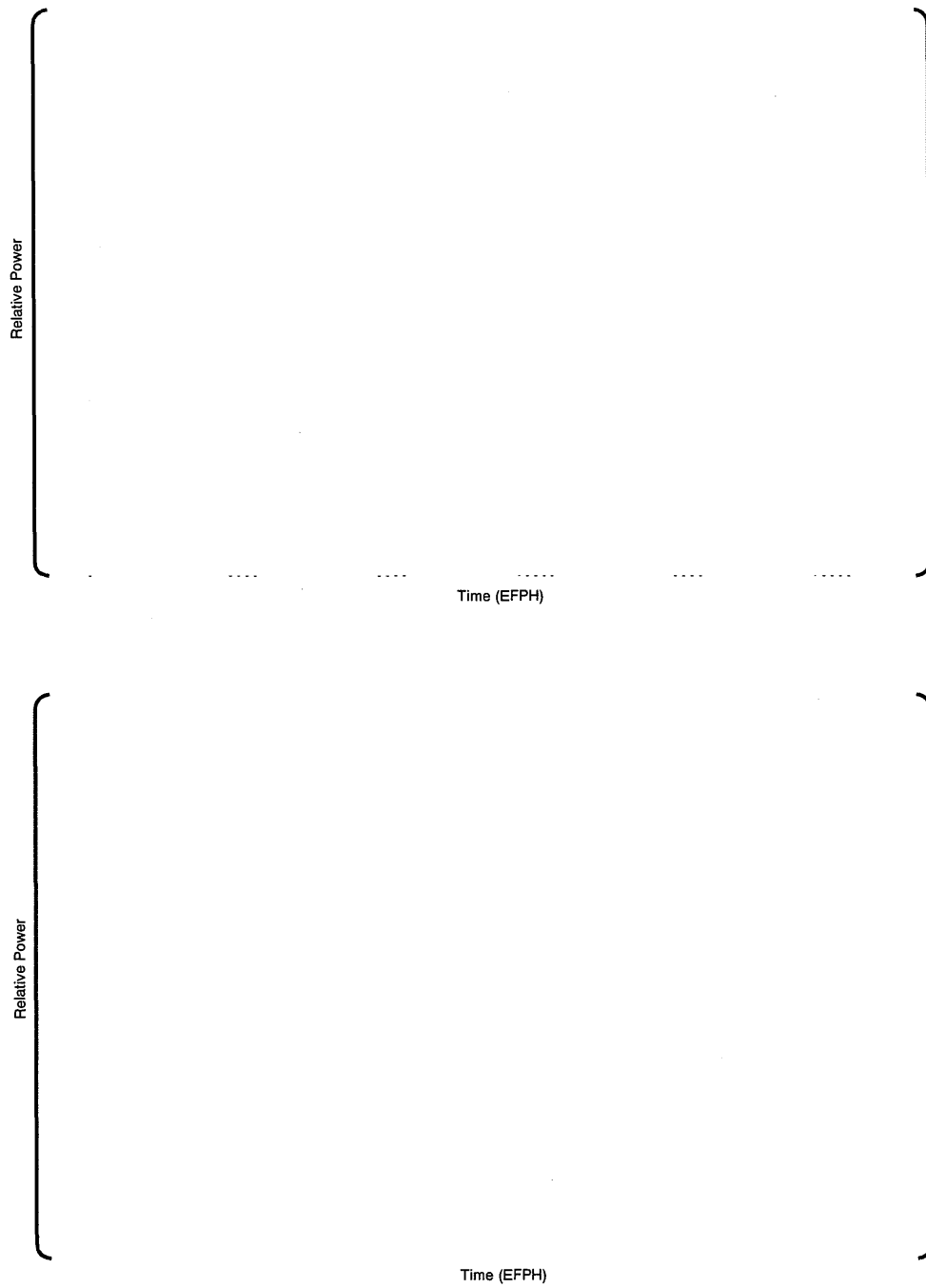


Figure 3.1-2 Examples of (U,Gd)O₂ Rod Power Histories Based on the US-APWR Equilibrium Core

3.2 Design Interface Data

Interface information is exchanged between fuel rod design and reactor core design, thermal-hydraulic design, safety analysis, reactor system design, and manufacturing. The core design and thermal-hydraulic design interfaces with fuel rod design are described in the following subsections.

3.2.1 Core Design Interface

The interface information from reactor core design is the reactor core operational conditions. The reactor core operational conditions include data for both normal operation and AOOs.

(1) Power History

The power of the fuel rod as a function of the irradiation time, or power history, is the most important parameter obtained from core design. The power history information is provided according to the guidelines given in subsection 3.1.2.

(2) AOO Power Level

The selection of the limiting AOO events, with respect to each fuel rod performance criterion addressed in the fuel system design is described in "Transient and Accident Analysis" (Chapter 15 of Safety Analysis Report) ⁽³⁻²⁾. The assessment of the impact of the limiting event on the local power duty is determined by reactor core analysis.

The limiting AOO events are selected in "Transient and Accident Analysis" (Chapter 15 of Safety Analysis Report) from the perspective of fuel performance that is most important for each fuel system design criterion.

The design assessment of the AOO is done, based on the reactor core analysis results for the local linear power density for the selected event, by setting the design maximum local linear power density (Local Power Limits: L.P.L.) to include the reactor core analysis results, with consideration of () data obtained from the reactor core calculation are included and considered in fuel rod evaluation:

$$\text{L.P.L.} = (\quad)$$

()

(3) Axial Power Distribution

The fuel irradiation conditions in the fuel rod design evaluation are defined by considering the time varying axial power distribution in the reactor core as well as the rod average power history. The FINE code allows for the input of a time varying axial power distribution, so that the change in the axial power distribution during each cycle is input. Typically, the change in the axial power distribution is characterized by defining the initial, middle and end of cycle shapes based on the reactor core calculation results. Typical axial distributions derived in this way are shown in Figure 3.2-1. In these axial power distributions, the initial shape is characterized by peaking in the middle of the rod, but as the burnup progresses, the power at the center of the

fuel rod reduces due to burnup effects and the peak rod powers shift to the upper and lower portions of the rod. Figure 3.2-1 also shows a cycle averaged axial power distribution.

(4) Fast Neutron Flux/Fluence

Since the cladding creep and irradiation growth depend on the fast neutron flux and fluence, conversion factors relating flux and fluence to power and burnup, respectively, are provided by reactor core design.

(5) Overshoot during Load Follow Operation

When evaluating the impact of load follow operation, the design evaluation accounts for the local power overshoots when the reactor power changes from a low power to a high power. The impact of load follow operation is accounted for by using the reactor core analysis values for the overshoot power.

3.2.2 Thermal-Hydraulic Design Interface

The interface information from the thermal-hydraulic design is the primary coolant system information.

(1) Primary Water Condition

The primary coolant flow rate, the primary coolant inlet temperature and the system pressure are required inputs for the fuel design evaluation. Typical primary coolant conditions for the US-APWR, are shown in Table 3.2-1.

(2) Linear Heat Rate

The core average linear heat generation rate is another critical input to the fuel design evaluation. Table 3.2-1 shows the core average linear heat generation rate for the US-APWR fuel rod design.

Table 3.2-1 US-APWR Thermal-Hydraulic Conditions

| | US-APWR |
|----------------------------------|--|
| Flow Rate* | $2.28 \times 10^6 \text{ lb/ft}^2/\text{hr}$ |
| Inlet Temperature* | 550.6deg.F |
| System Pressure | 2250psi |
| Core Average Linear Heat Rate | 4.6kW/ft |

* TDF, 10% Plugging

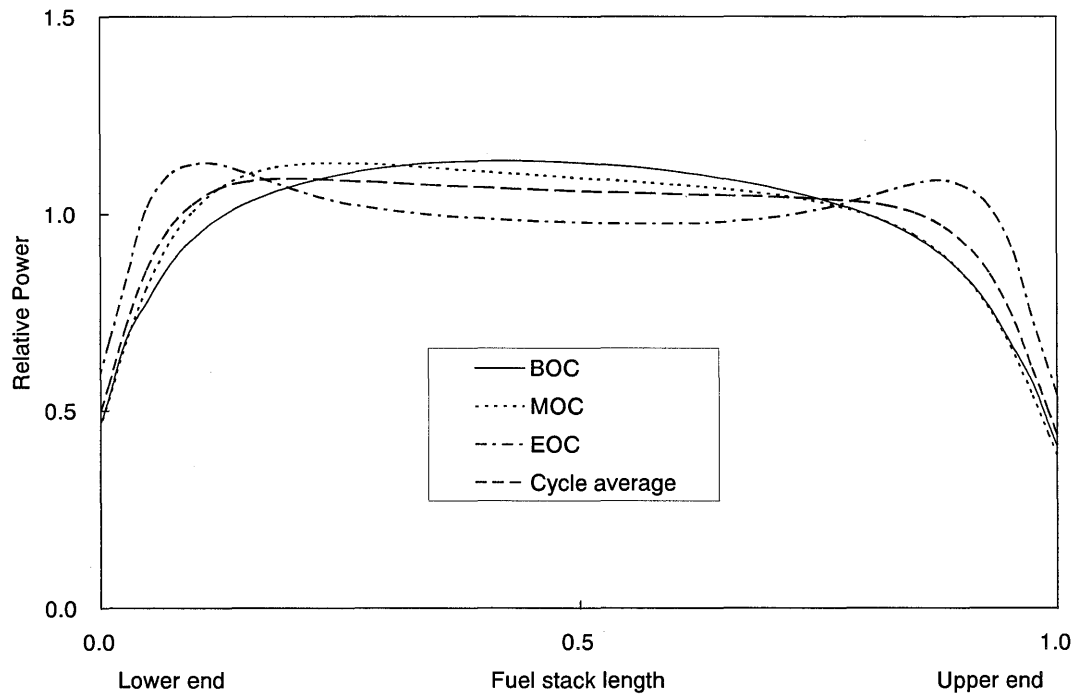


Figure 3.2-1 Typical Axial Power Distributions

3.3 Fuel Rod Internal Pressure

3.3.1 Design Bases and Criteria

The fuel system will not be damaged due to excessive rod internal pressure under normal operation.

The fuel rod internal pressure must be below the lowest internal pressure limit among the following three internal pressure limits.

- No cladding liftoff during normal operation
- No reorientation of the hydrides in the radial direction in the cladding
- A description of any additional failures resulting from departure of nuclear boiling (DNB) caused by fuel rod overpressure during transients and postulated accidents

3.3.2 Evaluation

(a) Liftoff Pressure

The FINE code is used both to calculate the rod internal pressure and to calculate the pressure at which cladding liftoff can occur.

The rod internal pressure is maintained below the cladding liftoff pressure, which is defined as the pressure at which the pellet-cladding gap increases due to outward cladding creep. Cladding liftoff is prevented to eliminate the possibility of thermal feedback where an increasing pellet-cladding gap leads to increased pellet temperatures, which accelerate the fission gas release and thus further increases the internal pressure. In the US-APWR fuel design, the rod internal pressure is evaluated using the FINE code⁽³⁻¹⁾. The evaluation takes into account the uncertainties in the fuel fabrication and the fuel performance models. These uncertainties are considered statistically and the total uncertainty is evaluated by Square Root of the Sum of the Squares (SRSS) method at a 95 % probability at a 95 % confidence level.

The assessment of the liftoff pressure limit, using the FINE code, considers the power histories which give high internal pressures and high cladding creep rates, including the power history which gives the highest rod internal pressure. These power histories are based on the actual core analysis. The FINE Code analyses making the liftoff situation analytically is performed by () using these power histories. These pressure analyses determine the internal pressure when liftoff occurs for each power history, and the lowest internal pressure with liftoff is determined. Uncertainties are accounted for in this determination of the liftoff pressure. For the US-APWR fuel design, this process has determined that the liftoff pressure limit is () psi (() MPa). It is confirmed that the rod internal pressure evaluated by FINE code with uncertainties is below the liftoff pressure limit for any rods. If rod internal pressure, including uncertainties, for any rods exceeds this limit, it is verified that liftoff does not occur for this specific power history. The applicability of this liftoff pressure limit is confirmed if there is any fuel design change in the fuel dimensions or materials.

The US-APWR fuel rod, with upper and lower plenums, has enough free volume to accommodate the fission gas release. Table 3.3-1 shows that the internal pressure of the

limiting rod in the US-APWR equilibrium core is well below the liftoff pressure. For the liftoff pressure criterion, the limiting UO_2 rod is (), and the limiting (U,Gd) O_2 rod is (), using the identification of the region names given in Appendix A.

(b) Hydride Reorientation Pressure

Hydride reorientation does not occur if the rod internal pressure is below approximately 3900psi (27MPa) ⁽³⁻¹⁾. The liftoff pressure limit discussed in subsection 3.3.2(a) is less than this hydride reorientation limit, which assures that radial hydride reorientation will not occur for the US-APWR fuel.

(c) DNB Propagation

The Mitsubishi fuel rod design criteria allow the rod internal pressure to exceed the system pressure as long as cladding liftoff does not occur. If DNB occurs, there is then a small probability to have DNB propagation when there are fuel rods with internal pressures above the system pressure (over pressure rods), as follows.

If DNB occurs on an over pressure rod, the temperature rise due to the DNB and the differential pressure across the fuel rod cladding can lead to ballooning or fracturing of the cladding and reducing the flow channel between the adjacent rods. Assuming this interferes with the cooling of adjacent rods significantly, DNB can then propagate to the adjacent rods. If any of these adjacent rods has an internal pressure greater than the system pressure, it is assumed that this rod will also balloon when it goes into DNB and that the resulting cladding deformation for this rod will reduce the flow channels of its adjacent rods. This process of DNB propagation to adjacent rods continues until all adjacent rods are below system pressure.





This shows that the number of the rods that initially have both DNB and over pressure is less than 1. Therefore DNB propagation will not occur during an AOO.





Table 3.3-1 Rod Internal Pressure Evaluation Results

| | | unit:psi (unit:MPa) | |
|--|-----------------------|------------------------|---------------------------|
| | Uncertainty Parameter | UO ₂ fuel | (U,Gd)O ₂ fuel |
| | | | |

Table 3.3-2 Evaluation of DNB Propagation in AOO

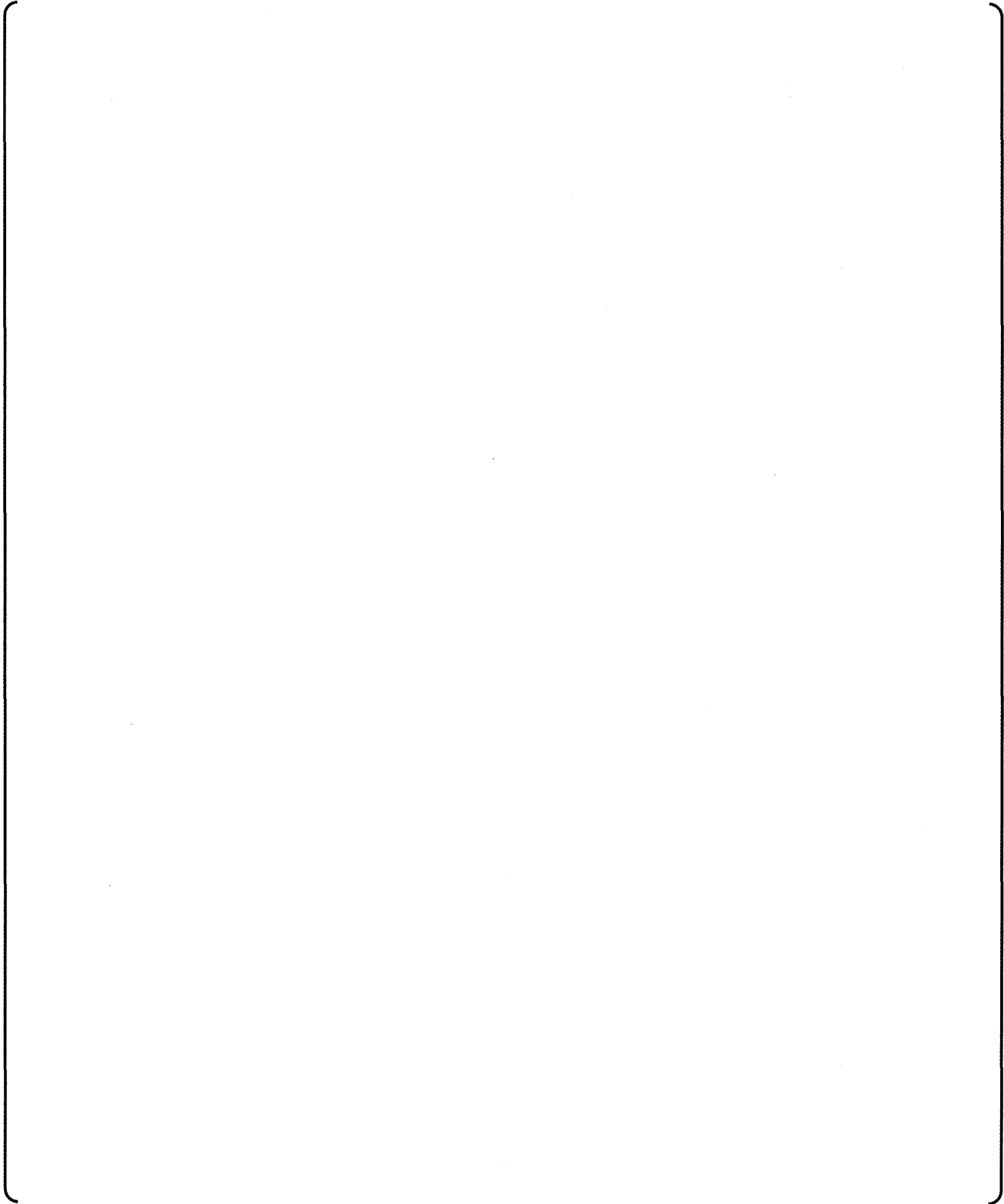
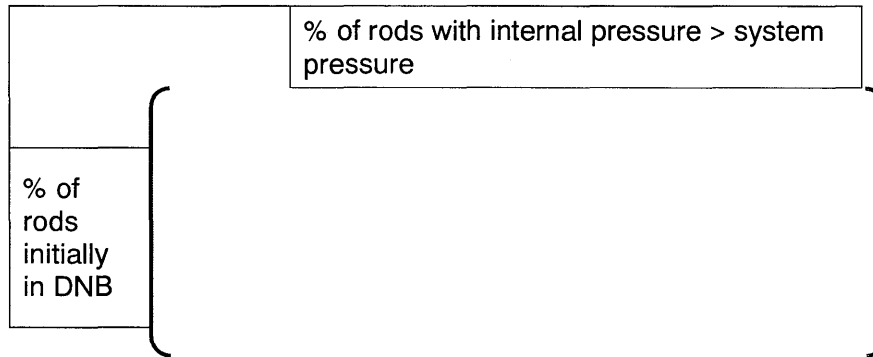


Table 3.3-3 Parametric Survey of DNB Propagation for Postulated Accidents



3.4 Cladding Stresses

3.4.1 Design Bases and Criteria

The fuel system will not be damaged due to excessive stress under normal operation including AOOs.

The cladding stress criteria are based on the ASME Section III ⁽³⁻³⁾ pressure vessel criteria. All cladding stresses except for pellet-cladding mechanical interaction (PCMI) related stresses, are considered in the stress evaluation and are assessed according to ASME Section III ⁽³⁻³⁾.

PCMI stresses are excluded from the cladding stress evaluation because they are addressed by the cladding strain criterion and the no fuel melting criterion.

3.4.2 Evaluation

The evaluation of the cladding stress criterion takes into account the differential pressure across the cladding wall, the thermal stresses, hydraulic and seismic vibration, grid spacer contact, fuel rod bowing and cladding ovality ⁽³⁻¹⁾. The category of each stress is based on ASME stress categories ⁽³⁻³⁾, and is summarized in Table 3.4-1. The effect of grid spacer contact is categorized as a secondary stress because the spring force decreases as the grid spring deflection decreases. However, for conservatism the stresses due to grid spacer contact are categorized as local primary stresses for the cladding stress criterion evaluation. The stresses due to grid spacer contact force, fuel rod bowing and cladding ovality are assessed based on basic equations, conservatively using only elastic assumptions.

(a) Cladding inner diameter-outer diameter differential pressure ⁽³⁻⁴⁾

Stresses due to the pressure difference across the cladding wall are calculated by the FINE code, using the following equations with the FINE results for P_1 , P_2 , r_1 and r_2 :

$$\text{For } r=r_1 \text{ (inner surface): } \sigma_r = -P_1, \quad \sigma_\theta = \frac{P_1(r_2^2 + r_1^2) - 2P_2r_2^2}{r_2^2 - r_1^2}, \quad \sigma_z = \frac{P_1r_1^2 - P_2r_2^2}{r_2^2 - r_1^2}$$

$$\text{For } r=r_2 \text{ (outer surface): } \sigma_r = -P_2, \quad \sigma_\theta = \frac{2P_1r_1^2 - P_2(r_2^2 + r_1^2)}{r_2^2 - r_1^2}, \quad \sigma_z = \frac{P_1r_1^2 - P_2r_2^2}{r_2^2 - r_1^2}$$

where

P_1 : internal pressure; P_2 : external pressure; r_1 : inner radius; r_2 : outer radius;

r, θ, z : radius, tangential and axial directions in cylindrical coordinates

(b) Hydraulic and seismic vibration ⁽³⁻⁴⁾

The deflections due to hydraulic vibration are calculated by vibration analysis as described in section 4.6. The following basic equations are used to calculate the stresses due to the hydraulic and seismic vibration:

$$\text{For } r=r_1 \text{ (inner surface): } \left(\right)$$

For $r=r_2$ (outer surface) : ()

where

()

The axial stress due to hydraulic vibration is less than () psi () MPa).

The axial stress due to seismic vibration for the US-APWR fuel design is assumed to be () psi () MPa). This stress is corresponding operating basis earthquake (OBE), and is one third of () psi () MPa) which is provided from stress evaluation for postulated earthquakes in Japanese plants. The OBE is less than one third of SSE (Safe Shutdown Earthquake) ⁽³⁻⁵⁾ which is conservatively assumed to be comparable with the postulated earthquakes in Japanese plants. The cladding stress analysis is re-estimated if the seismic analysis requires an evaluation of seismic vibrations beyond the OBE conditions.

(c) Grid contact ⁽³⁻⁴⁾

The following basic equations are used to calculate the stresses due to grid contact:

For $r=r_1$ (inner surface) :

()

For $r=r_2$ (outer surface) :

()

where

()

For the US-APWR fuel design the grid contact force is () lbf () N) and the half length of contact area is () inch () mm).

(d) Fuel bowing ⁽³⁻⁴⁾

The following basic equations are used to calculate the stresses due to fuel bowing:

$$\begin{aligned} \text{For } r=r_1 \text{ (inner surface) : } & \left[\right] \\ \text{For } r=r_2 \text{ (outer surface) : } & \left[\right] \\ \text{where} & \\ & \left[\right] \end{aligned}$$

For the US-APWR fuel design the deflection due to rod bowing is calculated on the basis of ()% gap closure between rods. This value is obtained from the fuel rod bowing data as described subsection 4.3.1, and considered in this evaluation as a 95% probability and a 95% confidence level.

(e) Ovality ⁽³⁻⁶⁾

The following basic equations are used to calculate the stresses due to cladding ovality:

$$\begin{aligned} \text{For } r=r_1 \text{ (inner surface) : } & \left[\right] \\ \text{For } r=r_2 \text{ (outer surface) : } & \left[\right] \end{aligned}$$

()

where

()

For the US-APWR fuel design the cladding ovality is () inch () mm).

(f) Thermal stress ⁽³⁻⁷⁾

Stresses due to the temperature gradient across the cladding wall are calculated by the FINE code using the following equations:

$$\text{For } r=r_1 \text{ (inner surface): } \sigma_r=0, \sigma_\theta=\sigma_z=\frac{\alpha \cdot E \cdot \Delta T}{2(1-\nu)} \left(\frac{1}{Ln \frac{r_2}{r_1}} - \frac{2r_2^2}{r_2^2 - r_1^2} \right)$$

$$\text{For } r=r_2 \text{ (outer surface): } \sigma_r=0, \sigma_\theta=\sigma_z=\frac{\alpha \cdot E \cdot \Delta T}{2(1-\nu)} \left(\frac{1}{Ln \frac{r_2}{r_1}} - \frac{2r_1^2}{r_2^2 - r_1^2} \right)$$

where

P₁: internal pressure; P₂: external pressure; r₁: inner radius; r₂: outer radius;

E: Young's modulus; ν: Poisson's ratio; α: coefficient of thermal expansion;

ΔT: temperature difference between the inner and outer cladding surfaces

r,θ,z: radius, tangential and axial direction in cylindrical coordinates

These (a), (b), (c), (d), (e) and (f) stresses determine the total stress as following.

The FINE code is used to account for the effects of the power increase from normal operational condition to the AOO condition, which is obtained from core analysis. The total stress is determined by summing these different contributions to the stresses. The stress intensity is evaluated as the differential stress between the maximum stress and minimum stress, as specified by the ASME Section III ⁽³⁻³⁾ criteria. The allowable stress intensity, S_m, is the minimum of two thirds of the cladding yield stress and one third of the cladding ultimate stress as shown in Table 3.4-2, with consideration of temperature and irradiation effects ⁽³⁻¹⁾. The stress evaluation takes into account of the effect of fuel cladding wear and oxidation. The cladding wear is on the outer surface of the cladding, and affects only a small and local part of cladding. Therefore, the effect of fuel cladding wear can be defined ⁽³⁻¹⁾. Cladding oxidation is accounted for by using a cladding wall thickness that includes the effects of wall thinning due to the cladding oxidation.

The cladding stress evaluation takes into account the uncertainties in the fuel fabrication and the fuel performance models. These uncertainties are considered statistically and the total

uncertainty is evaluated by Square Root of the Sum of the Squares (SRSS) method at a 95 % probability at a 95 % confidence level. The total stress of the limiting rod in the US-APWR fuel rod design during AOOs is below the allowable stress intensity as shown in Table 3.4-3. For the cladding stress criterion the limiting UO_2 rod is (), and the limiting $(\text{U,Gd})\text{O}_2$ rod is (), using the identification of the region names given in Appendix A.

Table 3.4-1 Stress Categories

| Loading Conditions | Stress Category | Classification | Approach |
|-----------------------------------|-------------------------------|----------------|--------------------|
| Inner-outer differential pressure | Primary Membrane Stress | Pm | FINE Analysis |
| Hydraulic and seismic vibration | Primary Bending Stress | Pb | Vibration Analysis |
| Grid contact | Local Primary Membrane Stress | Pl | Basic Equations |
| Fuel bowing | Primary Bending Stress | Pb | Basic Equations |
| Ovality | Primary Bending Stress | Pb | Basic Equations |
| Thermal stress | Secondary Stress | Q | FINE Analysis |

Table 3.4-2 Stress Intensity Limits

| Stress | Stress Intensity Limits |
|------------------|--|
| Pm | $S_m = \text{Min} \left(\frac{1}{3} \sigma_{UTS}, \frac{2}{3} \sigma_y \right)$ |
| Pm + Pb + Pl | $1.5S_m = \text{Min} \left(\frac{1}{2} \sigma_{UTS}, \sigma_y \right)$ |
| Pm + Pb + Pl + Q | $3S_m = \text{Min} \left(\sigma_{UTS}, 2\sigma_y \right)$ |

σ_{UTS} : Ultimate tensile stress

σ_y : 0.2% offset yield stress

Table 3.4-3 Cladding Stresses Evaluation Results

| | | unit | UO ₂ fuel | (U,Gd)O ₂ fuel | |
|------------------------|--|------------|----------------------|---------------------------|---|
| Best Estimate Value | Pm | psi MPa | | | |
| Stress intensity limit | Sm | psi MPa | | | |
| Design Ratio | (Best estimate value / Stress intensity limit) | - | | | |
| Best Estimate Value | Pm+Pb+PI | psi MPa | | | |
| Stress intensity limit | 1.5Sm | psi MPa | | | |
| Design Ratio | (Best estimate value / Stress intensity limit) | - | | | |
| Best Estimate Value | Pm+Pb+PI+Q | psi MPa | | | |
| Stress intensity limit | 3.0Sm | psi MPa | | | |
| Design Ratio | (Best estimate value / Stress intensity limit) | - | | | |
| Max Design Ratio | | - | | | |
| Limit | | - | | | 1 |

Uncertainty Evaluation Relative to the Design Ratio

| | | unit: [-] |
|--|-----------------------|--|
| | Uncertainty Parameter | UO ₂ fuel (U,Gd)O ₂ fuel |
| | | |

3.5 Chemical Reaction

3.5.1 Design Bases and Criteria

The fuel system will not be damaged due to excessive cladding corrosion during normal operation and AOOs.

During normal operation and AOOs the cladding surface temperature shall remain below the temperature at which an acceleration of corrosion could occur, as determined by the out of pile Zircaloy-4 cladding corrosion tests. To prevent this acceleration of the cladding corrosion, the calculated cladding metal-oxide interface temperature shall be less than ()deg.F during normal operation, and less than ()deg.F during AOOs ⁽³⁻¹⁾. These are the conservative design limits because they are based on Zircaloy-4 cladding corrosion tests, and the temperature required for accelerated corrosion of ZIRLO cladding is higher than that of Zircaloy-4.

The cladding hydrogen content shall remain below the value required to prevent degradation of cladding mechanical properties. Based on mechanical test data for irradiated and un-irradiated cladding material, the hydrogen content limit is established as () ppm ⁽³⁻¹⁾.

3.5.2 Evaluation

During normal operation and AOOs, the cladding surface temperature is limited to be less than the temperature at which an accelerated corrosion could occur.

The cladding metal-oxide interface temperature during irradiation is evaluated by the FINE code for both normal operation and AOO conditions. The metal-oxide interface temperature increases as the power increases during AOOs, but the cladding oxidation does not increase during an AOO due to the short duration of the AOOs. The evaluation takes into account the uncertainty in the fuel performance models. The uncertainty is ()deg.F (()deg.C) based on { ()kW/ft (() kW/m), determined from () ⁽³⁻¹⁾, assuming ()}. This uncertainty is considered statistically at a 95 % probability at a 95 % confidence level. The cladding metal-oxide interface temperature of the limiting rod in the US-APWR equilibrium core during normal operation and AOOs is below the limits given above, as shown in Table 3.5-1. For the cladding corrosion criterion, the limiting UO₂ rod is (), and the limiting (U,Gd)O₂ rod is (), using the identification of the region names as given in Appendix A.

Hydrogen generated due to cladding corrosion is partially absorbed by the cladding. To maintain cladding ductility, the criterion requires that the hydrogen absorbed by the cladding is less than the hydrogen absorption limit. High temperature mechanical properties data for un-irradiated cladding show that the cladding retains its ductility up to the hydrogen absorption limit.

The cladding hydrogen content at the end of irradiation is also calculated by the FINE code for normal operation. Since oxidation is negligible during AOOs, as described above, hydrogen absorption does not increase during AOOs. The evaluation takes into account the hydrogen absorption model uncertainty of () ppm. This uncertainty is considered to be statistically at a 95 % probability at a 95 % confidence level. The cladding hydrogen content of the limiting rod in the US-APWR fuel rod design at the end of irradiation is below the hydrogen absorption

criteria, as shown in Table 3.5-1. For the hydrogen absorption criterion, the limiting UO_2 rod is
{
in Appendix A. } , and the limiting $(\text{U,Gd})\text{O}_2$ rod is the
} , using the identification of the region names given

Table 3.5-1 Chemical Reaction Evaluation Results

| | | UO ₂ fuel | (U,Gd)O ₂ fuel |
|--|------------------|----------------------|---------------------------|
| The cladding metal-oxide interface temperature | Normal operation | | |
| | AOO | | |
| Cladding corrosion thickness | | | |
| Cladding hydrogen content | | | |

3.6 Cladding Fatigue

3.6.1 Design Bases and Criteria

The fuel system will not be damaged due to excessive fatigue during normal operation and AOOs.

The cumulative number of strain fatigue cycles shall be less than the design fatigue lifetime, which includes a safety factor of 2 on stress amplitude or a safety factor of 20 on the number of cycles, whichever is most limiting. The Langer-O'Donnel model ⁽³⁻⁸⁾ for the fatigue design curve is used..

3.6.2 Evaluation

The cladding fatigue is evaluation accounts for reactor startup/shutdown operation, AOOs and other power change operations, including load follow operation.

The cumulative number of strain fatigue cycles is less than the design fatigue lifetime, which includes a safety factor of 2 on the stress amplitude or a safety factor of 20 on the number of cycles, whichever is most limiting. The Langer-O'Donnel model ⁽³⁻⁸⁾ is used as the fatigue design curve. Fatigue tests on irradiated fuel cladding give results consistent with Langer-O'Donnel best fit model, and this design curve, with the specified safety factors, is applicable to high burnup fuel design. The cumulative fatigue damage is assessed by summing the fatigue usage over the fuel rod's life. The usage is determined by dividing the number of anticipated load cycles by the number of cycles to failure obtained from the fatigue design curve at the load condition, using the cladding stresses calculated by the FINE code ⁽³⁻¹⁾. The stress evaluation takes into account of the effect of fuel cladding wear and oxidation. The cladding wear is on the outer surface of the cladding, and affects only a small and local part of cladding. Therefore, the effect of fuel cladding wear can be defined ⁽³⁻¹⁾. Cladding oxidation is accounted for by using a cladding wall thickness that includes the effects of wall thinning due to the cladding oxidation. The contact pressure between the pellets and the cladding and the thermal stresses are accounted for in the calculation of the stress amplitudes during the load cycles.

The number of load cycles assumed in the fatigue evaluation is defined below for startup/shutdown, power variations during normal operation and AOOs. The stress amplitudes for the cyclic loads, including the effects of irradiation, are calculated using the FINE code. The cyclic stress amplitudes are principally due to the differences in the pellet thermal expansion during the load cycle.

a) Startup/shutdown

A startup/shutdown cycle is defined as the change from the 0% Cold Stand-by state to the 0% Hot Stand-by state. The fatigue evaluation assumes () startup/shutdown cycles per year.

b) Power variation during normal operation, including load follow

Load follow during normal operation defines the limiting fatigue duty for the power variations during normal operation. The evaluation of the fatigue usage due to load follow operation includes the effects of the power overshoot during the return to 100% power. The fatigue evaluation conservatively assumes () load follow cycles per year.

c) Anticipated Operational Occurrences (0% <---> 100% nuclear reactor trip)

The limiting fatigue duty for power changes due to AOOs is given by the reactor trip from 100% power, including the AOO overpower, to 0% power, conservatively. The fatigue evaluation assumes () cycles per year due to AOOs.

The fatigue criterion evaluation accounts for the uncertainties in the fuel fabrication and the fuel performance models. These uncertainties are considered statistically and the total uncertainty is evaluated by Square Root of the Sum of the Squares (SRSS) method at a 95 % probability at a 95 % confidence level.

The results for the US-APWR cladding fatigue criterion evaluation show that there is significant margin to the limit, as shown in Table 3.6-1. For the cladding fatigue criterion, the limiting UO₂ rod is (), and the limiting (U,Gd)O₂ rod is the (), using the identification of the region names given in Appendix A.

Table 3.6-1 Cladding Fatigue Evaluation Results

| | | unit: [-] | |
|--|-----------------------|----------------------|---------------------------|
| | Uncertainty Parameter | UO ₂ fuel | (U,Gd)O ₂ fuel |
| | | | |

3.7 Creep Collapse

3.7.1 Design Bases and Criteria

Fuel rod failure will not occur due to cladding collapse.

The number of fuel rods that experience cladding collapse shall be less than 1 rod during the fuel lifetime.

3.7.2 Evaluation

The Mitsubishi fuel design uses high density fuel pellets of more than 95%TD density which are stable with respect to fuel densification. In addition, the fuel rods are initially pressurized with helium. The combination of stable fuel and pre-pressurized fuel rods has been demonstrated to be very effective in eliminating the formation of axial gaps in the fuel column due to densification, which precludes cladding collapse. Mitsubishi has more than 30 years experience with no incident of cladding collapse since the adoption of the 95%TD pellet density and initial pressurization with helium in the fuel design⁽³⁻¹⁾. The US-APWR fuel design uses fuel pellets with a higher initial density of 97%TD. The US-APWR pellet design is even more stable with respect to fuel densification due to this additional reduction in the fuel's initial porosity, and therefore have greater margin to cladding collapse than the Mitsubishi fuel design with the 95%TD pellet density.

For information, Appendix D gives the results of the creep collapse evaluation for the US-APWR fuel design, with ZIRLO cladding and 97%TD pellet density.

3.8 Cladding Strain

3.8.1 Design Bases and Criteria

The Fuel system will not be damaged due to excessive strain during normal operation and AOOs.

Cladding permanent strain during normal operation shall be less than 1 % relative to the un-irradiated condition. This criterion assures that the dimensional change of the cladding due to cladding creep under normal operation remains within the ductility limits for the cladding. During power transients associated with AOOs, the total cladding strain change, elastic plus plastic, shall remain below 1 % relative to the pre-transient condition. This criterion limits the cladding strain due to PCMI.

3.8.2 Evaluation

Cladding strain under normal operation and AOOs is evaluated using the FINE code ⁽³⁻¹⁾.

During normal operation, the calculation of the cladding strain accounts for the cladding creepdown due to the pressure differential between the coolant system pressure and the rod internal pressure, and the outward deformation due to pellet swelling after pellet-cladding contact occurs. The cladding strain of the limiting rod in the US-APWR fuel rod design during normal operation is well below the criterion, (). For this criterion, the limiting UO₂ rod is (), and the limiting (U,Gd)O₂ rod is (), using the identification of the region names given in Appendix A. Uncertainties for the strain evaluation during normal operation are (), as described below.

The cladding strain during normal operation is primarily due to PCMI and determined by the pellet densification, swelling and thermal expansion as well as by the cladding creep. The power variation during normal operation is generally very moderate, and the zirconium based alloy cladding readily deforms due to creep. There is therefore little possibility that the zirconium based alloy cladding could experience an unstable condition, with subsequent deformation beyond the one percent limit ^{(3-9), (3-10)}. Though the integrity of the cladding will be maintained until the cladding strain during normal operation reaches several percent, limiting the strain increment to 1% relative to the un-irradiated state is conservatively used as the criterion to limit PCMI during normal operation.

For power transients associated with AOOs, the change in the cladding strain from normal operation to the maximum power of the AOO is evaluated as the total tensile strain change (elastic and inelastic). This strain is principally due to the pellet expansion resulting from the pellet thermal expansion and fission gas bubble swelling. The local power increase during the AOO causes both PCMI and gas bubble swelling. The evaluation takes into account the uncertainties in the fuel fabrication and the fuel performance models. These uncertainties are considered statistically and the total uncertainty is evaluated by Square Root of the Sum of the Squares (SRSS) method at a 95 % probability at a 95 % confidence level. The cladding strain during AOOs of the limiting rod in the US-APWR fuel rod design is below the criterion, as shown in Table 3.8-1. For this criterion, the limiting UO₂ rod is (), and the limiting (U,Gd)O₂ rod is (), using the identification of the region names given in Appendix A.

Table 3.8-1 Cladding Strain during AOOs Evaluation Results

| | Uncertainty Parameter | UO ₂ fuel | (U,Gd)O ₂ fuel |
|----------|-----------------------|----------------------|---------------------------|
| unit:[%] | | | |
| | | | |

3.9 Fuel Temperature

3.9.1 Design Bases and Criteria

Fuel rod failure will not occur due to overheating of fuel pellets during normal operation and AOOs.

There shall be at least a 95-percent probability at a 95-percent confidence level that the fuel rod with the most limiting linear heat rate (kW/ft) does not cause the fuel pellet to melt during normal operation and AOOs. To prevent fuel from overheating under normal operation and AOOs, the calculated fuel centerline temperature shall not exceed the melting temperature of the fuel. The melting temperature of the UO_2 pellet is 5072deg.F (2800deg.C) for un-irradiated fuel and decreases by 58deg.F(32deg.C) per 10,000MWD/MTU ⁽³⁻¹⁾.

3.9.2 Evaluation

FINE code best estimate models are used for fuel temperature analysis, with exception that a conservative model for the fuel densification, based on RG-1.126 ⁽³⁻¹¹⁾, is used for fuel densification in conjunction with manufacturing data for the fuel density change after sintering for 24 hours at a temperature of 1700 deg.C. The following is the design procedure to obtain linear heat rate limit that will preclude fuel melting.

(a) Fuel centerline temperature analysis (Best estimate calculation)



The UO_2 fuel centerline temperature as a function of the local linear heat rate is calculated at various burnups by the FINE code (Figure 3.9-1). For (U,Gd) O_2 fuel rods, due to the lower melting temperature and the lower thermal conductivity, fuel temperature analysis will provide more severe result than that of UO_2 fuel on the same linear heat rate condition. However, the (U,Gd) O_2 fuel centerline temperature is less than the UO_2 fuel centerline temperature because the peak linear heat rate for (U,Gd) O_2 fuel rods is decreased by their reduced enrichment content, as shown in (e).

(b) Fuel centerline temperature uncertainties

Fuel centerline temperature uncertainties due to manufacturing tolerances and fuel performance model uncertainties are evaluated at a 95 % probability at a 95% confidence level using the Square Root of the Sum of the Squares (SRSS) method. Table 3.9-1 shows the result of UO_2 fuel centerline temperature uncertainty evaluation, which is bounding for (U,Gd) O_2 fuel.

(c) Fuel temperature design limit

The design limit for the fuel temperature is obtained by subtracting the uncertainties due to the manufacturing tolerances and the fuel performance models from the melting temperature. The

resulting design limit for the fuel centerline temperature is 4620deg.F (2550deg.C) at the beginning of life and decreases with burnup, as shown in Figure 3.9-2.

(d) Linear heat rate corresponding to the design limit for fuel temperature

The linear heat rate which corresponds to the design limit for fuel temperature is calculated at various burnups using the relationship between the fuel centerline temperature and the linear heat rate obtained from the best estimate fuel centerline temperature analysis described in subsection 3.9.2(a). The result is the dotted line shown in Figure 3.9-3.

(e) Local linear heat rate limit

The local linear heat rate limit as a function of burnup, the solid line in Figure 3.9-3, is specified with additional margin below the linear heat rate which corresponds to the design limit for fuel temperature. The allowable peak linear heat rate for UO_2 fuel to preclude fuel melting, which corresponds to this maximum allowable centerline temperature, is 21.9kW/ft (72.0kW/m) at the beginning of life and decreases with burnup by [] kW/ft ([] kW/m) per [] MWD/MTU. For $(\text{U,Gd})\text{O}_2$ fuel, the allowable peak linear heat rate is [] kW/ft ([] kW/m) at the beginning of life and decreases with burnup by [] kW/ft ([] kW/m) per [] MWD/MTU. The peak linear heat rates during normal operation and AOOs are confirmed to be less than this linear heat rate limit for the first and reload cores.

Table 3.9-1 Fuel Centerline Temperature Uncertainty Evaluation (UO₂ fuel)

| | Uncertainty Parameter | unit:deg.F (unit:deg.C) UO ₂ fuel |
|--|-----------------------|--|
| | | |

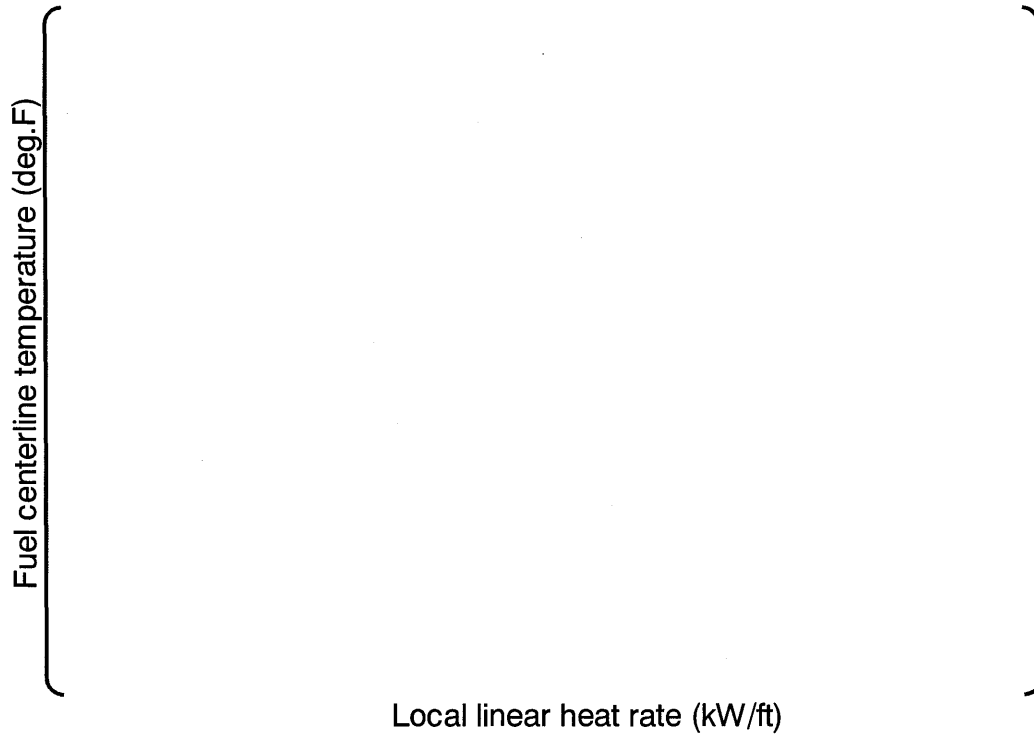


Figure 3.9-1 Fuel Centerline Temperature versus Local Linear Heat Rate (UO₂ fuel)

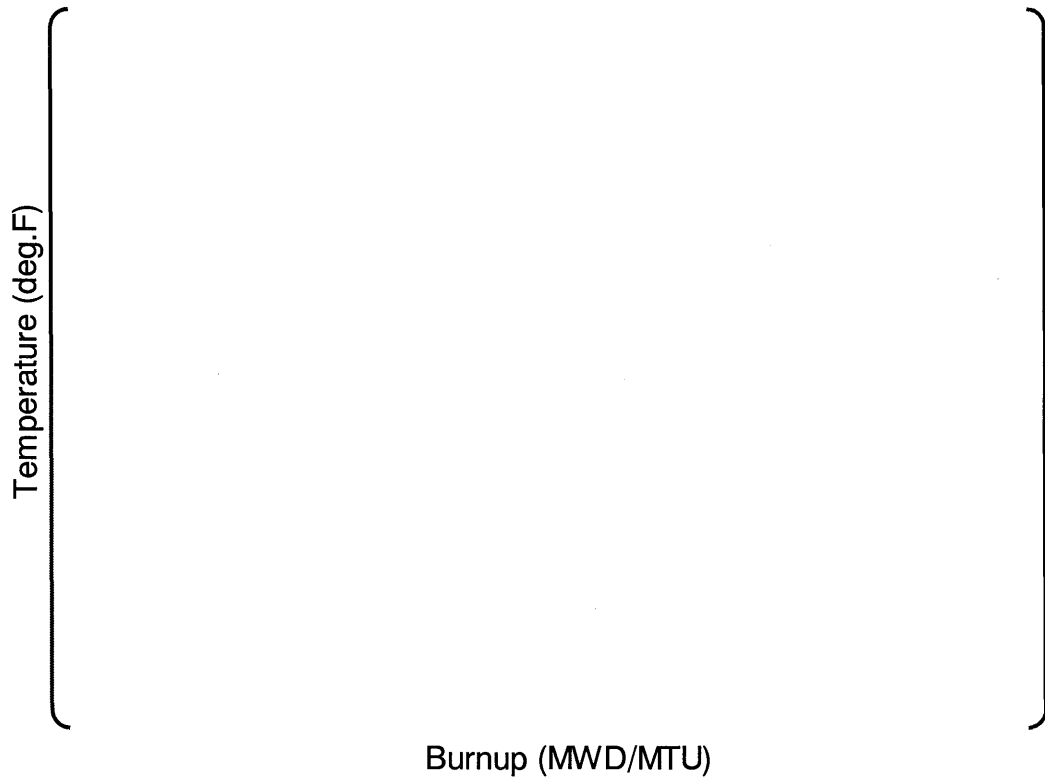


Figure 3.9-2 Fuel Temperature Design Limit versus Burnup (UO₂ fuel)

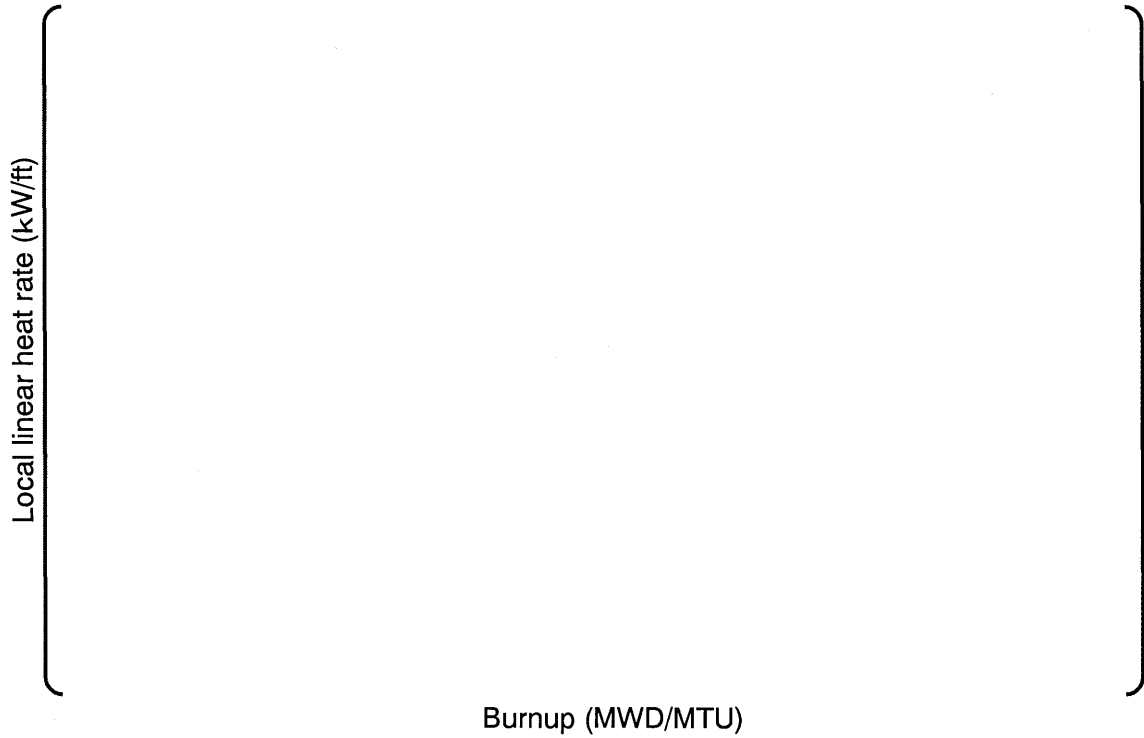


Figure 3.9-3 Local Linear Power Limit versus Burnup (UO₂ fuel)

3.10 Fuel-Cladding Mechanical Interaction

3.10.1 Design Bases and Criteria

Fuel failure will not occur due to pellet cladding interaction (PCI) during normal operation and AOOs. PCI is addressed by two previous criteria:

(1) cladding strain during AOOs must remain below 1%

The cladding strain criterion is described in section 3.8.

(2) fuel centerline melting does not occur

The fuel centerline melting criterion is described in section 3.9.

3.10.2 Evaluation

The methodology for the cladding strain design evaluation is described in section 3.8 and the methodology for fuel centerline melting is described in section 3.9.

The US-APWR fuel rod design meets these criteria during normal operation and AOOs.

3.11 References

- (3-1) "Mitsubishi Fuel Design Criteria and Methodology", MUAP-07008-P (Proprietary) and MUAP-07008-NP (Non-Proprietary), May 2007
- (3-2) "US-APWR Design Control Document", December 2007
- (3-3) 2001 American Society of Mechanical Engineers Boiler and Pressure Vessel Code with 2002 and 2003 Addenda Section III Division 1 NB
- (3-4) Raymond J. Roark, Warren C. Young, "Formulas for Stress and Strain", Fifth edition, McGraw-Hill, 1954
- (3-5) 10 CFR Part 50 Appendix S
- (3-6) S. P. Timoshenko, J. M. Gere, "Theory of Elastic Stability", Second Edition, McGraw-Hill, 1961
- (3-7) S. P. Timoshenko, J. N. Goodier, "Theory of Elasticity", Third Edition, McGraw-Hill, 1951
- (3-8) W. J. O'Donnell and B. F. Langer, "Fatigue Design Basis for Zircaloy Components", Nuclear Science and Engineering 20, pp.1-12, 1964
- (3-9) B.Watkins and D.S.Wood, "The Significance of Irradiation-Induced Creep on Reactor Performance of a Zircaloy-2 Pressure Tube Applications - Related Phenomena for Zirconium and its Alloys", ASTM STP 458, American Society for Testing and Materials, PP.226-240, 1969
- (3-10) D.S.Wood and B.Watkins, "A Creep Limit Approach to the Design of Zircaloy-2 Reactor Pressure Tubes at 275 C", Journal of Nuclear Materials 41 327-340, May 1971
- (3-11) U.S.Nuclear Regulatory Commission, Regulatory Guide 1.126

4.0 FUEL ASSEMBLY DESIGN EVALUATION

4.1 Loads under Normal Operation and AOOs

4.1.1 Design Basis and Criteria

To supply the expected thermal power and to maintain coolable geometry of the core and safe shutdown of the reactor, significant deformation in the fuel assembly should not occur under anticipated loads during normal operation (NO) and AOOs.

- Under the loads imposed by a RCCA scram during normal reactor operation, the stresses in the top nozzle and the control rod guide thimbles, except for the dashpot region, are less than the acceptance limit based on ASME Section III ⁽⁴⁻¹⁾.
- Stresses in the bottom nozzle and the dashpot region of control rod guide thimbles during normal operation and reactor trip are less than the acceptance limit based on ASME Section III ⁽⁴⁻¹⁾. The loads considered are defined by adding the load during normal operation to the impact force of the RCCA on the top nozzle and the reaction force when the RCCA is decelerated in the dashpot region.
- Fatigue usage factors of the top and bottom nozzles and the control guide thimbles are less than 1.0 considering cyclic loading during normal operation and AOOs.
- The grid spacer spring shall not fail throughout the fuel life due to fatigue which results from hydraulic vibration of the fuel rod.

The grid spacer spring fatigue described above, and the other criteria for preventing significant structural deformation of fuel assembly, such as fuel assembly growth, fuel rod growth and fuel rod bowing, are addressed in Sections 4.3 and 4.4.

4.1.2 Evaluation

For the loads in normal operation and AOOs, which includes loads by the core restraint system, the stresses on the above components are evaluated and confirmed to be within acceptance limits. The following loads under normal operation and AOOs are considered in the evaluation:

- Loads under normal operation: Holddown spring force, hydraulic lift force, buoyancy force, self-weight and reaction force from lower core plate.
- Loads in AOOs: Reaction force by deceleration of the RCCA in the dashpot and impact force of the RCCA are added to the loads in normal operation.

The RCCA scram incident is selected as the limiting AOOs, since the loads at RCCA scram have a larger influence on the fuel assembly mechanical performance. The impact force on the top nozzle due to dropping the RCCA is obtained by solving the momentum equation for the drop velocity while the retainer spring within the rod control cluster is being compressed after the rod control cluster contacts the top nozzle plate. The reaction force as the RCCA is decelerated is calculated from the internal pressure increase in the control rod guide thimble, which is obtained from the drop-time analysis of the RCCA.

The stresses in the top and bottom nozzles and the control rod guide thimbles are evaluated by finite element method (FEM) analyses. Manufacturing tolerances are considered to obtain a conservative result in the stress analysis of the top and bottom nozzles. The un-irradiated material yield stresses are conservatively used to determine the acceptance limits, rather than the yield stresses of irradiated materials, which are increased due to irradiation hardening.

In compliance with ASME Section III ⁽⁴⁻¹⁾, the primary general membrane stress and bending stress strength (P_m+P_b) of the top and bottom nozzles are determined from the analysis results and compared with the allowable value ($1.5S_m$) to confirm that no plastic deformation occurs.

For the stress evaluation of the control rod guide thimbles, an FEM analysis is used to obtain the load sharing ratio in between the fuel rods and the control rod guide thimbles. After obtaining the load on the control rod guide thimbles by the ratio, the maximum stress of the control rod guide thimble is obtained by dividing the load by the product of the number of control rod guide thimbles and the cross-sectional area of a control rod guide thimble.

The load at RCCA scram is chosen as the cyclic load in the fatigue usage evaluation for the top and bottom nozzles and the control rod guide thimbles. The fatigue usage factor is the ratio of the cumulative numbers of RCCA scrams during the fuel lifetime to the number of load cycles to failure at the fatigue load stresses. The Langer-O'Donnell fatigue design curve ⁽⁴⁻²⁾ is used for the Zircaloy-4 control rod guide thimble and the fatigue design curve given in ASME Section III ⁽⁴⁻³⁾ is used for the austenitic stainless steel top and bottom nozzles.

The material properties of fuel assembly structural components, such as Young's modulus, Poisson's ratio, yield strength, and ultimate tensile strength, are described in Appendix B of this report.

The fatigue life of the grid spacer spring is determined by fatigue testing, where a vibration is induced in the spring for a prescribed period under conditions simulating the operating temperature and hydrogen absorption of the grid spacer springs in-reactor, as discussed in Section 4.4.

4.1.2.1 Loads during Normal Operation

4.1.2.1.1 Top and Bottom Nozzles

As for the top nozzle, since loading conditions are different in normal operation and AOOs, it is necessary for the stresses under both conditions to be respectively evaluated. In normal operation, the holddown spring force is applied to the top nozzle. From the FEM analysis of the holddown spring, the force is estimated to be approximately { } lbf ({ } N) which is obtained by rounding up { } lbf ({ } N) in SI unit as evaluated in Table 4.6-1 of Section 4.6. Adding this load on the corner of the top nozzle, the stresses in the nozzle are obtained from the FEM analysis, an example of which is shown in Figure 4.1-1. The results are summarized in Table 4.1-1(a). The stresses are below the acceptance limits.

For the bottom nozzle, the results for the stress analysis during normal operation is described in Subsection 4.1.2.2 including the load at RCCA scram, since the load during normal operation is added on the adapter plate equally in the same way at RCCA scram.

4.1.2.1.2 Control Rod Guide Thimbles

The stresses in the guide thimbles are obtained using the fuel assembly axial structural analysis model shown in Figure 4.1-2. The applied loads are:

- Fuel assembly dead weight : [] lbf ([] N) ,
- Holddown force : [] lbf ([] N) ,
- Buoyancy : [] lbf ([] N) (obtained from the fuel assembly volume and the coolant density), and
- Lift force : [] lbf ([] N) (including the uncertainties in the assembly shape and the lift force evaluation).

The result is given in Table 4.1-1(c) and shows that the stress in control rod guide thimble is below the acceptance limit.

4.1.2.2 Loads during AOOs

4.1.2.2.1 Top and Bottom Nozzles

For the AOO loads on the top nozzle, the scram load from the RCCA is added to the top nozzle adapter plate. The maximum load produced when retainer spring has its maximum deflection on the top nozzle during RCCA dropping, is approximately [] lbf ([] N). For the FEM analysis the load condition is that this load is applied at the center of the adapter plate where retainer impacts. The results are summarized in Table 4.1-1(a), which shows that the loads are less than the acceptance limits.

For the bottom nozzle, from the analysis for the loads during normal operation and with an RCCA scram load of [] lbf ([] N), the reaction force at the bottom nozzle is [] lbf ([] N), including the uncertainties in assembly specification and the evaluation. The stresses obtained from the FEM analysis of the bottom nozzle, are summarized in Table 4.1-1(b), which shows that the loads are less than the acceptance limits.

4.1.2.2.2 Control Rod Guide Thimbles

(1) At the Time When the Control Rod Reaches the Thimble Dashpot Position

At this time the internal pressure in the thimble increases significantly and the RCCA is decelerated. The internal pressure is obtained from the motion equation of the RCCA and the maximum pressure is conservatively calculated to be [] ksi ([] MPa). Using the thin cylinder formula, the differential principal stress is below the acceptance limit, as shown in Table 4.1-1(c).

(2) At the Time When the RCCA Retainer Impacts with the Top Nozzle Adapter Plate

The loads in normal operation and the RCCA scram are added in the model shown in Figure 4.1-2. The resulting stress is below the acceptance limit, as shown in Table 4.1-1(c).

Table 4.1-1 Stress Evaluation Results for the Fuel Assembly Components during NO and AOOs

(a) Top Nozzle *

Unit: ksi (MPa)

| Stress category | Stress | | Acceptance limit at () deg.F |
|----------------------------|--------|-----|-------------------------------|
| | NO | AOO | |
| Primary membrane + bending | | | |
| Primary local + secondary | | | |

* [Primary membrane + bending] and [primary local + secondary] stresses are shown because they are relatively high.

(b) Bottom Nozzle *

Unit: ksi (MPa)

| Stress category | Stress in AOO ** | Acceptance limit at () deg.F |
|----------------------------|------------------|-------------------------------|
| Primary membrane + bending | | |
| Primary local + secondary | | |

* [Primary membrane + bending] and [primary local + secondary] stresses are shown because they are relatively high.

** Stress in AOO includes the load during NO.

(c) Control Rod Guide Thimble

Unit: ksi (MPa)

| Item | NO | AOOs | | Acceptance limit at () deg.F |
|---------------------------|----|--------------------------|-----------------------------|-------------------------------|
| | | Control rod at dashpot * | RCCA impact with top nozzle | |
| Control rod guide thimble | | | | |

* Differential primary stress between circumferential and axial stress due to the increase in internal pressure.



Figure 4.1-1 Sample Analytical Model, Top Nozzle FEM Analysis

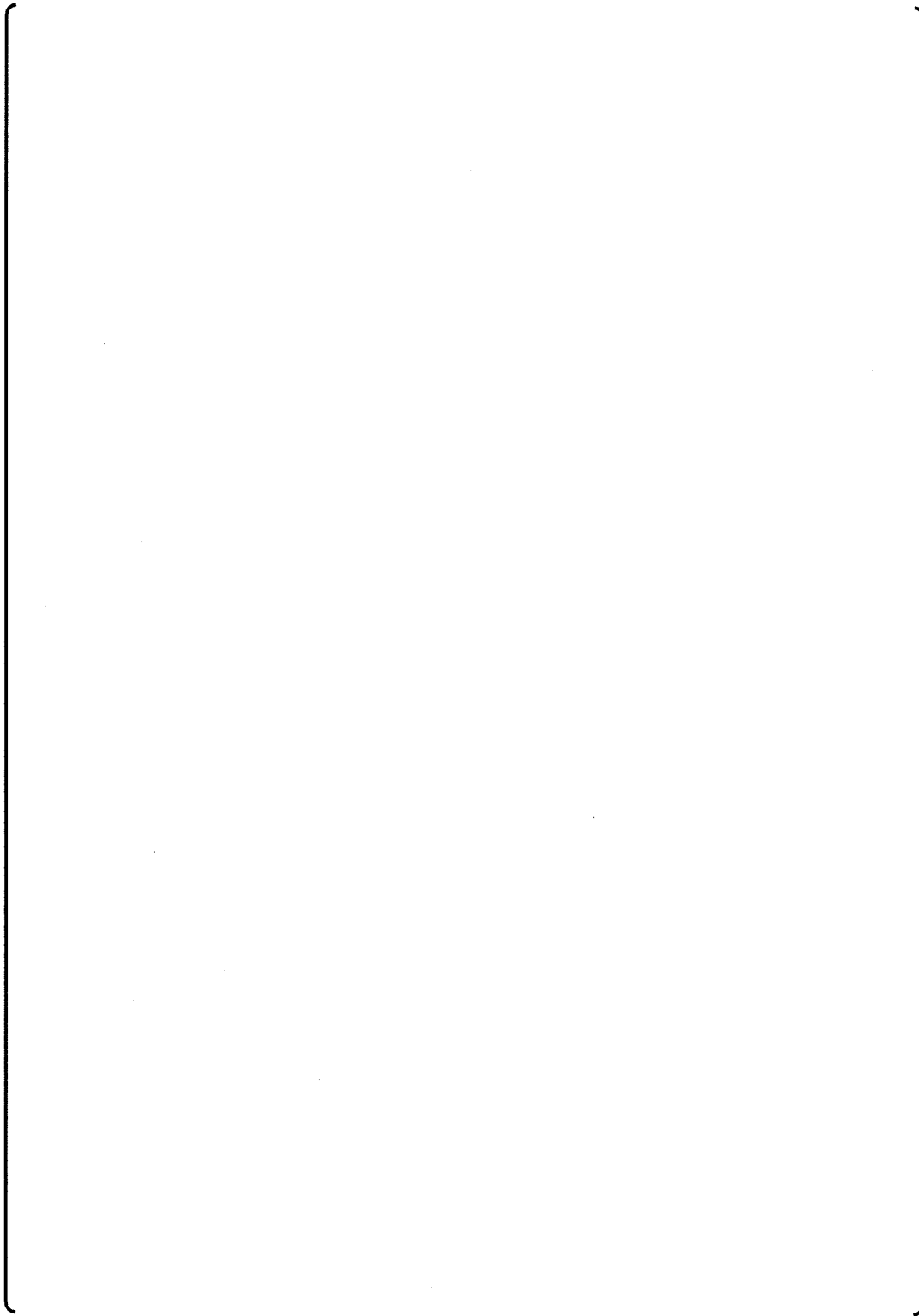


Figure 4.1-2 Analytical Model for Assembly Axial Mechanical Behavior

4.2 Loads in Fuel Shipping and Handling

4.2.1 Design Basis and Criteria

To obtain expected performance in the reactor, the fuel assembly will not experience excessive deformation during shipping and handling, including uncertainties.

- Under axial loading during shipping and handling, the stresses in the top and bottom nozzles and the control rod guide thimbles shall be less than the acceptance limits.
- Under axial loading during shipping and handling, forces occurring at the connection points between the top nozzle, the grid spacers and the control rod guide thimbles shall be less than the acceptance limit.
- Under lateral loading during shipping and handling, inelastic deformation of the grid spacer spring shall not be increased.
- The grid spacer spring shall not be damaged due to vibration during shipping.

4.2.2 Evaluation

The stress analysis is done by using the nominal dimension, without considering uncertainties from the manufacturing tolerance. Alternatively, the yield stress and the ultimate tensile stress (UTS) of un-irradiated materials are conservatively used in deciding the acceptance limits, instead of using the values of irradiated materials which are increased by irradiation hardening described in Appendix B of this report.

FEM stress analyses are used to determine the stresses in the top and bottom nozzles, using the loads imposed during shipping and handling. The stresses have been confirmed to be within the acceptance limits on ASME Section III ⁽⁴⁻¹⁾.

Using a structural analysis with an analytical model which simulates the mechanical characteristics of the fuel assembly in the axial direction, the loads imposed during fuel handling and shipping are determined for the linkages between the control rod guide thimbles and the top nozzle and the grid spacers. It is confirmed that the analytically calculated loads are less than the limiting elastic loads determined from tensile tests of the linkages.

For the control rod guide thimble, the maximum stress occurs just beneath the top nozzle because the guide thimble bears the entire axial load without sharing with the fuel rods at that point. The calculated maximum stress is confirmed to be less than the acceptance limit on ASME Section III ⁽⁴⁻¹⁾.

It is confirmed that plastic deformation of the grid spacer spring does not occur due to the lateral loads during handling and shipping.

A maximum acceleration of more than four times of gravity (4G) in axial direction has never been experienced during shipping and handling of the Mitsubishi conventional fuel assemblies. A 4G axial load is therefore used for the fuel shipping and handling evaluations for the US-APWR fuel assembly.

4.2.2.1 Top Nozzle

A 4G load is added at the corners of the nozzle to account for the effect of the shipping fixture. The 4G load is given by $4 \times \{ \quad \} \text{ N (assembly weight)} = \{ \quad \} \text{ lbf (} \{ \quad \} \text{ N)}$.

The weight of the in-core control component (ICCC) is not included in this evaluation, even if they are transported within the assembly, since the ICCC weight doesn't bear on the nozzle.

The stresses of the top nozzle during handling are obtained by adding a 4G upward load to the side of the nozzle, which is the interface with the handling tool. In the case the ICCC weight bears on the nozzle when an ICCC is in the fuel assembly and the heaviest ICCC weight (RCCA, approximately $\{ \quad \} \text{ lbf (} \{ \quad \} \text{ N)}$) is added to determine the total load. The 4G load is $4 \times (\{ \quad \} \text{ N})$, which gives a force of $\{ \quad \} \text{ lbf (} \{ \quad \} \text{ N)}$. These loads are used as the inputs to the FEM analysis to determine the stress distribution in the nozzle. An example of the FEM analysis of the top nozzle is shown in Figure 4.1-1. The stress in both shipping and handling is below the acceptance limit on ASME Section III ⁽⁴⁻¹⁾, as shown in Table 4.2-1(a).

4.2.2.2 Bottom Nozzle

In both shipping and handling the loads on the bottom nozzle are transferred from the control rod guide thimbles. Since the weight of the ICCC bears on the nozzle, the shipping and handling load on the bottom nozzle are $\{ \quad \} \text{ lbf (} \{ \quad \} \text{ N)}$. The results of the FEM analysis for this loading mode show that the stress in the bottom nozzle is less than the acceptance limit on ASME Section III ⁽⁴⁻¹⁾, as shown in Table 4.2-1(b).

4.2.2.3 Grid spacer

The inelastic deformation of grid spacer spring shall not be increased against a lateral 6G load during shipping and handling. Considering the fuel rod weight of upper and lower half span of the grid spacer, a 6G load is determined as $\{ \quad \} \text{ lbf (} \{ \quad \} \text{ N)}$.

Since the initial grid spacer spring force is more than $\{ \quad \} \text{ lbf (} \{ \quad \} \text{ N)}$, the inelastic deformation of spring is not increased.

4.2.2.4 Other Components

A load of $\{ \quad \} \text{ lbf (} \{ \quad \} \text{ N)}$ is used for the following analysis.

[

The bulge joint between the intermediate grid spacer and the control rod guide thimble propagates the load equivalent to fuel rod restraint force. The thimble screw preload may be transferred to the weld joint between the bottom grid spacer and the insert, due to flatness of the edge face in the insert. The control rod guide thimbles propagate the axial load of the fuel rods and the load distribution is analyzed using the fuel assembly axial model shown in Figure 4.1-2. The load distribution in the US-APWR fuel assembly is shown in Figure 4.2-1. Because it is easier for the fuel rods to slip in the top and bottom grid spacers, the thimbles mainly bear the

loads just beyond the top and beneath the bottom grid spacers and fuel rods mainly bear the loads among the intermediate grid spacers.

The stress and loads on these components are confirmed to be below the acceptance limits, as shown in Table 4.2-1(c) where allowable loads for the joint are obtained by tensile testing for these components.

Table 4.2-1 Strength Evaluation for Shipping and Handling Loads

(a) Top Nozzle *

| Category | Stress | | Acceptance limit |
|-------------------------------|----------|----------|------------------|
| | Shipping | Handling | |
| Primary membrane + bending | | | |
| Primary local + secondary | | | |

Unit: ksi (MPa)

* [Primary membrane + bending] and [primary local + secondary] stresses are shown because they are relatively high.

(b) Bottom Nozzle *

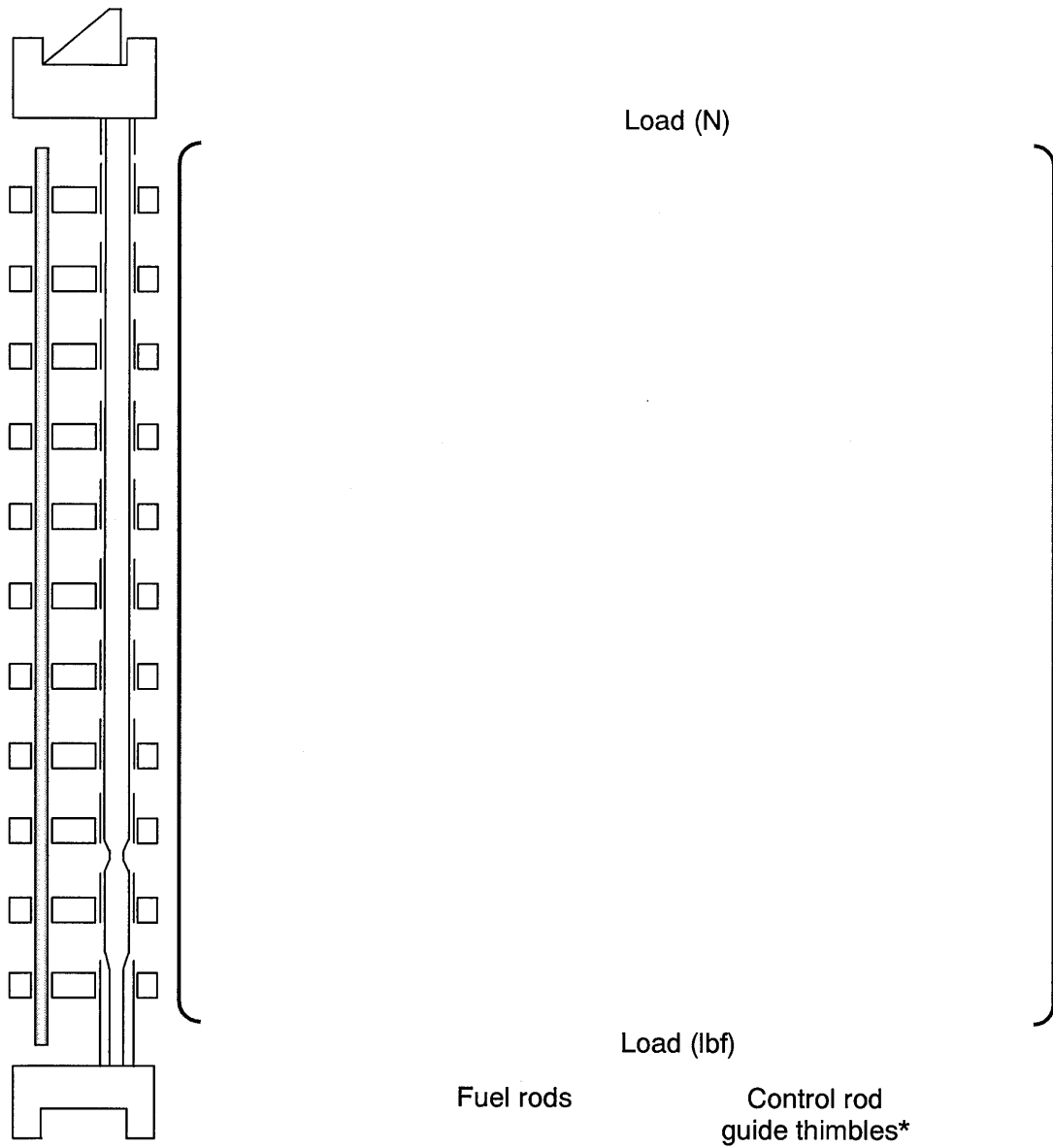
| Category | Stress | | Acceptance limit |
|-------------------------------|----------|----------|------------------|
| | Shipping | Handling | |
| Primary membrane + bending | | | |
| Primary local + secondary | | | |

Unit: ksi (MPa)

* [Primary membrane + bending] and [primary local + secondary] stresses are shown because they are relatively high.

(c) Other Components

| Components | Load (lbf (N)) | | Stress (ksi (MPa)) | | | |
|---|-------------------|-------|-----------------------|-------|--|--|
| | Max | Limit | Max | Limit | | |
| Control rod guide thimble | | | | | | |
| Top grid spacer joint (stainless steel sleeve) | | | | | | |
| Intermediate grid spacer joint (Zircaloy-4 sleeve) | | | | | | |
| Insert | | | | | | |



* Loads on the control rod guide thimbles and the fuel rods are compressive.

Figure 4.2-1 Fuel Rod and Control Rod Guide Thimble Load Distribution

4.3 Fuel Assembly Dimensional Changes

4.3.1 Rod Bowing

4.3.1.1 Design Basis and Criteria

To avoid fuel rod damage due to obstruction of coolant flow, excessive fuel rod bowing shall not occur. Departure from nucleate boiling (DNB) shall not occur at a 95 % probability at a 95 % confidence level basis with consideration of the DNB penalty due to rod bowing during normal operation and AOOs.

4.3.1.2 Evaluation

Fuel rod bowing is a phenomenon observed in irradiated fuel assemblies and leads to spacing closure between adjacent fuel rods. While the mechanism is not yet fully understood, it is related to the as-fabricated bowing of the fuel rods, the restraint force due to the grid spacers and the differential irradiation growth of the fuel rods and the control rod guide thimbles.

Significant fuel rod bowing may influence thermal-hydraulic characteristics, such as the departure from nucleate boiling ratio (DNBR).

The rod to rod spacing on all four faces of each fuel assembly has been image-analyzed from TV-tapes of irradiated fuel assemblies' visual inspections. The mean values and standard deviations of the rod to rod spacing are obtained for each span (the longitudinal space between consecutive grid spacers), and the rod to rod spacing rate is estimated from the worst span data. The design envelope for the rod to rod spacing rate at the worst span of each fuel assembly is established as a function of fuel assembly burnup.

Fuel rod bowing data from current Mitsubishi 17x17 fuel assemblies are shown in Figure 4.3-1. DNBR evaluation for The US-APWR fuel assembly is based on these data. It is assumed that the rod bowing of the US-APWR fuel can be estimated at the same level as the current Mitsubishi 17x17 fuel, for the following reasons:

- The US-APWR fuel uses Zircaloy-4 grid spacers. The data with Zircaloy-4 grid spacer in Figure 4.3-1 shows equal or smaller rod to rod spacing closure than is measured for 17x17 assemblies with Inconel grid spacers, and
- Data shown in Figure 4.3-1 are corrected for span length (distance between the grid spacers) of { } inch ({ } mm), which is the span length averaged in the conventional 17x17 fuel assembly. Since the span lengths for the US-APWR fuel assembly are { } inch ({ } mm), qualitatively speaking, the shorter span length leads to less rod bowing for the same bending moment condition.

The shorter span length and the grid spacer spring restraint force on the fuel rods in the US-APWR fuel assembly are adequately designed to reduce the fuel rod bowing and the consequent DNB penalty to an acceptable level.

In addition to large scattering in the rod bowing data, the grid spacer made of Inconel is regarded to show bigger rod bowing than that of Zircaloy-4, owing to less relaxation of the spring force.

With considering safety factor and statistical probability, the rod to rod spacing closure at EOL in the US-APWR fuel assembly is obtained from the closure rates of the conventional fuel assemblies with Inconel grid spacers in the figure. The provided closure rate is used in the DNB penalty evaluation for the rod bowing.

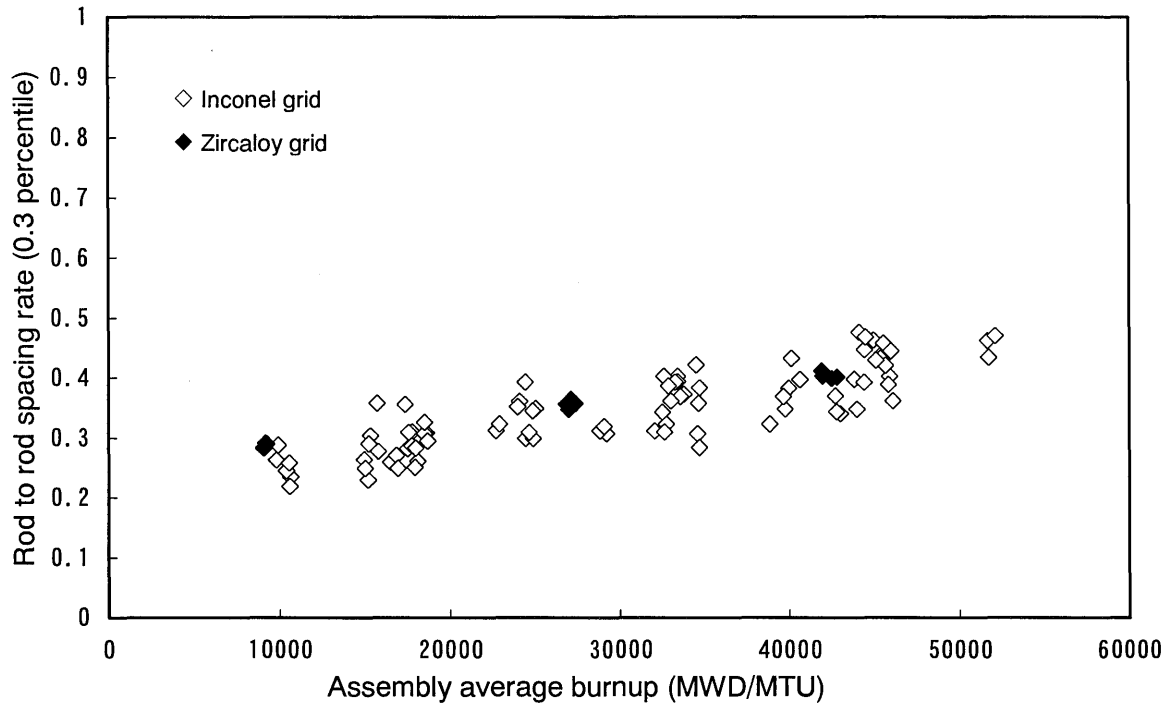


Figure 4.3-1 Rod Bowing of Mitsubishi 17x17 Fuel Assemblies

4.3.2 Fuel Assembly Growth Evaluation

4.3.2.1 Design Basis and Criteria

To maintain a coolable geometry in the core and assure safe shutdown of the reactor, the fuel assembly will not be excessively distorted nor damaged by compressive loads due to interference with the upper and lower core plates during irradiation.

Clearance between the top nozzle and the upper core plate shall be maintained throughout the fuel assembly irradiation.

4.3.2.2 Evaluation

The fuel assembly growth is evaluated at the cold condition because the thermal expansion between the core plates is more than that of the fuel assembly at the hot condition.

Fuel assembly growth as a function of burnup is defined on the basis of measured assembly length change data. Considering the fuel assembly maximum growth at the end of life predicted by this function and the minimum distance between the core plates, the overall length of the fuel assembly is determined to maintain clearance between the top nozzle and the upper core plate during the fuel life.

The growth of the US-APWR assembly is evaluated using a design curve based on assembly growth data obtained from fuel assemblies with the current Inconel grid spacer design. The design curve is a 95% probability at a 95% confidence level upper bound of the data shown in Figure 4.3-2.

The upper bound of assembly growth is approximately { } % at 60 GWD/MTU, which is less than the assembly growth limit of { } % required to prevent the interference between the fuel assembly and the core plates.

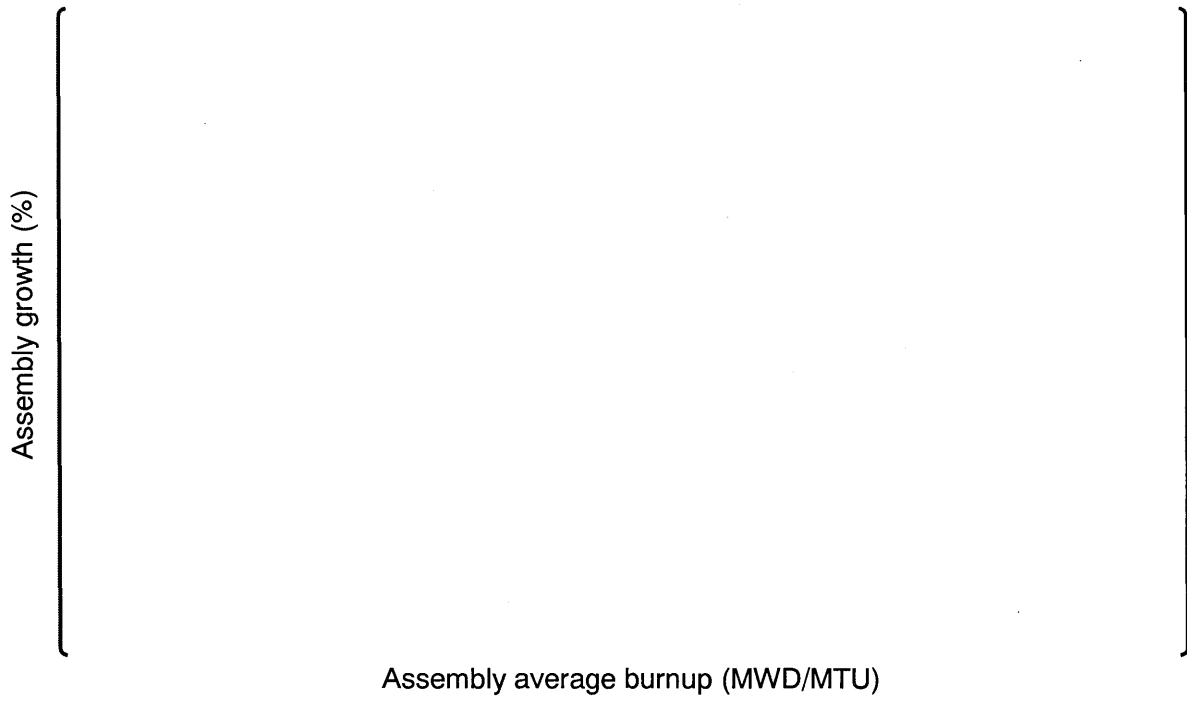


Figure 4.3-2 Mitsubishi 17x17 Fuel Assembly Growth Data with Inconel Grid Spacers

4.3.3 Fuel Rod Growth (Total Gap Change)

4.3.3.1 Design Basis and Criteria

To supply expected thermal power and maintain fuel rod integrity during irradiation, the fuel rods should not experience excessive bowing, nor be damaged by excessive compressive loading due to interference between the fuel rod and the top and bottom nozzles during irradiation, that results from the difference in the axial growth of the fuel rods and the fuel assembly.

Clearance between the fuel rod and the top and bottom nozzles shall be maintained throughout the fuel assembly life.

4.3.3.2 Evaluation

To preclude interference between the fuel rod and the nozzles, the fuel rods and fuel assembly are designed with an initial clearance between the fuel rod ends and the top and bottom nozzles.

The total gap is defined as a sum of clearance between the top and bottom nozzles, and both ends of the fuel rod. The variation of the total gap with burnup, which is the difference between the fuel rod growth and the fuel assembly growth, is used for the design curve for the total gap evaluation. The design curve is determined based on data obtained from the irradiated fuel assemblies.

This initial total gap is designed to be sufficient to accommodate the maximum anticipated fuel rod growth in combination with the minimum fuel assembly growth, with appropriate consideration of manufacturing tolerances.

Figure 4.3-3 shows total gap change for the conventional 17x17 fuel assemblies. The best estimate line and a [] level upper bound line are also shown in the figure.

For the US-APWR fuel, the design curve is set by correcting the extended fuel length and the thermal expansion difference between the fuel rod and the control rod guide thimble, since the data of the figure are obtained from the 12ft fuel assemblies under cold condition.

The total gap change for the US-APWR fuel is estimated to be [] inch ([] mm) at 60 GWD/MTU, which is less than the as-fabricated minimum total gap of [] inch ([] mm). This confirms that clearance between the fuel rods and the top and bottom nozzles is maintained throughout the US-APWR assembly lifetime.

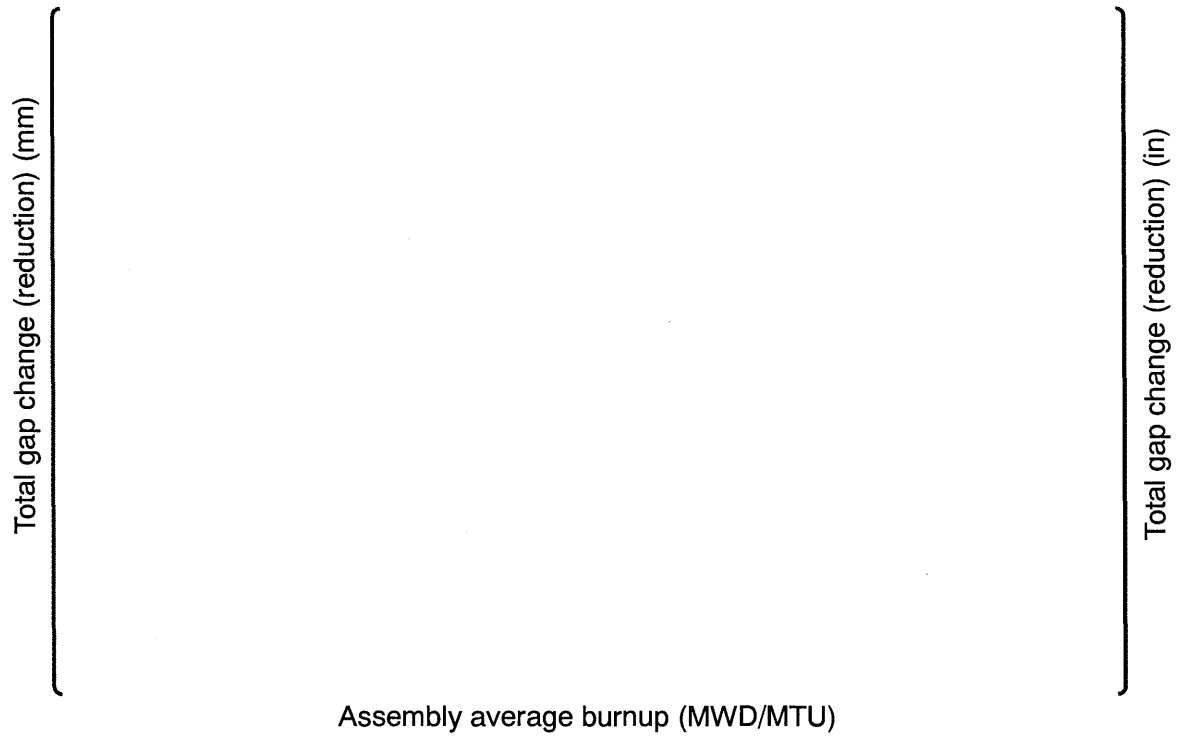


Figure 4.3-3 Total Gap Change of Mitsubishi 17×17 Fuel Assemblies

4.3.4 Fuel Assembly Bowing

Fuel assembly bowing data for Mitsubishi conventional 17x17 fuel assemblies with Zircaloy-4 grid spacers are shown in Figure 4.3-4. Bowing data of the fuel assemblies with Zircaloy-4 grid spacers are the open circles in the figure. In general the fuel assembly bowing for the assemblies with Zircaloy-4 grid spacers is less than the bowing of the assemblies with Inconel grid spacers because the spring force relaxation of the Zircaloy-4 grid spacer is larger than that of the Inconel grid spacer described in Section 4.4.

By applying 11 grid spacers, the US-APWR fuel assembly has shorter grid spacer spacing compared with the current 14 ft fuel with 10 grid spacers for US reactor. This shorter spacing contributes to increase lateral stiffness of fuel assembly. The higher stiffness compensates reduction of the stiffness by axial extension of 12 to 14 ft. Mitsubishi expects that a bowing of the US-APWR 14 ft fuel is comparable to current 12 ft fuel with 9 grid spacers design.

Fuel assembly bowing may affect incomplete rod insertion (IRI). Mitsubishi has been applied improved dashpot design of fuel assembly thimble tubes to domestic plants. By reducing axial length with slenderized diameter of the dashpot, the improved design contributes to lower the risk of IRI. This design is also applied to the US-APWR fuel assembly.

As the same with conventional Mitsubishi 12ft fuel assemblies, there is little possibility for the US-APWR fuel assembly to cause serious issue in loading and unloading, and the control rod insertion due to the fuel assembly bowing.

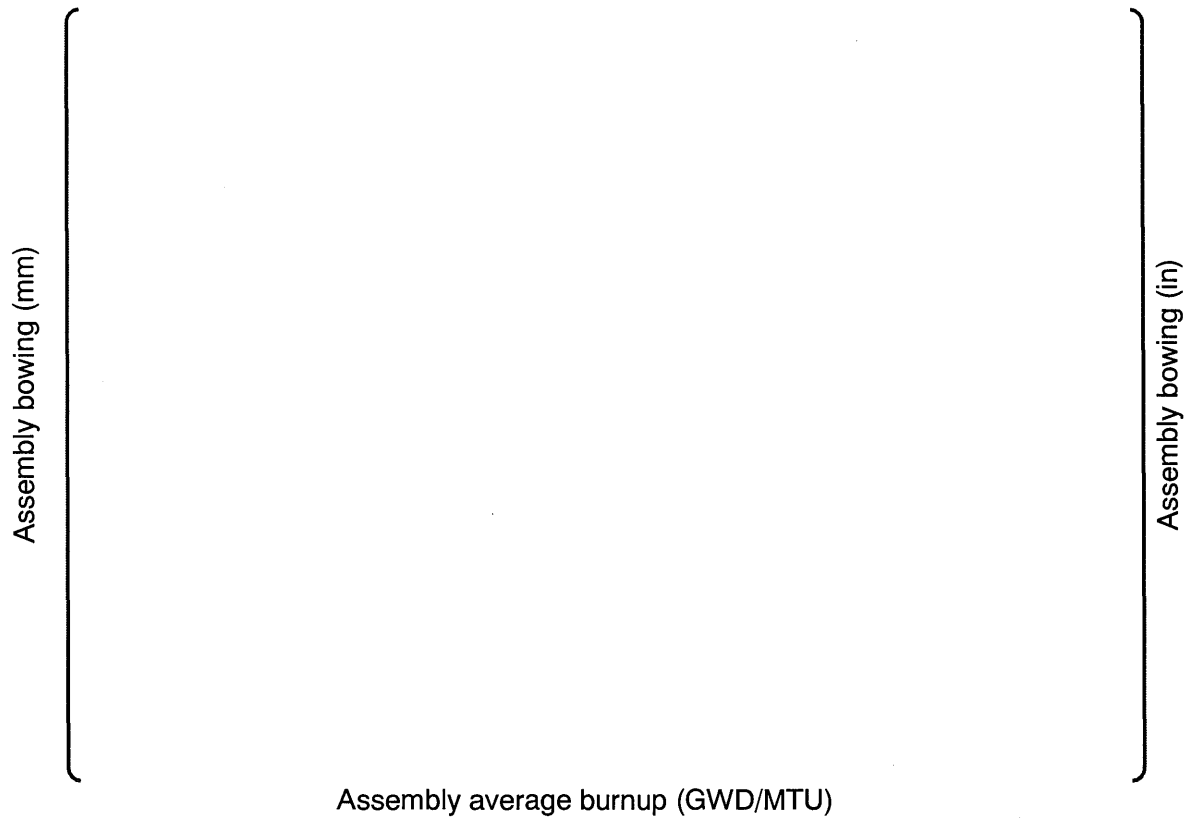


Figure 4.3-4 Fuel Assembly Bowing of Mitsubishi 17x17 Fuel Assemblies

4.4 Grid Spacer Irradiation Behavior

4.4.1 Zircaloy-4 Material Properties

Zircaloy-4 is used for the intermediate grid spacers, control rod guide thimbles, an in-core instrumentation guide tube and the sleeves joining them. Zircaloy-4 material properties are described in Appendix B of this report and the corrosion behavior is confirmed not to affect the mechanical integrity as summarized below.

The oxide thickness at assembly burnup of 60 GWD/MTU is conservatively estimated to be less than [] mil ([] μm) which corresponds to [] mil ([] μm) of reacted thickness. It is approximately [] % of wall thickness of the thimble and less than [] %, beyond which mechanical integrity check is required.

The absorbed hydrogen at assembly burnup of 60 GWD/MTU is conservatively estimated to be less than [] ppm which does not reach to acceptance limit of [] ppm.

4.4.2 Inconel-718 Material Properties

Inconel-718 is used for the top and bottom grid spacers. Inconel-718 material properties are described in Appendix B of this report.

The corrosion of Inconel-718 is well-known to be very small.

4.4.3 Grid Spacer Spring Evaluation

4.4.3.1 Initial Spring Force

The US-APWR fuel assembly uses the Zircaloy-4 grid spacer named "Z3", described in Chapter 2. As shown in Figure 4.4-1, the initial spring force of the Z3 grid spacer is the same as for the Z2 grid spacer spring, which has been used in the current Mitsubishi 17x17 fuel assembly. The spring shape in inner cell of Z3 is different from that of Z2 in order to reduce hydraulic resistance.

4.4.3.2 Irradiation Induced Relaxation of Spring Force

Data from US reactors for the Inconel-718 and Zircaloy-4 grid spacer spring force relaxation due to fast neutron irradiation are shown in Figure 4.4-2. Vertical axis of the figure means the rate of lost restraint force which is measured by withdrawing fuel rods from fuel assembly. The spring force relaxation saturates after an exposure of [] (n/cm^2 , $E>1.0\text{MeV}$) for the Inconel grid spacer and [] (n/cm^2 , $E>1.0\text{MeV}$) for the Zircaloy-4 grid spacer, with approximately [] % and [] % of spring force remaining for the Inconel and Zircaloy-4 grid spacers, respectively. Figure 4.4-3 shows spring force relaxation data from Japanese plants. The relaxation design curve for the Zircaloy-4 grid spacer is also shown in Figure 4.4-3. The Zircaloy-4 grid spacer data (open and closed circle symbols in the figure) show that more than [] % of the spring force is retained and is consistent with the US reactor data. Since the Z3 grid spacer spring has similar spring properties as the Z2 grid spacer, these data confirm that the relaxation of the Z3 grid spacer springs is acceptable.

4.4.3.3 Spring Fatigue Properties

4.4.3.3.1 Design Basis and Criteria

To supply expected thermal power and to maintain coolable geometry of the core and safe shutdown of the reactor, significant deformation in the fuel assembly should not occur under anticipated loads during normal operation and AOOs.

- The grid spacer spring shall not fail throughout the fuel life due to fatigue which results from hydraulic vibration of the fuel rod.

4.4.3.3.2 Evaluation

Data for the fatigue property of Z3 grid spacer spring is shown in Figure 4.4-4. Vibration amplitude as fatigue limit is estimated to be at least { } mil ({ } mm) in the figure.

Since the vibration amplitude given to the grid spacer spring due to fuel rod vibration is generally less than one hundredth of the fatigue limit amplitude obtained in the test, it is confirmed that the fatigue characteristic of the Z3 grid spacer spring is acceptable.

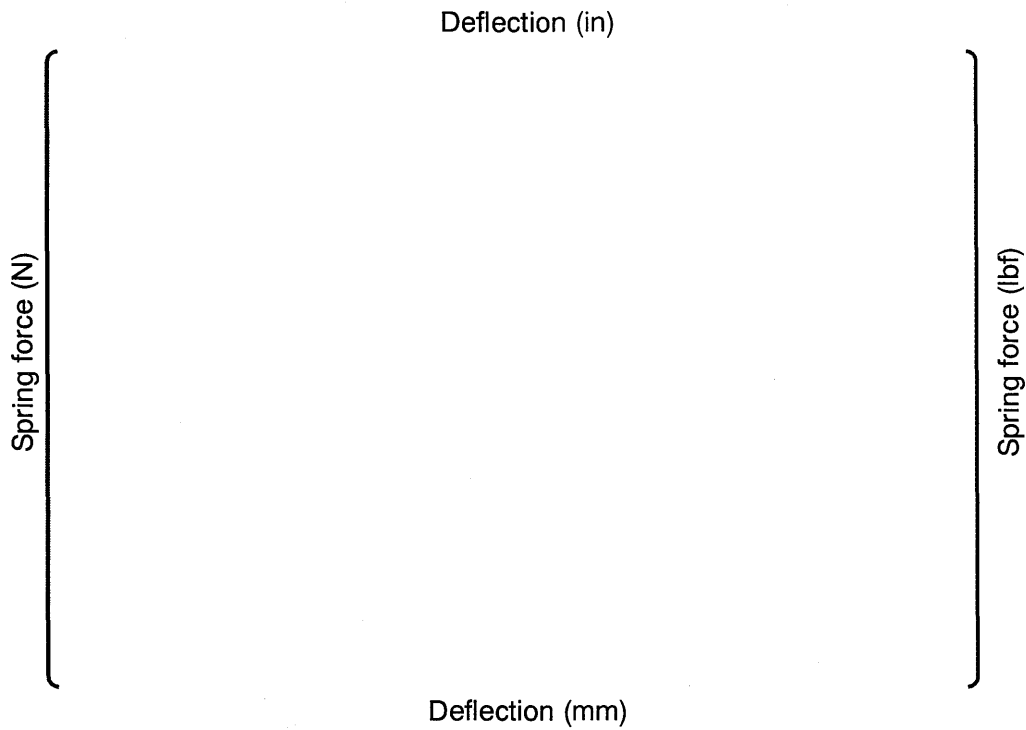


Figure 4.4-1 Load-Deflection Curve of the Inner Grid Spring (at Room Temperature)

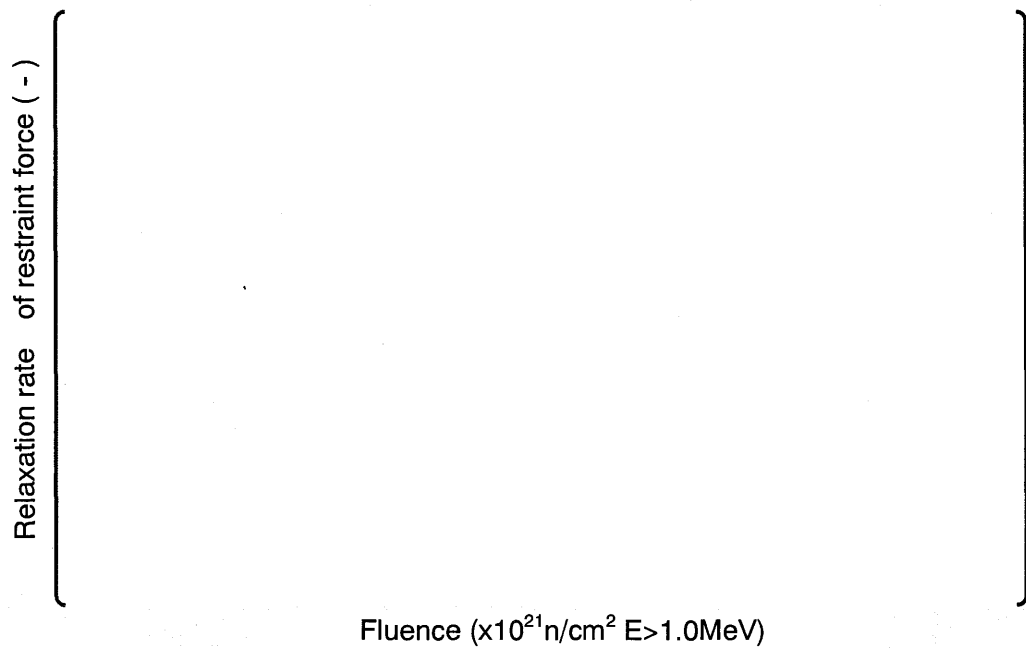


Figure 4.4-2 Grid Spacer Spring Relaxation Rate (US Reactor Data)

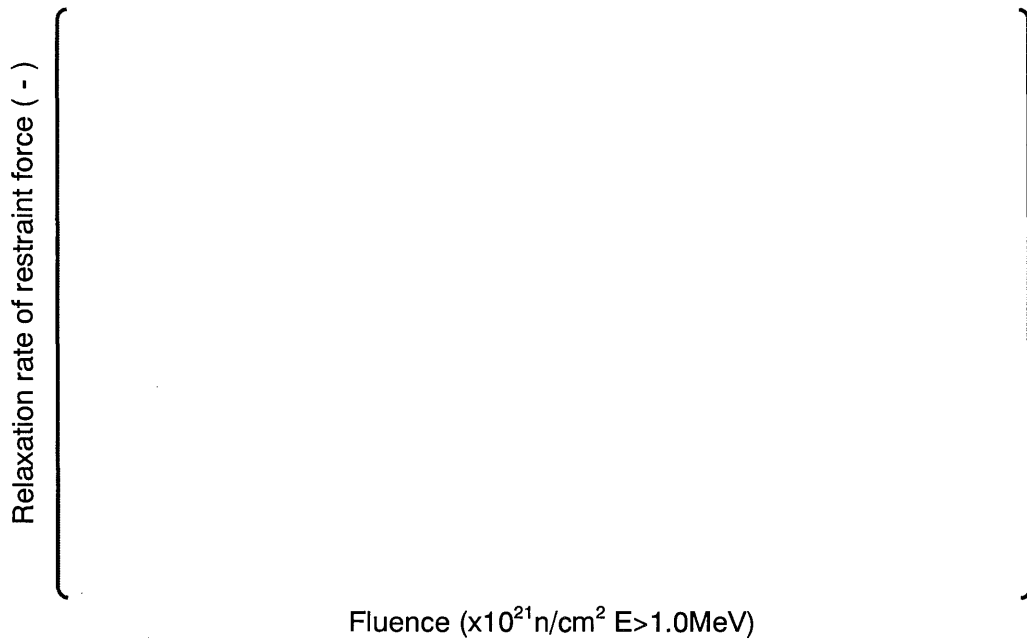


Figure 4.4-3 Grid Spacer Spring Relaxation Rate (Japanese Reactor Date)

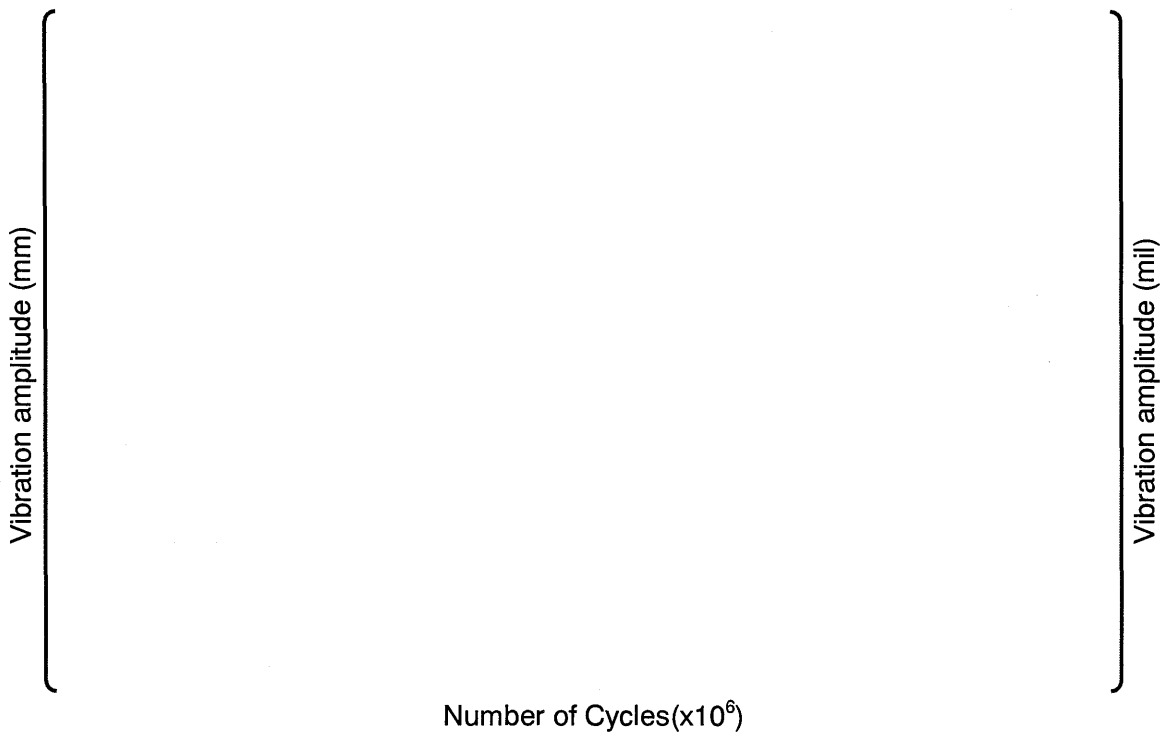


Figure 4.4-4 Grid Spring Fatigue Properties

4.4.4 Grid Spacer Dimensional Stability

4.4.4.1 Design Basis and Criteria

To maintain sufficient restraint on the fuel rods during irradiation, and during loading and unloading of the fuel assemblies, the grid spacer will maintain dimensional stability during irradiation.

The grid spacers shall maintain fuel rod to rod spacing during irradiation. The grid spacers also contribute to locating the fuel assemblies in their correct core position. In addition, the dimensional change of the grid spacers shall not cause excessive interference with neighboring structures such as other fuel assemblies and neutron reflectors.

4.4.4.2 Evaluation

Particularly with regard to the Zircaloy-4 grid spacer which experiences irradiation growth during its in-reactor exposure, the increase of the grid spacer's outer size at the end of life is evaluated based on data for the grid spacer's outer size in irradiated fuel assemblies.

Based on measurement from the irradiated fuel assemblies, Mitsubishi sets a line shown in Figure 4.4-5 as the relationship between burnup and irradiation growth rate of outer size in Zircaloy-4 grid spacer,,

The relationship is expressed by following equations:

$$GR(Bu) = \left(\begin{array}{c} \\ \end{array} \right) \quad (BU > \left(\begin{array}{c} \\ \end{array} \right))$$

$$GR(Bu) = \left(\begin{array}{c} \\ \end{array} \right) \quad (BU \leq \left(\begin{array}{c} \\ \end{array} \right))$$

where

GR(Bu): Growth rate of outer size in Zircaloy-4 grid spacer as a function of Bu, (%)

Bu : Fuel assembly average burnup (MWD/MTU)

By using above equation and burnup of each US-APWR fuel assembly described in Appendix A of this report, core average growth rate of outer size in the grid spacer is calculated at the end of cycle in equilibrium core:

$$GR_{Ave} = \frac{\sum_{i=1}^{257} GR(Bu_i)}{257}$$

where

GR_{Ave} : Core average growth rate of outer size in the Zircaloy-4 grid spacer at the end of cycle in equilibrium core

i : i-th fuel assembly, from 1 to 257

Bu_i : Average burnup of the i-th fuel assembly

Since the GR_{Ave} is estimated to be { } % by core design of the US-APWR, one-sided growth length of the outer size in the grid spacer is provided as follows.

$$GL = (WD_{Nominal} + TL) \times GR_{Ave} / 2$$

where

GL ; One-sided growth length of outer size in the Zircaloy-4 (inch)

$WD_{Nominal}$: Nominal outer size of the Zircaloy-4 grid spacer (inch)

TL : Manufacturing tolerance of the Zircaloy-4 grid spacer's outer size (inch)

In the case of the US-APWR,

$$GL = \{ \quad \quad \quad \}$$

Compared with half clearance in adjacent fuel assemblies of 0.02 inch (0.5 mm), the one-sided growth length of { } inch ({ } mm) is small enough, which provides less interaction for locating the fuel assemblies in correct position during irradiation and for handling the fuel assemblies during loading and unloading.

Although maximum growth rate of the Zircaloy-4 grid spacer is calculated to be about { } % at 60 GWD/MTU and fuel rod pitch is expanded according to the rate, the expansion does not bring significant effect in terms of the core design.

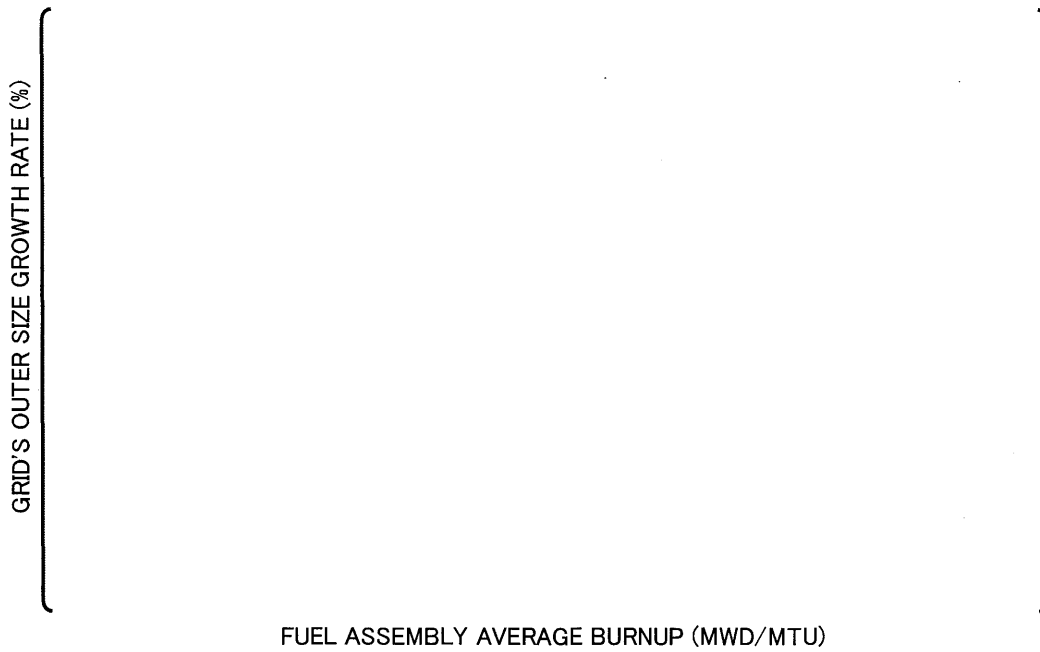


Figure 4.4-5 Burnup Dependence of Outer Size Increase in Zircaloy-4 Grid Spacer

4.5 Fuel Cladding Fretting Wear

4.5.1 Design Basis and Criteria

To supply expected thermal power and to prevent leakage from the fuel rod, the fuel rod will not be damaged by fuel cladding fretting wear due to hydraulic vibration during normal operation.

The maximum fretting wear depth on the cladding surface shall be less than [] % of the initial wall thickness.

4.5.2 Evaluation

4.5.2.1 Evaluation Methodology

The fretting wear of the fuel rod cladding is evaluated by long-term hydraulic-flow tests and analytical evaluations discussed in detail in Appendix C of this report.

The fuel rod vibration characteristics and measured wear depth are obtained from hydraulic flow tests and used as reference data for the analytical evaluation, where the wear depth is extrapolated to predict the expected maximum wear depth at the end of life in the reactor.

The analytical evaluation for predicting fretting wear in the fuel rod cladding is based on test results and developed in a semi-empirical manner. The fretting wear calculation requires three steps: evaluation of the fuel rod vibration, amplitude evaluation of the fuel rod vibration due to hydraulic flow, and the wear depth evaluation for the cladding at the grid spacer support points.

The characteristics of each step of the analytic evaluation are below.

- Modal analysis of the fuel rod vibration

This step calculates the fuel rod vibration characteristics, such as natural frequencies and mode shapes, using an FEM analysis that simulates one fuel rod considering its stiffness, mass distribution and axial support conditions. The analysis considers characteristics such as the variation of the vibration due to relaxation of the grid spacer spring force, using an algorithm that is based on the results of fuel rod vibration tests performed with the fuel rod restraint condition as a parameter.

- Calculation of the amplitude of the fuel rod vibration due to hydraulic flow

Using the fuel rod vibration characteristics provided by the modal analysis described above and an experimentally defined damping factor, the amplitude of the fuel rod vibration due to the axial coolant flow is calculated. A semi-empirical equation developed by J. R. Reavis⁽⁴⁻⁴⁾ has been adopted for this calculation. The equation gives the vibration amplitude of the fuel rod at the center between adjacent grid spacers. The amplitude is used to calculate the vibration amplitude at the dimple location in the grid spacer by considering the vibration mode shapes. In addition, the force resulting from the vibration is compared with the slippage limiting force of the grid spacer spring to determine if fuel rod slippage occurs and, if so, the slippage distance at the dimple is calculated.

Flow velocity

{ } given in US-APWR Thermal and Hydraulic Design Parameters is used.

Evaluation time period

-{ }

Grid spacer spring force

As described in Section 4.4, the grid spacer spring force for Zircaloy-4 grid spacers rapidly relaxes at the beginning of irradiation, but the relaxation saturates and approximately { } force remains at end of life. In this evaluation the grid spring force is conservatively set as follows:

- In the first cycle, the grid spring force for the Zircaloy-4 grid spacer is set to { } % of the as-fabricated grid spacer spring force and to { } % ({ } %) for the top (bottom) Inconel grids. The Inconel grid values are { } % of their second cycle values.
- The grid spring force for the Zircaloy-4 grid spacers is kept at { }% throughout the second cycle. The grid spring spacer force for the top (bottom) Inconel grids is set to { } % ({ } %), based on the minimum values for the end of life grid spacer restraint force measured for a Zircaloy-4 grid spacers lead use assembly. These data are shown in Figure 4.5-1.

Cladding surface oxidation

A maximum cladding surface oxide thickness of { } mil ({ } μm) at the end of second cycle is assumed, based on a cladding corrosion evaluation for the minimum burnup gadolinia fuel rod. In the fretting wear calculations the cladding oxidation is assumed to vary linearly with the irradiation time and its axial distribution is given by Figure 4.5-2.

4.5.2.3 Evaluation Result

Using the conditions and the cladding fretting wear model described above, the cladding wear for the maximum burnup rod at the end of two cycles has been calculated. The time dependence of the cladding corrosion is included in the analysis.

Resulting wear depths at the end of life are shown in Table 4.5-1. Fretting wear develops at the intermediate grid spacers, but the maximum wear depth is approximately { } mil ({ } μm), which is less than { } % of cladding wall thickness.

Table 4.5-1 US-APWR EOL Wear Depth Evaluation Results

| Grid spacer | Wear depth (mil (μm)) |
|--------------------|---------------------------------------|
| [Empty table body] | |

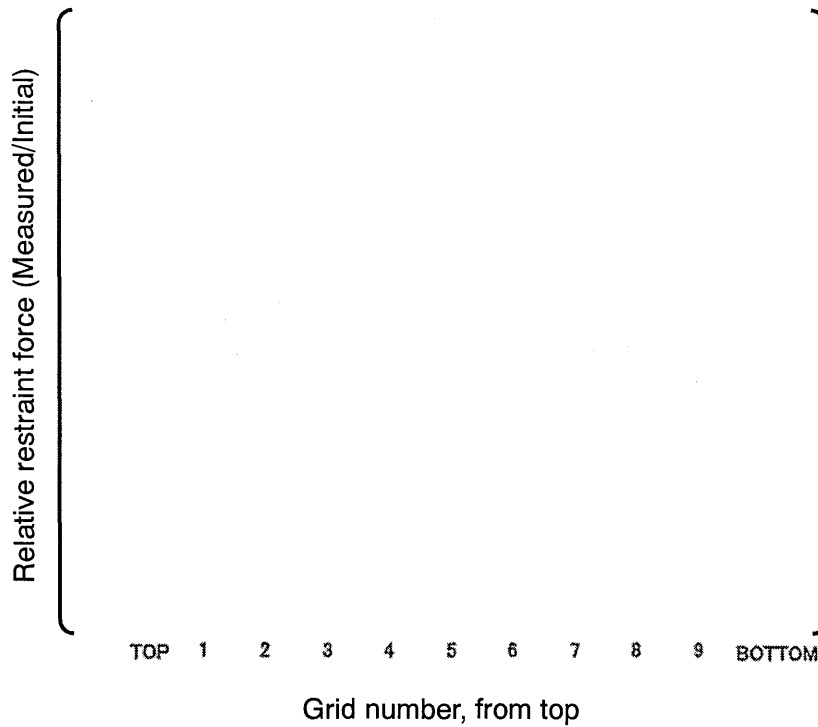


Figure 4.5-1 Zircaloy-4 Grid Relative Restraint Force after 2 Cycles of Irradiation

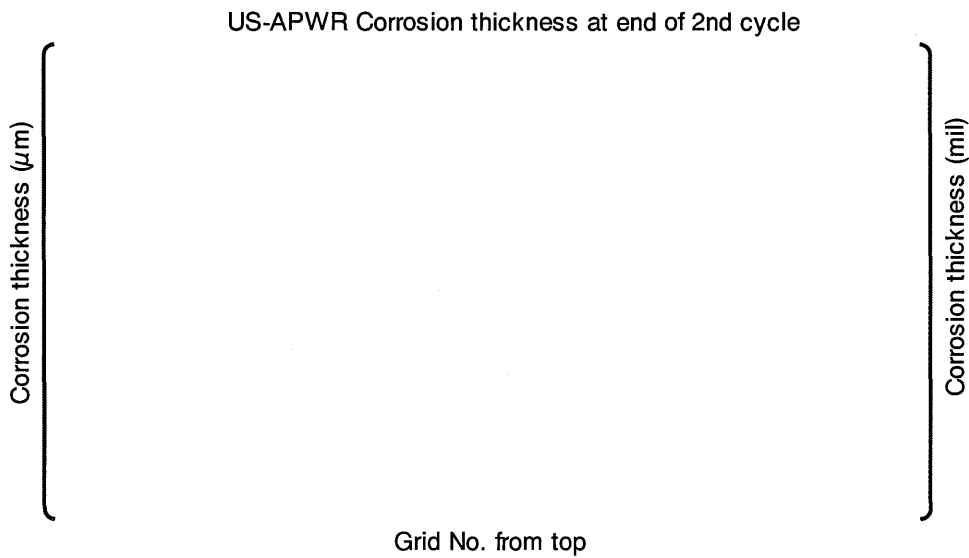


Figure 4.5-2 Corrosion Thickness Axial Distribution

4.6 Fuel Assembly Liftoff

4.6.1 Design Basis and Criteria

To keep the fuel stack in the proper position and to prevent fuel assembly damage due to impact following liftoff, fuel assembly liftoff will not occur due to hydraulic forces during normal operation and AOOs, except for pump-over-speed condition.

If fuel assembly liftoff does occur during pump-over-speed condition, the function of the fuel assembly holddown spring will not be degraded.

- Normal operation and AOOs except pump-over-speed condition:

At the cold condition for reactor startup in the beginning of life, which is the most critical period for the liftoff evaluation of the fuel assembly, the holddown spring force of the top nozzle shall be larger than the residual force which is calculated as "hydraulic lift force + buoyant force – fuel assembly weight".

- At pump-over-speed condition:

Inelastic deformation of the holddown spring shall not occur during lifting of the fuel assembly due to the hydraulic force at pump-over-speed condition.

4.6.2 Evaluation

Since the overall length of the fuel assembly is increased by irradiation, the force of the holddown spring increases as it is irradiated. Consequently, the function of the holddown spring to prevent the fuel assembly liftoff is evaluated in the non-irradiated state where the spring force is the smallest. A mechanical force balance calculation, considering the fuel assembly weight, the holddown force, the hydraulic lift force and the buoyant force, is used to determine that the fuel assembly does not experience liftoff at the cold startup condition at the beginning of life.

A hydraulic test of the fuel assembly is carried out for evaluation of the design margin.

Additional plastic deformation of the holddown spring does not occur, as long as the deflection of the holddown spring due to the liftoff at pump-over-speed condition is not beyond the maximum deflection at the cold startup condition. This is verified by the same mechanical balance calculation as used for normal operation and AOOs.

4.6.2.1 Function of the Holddown Spring

The holddown spring keeps the fuel assembly from lifting off due to upward coolant flow. The required force is the lift force plus the buoyancy minus the assembly weight. There is a large deflection of the holddown spring and hence there will be plastic deformation of the spring. The detailed behavior of the holddown spring is described below.

Figure 4.6-1 illustrates variation of the holddown spring deflection in the reactor conditions.

4.6.2.2 Cold Condition

The upper core plate is put into position and bears on the fuel assembly, after the assembly has been positioned on the lower core support plate. The deflection of the spring, δC in Figure 4.6-1 is the difference between nominal overall length of the US-APWR fuel assembly including the holddown spring height and the distance from upper core plate to lower core support plates. The deflection of the spring with plastic deformation is expressed as point (a) in Figure 4.6-2.

4.6.2.3 Hot Condition

The assembly length and the distance between the upper core and lower core support plates both increase due to thermal expansion in the hot condition. The thermal expansion of the fuel assembly is subjected to the expansion of the Zircaloy-4 control rod guide thimbles and ZIRLO fuel rod claddings. Since the thermal expansion of the stainless steel core internals is greater than the Zircaloy-4 thermal expansion, increase in length of the fuel, A in the schematic diagram (a) in Figure 4.6-1, is less than the increase in the distance between the core plates, B in the schematic diagram (b) in Figure 4.6-1. Hence the holddown spring deflection in the hot condition, $\delta H = \delta C - (B - A)$, point (b) in Figure 4.6-2, is less than it is in the cold condition. The force of the spring after it has experienced plastic deformation decreases linearly with a decrease in the deflection. The spring constant also decreases in the hot condition due to the decrease of the Young's modulus of the Inconel-718 spring as the temperature increases. Accordingly the load in the hot condition changes from point (a) to point (b) in Figure 4.6-2.

In addition, in the hot condition the lift and the buoyancy force both decrease due to the decrease of the coolant density. The decreased spring force in the hot condition is still large enough to prevent assembly liftoff.

Quantitative results for the force balance on the assembly at cold and hot conditions are given in Table 4.6-1. These quantitative results confirm that fuel assembly liftoff does not occur at the cold and hot conditions.

4.6.2.4 Pump-Over-Speed Condition

If the fuel assembly lifts off due to the increase in flow at the pump-over-speed condition, the deflection of spring increases to point (c) in Figure 4.6-2. There will be no additional plastic deformation of the holddown springs if the deflection at the pump-over-speed condition does not exceed the deflection δC at cold condition. However, if the deflection at the pump-over-speed condition exceeds the deflection at the cold conditions, there will be additional plastic deformation of the holddown springs at the pump-over-speed condition, as shown by points (d) and (e) in Figure 4.6-2. In this case the design criteria for the pump-over-speed condition will not be met.

The pump-over-speed condition evaluation results are shown in Table 4.6-2. The fuel assembly lifts off at the pump-over-speed condition, but the resulting force on the holddown springs is less than the force that corresponds to the deflection at the cold condition, point (c) of Figure 4.6-2, and there will be no additional plastic deformation of the holddown springs.

4.6.2.5 Fatigue of the Holddown Spring

The fatigue usage factor of the holddown spring is required to be less than 1.0. In the evaluation, the spring force at cold condition is considered as the maximum spring force until loading condition.

Cycle numbers of loading and unloading are conservatively assumed as [] times a year in each, total [] times during [] years of the fuel assembly life.

The design fatigue curve for Inconel is obtained from ASME code ⁽⁴⁻³⁾ and the fatigue usage factor is evaluated to be less than 1.0.

Table 4.6-1 Holddown Spring Evaluation at Cold and Hot Conditions

Unit: lbf (N)

| Condition | Upward force* | | Downward force | | | Evaluation |
|----------------|----------------------|----------|----------------|-----------------------------------|---|------------|
| | Hydraulic lift force | Buoyancy | Dead weight | Required force in holddown spring | Holddown force per Assembly (Force per spring x 4 springs per assembly) | |
| | L | B | W | $R = L + B - W$ | F | |
| Cold startup | | | | | | |
| Hot full power | | | | | | |

* Uncertainties in assembly shape and evaluation are included.

Table 4.6-2 Holddown Spring Evaluation at Pump-over-speed Condition

Unit: lbf (N)

| Condition | Upward force* | | Downward force | | Limit force for no additional plastic Deformation** | Evaluation |
|-----------------|----------------------|----------|----------------|-----------------|---|------------|
| | Hydraulic lift force | Buoyancy | Dead weight | Spring force | | |
| | L | B | W | $R = L + B - W$ | | |
| Pump-over-speed | | | | | | |

* Uncertainties in assembly shape and evaluation are included.

** Limit force is corresponding to the point (c) in the Figure 4.6-2.

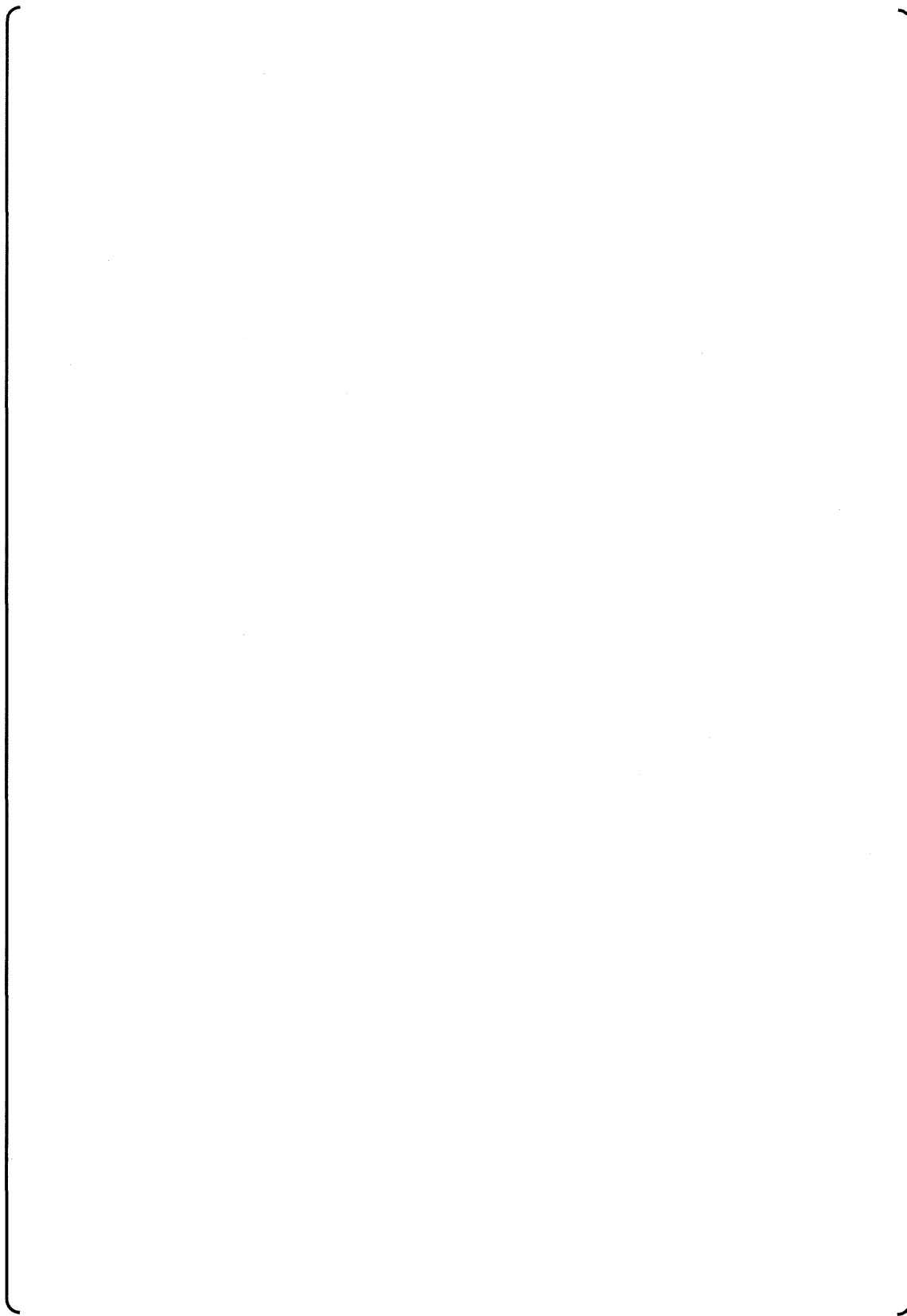


Figure 4.6-1 Holddown Spring Deformation

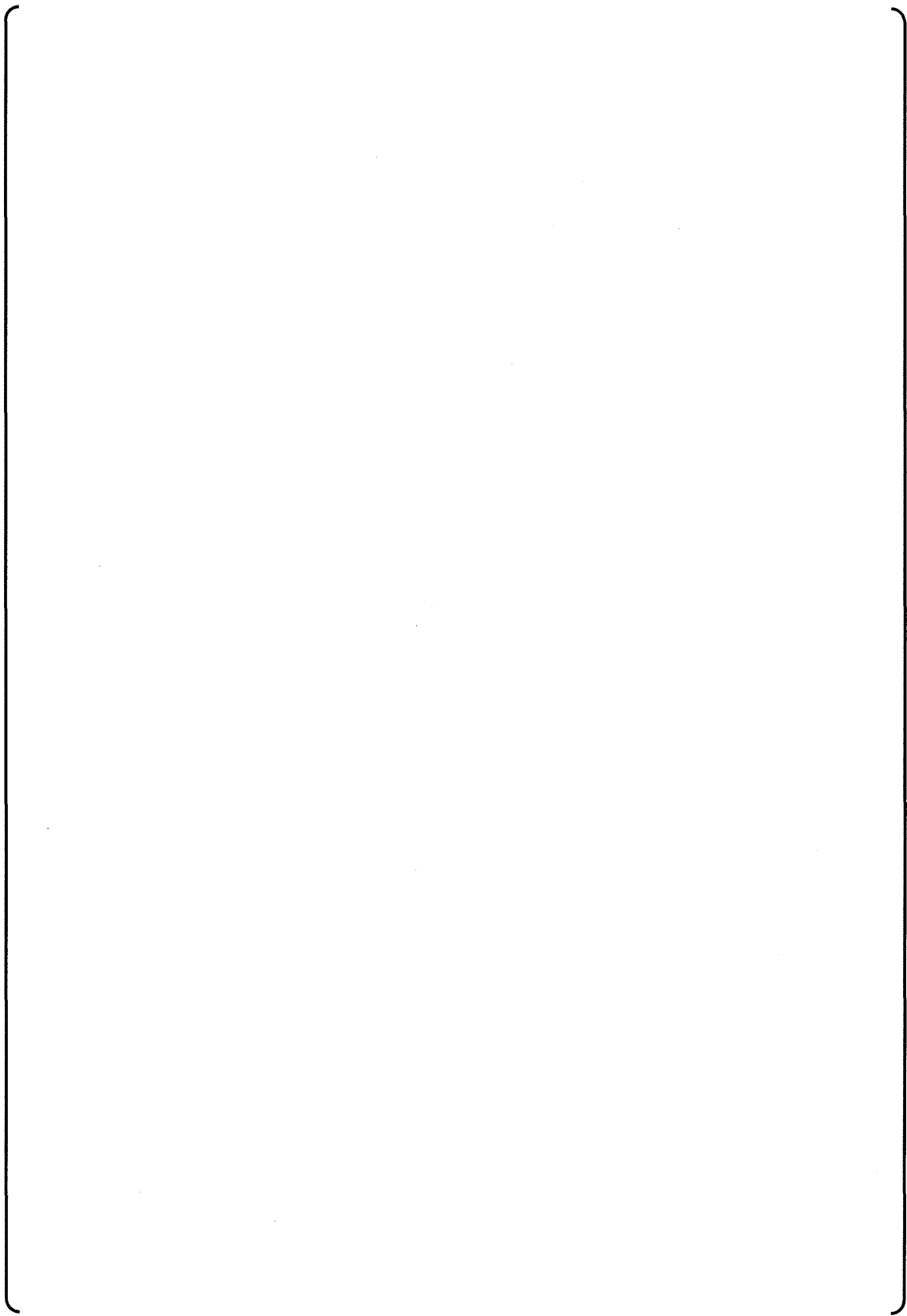


Figure 4.6-2 Spring Characteristics and the Holddown Force of Top Nozzle Spring

4.7 References

- (4-1) 2001 American Society of Mechanical Engineers Boiler and Pressure Vessel Code with 2002 and 2003 Addenda, Section III, Division 1, NG
- (4-2) "Mitsubishi Fuel Design Criteria and Methodology", MUAP-07008-P (Proprietary) and MUAP-07008-NP (Non-Proprietary), May 2007
- (4-3) 2001 American Society of Mechanical Engineers Boiler and Pressure Vessel Code with 2002 and 2003 Addenda, Section III, Division 1, MANDATORY APPENDIX I
- (4-4) J. R. Reavis, "Vibration Correlation for Maximum Fuel-Element Displacement in Parallel Turbulent Flow", Nucl. Sci. Eng. 38, 63-69 (1969)
- (4-5) J. F. Archard, "Contact and Rubbing of Flat Surfaces", J. Applied Physics 24, p981, (1953)

5.0 IN-CORE CONTROL COMPONENTS DESIGN EVALUATION

The functions and kinds of in-core control components used in the US-APWR are described below.

- Rod cluster control assembly (RCCA): For reactor shutdown and reactivity control
- Burnable absorber assembly: For reactivity control
- Neutron source assembly: For supplying neutrons at reactor startup and to increase the sensitivity of the neutron detectors that monitor sub-criticality
- Thimble plug assembly: For limiting bypass flow in the reactor

Design requirements for these in-core control components are described in the NRC Standard Review Plan (SRP) Section 4.2 (NUREG-0800)⁽⁵⁻¹⁾. They are also consistent with Section C.I.4.2 of Regulatory Guide 1.206⁽⁵⁻²⁾.

For the purpose of safe shutdown, maintaining sub-criticality and adequate reactivity control of the reactor, design bases for in-core control components are established in terms of thermal physical properties of absorber material, compatibility of the absorber and cladding material, cladding mechanical properties, and irradiation behavior of absorber material. These material properties of materials used in the in-core control components are described in Appendix B of this report.

In the cladding stress evaluations described below, the allowable stress intensity S_m is two thirds of the yield stress, S_y , described in Appendix B of this report, considering the mechanical properties of cold-worked type 304 stainless steel with consideration of operating temperatures.

5.1 Rod Cluster Control Assembly

The functions of the RCCA are to provide for reactivity control, normal shutdown and rapid shutdown of the core by insertion and withdrawal of control rods for the fuel assemblies. To fulfill those functions, the RCCA is designed to meet the criteria described below for a postulated 15-year design lifetime.

5.1.1 Absorber Temperature

5.1.1.1 Design Bases and Criteria

The silver-indium-cadmium (Ag-In-Cd) alloy absorber material and the stainless steel cladding material generate heat by gamma (γ)-heating. As the result of this heating, the temperature of the absorber increases during operation. Melting of the absorber material would lead to loss of dimensional stability, filling of the cladding-absorber gap, and possible cladding-absorber interaction. Therefore, the absorber temperature during use shall be less than its melting point, as described in Appendix B.

5.1.1.2 Evaluation

The absorber temperature during normal operation and AOOs is evaluated by solving the heat conduction equation for the concentric arrangement of the absorber, the cladding-absorber gap

filled with air, and the cladding. Gamma heating of the absorber material and the cladding material that bounds normal operation and AOOs is taken into account.

Figure 5.1-1 summarizes procedure of the absorber temperature calculation.

The maximum temperature of the absorber, is no more than { } deg.F ({ } deg.C), and is less than the absorber melting point of 1454 deg.F (790 deg.C).

5.1.2 Insertability

5.1.2.1 Design Bases and Criteria

To ensure smooth insertion and withdrawal of the control rods, adequate diametrical clearance shall be maintained between the control rod cladding and the control rod guide thimble throughout the lifetime of the rod cluster control assembly. Insertion of the control rods shall not be affected by misalignment of the control rod guide thimbles.

5.1.2.2 Evaluation

The diameter of the control rod increases due to thermal expansion and the in-reactor swelling of stainless steel, and decreases due to cladding creepdown as described in Appendix B of this report. The maximum increase of the control rod diameter during its lifetime is { } mil ({ } mm). The minimum clearance between the control rod and the control rod guide thimble, at the guide thimble dash pot region, is { } mil ({ } mm), taking into account manufacturing tolerances. Therefore, the swelling of the cladding and the difference in thermal expansion of the cladding and the control rod guide thimble does not result in closure of the diametrical clearance between them during operation. To facilitate control rod insertion into the guide thimble when there is misalignment between the RCCA and the fuel assembly, a section of the control top end plug has a reduced diameter for stiffness flexibility and this design has a good experience in Japan.

5.1.3 Material Requirement

5.1.3.1 Design Bases and Criteria

The cladding of the control rod functions as a boundary between the absorber material and the primary coolant to prevent corrosion and solubility of the absorber material. To ensure satisfactory operation throughout the design life and to minimize plant radiation levels, the materials used in the RCCA shall be stable against corrosion, degradation of strength, and irradiation effects throughout the design lifetime of 15 years.

The absorber material shall have no significant chemical reaction with the coolant water and sufficient compatibility with the cladding material to preclude the coolant contamination and the cladding failure.

5.1.3.2 Evaluation

Stainless steel, which has high corrosion resistance, is used in the components of the rod cluster control assembly, including the control rod cladding, that are directly exposed to the high temperature coolant as described in Appendix B of this report.

The cladding material has a high ultimate tensile strength and is therefore capable of remaining water tight during normal operation, AOOs and postulated accidents. In the event of a cladding failure, with subsequent water logging, the cladding would maintain its integrity.

The Ag-In-Cd absorber material has shows the good corrosion resistance in the PWR primary coolant which is controlled to the appropriate dissolved oxygen concentration and it is expected that the Ag-In-Cd absorber material does not react with the stainless steel cladding at the operating temperature, as described in Appendix B of this report.

5.1.4 Cladding Stress

5.1.4.1 Design Bases and Criteria

To ensure satisfactory operation throughout the design life, the cladding stress meets stress intensity limits in ASME Section III ⁽⁵⁻³⁾ during normal operation, AOOs and postulated accidents, with consideration of the irradiation behavior of the control rod cladding and the contained absorber materials, and the acceleration due to the stepped movement of control rod drive mechanism (CRDM).

The limiting stresses for the various stress categories are described in Table 5.1-1 for normal operation and AOOs.

5.1.4.2 Evaluation

The Ag-In-Cd absorber material does not generate gas by neutron absorption and the clearance between the Ag-In-Cd absorber material and cladding will be maintained throughout the design lifetime of 15 years. Therefore, the pressure loads on the cladding are always compressive. The mechanical loads applied to the cladding are due to the stepping motion of the CRDM and the scram loads. The CRDM stepping loads are obtained from dynamic analyses performed on the overall CRDM system and the scram loads are obtained by solving the motion equation for the drive rod and RCCA in free fall. The scram loads are lower than the CRDM stepping loads. Therefore, the control rod integrity is determined by the combination of the stepping loads and the external pressure loads. Loads on the absorber rods during normal operation and AOOs are shown in Table 5.1-2. The temperature of the cladding is obtained from thermal analyses performed for the absorber rods and the cladding design temperature assumed in the evaluation is set to ()deg.F (() deg.C), the conservatively bounding saturation temperature of the coolant water. The cladding stresses due to the combination of the stepping loads and the differential pressure satisfy the ASME Section III criteria during normal operation and AOOs, as summarized in Table 5.1-3. These stresses are bounding for postulated accidents because the applied loads are less and the allowable stresses of Appendix F in ASME Section III ⁽⁵⁻⁴⁾ are higher than those of normal operation and AOOs.

5.1.5 Fatigue

5.1.5.1 Design Bases and Criteria

To ensure safe shutdown and reactivity control, and efficient performance during the RCCA lifetime, the control rod cladding shall not fail due to fatigue during the RCCA lifetime. The cumulative fatigue usage factor shall be less than 1.0. The maximum allowable alternating stress is determined from Figure I-9.2 of Appendix I in ASME section III ⁽⁵⁻⁴⁾.

5.1.5.2 Evaluation

The cladding fatigue is determined by the combination of the stepping loads and the external pressure loads during reactor startup and shutdown operation. The number of stress cycles due to the stepping loads is conservatively assumed to be [] during the RCCA lifetime. And the number of stress cycles due to a change of the external pressure is conservatively assumed to be [] times during the RCCA lifetime. The cumulative usage factor is [] and is less than 1.0.

5.1.6 Control Rod Wear

5.1.6.1 Design Bases and Criteria

Wear of the control rod cladding may occur due to misalignment and turbulent flow around the rods in the guide tube assembly and the fuel assembly. Wear of the control rod cladding prevents smooth movement of RCCA and affects the structural integrity of the control rod cladding. No significant wear of the control rod cladding shall occur during the rod cluster control assembly lifetime.

5.1.6.2 Evaluation

A section of the control rod top end plug has a reduced diameter for stiffness flexibility, which prevents significant wear by reducing the mutual contact force between the control rod and the continuous guide sheath, the guide card and the guide thimble.

Chromium plating of the cladding surface also contributes to increased cladding wear resistance. This design has been used in the RCCAs used by Mitsubishi in conventional PWRs, and Mitsubishi irradiation experience has shown that it effectively eliminates control rod cladding wear.

Table 5.1-1 Stress Limits

| Stress Category | Limit |
|---------------------------------------|--------|
| General Primary Membrane | Sm |
| Local Primary Membrane | 1.5 Sm |
| Primary Membrane plus Primary Bending | 1.5 Sm |
| Total Primary plus Secondary Stress | 3.0 Sm |

Table 5.1-2 Typical Loads Applied to the Control Rods under Normal Operation and AOOs

| Type of Load | Design Load | Remarks |
|-----------------------|-------------|---------|
| 1. CRDM Stepping Load | | |
| 2. Scram Loads | | |
| 3. External Pressure | | |
| 4. Internal Pressure | | |

Table 5.1-3 Summary of the Evaluation during Normal Operation and AOOs

| Stress Category | Result | Limit |
|---------------------------------------|--------|-------|
| General Primary Membrane | | |
| Primary Membrane plus Primary Bending | | |
| Total Primary plus Secondary Stress | | |

- ✓ Temperature distribution of the content in the in-core control component rod is calculated by solving an axisymmetric heat conduction equation as follows.

$$\frac{\partial^2 T}{\partial r^2} + \frac{1}{r} \frac{\partial T}{\partial r} + \frac{S}{\lambda} = 0$$

Where

T: Temperature in the content

r: Radial coordinate

S: Volumetric heat generation

λ : Thermal conductivity

- ✓ The temperature is evaluated based on following assumptions.
- Assuming steady state and one dimensional heat transfer (a cylindrical symmetry)
 - Assuming maximum power generated during AOOs
 - Conservatively assuming the temperature of the cladding outer surface which is based on the coolant temperature, when boiling occurs in the control rod guide thimble
 - Conservatively assuming heat transfer resistances through multiple layer of the cladding and the content
 - Considering manufacturing tolerances which provides higher temperature of the contents
- ✓ The temperature distribution is calculated starting from the cladding outer surface to the center of the content by the above heat conduction and the conditions.

Figure 5.1-1 Summary of the ICC Content Temperature Calculation

5.2 Burnable Absorber Assembly

The function of the burnable absorber assembly is to provide for reactivity control during the first fuel cycle and/or reload cycles through the use of a burnable absorber inserted in the fuel assembly.

To fulfill this function, the burnable absorber assembly is designed to meet the criteria described below.

5.2.1 Absorber Temperature

5.2.1.1 Design Bases and Criteria

The borosilicate glass of the absorber material generates heat by γ -heating and the (n,a) reaction of the boron(^{10}B). The stainless steel cladding and the stainless steel inner spacer tube material of stainless steel also generate heat by γ -heating.

The temperature of borosilicate glass absorber increases due to this heating during use. Softening of the absorber material would lead to loss of dimensional stability, filling of the clad-absorber gap, and induce significant stress in the cladding. Therefore the absorber temperature during use shall be less than its softening point.

5.2.1.2 Evaluation

The absorber temperature during normal operation and AOOs is evaluated by solving the heat conduction equation for the concentric arrangement of the inner spacer tube, the absorber, the cladding and the gaps between the absorber and the tubes. To calculate the absorber's maximum temperature, γ -heating of absorber material that bounds normal operation and AOOs condition is considered.

Procedure for the absorber temperature calculation is summarized in Figure 5.1-1 shown previously.

The limiting result of the burnable absorber temperature evaluation, accounting for the γ -heating and the (n,a) reaction of the boron(^{10}B), and the outer surface temperature of the cladding, is that the maximum temperature of absorber material is []deg.F ([]deg.C), and is less than the softening point of []deg.F ([]deg.C).

5.2.2 Insertability

5.2.2.1 Design Bases and Criteria

The burnable absorber assembly is inserted and statically placed into the fuel assembly. To ensure smooth insertion and withdrawal of the burnable absorber rods, diametrical clearance shall be maintained between the burnable absorber rod cladding and the control rod guide thimble during use.

5.2.2.2 Evaluation

The diameter of the burnable absorber rod increases due to the thermal expansion and in-reactor swelling of the stainless steel cladding, and decreases due to cladding creepdown

due to a compressive pressure differential across the cladding wall. The maximum diameter increase of the burnable absorber rod during the postulated 15 years is () mil (() mm). The minimum clearance between the burnable absorber rod and the control rod guide thimble, at the guide thimble dash pot region, is () mil (() mm), taking into account manufacturing tolerances.

Therefore, the swelling of the cladding and the difference in thermal expansion of the cladding and the control rod guide thimble does not result in closure of the diametrical clearance between them during operation.

5.2.3 Material Requirement

5.2.3.1 Design Bases and Criteria

The cladding of the burnable absorber rod functions as a boundary between the burnable absorber material and the primary coolant to prevent corrosion and solubility of the absorber material. To ensure satisfactory operation throughout the design life and to minimize plant radiation levels, the materials used in the burnable absorber assembly shall be stable against corrosion, degradation of strength, and irradiation effects.

The absorber material and nuclear reaction products shall have sufficient compatibility with the cladding material and no significant chemical reaction with the coolant water in case of cladding failure to preclude the coolant contamination and the cladding failure.

5.2.3.2 Evaluation

Austenitic stainless steel, which has high corrosion resistance, is used in the components of the burnable absorber assembly, including the burnable absorber rod cladding, that are directly exposed to the high temperature coolant and exposed to rapid coolant flow.

The burnable absorber cladding material has a high ultimate tensile strength and is therefore capable of remaining water tight during normal operation, AOOs and postulated accidents. In the event of a cladding failure, with subsequent water logging, the cladding would maintain its integrity.

The absorber material has no reaction with the cladding material and, should cladding failure occur, the absorber material is not under tension to reduce the strength and maintains its configurations, as described in Appendix B of this report.

5.2.4 Cladding Stress

5.2.4.1 Design Bases and Criteria

To ensure satisfactory operation throughout the design life, the cladding stress meets the stress intensity limits in ASME Section III ⁽⁵⁻³⁾ during normal operation, AOOs and postulated accidents, with consideration of the irradiation behavior of the burnable absorber rod cladding and the contained burnable absorber materials.

The limiting stresses for the various stress categories are described in Table 5.2-1 for normal operation and AOOs.

5.2.4.2 Evaluation

The ^{10}B neutron absorption in the burnable absorber borosilicate glass produces helium, as described in Appendix B of this report. The released helium gas increases the burnable absorber rod internal pressure, which reaches its maximum value within one cycle of operation. The internal pressure of the burnable absorber rod is less than the reactor system pressure at all times during operation. The cladding stress is conservatively evaluated at BOL, when the differential pressure between the inside and outside of the cladding is at a maximum.

The evaluation results show that the cladding stress meets the ASME Section III criteria.

Typical loads on the absorber rods during normal operation and AOOs are shown in Table 5.2-2.

The results of the stress evaluation during normal operation and AOOs are summarized in Table 5.2-3. These stresses are bounding for postulated accidents because that the applied loads are less and the allowable stresses of Appendix F in ASME Section III ⁽⁵⁻⁵⁾ are higher than those of normal operation and AOOs.

5.2.5 Fatigue

5.2.5.1 Design Bases and Criteria

To ensure control of the excessive core reactivity, and efficient performance during the burnable absorber lifetime, the burnable absorber cladding shall not fail due to fatigue during the lifetime of the burnable absorber assembly. The cumulative fatigue usage factor shall be less than 1.0.

5.2.5.2 Evaluation

Cladding fatigue is evaluated considering reactor startup/shutdown operation, AOOs and other power change operations. The number of stress cycles due to a change of the external pressure is conservatively assumed to be [] times during the postulated 15 years. The cumulative usage factor is [] and is less than 1.0.

5.2.6 Absorber Rod Wear

5.2.6.1 Design Bases and Criteria

Significant wear of the burnable absorber cladding shall not occur during use.

5.2.6.2 Evaluation

The burnable absorber rod is fully inserted in the control rod guide thimble during operation and there is no turbulent flow to induce the wear on the burnable absorber cladding. The significant wear is not expected during use.

Table 5.2-1 Stress Limits

| Stress Category | Limit |
|---------------------------------------|--------|
| General Primary Membrane | Sm |
| Local Primary Membrane | 1.5 Sm |
| Primary Membrane plus Primary Bending | 1.5 Sm |
| Total Primary plus Secondary Stress | 3.0 Sm |

Table 5.2-2 Typical Loads Applied to the Absorber Rods under Normal Operation and AOOs

| Type of Load | Design Load | Remarks |
|----------------------|-------------|---------|
| 1. External Pressure | | |
| 2. Internal Pressure | | |

Table 5.2-3 Summary of the Evaluation during Normal Operation and AOOs

| Stress Category | Result | Limit |
|---------------------------------------|--------|-------|
| General Primary Membrane | | |
| Primary Membrane plus Primary Bending | | |
| Total Primary plus Secondary Stress | | |

5.3 Neutron Source Assembly

The functions of the primary and secondary neutron source assemblies are to supply neutrons at reactor startup and to increase the sensitivity of the neutron detectors that monitor sub-criticality. The neutron source assemblies are statically inserted into the control rod guide thimbles of the fuel assemblies.

To fulfill these functions, the neutron source assemblies are designed to meet the criteria described in below.

5.3.1 Neutron Source Temperature

5.3.1.1 Design Bases and Criteria

The primary neutron source material is a very small amount of californium and generates no significant heating. The secondary source material is a mixed antimony and beryllium pellet and generates heat by γ -heating. The secondary source stainless steel cladding and inner capsule tube also generate heat by γ -heating. As the result of this heating, the temperature of the neutron source increases during use. Melting of the secondary neutron source material leads to loss of dimensional stability, filling of the clad-neutron source gap, and induces a significant stress on the cladding. Therefore the temperature of the secondary source during use shall be less than its melting point.

5.3.1.2 Evaluation

The secondary neutron source temperature during normal operation and AOOs is calculated by solving the heat conduction equation for the concentric arrangement of the secondary neutron source, the inner capsule tube and the cladding. Gamma heating of absorber material that bounds normal operation and AOOs is taken into account.

Procedure for the temperature calculation of the neutron source is summarized in Figure 5.1-1 shown previously.

The maximum temperature of secondary source material, accounting for the γ -heating of the source material, the cladding and the inner capsule tube, and the outer surface temperature of cladding, is () deg.F (() deg.C) , and is less than the melting point of () deg.F (() deg.C).

5.3.2 Material Requirement

5.3.2.1 Design Bases and Criteria

The cladding of the neutron source rod functions as a boundary between the neutron source material and the primary coolant to prevent corrosion and dissipation of the neutron source material. To ensure satisfactory operation throughout the design life and to minimize plant radiation levels, the materials used in the neutron source assembly shall be stable against corrosion, degradation of strength, and irradiation effects throughout the design lifetime.

The neutron source materials and their neutron reaction products shall have sufficient compatibility with the cladding material and, in the event of cladding failure, shall have low

chemical reactivity with the coolant to preclude the coolant contamination and the cladding failure.

5.3.2.2 Evaluation

Both of the neutron source rods feature a duplex cladding design, with a very low probability for exposing the source material to the coolant. With respect to the compatibility of the antimony and beryllium pellet and the stainless steel capsule, it is expected that the reaction between both materials does not occur from studies of binary state diagrams for Sb and Be and the main constituent elements of stainless steel at temperature of [] deg.F ([] deg.C) or less.

5.3.3 Cladding Stress

5.3.3.1 Design Bases and Criteria

To ensure satisfactory operation throughout the design lifetime, the cladding stresses due to the pressure differential between the inside and outside of both neutron source rods shall meet stress intensity limits in ASME Section III ⁽⁵⁻³⁾ during normal operation, AOOs and postulated accidents.

The limiting stresses for the various stress categories are described in Table 5.3-1 for normal operation and AOOs.

5.3.3.2 Evaluation

The primary neutron source material does not generate gas by neutron absorption and the clearance between primary source and capsule and cladding. Therefore, the pressure loads on the cladding are always compressive.

The stress in the primary neutron source rod cladding due to the loads during normal operation, AOOs and postulated accidents satisfy the stress criteria in ASME Section III.

The beryllium neutron absorption in the antimony-beryllium pellet produces helium. The released helium gas increases the capsule internal pressure in the neutron source rod, which reaches the maximum and exceeds the external pressure at the end of life.

The secondary neutron source rod has a duplex structure that consists of a capsule containing the neutron source and an outer cladding encasing the capsule. The stresses in the capsule and the outer cladding, due to the differential pressure between inside and outside of each cladding, are evaluated. Both the capsule and the cladding that encases the capsule are pressurized during fabrication. The internal pressure of the capsule also increases due to the release of helium during irradiation. Taking into account irradiation behavior, including the gas release from the neutron source and the swelling of austenitic stainless steel cladding, the stresses on the cladding of the capsule and the outer cladding meet the ASME Section III stress criteria.

Typical evaluation results for the loads on the neutron source rods under normal operation and AOOs are shown in Table 5.3-2.

The results of the stress evaluation during normal operation and AOOs are summarized in Table 5.3-3. These stresses are bounding for postulated accidents because that the applied

loads are less and the allowable stresses of Appendix F in ASME Section III ⁽⁵⁻⁵⁾ are higher than those of normal operation and AOOs.

5.3.4 Neutron Source Rod Wear

5.3.4.1 Design Bases and Criteria

No significant wear in the cladding of the neutron source occurs during use.

5.3.4.2 Evaluation

The neutron source rod is fully inserted in the control rod guide thimble during operation and there is no turbulent flow to induce the wear on the burnable absorber cladding. The significant wear is not expected during use.

Table 5.3-1 Stress Limits

| Stress Category | Limit |
|---------------------------------------|--------|
| General Primary Membrane | Sm |
| Local Primary Membrane | 1.5 Sm |
| Primary Membrane plus Primary Bending | 1.5 Sm |
| Total Primary plus Secondary Stress | 3.0 Sm |

Table 5.3-2 Typical Loads Applied to the Neutron Source Rods under Normal Operation and AOOs

| Type of Load | Design Load | Remarks |
|----------------------|-------------|---------|
| 1. External Pressure | | |
| 2. Internal Pressure | | |

**Table 5.3-3 Summary of the Evaluation during Normal Operation and AOOs
(1) Outer Cladding of Secondary Neutron Source Rod**

| Stress Category | Result | Limit |
|---------------------------------------|--------|-------|
| General Primary Membrane | | |
| Primary Membrane plus Primary Bending | | |
| Total Primary plus Secondary Stress | | |

(2) Capsule of Secondary Neutron Source Rod

| Stress Category | Result (N/mm ²) | Limit (N/mm ²) |
|--|-----------------------------|----------------------------|
| General Primary Membrane | | |
| Primary Membrane plus Primary Bending | | |
| Total Primary plus Secondary Stress BOL | | |
| EOL | | |

5.4 Thimble Plug Rods and Assembly

The function of the thimble plug rod assembly is to limit bypass flow in the reactor. The thimble plug assembly is installed and statically placed into fuel assemblies that are not equipped with other in-core control components, such as the rod cluster control, burnable absorber and neutron source assemblies. The thimble plug assembly has a structure in which the thimble plug rods are fixed to the same hold-down assembly as other hold-down type of in-core control components. The thimble plug rods can also be used in other in-core control component assemblies.

Thimble plug rods, which are solid rod structures, do not require special design criteria.

5.5 References

- (5-1) U.S. Nuclear Regulatory Commission, "Standard Review Plan for the Review of Safety Analysis Reports for Nuclear Power Plants", NUREG-0800, Section 4.2, March 2007
- (5-2) "Combined License Applications for Nuclear Power Plants (LWR Edition)", NRC Regulatory Guide 1.206, Section C.I.4.2
- (5-3) 2001 American Society of Mechanical Engineers Boiler and Pressure Vessel Code with 2002 and 2003 Addenda, Section III, Division 1, Subsection NB
- (5-4) 2001 American Society of Mechanical Engineers Boiler and Pressure Vessel Code with 2002 and 2003 Addenda, Section III, Division 1, MANDATORY APPENDIX I
- (5-5) 2001 American Society of Mechanical Engineers Boiler and Pressure Vessel Code with 2002 and 2003 Addenda, Section III, Division 1, MANDATORY APPENDIX F

6.0 CONCLUSION

The US-APWR fuel system design is based on the significant experience with and demonstrated excellent performance and high reliability of Mitsubishi fuel in Japan.

This report describes the design features of the US-APWR fuel, such as ZIRLO cladding, higher 97 % theoretical density (TD) pellets, 10 wt% gadolinia doped fuel and features to reduce or eliminate debris fretting, grid fretting and incomplete rod insertion, and the materials, structure, and specification of the US-APWR fuel rod, fuel assembly structure components and in-core control components.

This report has given the results of the application of the fuel rod and fuel assembly design criteria and methodology, described in the topical report "Mitsubishi Fuel Design Criteria and Methodology"(MUAP-07008-P/-NP), to the US-APWR fuel:

- evaluation results for the fuel rod internal pressure, cladding stresses, fuel-cladding mechanical interaction, cladding strain, chemical reaction, cladding fatigue, creep collapse, and fuel temperature, which confirm that their respective design criteria are satisfied, and
- evaluation results for the loads during normal operation and AOOs, loads in shipping and handling, fuel assembly dimensional changes, such as fuel rod bowing, fuel assembly growth, fuel rod growth and fuel assembly bowing, irradiation behavior of the grid spacers, fuel cladding fretting wear, and fuel assembly liftoff, which have been shown to meet their design criteria.

This report has given the design bases and criteria for the in-core control components, and has given design evaluation results for their temperatures, insertability, material requirements, cladding stresses, cladding fatigue, and cladding wear, which have been shown to meet their design criteria.

Appendix A

**NUCLEAR DESIGN
(24-MONTH EQUILIBRIUM CORE)**

February 2008

**© 2008 Mitsubishi Heavy Industries, Ltd.
All Rights Reserved**

Table of Contents

| | |
|--|------|
| List of Tables..... | A-3 |
| List of Figures..... | A-3 |
| A.1.0 INTRODUCTION..... | A-4 |
| A.2.0 CORE PERFORMANCE..... | A-5 |
| A.2.1 Representative Fuel Management..... | A-5 |
| A.2.2 Fuel Assembly and Loading Pattern Data..... | A-5 |
| A.2.3 Operational Data..... | A-5 |
| A.2.3.1 Power and Burnup Distributions..... | A-6 |
| A.2.3.2 Boron Letdown Data..... | A-6 |
| A.2.4 Safety Analyses Parameters..... | A-6 |
| A.3.0 KEY INPUT PARAMETERS TO FUEL ROD DESIGN EVALUATIONS..... | A-8 |
| A.4.0 CONCLUSION..... | A-9 |
| A.5.0 REFERENCES..... | A-10 |

List of Tables

| | | |
|-----------|--|------|
| Table A-1 | Main Nuclear Design Parameters for the Equilibrium Cycle | A-11 |
|-----------|--|------|

List of Figures

| | | |
|-------------|--|------|
| Figure A-1 | Equilibrium Cycle Fuel Assembly Patterns | A-14 |
| Figure A-2 | Equilibrium Cycle Core Loading Pattern | A-15 |
| Figure A-3 | Fuel and Rod Cluster Control Assemblies Core Configuration..... | A-16 |
| Figure A-4 | Doppler Power Coefficient ^(A-1) | A-17 |
| Figure A-5 | Normalized Radial Power and Burnup Distribution at 0.15 GWD/MTU (HFP, EqXe, ARO [*]) | A-18 |
| Figure A-6 | Normalized Radial Power and Burnup Distribution at 11 GWD/MTU (HFP, EqXe, ARO [*]) | A-19 |
| Figure A-7 | Normalized Radial Power and Burnup Distribution at 23 GWD/MTU (HFP, EqXe, ARO [*]) | A-20 |
| Figure A-8 | Normalized Radial Power and Burnup Distribution at 0.15 GWD/MTU (HFP, EqXe, RIL) | A-21 |
| Figure A-9 | Normalized Radial Power and Burnup Distribution at 11 GWD/MTU (HFP, EqXe, RIL) | A-22 |
| Figure A-10 | Normalized Radial Power and Burnup Distribution at 23 GWD/MTU (HFP, EqXe, RIL) | A-23 |
| Figure A-11 | Rodwise Power Distribution at 0.15 GWD/MTU..... | A-24 |
| Figure A-12 | Rodwise Power Distribution at 11 GWD/MTU..... | A-25 |
| Figure A-13 | Rodwise Power Distribution at 23 GWD/MTU..... | A-26 |
| Figure A-14 | Axial Power Distribution of Core Average (HFP, ARO [*]) | A-27 |
| Figure A-15 | Core Average Axial Burnup Distribution..... | A-28 |
| Figure A-16 | Axial Offset versus Core Depletion (HFP, ARO [*]) | A-29 |
| Figure A-17 | $F_{\Delta H}^N$ versus Core Depletion (HFP, ARO [*]) | A-30 |
| Figure A-18 | Calculated Flux Difference versus F_Q Values for the Equilibrium Cycle | A-31 |
| Figure A-19 | Soluble Boron Concentration versus Core Depletion (HFP, ARO [*]) | A-32 |

A.1.0 INTRODUCTION

This document describes an evaluation of the US-APWR performance for typical reload cycle conditions, from the viewpoint of operations, safety analyses (transient and accident analyses), and fuel rod design evaluations. For this purpose, an equilibrium loading pattern for a representative 24-month cycle was developed for the US-APWR.

The US-APWR Design Control Document ^(A-1) describes the initial core and supporting safety analyses that are intended to bound the initial and reload cycles, and interface information to fuel rod design evaluation for reload cores is also evaluated. Because fuel rod design evaluation must be performed for the entire operating duty of a fuel assembly which may be loaded in two or more cycles, information from a reference reload core is necessary. Typical operating requirements for reload cycles are considered based on current fuel management practices.

This appendix provides a summary of the performance of a representative equilibrium loading pattern for the US-APWR. The equilibrium cycle described in this report is hypothetical, but reasonable and consistent with current fuel management practices and objectives. It is recognized that transition cores are necessary to reach an equilibrium condition, and utility requirements will determine the actual design for each cycle. It is not possible to anticipate all transition and equilibrium fuel management scenarios, but the equilibrium cycle described in this report presents a reasonable expectation of fuel duty and operational requirements.

Reload cores primarily change the characteristics of the plant in the following ways:

- Fuel inventory (core average enrichment and burnup)
- Fuel placement (loading pattern)
- Burnable absorbers (inventory, type, and location)

These changes, in turn, affect the following nuclear inputs to safety analyses in three main areas:

- Core power distributions
- Core kinetic characteristics
- Control rod worths, which include both local and global core effects

This loading pattern satisfies the following requirements:

- A cycle length equivalent to 23.5 effective full-power months (EFPM), which is similar to the upper limit of current operating cycles.
- Fuel rod burnup and rod design criteria are met.
- Compliance with Technical Specifications
- The safety analyses described in the US-APWR Design Control Document remain bounding

A.2.0 CORE PERFORMANCE

This section describes the equilibrium cycle fuel management and inventory, loading pattern, power distribution behavior, boron letdown data, and safety analyses parameters. The primary nuclear analysis code used for nuclear analyses is the ANC code ^(A-2) approved by NRC. ANC is a three dimensional two-group diffusion core calculation code based on nodal expansion method, and calculates nuclear parameters such as critical boron, power distribution, exposure, reactivity coefficients etc.

A.2.1 Representative Fuel Management

This equilibrium loading pattern is a representative 24-month cycle for the US-APWR. The loading pattern uses essentially a 'two-region' fuel management scheme; only one twice-burnt assembly is used for the center assembly. This equilibrium loading pattern uses a typical low-leakage loading pattern strategy (LLLP), which improves neutron economy and reduces reactor vessel fluence.

A.2.2 Fuel Assembly and Loading Pattern Data

The fuel rod loading patterns for each assembly type are shown in Figure A-1, and this equilibrium cycle core loading pattern is shown in Figure A-2, and then Figure A-3 shows the fuel assembly and control rod assembly configuration in the US-APWR core. This core loading consists of 128 fresh fuel assemblies, 128 once burnt fuel assemblies and one twice burnt fuel assembly.

Each fuel region of 128 fuel assemblies is composed of:

- 12 uranium-only fuel assemblies with 4.55 wt% ²³⁵U.
- 52 fuel assemblies with 16 part-length integral fuel burnable absorbers ((U,Gd)O₂ fuel rods) consisting of 2.95 wt% ²³⁵U and 6 wt% Gd₂O₃. The upper and lower 5.9 inches of the (U,Gd)O₂ fuel rods are filled with 2.95 wt% ²³⁵U enrichment UO₂ pellets. The remaining 248 fuel rods of each fuel assembly use 4.55 wt% ²³⁵U.
- 64 fuel assemblies with 24 part-length integral fuel burnable absorbers ((U,Gd)O₂ fuel rods) consisting of 2.95 wt% ²³⁵U and 10 wt% Gd₂O₃. The upper and lower 5.9 inches of the part-length (U,Gd)O₂ fuel rods are filled with 2.95 wt% ²³⁵U enrichment UO₂ pellets. The remaining 240 fuel rods of each fuel assembly use 4.55 wt% ²³⁵U.
- No discrete burnable absorbers (BAs such as borosilicate glass) were required, but actual loading patterns may use discrete BAs.

The reactor core description is the same as the first core described in the US-APWR Design Control Document ^(A-1). The main nuclear design parameters of this equilibrium cycle core are shown in Table A-1. Table A-1 contains important information to evaluate global core performance, including reactivity coefficients, delayed neutron fractions and neutron lifetimes. Design limits of Table A-1 and Figure A-4 are the same as the US-APWR Design Control Document ^(A-1).

A.2.3 Operational Data

Typical operational data includes radial and axial power distributions, and boron concentrations.

A.2.3.1 Power and Burnup Distributions

Figures A-5 through A-7 show the assembly-wise power and burnup distributions at hot full power almost all control rods out conditions (HFP, EqXe, ARO) for the beginning, middle, and end of cycle (BOC, MOC, EOC). Rodded cases, with control rods at their rod insertion limits (RIL) at hot full power described in Table A-1, are shown in Figures A-8 through A-10 for BOC, MOC, and EOC, respectively. Region average discharge burnups are approximately 36.8 GWD/MTU, with maximum assembly average burnup of 54.2 GWD/MTU, and a fuel rod maximum burnup of 60.2 GWD/MTU.

Figures A-11 through A-13 show typical rodwise power distributions, corresponding to the assembly with the highest relative power presented in Figures A-5 through A-7, respectively.

Figures A-14 and A-15 show the core average axial power and burnup distributions as function of the core active length. Figure A-16 shows the core axial offset (A.O.) as a function of the cycle burnup.

Figure A-17 shows the core peaking factor ($F_{\Delta H}^N$) as a function of the cycle burnup at HFP ARO equilibrium conditions. The maximum $F_{\Delta H}^N$ is 1.52.

Figure A-18 shows calculated flux difference versus F_Q values calculated for 24-month equilibrium cycle core employing a (+5 %, -10 %) target band for constant axial offset control (CAOC) procedure ^(A-3). All calculated F_Q values meet the design limit of 2.60 for normal operation of the 24-month equilibrium cycle core.

It is noted that power distributions, peaking factors, and axial offset parameters are smoothly varying, well within limits, and are consistent with typical operational experience.

A.2.3.2 Boron Letdown Data

The critical boron concentration as a function of the cycle burnup is shown in Figure A-19. Due to the relatively slow burnout of the Gadolinia burnable absorbers, the boron letdown curve is a fairly smooth and monotonically decreasing function of cycle burnup. As shown in the figure, the core reactivity allows a cycle burnup of 23 GWD/MTU, which corresponds to a cycle length of 23.5 EFPM.

A.2.4 Safety Analyses Parameters

Key input parameters to safety analyses of 24-month equilibrium cycle core in this report are evaluated based on Technical Report, "Mitsubishi Reload Evaluation Methodology" ^(A-4).

The objective of the safety analyses for each reload is to verify that the reference safety analysis limits are met, or to identify which transients need to be evaluated based on the changes caused by the reload or other factors. The Mitsubishi safety analysis methodology is based upon the 'bounding analysis' concept, in which a set of key safety input parameters to safety analysis are generated to bound all future anticipated operating cycles. For each reload, the key inputs to safety analyses are reevaluated or recalculated, and compared to the bounding values used for the reference safety analyses.

Table A-1 summarizes values for the main key safety input parameters. The input values for the reference safety analyses in the US-APWR Design Control Document ^(A-1) bound these values of this equilibrium cycle core.

The evaluation confirms that the representative equilibrium reload design is practical and operable.

A.3.0 KEY INPUT PARAMETERS TO FUEL ROD DESIGN EVALUATIONS

Fuel rod design evaluation have been performed for the equilibrium cycle described in this report. It must be shown that fuel rod design evaluations meet the fuel criteria during the entire anticipated fuel life, which may extend to two or more cycles. The fuel rod design is primarily performed using the FINE code ^(A-5).

Fuel rod design criteria include rod internal pressure, cladding stress, cladding corrosion, cladding fatigue, cladding creep collapse, cladding strain and fuel temperature.

Key inputs to fuel rod design include the following,

- Core average and fuel rod axial power distributions are generated at normal operations.
- Normal operation power histories of representative fuel rods in each fuel type are generated through the fuel rod life.
- Local linear power density changes are determined during AOOs events. Target events of AOOs are core power increase events and axial power distribution distortion events, in which local linear power density varies significantly.

A.4.0 CONCLUSION

The equilibrium fuel cycle described in this report is representative of fuel management anticipated for use in the US-APWR. The safety analyses described in the US-APWR Design Control Document ^(A-1) are applicable and bounding for this fuel management. Key input parameters are generated for the fuel rod design evaluation. It is not possible to anticipate all transition and equilibrium fuel management scenarios, but the equilibrium cycle described in this report presents a reasonable expectation of fuel duty and operational requirements.

A.5.0 REFERENCES

- (A-1) "US-APWR Design Control Document", December 2007.
- (A-2) Liu, Y. S., et al., "ANC – A Westinghouse Advanced Nodal Computer Code", WCAP-10965-P-A (Proprietary), and WCAP-10966-A (Non-Proprietary), September, 1986.
- (A-3) Morita, T., et al., "Power Distribution Control and Load Following Procedures", WCAP-8385 (Proprietary), September 1974.
- (A-4) "Mitsubishi Reload Evaluation Methodology", MUAP-07026-P (Proprietary) and MUAP-07026-NP (Non-Proprietary), December 2007.
- (A-5) "Mitsubishi Fuel Design Criteria and Methodology", MUAP-07008-P (Proprietary) and MUAP-07008-NP (Non-Proprietary), May 2007.

Table A-1 Main Nuclear Design Parameters for the Equilibrium Cycle

(sheet 1 of 3)

| Parameter | Design limits ^(A-1) | Best estimate |
|---|--------------------------------|--------------------------------|
| Total heat flux hot channel factor, F_Q | 2.60 | 1.82 ^{*1} |
| Nuclear enthalpy rise hot channel factor (full power), $F_{\Delta H}^N$ | 1.73 | 1.52 |
| Delayed neutron fraction, β_{eff} (%) | 0.44 to 0.75 | 0.50 to 0.62 |
| Prompt neutron lifetime, l^* (μ s) | 8 to 20 | 11.5 to 13.1 |
| Reactivity coefficients | | |
| Doppler power coefficient (pcm/%power) | See Figure A-4 | -12.4 to -7.4 -12.5 to -7.6 |
| BOC EOC | | |
| Moderator temperature coefficient (pcm/°F) ^{*2} | negative | -44.2 to -1.0 |
| Moderator density coefficient (pcm/g/cm ³) | $< 0.51 \times 10^5$ | $< 0.35 \times 10^5$ |
| Maximum ejected rod worth (pcm) at HFP | 110 120 | 18 80 |
| BOC EOC | | |
| Maximum ejected rod worth (pcm) at HZP | 600 800 | 190 602 |
| BOC EOC | | |
| Maximum dropped rod worth (pcm) at HFP | 250 | 107 |
| Maximum rod reactivity insertion rate (pcm/s) | 75 | 45 |

NOTE:

- *1 Normal base load operation
- *2 In the power operating range

Table A-1 Main Nuclear Design Parameters for the Equilibrium Cycle

(sheet 2 of 3)

| Boron concentration (ppm) | | Best estimate | |
|--|-----------------------|-----------------------|--|
| Cold shutdown ^{*1} , BOC, no xenon, ARO, $k_{\text{eff}}=0.99$ | | 2162 | |
| Hot shutdown ^{*2} , BOC, no xenon, ARO, $k_{\text{eff}}=0.99$ | | 2193 | |
| Cold shutdown ^{*1} , BOC, no xenon, ARI ^{*3} , $k_{\text{eff}}\leq 0.95$ | | 2066 | |
| Hot zero power, BOC, no xenon, ARO, $k_{\text{eff}}=1.00$ | | 2029 | |
| Hot full power, BOC, no xenon, ARO, $k_{\text{eff}}=1.00$ | | 1836 | |
| Hot full power, BOC, equilibrium xenon, ARO, $k_{\text{eff}}=1.00$ | | 1419 | |
| Boron coefficient (pcm/ppm) | | -7.9 to -6.0 | |
| Rod worth (%$\Delta\rho$) | | BOC, HZP, NoXe | |
| Bank D | | 0.89 | |
| Bank C (D in) | | 1.00 | |
| Bank B (D+C in) | | 1.06 | |
| Bank A (D+C+B in) | | 0.56 | |
| Reactivity requirements (%$\Delta\rho$) | BOC worths | EOC worths | |
| Power defect including void and Tav _g uncertainty [1] | 1.49 | 3.13 | |
| Delta RIA ^{*4} [2] | 0.22 | - | |
| Trip rod worth | 4.99 | 5.58 | |
| Trip rod worth (Less 10 %) [3] | 4.49 | 5.02 | |
| Shutdown margin (%$\Delta\rho$) | | | |
| Calculated margin [3] – [1] – [2] | 2.78 | 1.89 | |
| Required shutdown margin | 1.60 ^(A-1) | | |

NOTE:

- *1 Temperature of cold shutdown is 68 deg.F
- *2 Temperature of hot shutdown is 557 deg.F
- *3 All control rods inserted
- *4 Delta RIA: limiting RIA – HFP RIA, RIA: rod insertion allowance

Table A-1 Main Nuclear Design Parameters for the Equilibrium Cycle Core**(sheet 3 of 3)**

| Expected RCCAs positions at different core conditions (step) | | | | | | | | |
|--|---------------|-----|-----|-----|--------------|------|-----|------|
| Core Condition | BOC and EOC | | | | | | | |
| | Shutdown bank | | | | Control bank | | | |
| | SA | SB | SC | SD | A | B | C | D |
| Cold | 0 | 0 | 0 | 0 | 0 | 0 | 0 | 0 |
| Hot zero power | 265 | 265 | 265 | 265 | 265 | ≥205 | ≥70 | ≥0 |
| Full power | 265 | 265 | 265 | 265 | 265 | 265 | 265 | ≥205 |

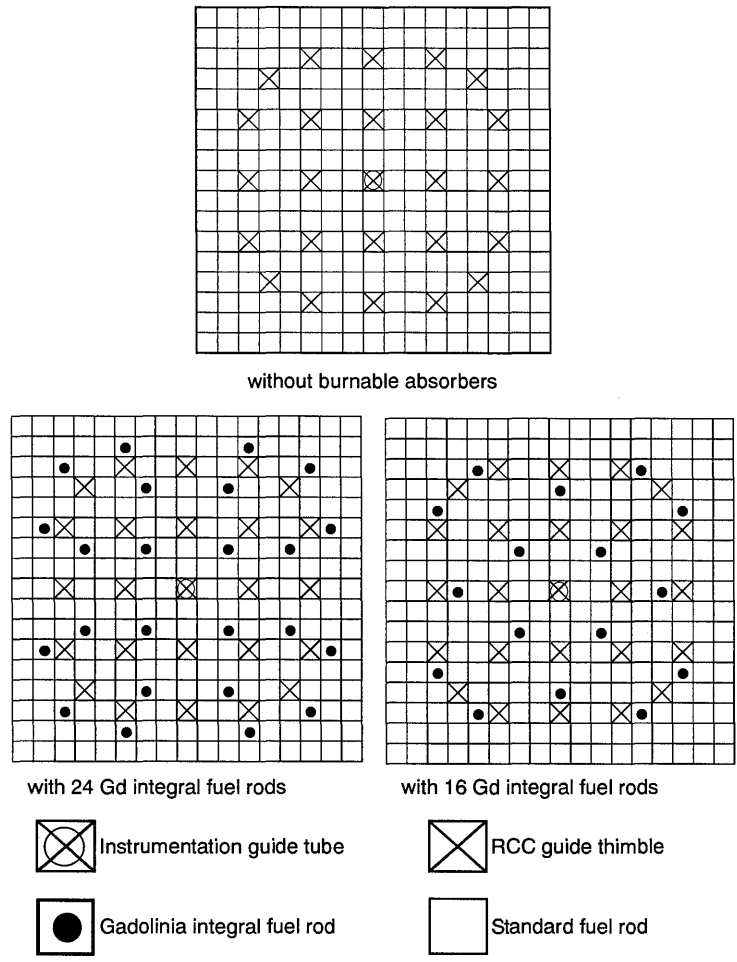
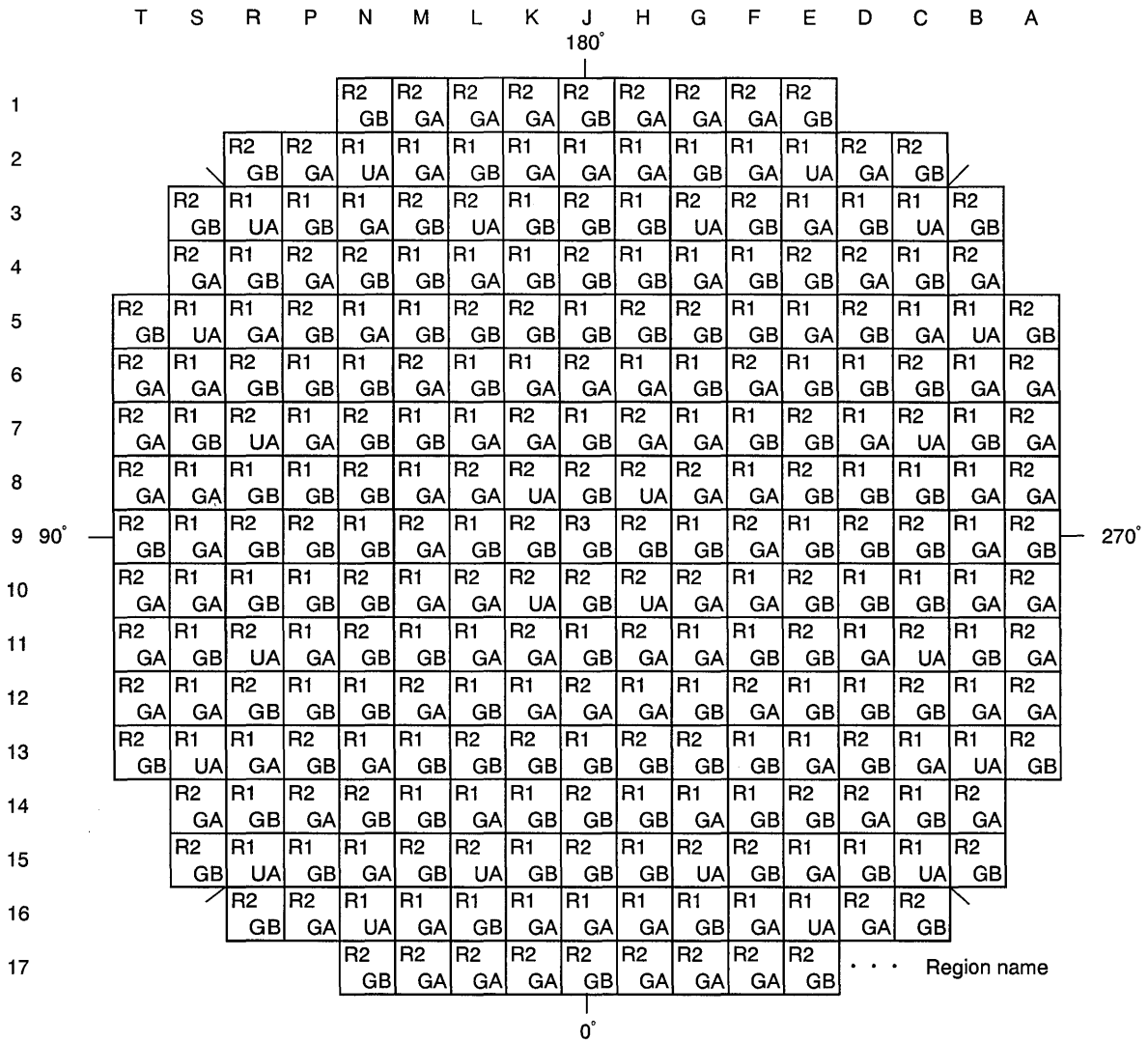


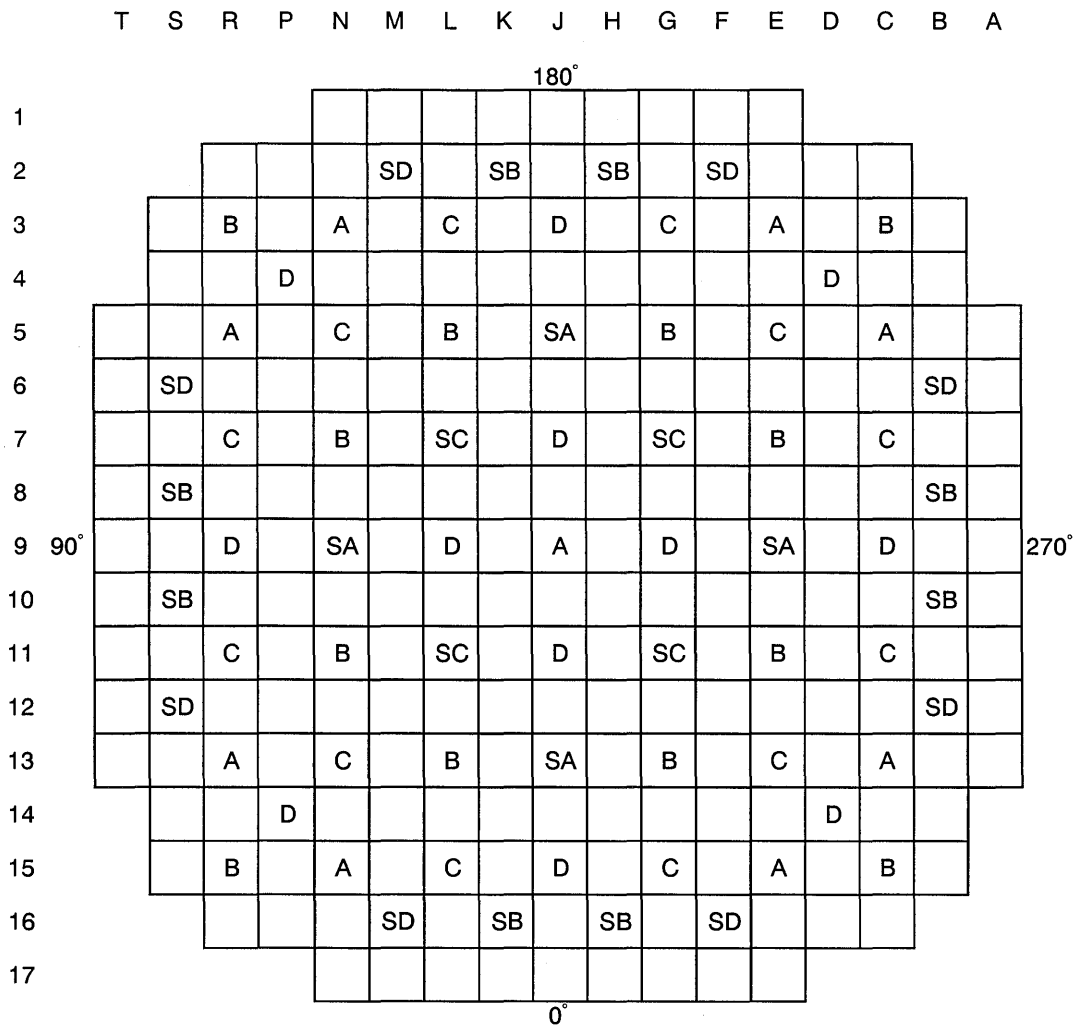
Figure A-1 Equilibrium Cycle Fuel Assembly Patterns



| Region | Number | Uranium rods/FA | | Gadolinia rods/FA | | | | notes |
|--------|--------|-----------------|-----------|-------------------|-----------|------------|--------------|-------------|
| | | Number | U-Enrich. | Number | U-Enrich. | Gd-Content | Abs.Length | |
| R1UA | 12 | 264 | 4.55 wt% | - | - | - | - | fresh |
| R1GA | 52 | 248 | 4.55 wt% | 16 | 2.95 wt% | 6 wt% | 153.5 inches | fresh |
| R1GB | 64 | 240 | 4.55 wt% | 24 | 2.95 wt% | 10 wt% | 153.5 inches | fresh |
| R2UA | 12 | 264 | 4.55 wt% | - | - | - | - | once burnt |
| R2GA | 52 | 248 | 4.55 wt% | 16 | 2.95 wt% | 6 wt% | 153.5 inches | once burnt |
| R2GB | 64 | 240 | 4.55 wt% | 24 | 2.95 wt% | 10 wt% | 153.5 inches | once burnt |
| R3GB | 1 | 240 | 4.55 wt% | 24 | 2.95 wt% | 10 wt% | 153.5 inches | twice burnt |

Abs. length: the upper and lower approximately 5.9 inches of the absorber rod does not contain absorber material

Figure A-2 Equilibrium Cycle Core Loading Pattern



| Number of RCCAs | |
|----------------------------|----|
| A: Control group, Bank A | 9 |
| B: Control group, Bank B | 12 |
| C: Control group, Bank C | 12 |
| D: Control group, Bank D | 12 |
| SA: Shutdown group, Bank A | 4 |
| SB: Shutdown group, Bank B | 8 |
| SC: Shutdown group, Bank C | 4 |
| SD: Shutdown group, Bank D | 8 |

Figure A-3 Fuel and Rod Cluster Control Assemblies Core Configuration

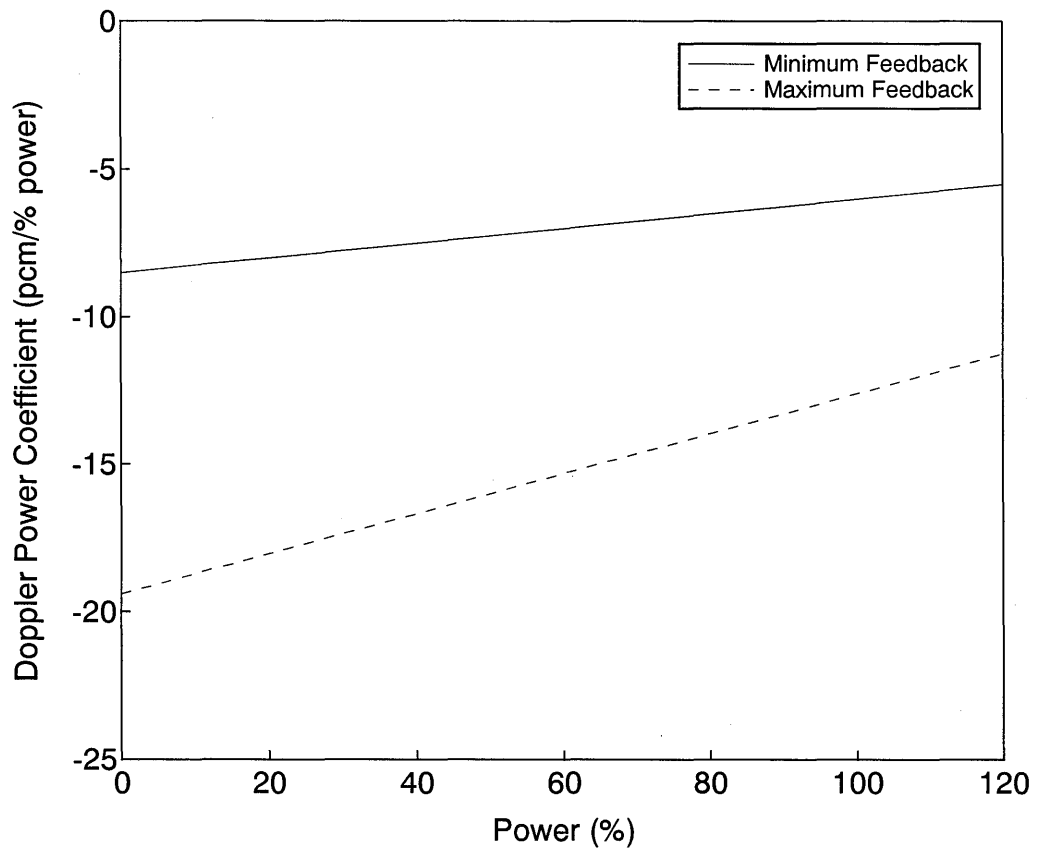


Figure A-4 Doppler Power Coefficient ^(A-1)

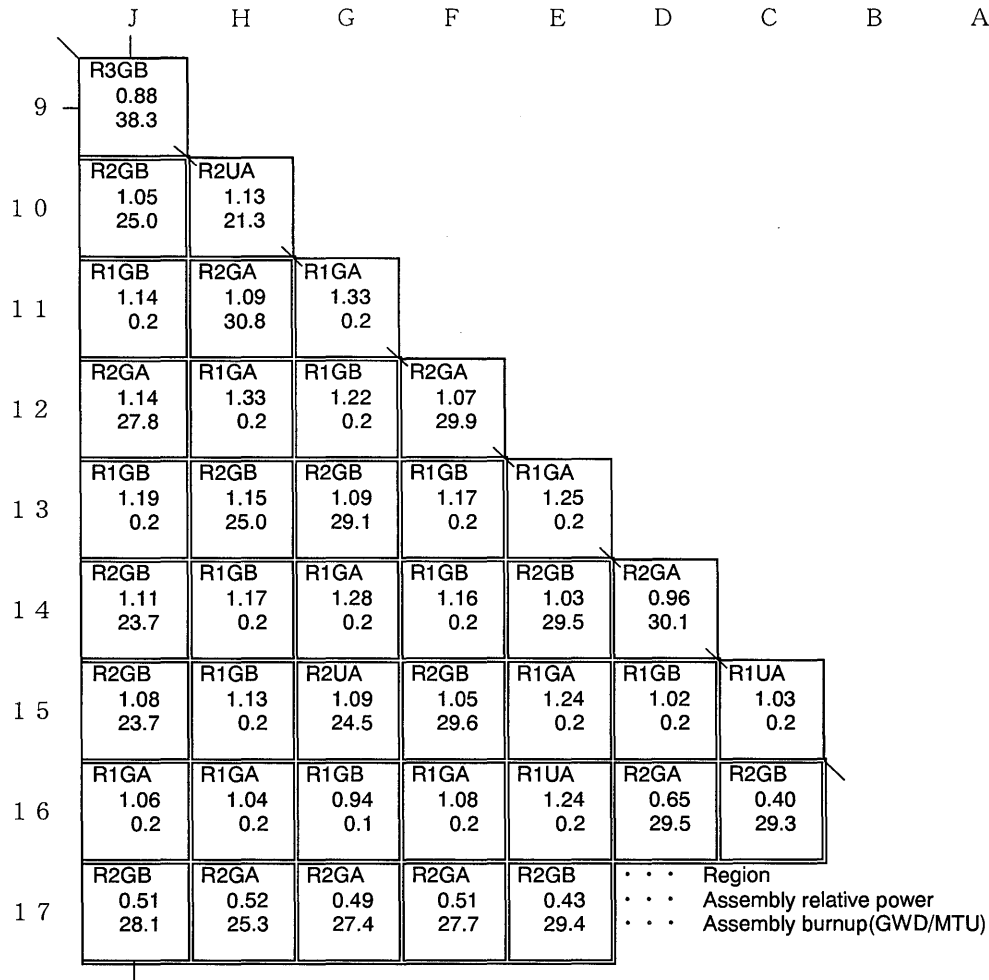


Figure A-5 Normalized Radial Power and Burnup Distribution at 0.15 GWD/MTU (HFP, EqXe, ARO)

NOTE: * Control Bank D withdrawn to 'bite' position

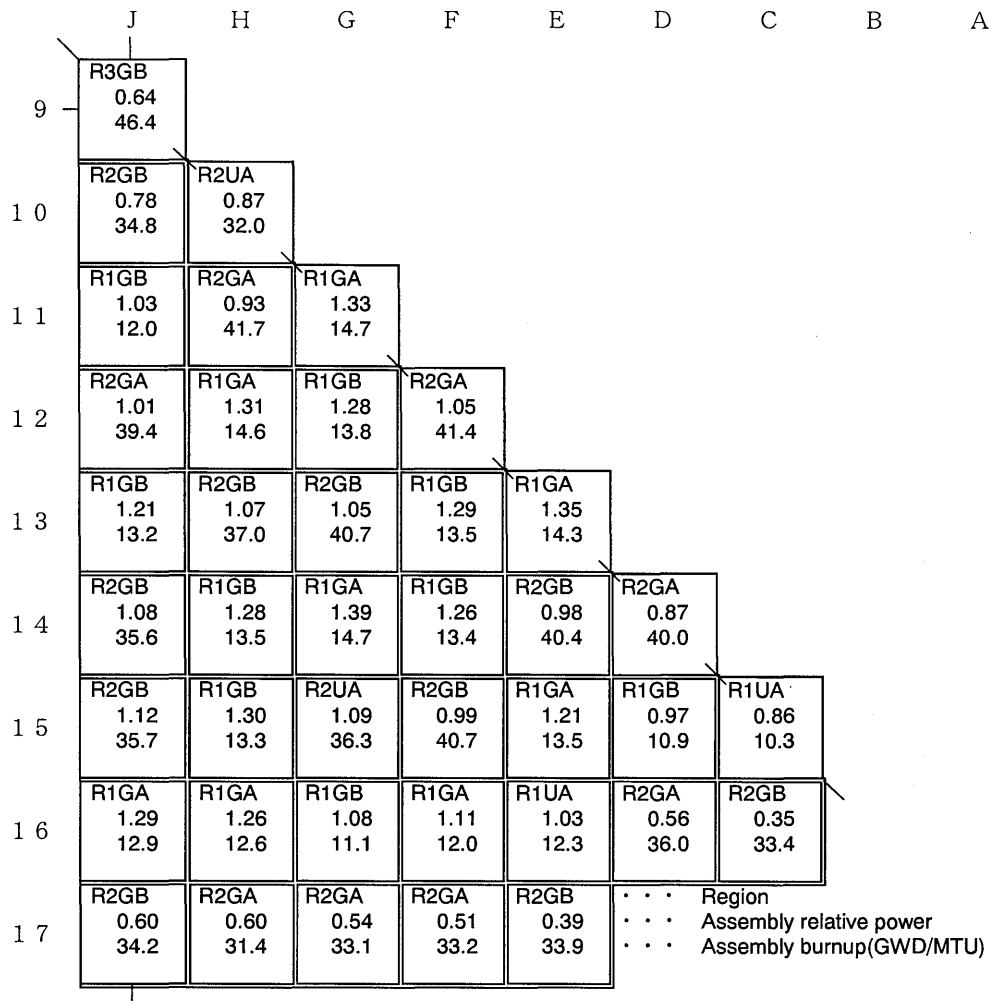


Figure A-6 Normalized Radial Power and Burnup Distribution at 11 GWD/MTU (HFP, EqXe, ARO)

NOTE: * Control Bank D withdrawn to 'bite' position

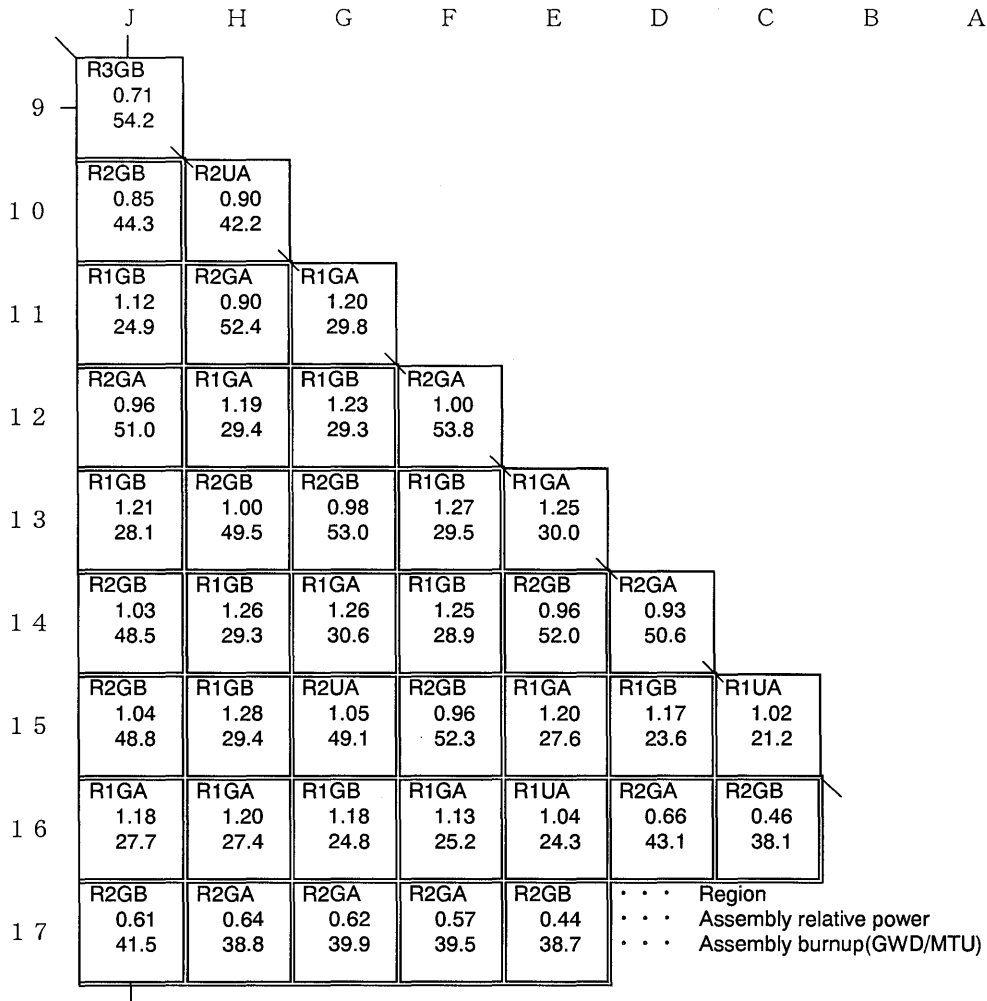


Figure A-7 Normalized Radial Power and Burnup Distribution at 23 GWD/MTU (HFP, EqXe, ARO)

NOTE: * Control Bank D withdrawn to 'bite' position

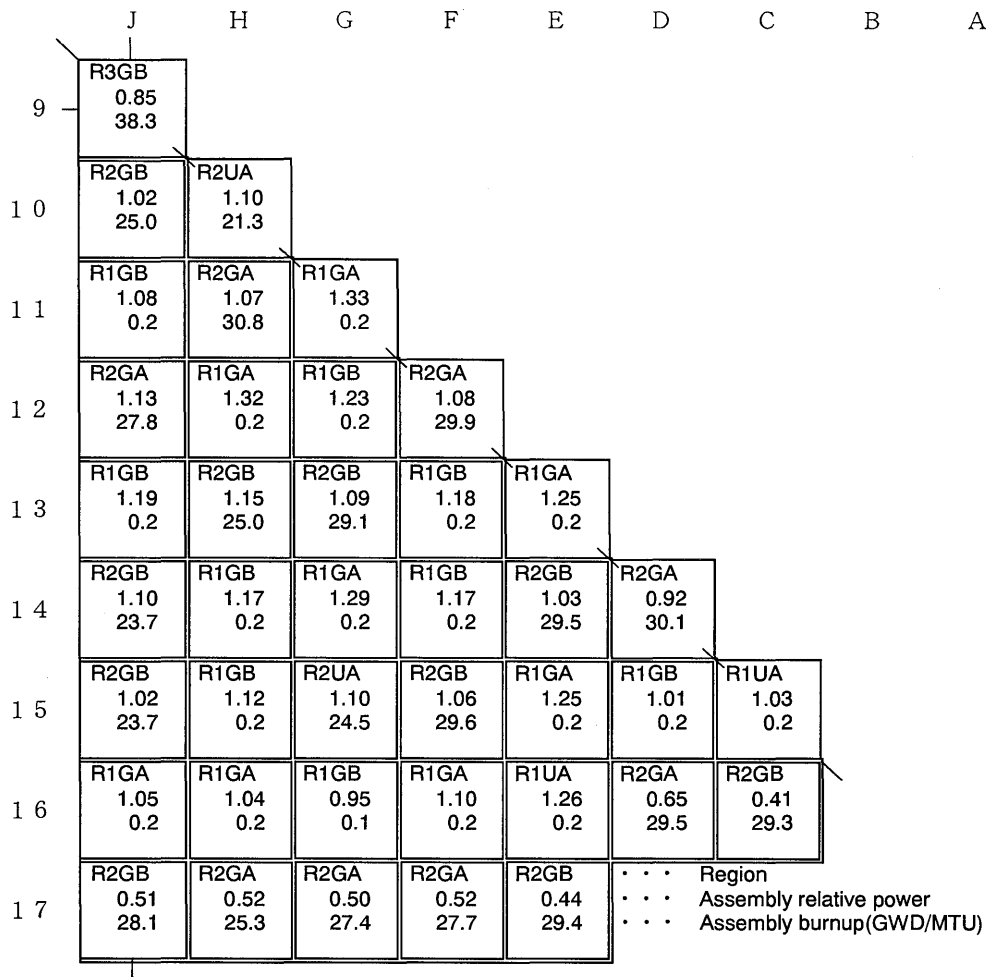


Figure A-8 Normalized Radial Power and Burnup Distribution at 0.15 GWD/MTU (HFP, EqXe, RIL)

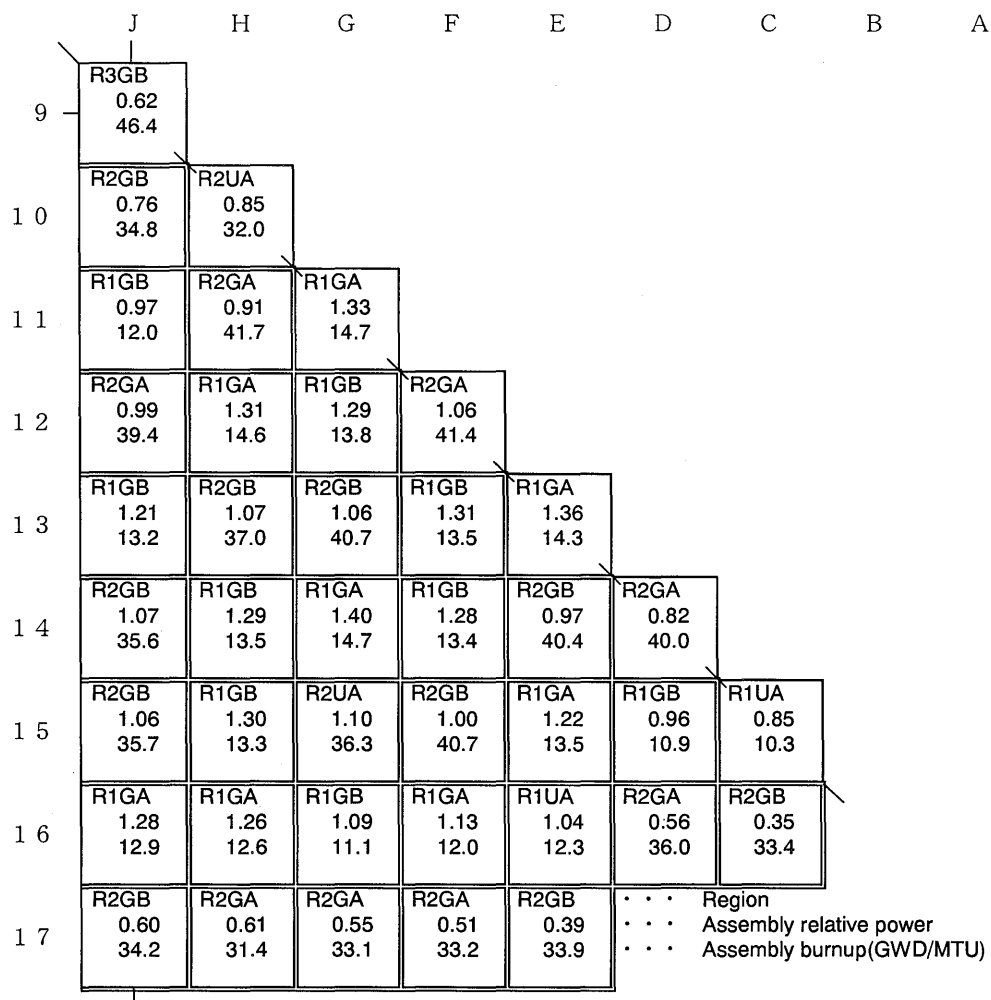


Figure A-9 Normalized Radial Power and Burnup Distribution at 11 GWD/MTU (HFP, EqXe, RIL)

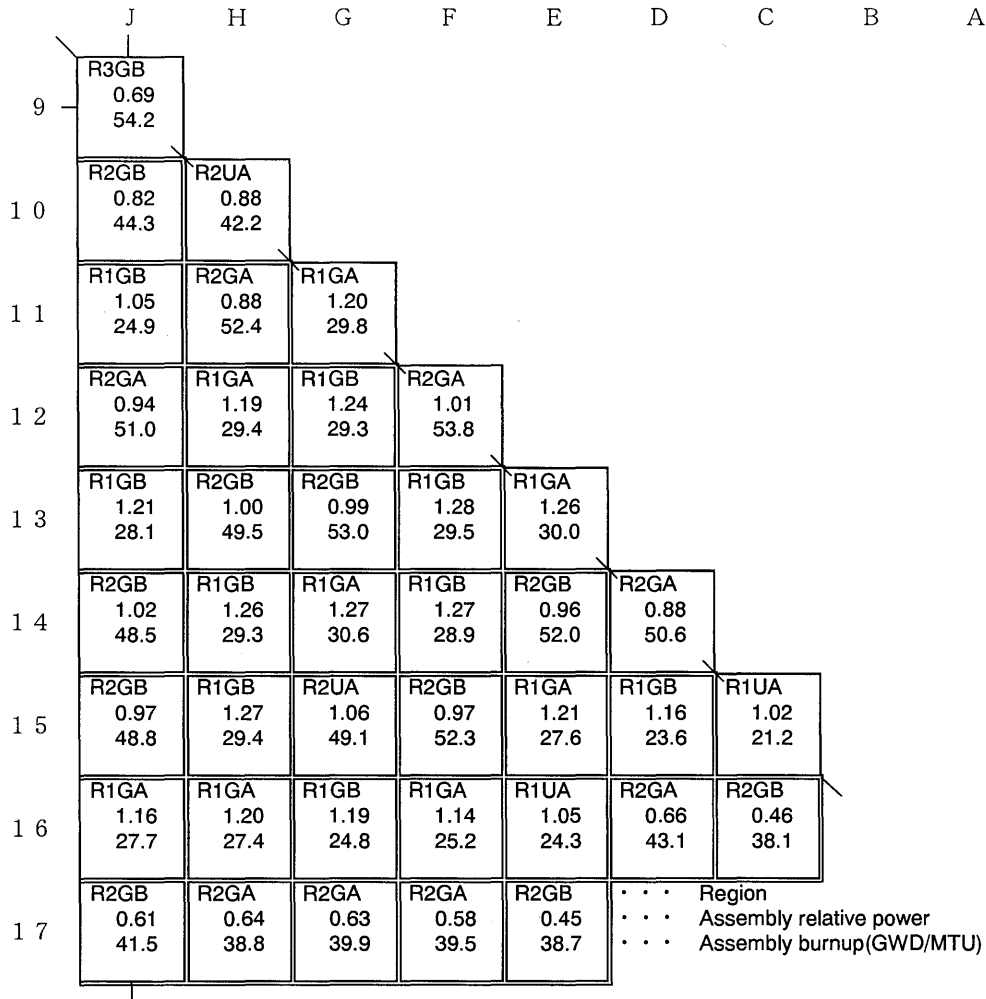


Figure A-10 Normalized Radial Power and Burnup Distribution at 23 GWD/MTU (HFP, EqXe, RIL)

Assembly (E-16)

| | 1 | 2 | 3 | 4 | 5 | 6 | 7 | 8 | 9 | 10 | 11 | 12 | 13 | 14 | 15 | 16 | 17 |
|----|-------|-------|-------|-------|-------|-------|-------|-------|-------|-------|-------|-------|-------|-------|-------|-------|-------|
| 1 | 1.358 | 1.356 | 1.369 | 1.389 | 1.407 | 1.422 | 1.418 | 1.414 | 1.413 | 1.397 | 1.382 | 1.367 | 1.332 | 1.296 | 1.258 | 1.225 | 1.202 |
| 2 | 1.347 | 1.346 | 1.365 | 1.396 | 1.426 | 1.477 | 1.431 | 1.426 | 1.461 | 1.409 | 1.393 | 1.416 | 1.345 | 1.295 | 1.244 | 1.202 | 1.173 |
| 3 | 1.349 | 1.354 | 1.396 | 1.475 | 1.505 | ⊗ | 1.491 | 1.482 | ⊗ | 1.463 | 1.449 | ⊗ | 1.414 | 1.361 | 1.262 | 1.197 | 1.158 |
| 4 | 1.356 | 1.373 | 1.463 | ⊗ | 1.519 | 1.509 | 1.444 | 1.433 | 1.471 | 1.414 | 1.401 | 1.438 | 1.421 | ⊗ | 1.313 | 1.201 | 1.150 |
| 5 | 1.361 | 1.389 | 1.478 | 1.505 | 1.470 | 1.497 | 1.435 | 1.425 | 1.462 | 1.404 | 1.389 | 1.422 | 1.369 | 1.373 | 1.317 | 1.205 | 1.141 |
| 6 | 1.362 | 1.425 | ⊗ | 1.481 | 1.482 | ⊗ | 1.466 | 1.457 | ⊗ | 1.433 | 1.417 | ⊗ | 1.375 | 1.343 | ⊗ | 1.225 | 1.130 |
| 7 | 1.345 | 1.367 | 1.436 | 1.403 | 1.407 | 1.452 | 1.400 | 1.390 | 1.427 | 1.366 | 1.349 | 1.371 | 1.299 | 1.265 | 1.261 | 1.165 | 1.104 |
| 8 | 1.327 | 1.348 | 1.413 | 1.379 | 1.383 | 1.428 | 1.376 | 1.367 | 1.401 | 1.343 | 1.324 | 1.344 | 1.272 | 1.237 | 1.233 | 1.141 | 1.080 |
| 9 | 1.313 | 1.368 | ⊗ | 1.402 | 1.407 | ⊗ | 1.400 | 1.389 | ⊗ | 1.363 | 1.345 | ⊗ | 1.289 | 1.251 | ⊗ | 1.149 | 1.060 |
| 10 | 1.285 | 1.306 | 1.367 | 1.334 | 1.337 | 1.378 | 1.327 | 1.317 | 1.350 | 1.292 | 1.273 | 1.290 | 1.219 | 1.183 | 1.178 | 1.088 | 1.030 |
| 11 | 1.255 | 1.275 | 1.338 | 1.305 | 1.307 | 1.346 | 1.295 | 1.284 | 1.316 | 1.258 | 1.239 | 1.255 | 1.186 | 1.151 | 1.144 | 1.053 | 0.996 |
| 12 | 1.223 | 1.278 | ⊗ | 1.322 | 1.320 | ⊗ | 1.298 | 1.286 | ⊗ | 1.258 | 1.239 | ⊗ | 1.192 | 1.158 | ⊗ | 1.046 | 0.960 |
| 13 | 1.173 | 1.195 | 1.268 | 1.287 | 1.252 | 1.270 | 1.213 | 1.200 | 1.227 | 1.172 | 1.154 | 1.175 | 1.124 | 1.119 | 1.066 | 0.968 | 0.909 |
| 14 | 1.121 | 1.131 | 1.200 | ⊗ | 1.235 | 1.221 | 1.162 | 1.148 | 1.173 | 1.121 | 1.103 | 1.125 | 1.103 | ⊗ | 0.999 | 0.904 | 0.856 |
| 15 | 1.067 | 1.066 | 1.093 | 1.149 | 1.165 | ⊗ | 1.140 | 1.126 | ⊗ | 1.097 | 1.078 | ⊗ | 1.033 | 0.983 | 0.900 | 0.841 | 0.799 |
| 16 | 1.017 | 1.009 | 1.016 | 1.031 | 1.046 | 1.076 | 1.035 | 1.024 | 1.041 | 0.996 | 0.976 | 0.981 | 0.921 | 0.874 | 0.826 | 0.782 | 0.743 |
| 17 | 0.974 | 0.963 | 0.963 | 0.967 | 0.971 | 0.973 | 0.962 | 0.951 | 0.943 | 0.925 | 0.906 | 0.885 | 0.850 | 0.812 | 0.771 | 0.729 | 0.687 |

Figure A-11 Rodwise Power Distribution at 0.15 GWD/MTU

Assembly (G-14)

| | 1 | 2 | 3 | 4 | 5 | 6 | 7 | 8 | 9 | 10 | 11 | 12 | 13 | 14 | 15 | 16 | 17 |
|----|-------|-------|-------|-------|-------|-------|-------|-------|-------|-------|-------|-------|-------|-------|-------|-------|-------|
| 1 | 1.300 | 1.288 | 1.293 | 1.308 | 1.323 | 1.336 | 1.336 | 1.339 | 1.346 | 1.343 | 1.345 | 1.351 | 1.343 | 1.333 | 1.323 | 1.322 | 1.337 |
| 2 | 1.291 | 1.280 | 1.294 | 1.323 | 1.356 | 1.398 | 1.355 | 1.357 | 1.400 | 1.360 | 1.363 | 1.410 | 1.372 | 1.344 | 1.319 | 1.309 | 1.323 |
| 3 | 1.302 | 1.301 | 1.338 | 1.421 | 1.118 | ⊗ | 1.429 | 1.431 | ⊗ | 1.434 | 1.435 | ⊗ | 1.129 | 1.439 | 1.359 | 1.325 | 1.330 |
| 4 | 1.325 | 1.337 | 1.429 | ⊗ | 1.477 | 1.464 | 1.407 | 1.414 | 1.128 | 1.416 | 1.411 | 1.471 | 1.488 | ⊗ | 1.446 | 1.356 | 1.346 |
| 5 | 1.348 | 1.378 | 1.132 | 1.486 | 1.443 | 1.472 | 1.422 | 1.423 | 1.477 | 1.424 | 1.424 | 1.476 | 1.450 | 1.495 | 1.140 | 1.391 | 1.363 |
| 6 | 1.368 | 1.428 | ⊗ | 1.480 | 1.479 | ⊗ | 1.486 | 1.478 | ⊗ | 1.479 | 1.487 | ⊗ | 1.482 | 1.484 | ⊗ | 1.435 | 1.376 |
| 7 | 1.373 | 1.390 | 1.459 | 1.427 | 1.434 | 1.492 | 1.107 | 1.445 | 1.483 | 1.445 | 1.107 | 1.491 | 1.434 | 1.427 | 1.458 | 1.390 | 1.374 |
| 8 | 1.380 | 1.395 | 1.464 | 1.438 | 1.439 | 1.488 | 1.449 | 1.441 | 1.484 | 1.440 | 1.447 | 1.485 | 1.435 | 1.434 | 1.459 | 1.389 | 1.374 |
| 9 | 1.389 | 1.442 | ⊗ | 1.150 | 1.496 | ⊗ | 1.489 | 1.486 | ⊗ | 1.484 | 1.486 | ⊗ | 1.489 | 1.142 | ⊗ | 1.430 | 1.377 |
| 10 | 1.386 | 1.401 | 1.469 | 1.443 | 1.442 | 1.491 | 1.451 | 1.442 | 1.484 | 1.440 | 1.447 | 1.484 | 1.433 | 1.431 | 1.455 | 1.385 | 1.368 |
| 11 | 1.387 | 1.402 | 1.470 | 1.437 | 1.442 | 1.498 | 1.112 | 1.448 | 1.485 | 1.446 | 1.104 | 1.489 | 1.429 | 1.420 | 1.450 | 1.380 | 1.361 |
| 12 | 1.390 | 1.448 | ⊗ | 1.495 | 1.492 | ⊗ | 1.494 | 1.484 | ⊗ | 1.480 | 1.486 | ⊗ | 1.475 | 1.473 | ⊗ | 1.417 | 1.356 |
| 13 | 1.377 | 1.405 | 1.152 | 1.508 | 1.461 | 1.486 | 1.432 | 1.430 | 1.482 | 1.426 | 1.423 | 1.471 | 1.439 | 1.480 | 1.123 | 1.368 | 1.336 |
| 14 | 1.361 | 1.371 | 1.461 | ⊗ | 1.501 | 1.483 | 1.420 | 1.423 | 1.133 | 1.418 | 1.409 | 1.464 | 1.475 | ⊗ | 1.421 | 1.327 | 1.312 |
| 15 | 1.346 | 1.340 | 1.374 | 1.454 | 1.141 | ⊗ | 1.447 | 1.443 | ⊗ | 1.437 | 1.433 | ⊗ | 1.115 | 1.416 | 1.330 | 1.291 | 1.289 |
| 16 | 1.341 | 1.326 | 1.336 | 1.360 | 1.388 | 1.424 | 1.375 | 1.371 | 1.409 | 1.364 | 1.360 | 1.399 | 1.354 | 1.318 | 1.287 | 1.270 | 1.277 |
| 17 | 1.356 | 1.340 | 1.340 | 1.350 | 1.359 | 1.366 | 1.359 | 1.355 | 1.356 | 1.347 | 1.342 | 1.339 | 1.322 | 1.304 | 1.286 | 1.277 | 1.286 |

Figure A-12 Rodwise Power Distribution at 11 GWD/MTU

Assembly (H-15)

| | 1 | 2 | 3 | 4 | 5 | 6 | 7 | 8 | 9 | 10 | 11 | 12 | 13 | 14 | 15 | 16 | 17 |
|----|-------|-------|-------|-------|-------|-------|-------|-------|-------|-------|-------|-------|-------|-------|-------|-------|-------|
| 1 | 1.231 | 1.219 | 1.222 | 1.232 | 1.249 | 1.271 | 1.259 | 1.254 | 1.256 | 1.255 | 1.263 | 1.278 | 1.258 | 1.244 | 1.234 | 1.231 | 1.242 |
| 2 | 1.219 | 1.208 | 1.226 | 1.237 | 1.264 | 1.060 | 1.272 | 1.258 | 1.287 | 1.258 | 1.275 | 1.064 | 1.271 | 1.246 | 1.236 | 1.218 | 1.227 |
| 3 | 1.226 | 1.230 | 1.016 | 1.308 | 1.318 | | 1.327 | 1.310 | | 1.311 | 1.329 | | 1.324 | 1.315 | 1.022 | 1.238 | 1.232 |
| 4 | 1.242 | 1.247 | 1.314 | | 1.335 | 1.345 | 1.055 | 1.298 | 1.320 | 1.299 | 1.057 | 1.348 | 1.338 | | 1.319 | 1.251 | 1.246 |
| 5 | 1.265 | 1.281 | 1.331 | 1.342 | 1.313 | 1.342 | 1.313 | 1.299 | 1.328 | 1.299 | 1.314 | 1.343 | 1.315 | 1.344 | 1.333 | 1.283 | 1.265 |
| 6 | 1.293 | 1.078 | | 1.358 | 1.348 | | 1.353 | 1.340 | | 1.340 | 1.354 | | 1.349 | 1.358 | | 1.077 | 1.290 |
| 7 | 1.286 | 1.300 | 1.351 | 1.070 | 1.324 | 1.358 | 1.070 | 1.319 | 1.342 | 1.320 | 1.071 | 1.358 | 1.323 | 1.069 | 1.349 | 1.296 | 1.280 |
| 8 | 1.284 | 1.288 | 1.338 | 1.319 | 1.313 | 1.348 | 1.322 | 1.310 | 1.342 | 1.312 | 1.323 | 1.348 | 1.312 | 1.317 | 1.334 | 1.282 | 1.276 |
| 9 | 1.288 | 1.320 | | 1.343 | 1.345 | | 1.348 | 1.344 | | 1.343 | 1.347 | | 1.343 | 1.340 | | 1.314 | 1.279 |
| 10 | 1.288 | 1.291 | 1.340 | 1.322 | 1.316 | 1.352 | 1.326 | 1.315 | 1.344 | 1.312 | 1.324 | 1.350 | 1.314 | 1.319 | 1.337 | 1.285 | 1.279 |
| 11 | 1.295 | 1.308 | 1.359 | 1.076 | 1.331 | 1.365 | 1.077 | 1.326 | 1.348 | 1.324 | 1.074 | 1.363 | 1.328 | 1.073 | 1.354 | 1.301 | 1.285 |
| 12 | 1.308 | 1.090 | | 1.369 | 1.358 | | 1.363 | 1.349 | | 1.348 | 1.362 | | 1.356 | 1.366 | | 1.083 | 1.297 |
| 13 | 1.285 | 1.299 | 1.348 | 1.357 | 1.327 | 1.355 | 1.325 | 1.310 | 1.340 | 1.310 | 1.324 | 1.354 | 1.325 | 1.354 | 1.343 | 1.292 | 1.274 |
| 14 | 1.268 | 1.270 | 1.336 | | 1.353 | 1.362 | 1.069 | 1.312 | 1.334 | 1.312 | 1.067 | 1.361 | 1.351 | | 1.331 | 1.262 | 1.256 |
| 15 | 1.256 | 1.258 | 1.038 | 1.332 | 1.340 | | 1.345 | 1.327 | | 1.327 | 1.345 | | 1.338 | 1.328 | 1.032 | 1.249 | 1.243 |
| 16 | 1.253 | 1.240 | 1.257 | 1.265 | 1.290 | 1.080 | 1.293 | 1.276 | 1.305 | 1.276 | 1.292 | 1.077 | 1.286 | 1.260 | 1.249 | 1.230 | 1.239 |
| 17 | 1.269 | 1.255 | 1.257 | 1.265 | 1.278 | 1.298 | 1.283 | 1.275 | 1.276 | 1.274 | 1.281 | 1.294 | 1.272 | 1.257 | 1.247 | 1.243 | 1.253 |

Figure A-13 Rodwise Power Distribution at 23 GWD/MTU

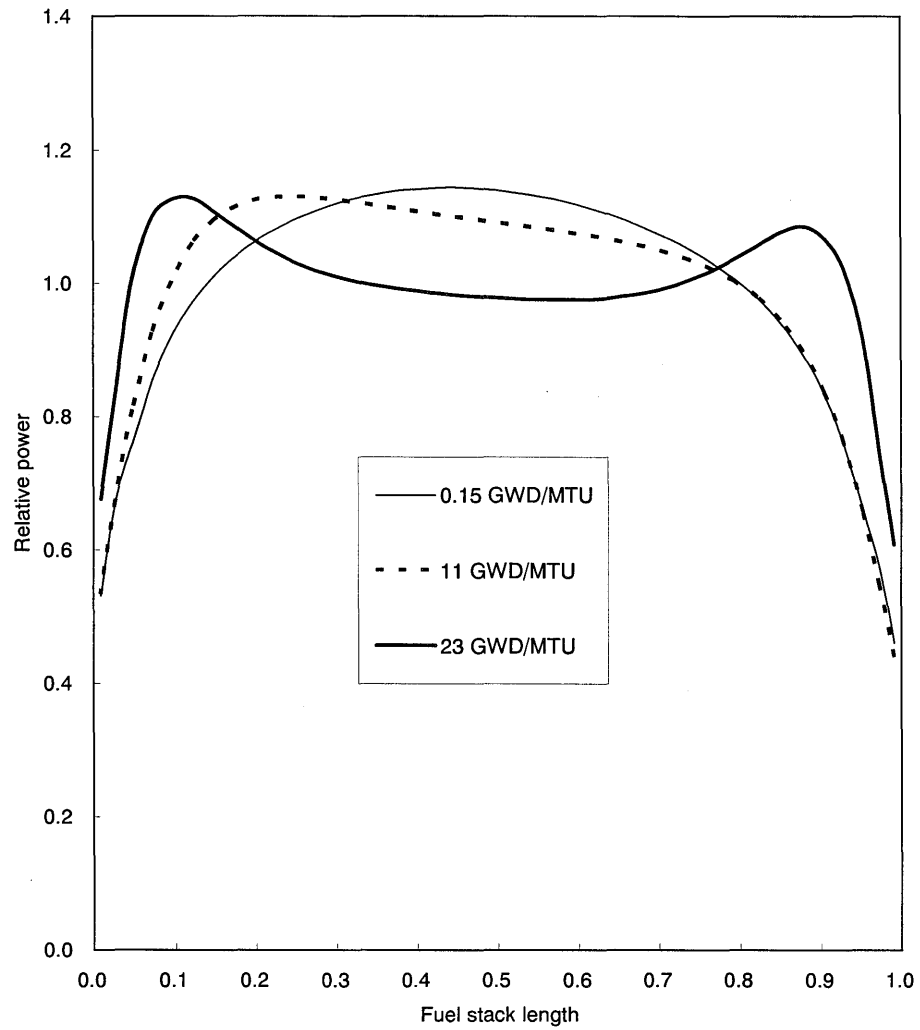


Figure A-14 Axial Power Distribution of Core Average (HFP, ARO *)

NOTE: * Control Bank D withdrawn to 'bite' position

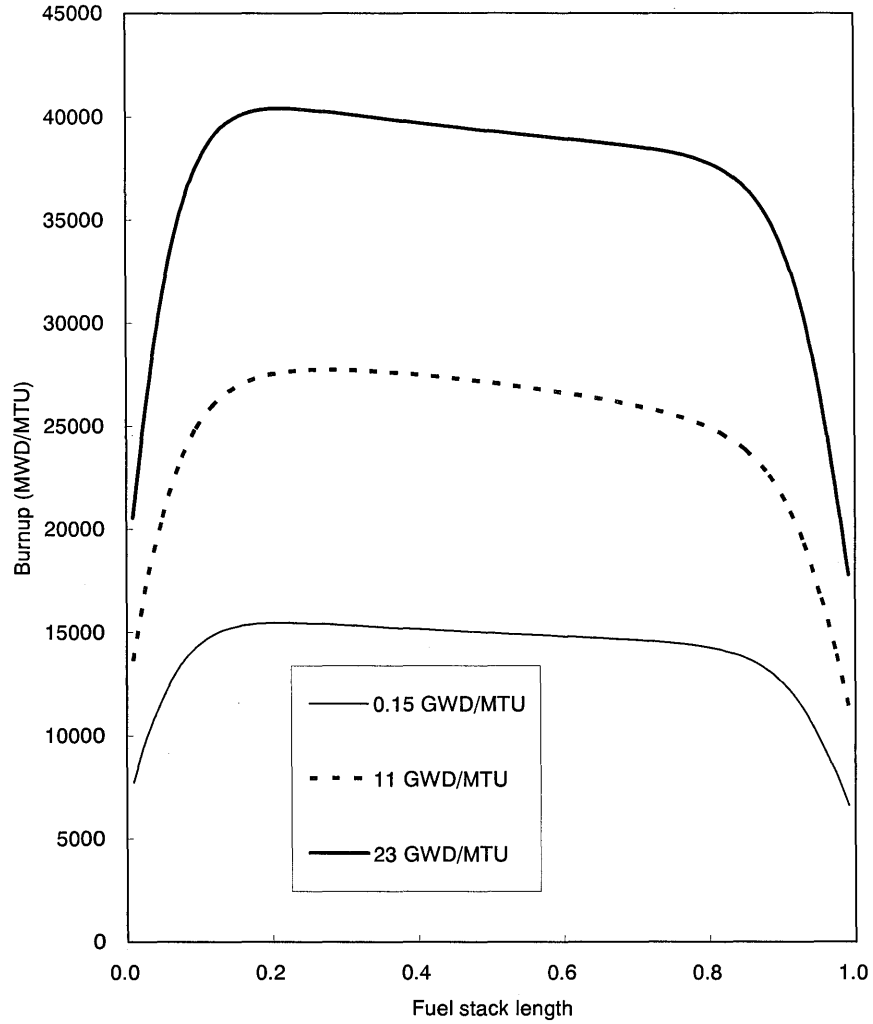


Figure A-15 Core Average Axial Burnup Distribution

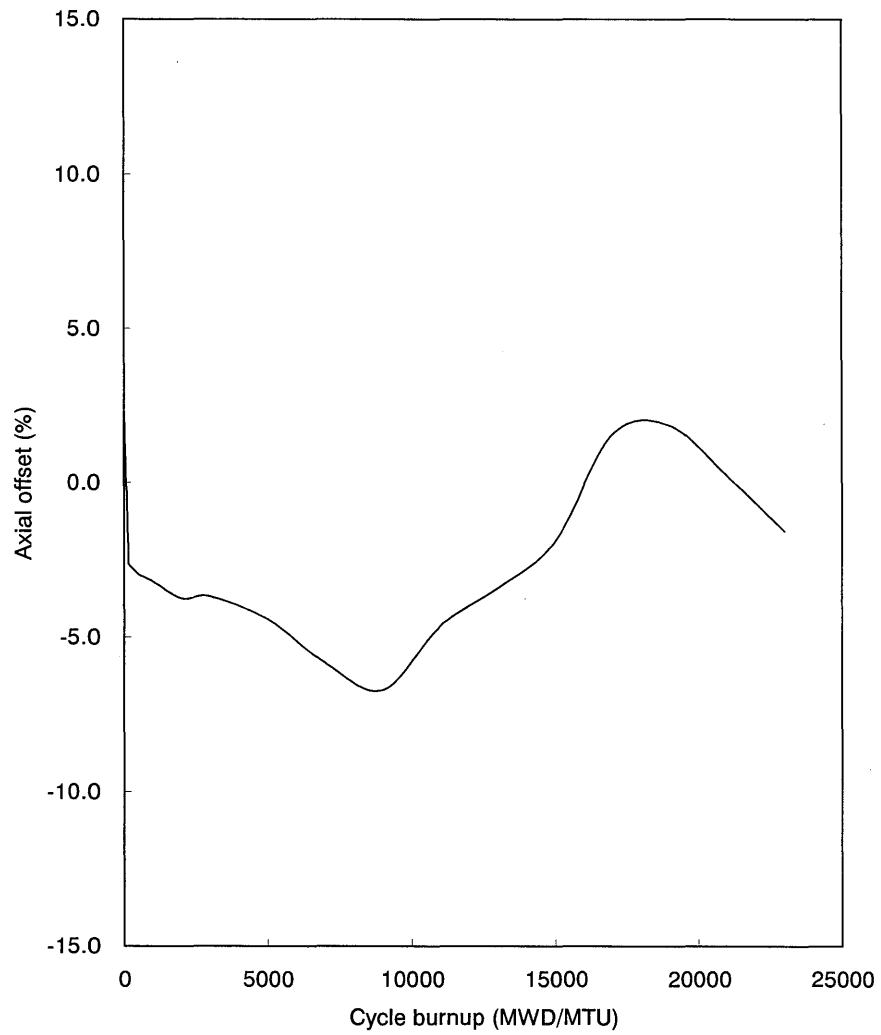


Figure A-16 Axial Offset versus Core Depletion (HFP, ARO *)

NOTE: * Control Bank D withdrawn to 'bite' position

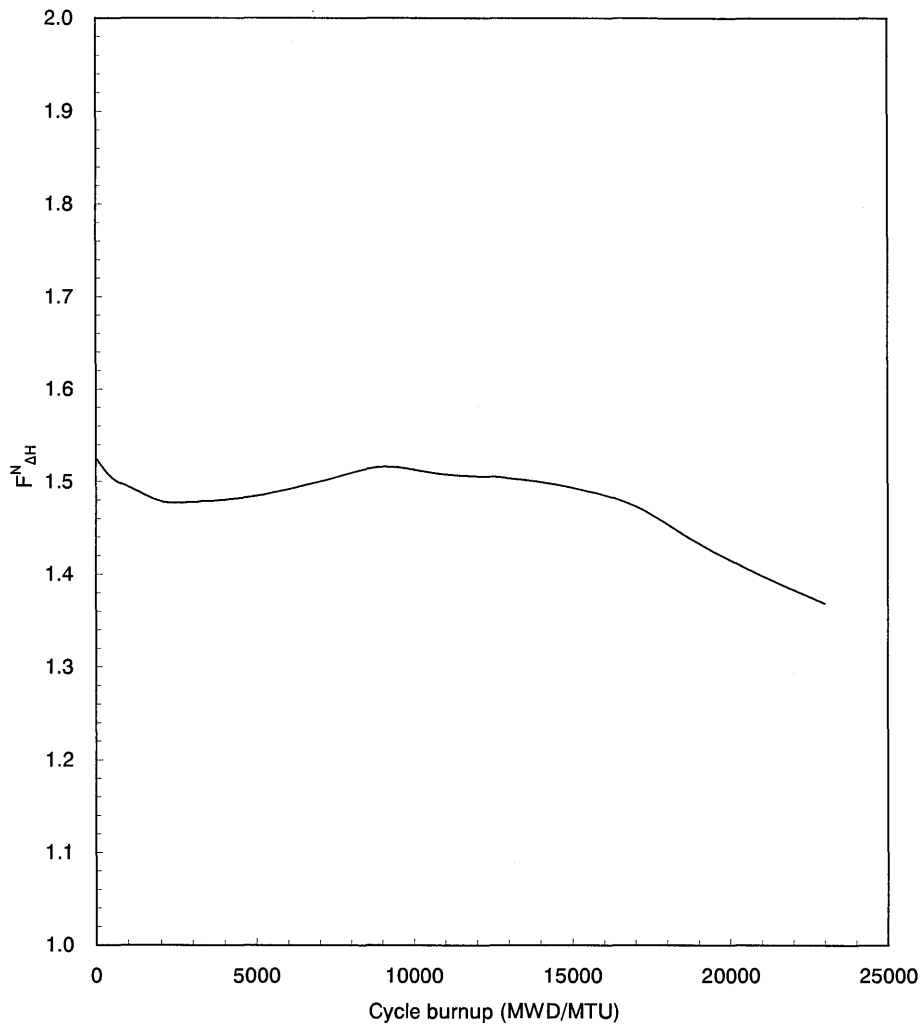


Figure A-17 $F_{\Delta H}^N$ versus Core Depletion (HFP, ARO *)

NOTE: * Control Bank D withdrawn to 'bite' position

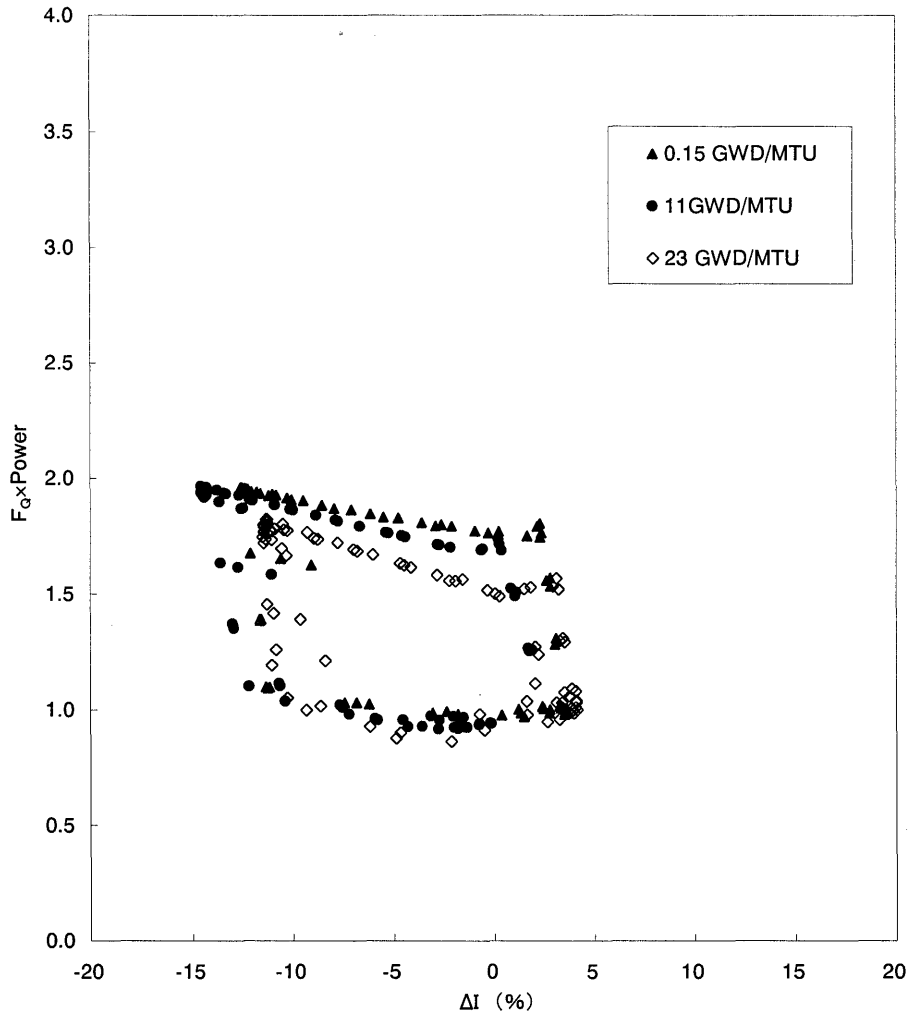


Figure A-18 Calculated Flux Difference versus F_Q Values for the Equilibrium Cycle

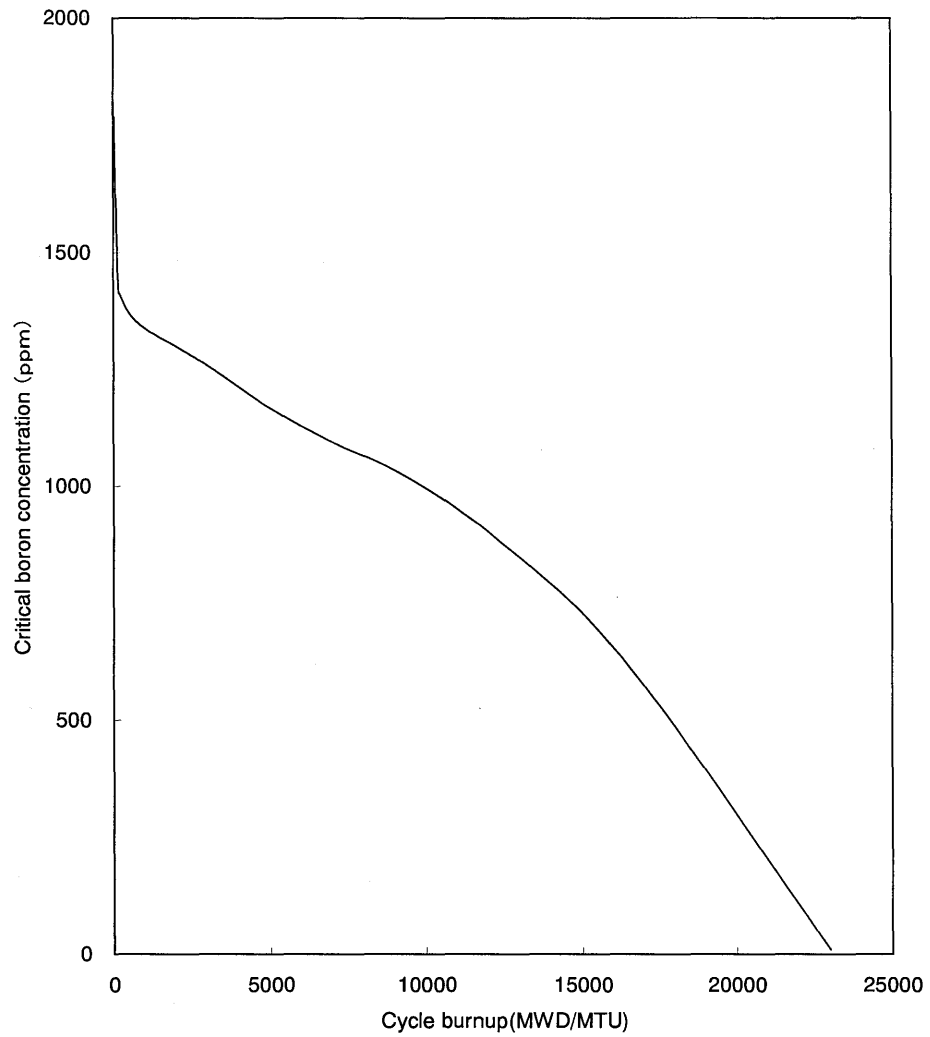


Figure A-19 Soluble Boron Concentration versus Core Depletion (HFP, ARO *)

NOTE: * Control Bank D withdrawn to 'bite' position

Appendix B

FUEL ASSEMBLY AND ICC MATERIAL PROPERTIES

February 2008

**© 2008 Mitsubishi Heavy Industries, Ltd.
All Rights Reserved**

Summary

This document provides the following material properties of fuel assembly structural parts and ICCCs for the US-APWR fuel system:

- Zircaloy-4
- Stainless Steel
- Inconel 718
- Silver-Indium-Cadmium
- Borosilicate Glass
- Antimony-Beryllium

Table of Contents

| | |
|---|------|
| List of Tables..... | B-4 |
| List of Figures..... | B-5 |
| | |
| B.1.0 ZIRCALOY-4 (Re-Crystallized Annealed)..... | B-6 |
| B.1.1 Physical/Thermal Properties..... | B-6 |
| B.1.2 Chemical Properties..... | B-6 |
| B.1.3 Mechanical Properties..... | B-7 |
| B.1.4 References..... | B-9 |
| B.2.0 TYPE 304 STAINLESS STEEL..... | B-14 |
| B.2.1 Physical/Thermal Properties..... | B-14 |
| B.2.2 Chemical Properties..... | B-15 |
| B.2.3 Mechanical Properties..... | B-15 |
| B.2.4 Irradiation Behavior..... | B-18 |
| B.2.5 References..... | B-18 |
| B.3.0 INCONEL-718..... | B-25 |
| B.3.1 Physical/Thermal Properties..... | B-25 |
| B.3.2 Chemical Properties..... | B-25 |
| B.3.3 Mechanical Properties..... | B-26 |
| B.3.4 References..... | B-29 |
| B.4.0 SILVER-INDIUM-CADMIUM (Ag-In-Cd) ALLOY..... | B-35 |
| B.4.1 Physical/Thermal Properties..... | B-35 |
| B.4.2 Chemical Properties..... | B-35 |
| B.4.3 Mechanical Properties..... | B-36 |
| B.4.4 References..... | B-37 |
| B.5.0 BOROSILICATE GLASS..... | B-42 |
| B.5.1 Physical/Thermal Properties..... | B-42 |
| B.5.2 Chemical Properties..... | B-42 |
| B.5.3 Chemical Compatibility..... | B-43 |
| B.5.4 Mechanical Properties..... | B-43 |
| B.5.5 Irradiation Behavior..... | B-43 |
| B.5.6 References..... | B-44 |
| B.6.0 ANTIMONY-BERYLLIUM..... | B-45 |
| B.6.1 Physical/Thermal Properties..... | B-45 |
| B.6.2 Chemical Properties..... | B-46 |
| B.6.3 Mechanical Properties..... | B-46 |
| B.6.4 Irradiation Behavior..... | B-46 |
| B.6.5 References..... | B-47 |

List of Tables

| | | |
|-----------------|---|------|
| Table B.1.1.1-1 | Result of Density Measurement..... | B-11 |
| Table B.1.1.3-1 | Thermal Expansion of Zircaloy-4 Annealed Sheet and Plate (Tube) | B-11 |
| Table B.2.3.4-1 | Yield Strength at over 650 deg.F (Annealed SUS 304) | B-20 |
| Table B.2.3.4-2 | Yield Strength at over 650 deg.F (Cold-Worked SUS 304) | B-20 |
| Table B.4.1.4-1 | Thermal Conductivity of 80 wt% Ag - 15 wt% In - 5 wt % Cd Alloy..... | B-38 |
| Table B.4.3.1-1 | Young's Modulus of 80 wt% Ag - 15 wt% In - 5 wt% Cd Alloy..... | B-38 |
| Table B.4.3.2-1 | Tensile Characteristics of Un-irradiated Ag - In - Cd Alloy | B-39 |
| Table B.4.3.2-2 | Post-irradiation Mechanical Characteristics of Ag -15 wt% In - 4.8 wt% Cd Alloy | B-39 |

List of Figures

| | | |
|------------------|--|------|
| Figure B.1.2.2-1 | Control Rod Guide Thimble Corrosion | B-12 |
| Figure B.1.2.2-2 | Control Rod Guide Thimble Hydrogen Absorption | B-12 |
| Figure B.1.3.6-1 | Mechanical Properties of the Control Rod Guide Thimble..... | B-13 |
| Figure B.2.1.3-1 | Thermal Expansion of SUS 304..... | B-21 |
| Figure B.2.2.2-1 | Results of Corrosion Tests for SUS 304 in High-Temperature Water with Boric Acid Added to Eliminate Dissolved Oxygen (Test Temperature: 572 deg.F) | B-22 |
| Figure B.2.2.2-2 | Mean Corrosion Rates for SUS 304 in High-Temperature Water with Boric Acid Added to Eliminate Dissolved Oxygen (Test Temperature: 572 deg.F) | B-22 |
| Figure B.2.3.4-1 | Tensile Strength of 10-12% Cold Worked Type 304 Stainless Steel | B-23 |
| Figure B.2.3.4-2 | Yield Strength of 10-12% Cold Worked Type 304 Stainless Steel | B-24 |
| Figure B.3.1.3-1 | Coefficient of Thermal Expansion for Inconel-718..... | B-30 |
| Figure B.3.2.2-1 | Corrosion Weight Increase for Inconel-718 (1499 deg.F) | B-31 |
| Figure B.3.3.1-1 | Young's Modulus Design Curve for Inconel-718 | B-32 |
| Figure B.3.3.1-2 | Shear Modulus Design Curve for Inconel-718..... | B-32 |
| Figure B.3.3.3-1 | Ultimate Tensile Strength for Unirradiated Inconel-718 | B-33 |
| Figure B.3.3.3-2 | Neutron Fluence Dependency of Tensile Strength in Inconel-718..... | B-33 |
| Figure B.3.3.3-3 | Ultimate Tensile Strength Design Curve for Unirradiated Inconel-718 | B-34 |
| Figure B.3.3.4-1 | 0.2% Yield Strength for Unirradiated Inconel-718 | B-34 |
| Figure B.4.2.2-1 | Corrosion Test Result for Ag - In - Cd Alloy (600 deg.F in Still Water) .. | B-40 |
| Figure B.4.2.2-2 | Corrosion Test Results for Ag - In -Cd Alloy (600 deg.F, Simulated Primary Coolant Water Quality) | B-40 |
| Figure B.4.3.3-1 | Radiation Swelling Characteristics of Ag - In - Cd Alloy (Irradiation Temperature: 347 - 599 deg.F) | B-41 |
| Figure B.6.1.3-1 | Thermal Expansion of Sb-Be Pellets | B-48 |

B.1.0 ZIRCALOY-4 (Re-Crystallized Annealed)

Re-crystallized annealed Zircaloy-4 is used for the intermediate grid spacers and their sleeves, the control rod guide thimbles and the in-core instrumentation guide tube in the US-APWR fuel assembly.

B.1.1 Physical/Thermal Properties

B.1.1.1 Density

Using the ASTM recommendation for the lattice parameter of Zircaloy-4, the ideal value of the Zircaloy-4 density is 0.236 lb/in^3 (6.53 g/cm^3)^(B.1-1). The Zircaloy-4 density obtained in Mitsubishi measurements is 0.2359 lb/in^3 (6.530 g/cm^3), as shown in Table B.1.1.1-1, which is essentially the same value as the ideal value.

The value 0.2366 lb/in^3 (6.55 g/cm^3) is conservatively used in weight calculation of the fuel assembly.

B.1.1.2 Melting Point and Phase Transformation

Mitsubishi measurements give 3317 deg.F (1825 deg.C) as the melting point of Zircaloy-4. With respect to phase transformations, 1508 deg.F (820 deg.C) has been measured as the temperature for transformation from the α phase to the $\alpha + \beta$ phase and 1778 deg.F (970 deg.C) has been measured for the transformation from the $\alpha + \beta$ phase to the β phase.

B.1.1.3 Thermal Expansion

The values used for the thermal expansion coefficients of annealed sheet, plate and tube are shown in Table B.1.1.3-1^(B.1-2).

B.1.2 Chemical Properties

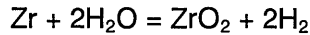
B.1.2.1 Chemical Composition

The main alloy composition of Zircaloy-4 is Zr. Fe and Cr are additives, and the composition of each element is specified as Grade R60804 in ASTM B351, B352 and B353^(B.1-3). Mitsubishi has so far manufactured two types of alloy within the composition specification range, one with the conventional content of Sn and the other with low Sn (1.20-1.45 wt.%). The low-Sn alloy is intended to improve corrosion characteristics rather than the conventional content.

| Element | wt% |
|---------|-------------|
| Sn | 1.20 ~ 1.70 |
| Fe | 0.18 ~ 0.24 |
| Cr | 0.07 ~ 0.13 |
| Fe+Cr | 0.28 ~ 0.37 |
| Nb | - |
| O | 0.09 ~ 0.16 |
| Zr | Balance |

B.1.2.2 Chemical Compatibility with Water

The chemical reaction between Zircaloy-4 and water forms zirconium oxide at surface of Zircaloy-4 and generates hydrogen as follows:



The generated hydrogen is partially absorbed in the components.

Corrosion may be accelerated in the reactor, due to the oxygen generated by radiolysis of the coolant. Hydrogen is added in the coolant in order to suppress this oxygen generation.

(1) Corrosion

The Zircaloy corrosion rate exhibits an Arrhenius dependence on the temperature at the interface between the oxide layer and the Zircaloy base metal, and the amount of corrosion (weight increase over time) initially follows the cube law (i.e., is proportional to the cubic root of time). After the oxidation layer exceeds the transition point of 2 - 3 μm , the layer increases linearly with time.

Figure B.1.2.2-1 shows control rod guide thimble corrosion data. The oxide thickness increases with burnup. These data are applicable to other components, such as the grid spacers, since the operating conditions for these components are similar with those of the thimbles. For these unheated components the temperature at the interface between the oxide layer and the Zircaloy base metal is the same as that at outside of the oxide layer.

(2) Hydrogen absorption

Hydrogen generated from reaction of zirconium with the coolant is partially absorbed into the metal. The hydrogen absorption data for control rod guide thimbles are shown in Figure B.1.2.2-2. The data show that absorbed hydrogen increases with burnup.

The data are applicable to the other components made of Zircaloy-4, since their reactor operating conditions are similar to those of the control rod guide thimbles.

B.1.3 Mechanical Properties

B.1.3.1 Young's Modulus

Young's modulus ^(B.1-2) of Zircaloy-4 is

For 0 to 1200 deg.F (-18 to 649 deg.C);

$$E(\text{psi}) = \left[\right]$$

where

T: Temperature (deg.F)

B.1.3.2 Poisson's Ratio

Poisson's ratio is given by the following formula for isotropic materials:

$$\nu = \frac{E}{2G} - 1$$

The above formula cannot be applied to anisotropic materials such as Zircaloy-4. The value of ν for Zircaloy-4 therefore depends on the texture orientation of the material.

The measured values for Zircaloy-2, Zr-Cr-Fe and Zr-2.5Nb alloys vary within the range 0.33 ~ 0.38^(B.1-4).

The following equations are applied to Zircaloy-4:

$$\text{Radial direction: } \nu = 0.3699 - 4.092 \times 10^{-5} T$$

$$\text{Axial direction : } \nu = 0.301 - 7.03 \times 10^{-5} T$$

where

$$T: \text{Temperature (deg.F), } T < 1000 \text{ deg.F (538 deg.C)}$$

A nearly identical expression for ν is given in Reference (B.1-2). The data of Northwood^(B.1-4) are extensive and have a smaller deviation. The expression for Poisson's ratio used in the US-APWR design is:

$$\nu = 0.370 - 4.09 \times 10^{-5} T$$

where

$$T: \text{Temperature (deg.F), } T < 1000 \text{ deg.F (538 deg.C)}$$

B.1.3.3 Yield Strength

Minimum yield strength of 35000 psi at room temperature is recommended by ASTM B353 Grade R60804. For the design values of elevated temperatures, the following equation is determined by Mitsubishi to meet the value at room temperature and the test data at hot conditions.

$$\text{Unirradiated design values} = \left[\right]$$

$$(70 \text{ deg. F} \leq T \leq 700 \text{ deg.F})$$

where

$$T: \text{temperature (deg.F)}$$

B.1.3.4 Ultimate Tensile Strength

Minimum ultimate tensile strength of 60000 psi at room temperature is recommended by ASTM B353 Grade R60804. For the design values of elevated temperatures, the following equation is determined by Mitsubishi to meet the value at room temperature and the test data at hot conditions:

$$\text{Unirradiated design values} = \left[\right]$$

where

T: temperature (deg.F)

B.1.3.5 Fatigue Property

The Langer-O'Donnel design curve^(B.1-5) is applicable to recrystallized Zircaloy-4, with consideration of a factor of safety of 2 applied to the stress amplitude or a factor of safety of 20 applied to the number of cycles to failure, whichever is most limiting.

B.1.3.6 Effect of Irradiation

Fast neutron irradiation produces lattice defect in Zircaloy-4. Mechanical property of material is influenced by irradiation induced defects which limit the movement of dislocations in metals. In general, it is thought that as lattice defects obstruct the movement of dislocations, and as the result the strength of the material increases and ductility decreases with irradiation.

Mechanical property of Zircaloy-4 control rod guide thimble with fast neutron irradiation is shown in Figure B.1.3.6-1^(B.1-6). The figure shows that ultimate tensile strength and yield strength increase with irradiation and saturate with increase of irradiation. 0.2% yield strength and ultimate tensile strength increase with irradiation. Elongation decreases with irradiation but it saturates with increase of irradiation.

Young's modulus and Poisson's ratio show little change with irradiation because they are not affected by the existence of defects.

Zircaloy-4 grid spacer, intermediate sleeves, end plug of fuel rod and end plug of thimble are made of Zircaloy-4 and fast neutron fluence exposures on these components are the same level, so the mechanical properties in Figure B.1.3.6-1 are applicable to these components.

B.1.4 References

- (B.1-1) B. Lustman and F. Kerze, "The Metallurgy of Zirconium", New York, McGraw-Hill, 1955, p. 349
- (B.1-2) P.J.Kuchirca, "Properties of Fuel and Core component Materials", WCAP-9179, revision 1 and WCAP-9224 (Non proprietary)
- (B.1-3) American Society for Testing and Materials (ASTM), B351, "Standard Specification for Hot-Rolled and Cold-Finished Zirconium and Zirconium Alloy Bars, Rod, and

Wire for Nuclear Application", B352."Standard Specification for Zirconium and Zirconium Alloy Sheet, Strip, and Plate for Nuclear Application", B353."Standard Specification for Wrought Zirconium and Zirconium Alloy Seamless and Welded Tubes for Nuclear Service (Except Nuclear Fuel Cladding)"

- (B.1-4) Northwood, D. O., London, I. M. and Bahen, L. E., "Elastic Constants of Zirconium Alloys", J. Nucl. Mater. 55, 299-310(1975)
- (B.1-5) W.J.O'Donnel and B.F.Langer, "Fatigue Design Basis for Zircaloy Components", Nuclear Science and Engineering 20 pp.1-12, 1964
- (B.1-6) RESEARCH REPORT EP80-16, HOT CELL EXAMINATION OF ZION FUEL CYCLE5, Empire State Electric Energy Research Corporation, June 1985

Table B.1.1.1-1 Result of Density Measurement

| Material | No. | Average Diameter (in.) | Average Length (in.) | Volume (in. ³) | Mass (lb × 10 ⁻³) | Density (lb/in. ³) |
|------------|-----|------------------------|----------------------|----------------------------|-------------------------------|--------------------------------|
| Zircaloy-4 | 1 | 0.1954 | 0.3977 | 0.01190 | 2.8063 | 0.2359 |
| | 2 | 0.1955 | 0.3959 | 0.01186 | 2.7966 | 0.2359 |
| | | | | | Ave. | 0.2359 |

(Remark)

Composition of Zircaloy-4 in this test

| Sn(wt%) | Fe(wt%) | Cr(wt%) | C(ppm) | O(ppm) | Zr |
|---------|---------|---------|--------|--------|------|
| 1.47 | 0.21 | 0.11 | 167 | 1300 | Bal. |

Table B.1.1.3-1 Thermal Expansion of Zircaloy-4 Annealed Sheet and Plate (Tube)

$$\Delta L = L_0 (a T + b T^2 + c T^3) \quad (\text{where } T = \text{deg.F} - 32)$$

Upper temperature limit = 1100 deg.F (580 deg.C)

| <u>Direction (for Tube)</u> | <u>a</u> | <u>b</u> | <u>c</u> |
|------------------------------|-----------------------|------------------------|-------------------------|
| Normal (radial) | 3.49×10^{-6} | 1.30×10^{-11} | 7.27×10^{-13} |
| Rolling (axial) | 2.44×10^{-6} | 6.64×10^{-10} | -2.37×10^{-13} |
| Transverse (circumferential) | 2.67×10^{-6} | 1.10×10^{-9} | -1.97×10^{-13} |

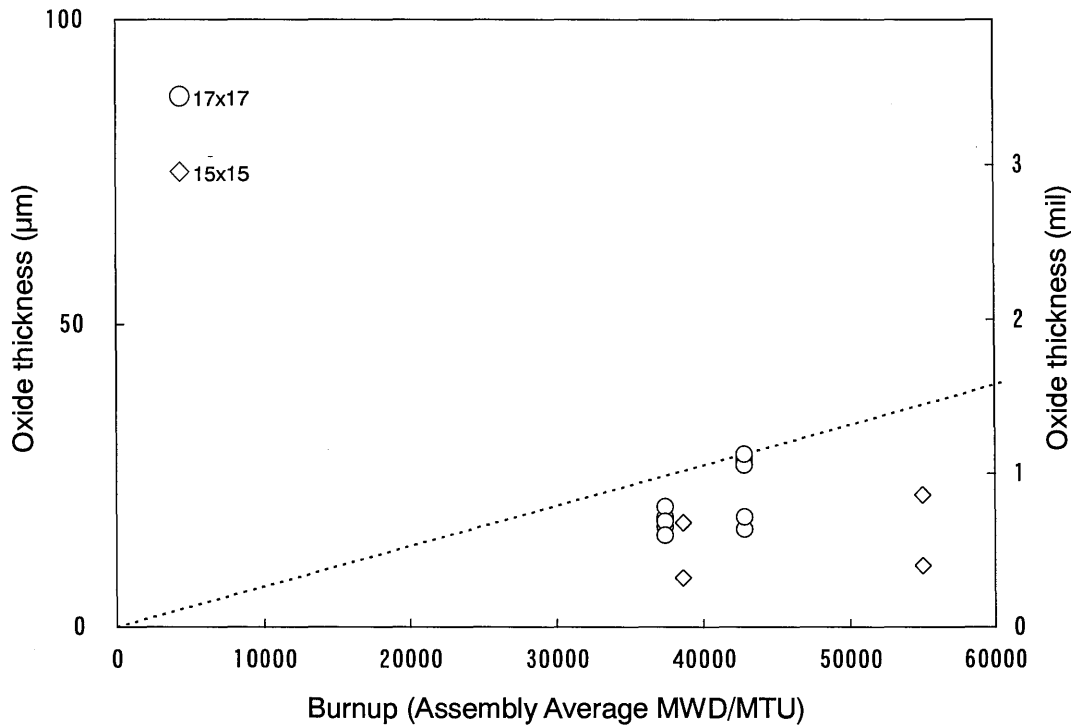


Figure B.1.2.2-1 Control Rod Guide Thimble Corrosion

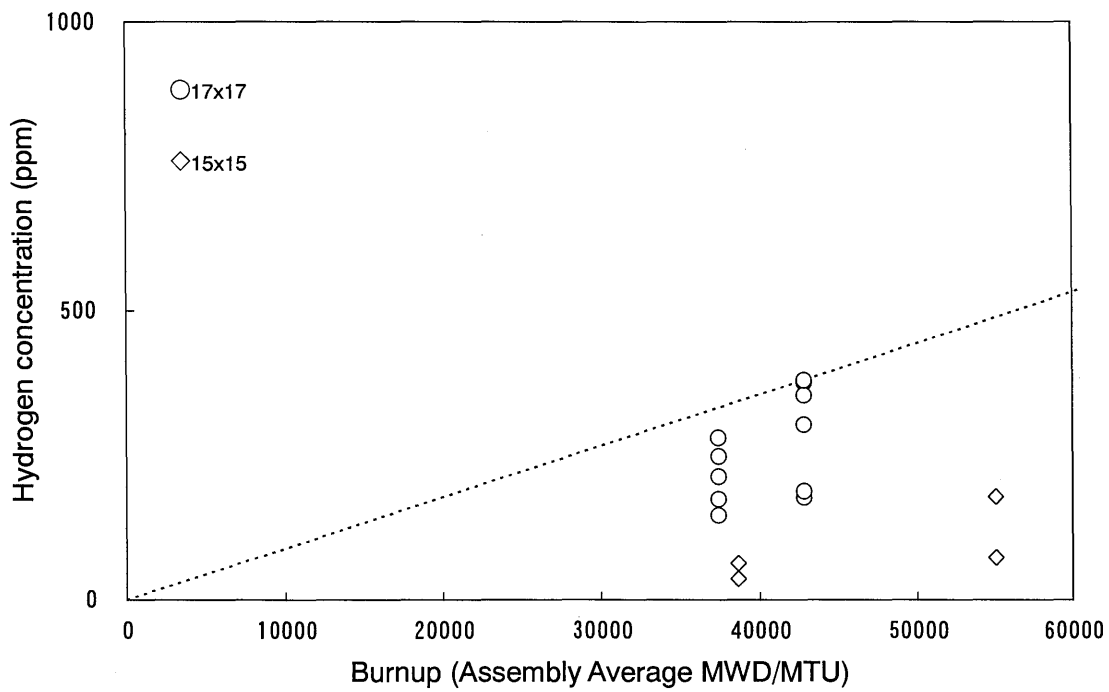


Figure B.1.2.2-2 Control Rod Guide Thimble Hydrogen Absorption

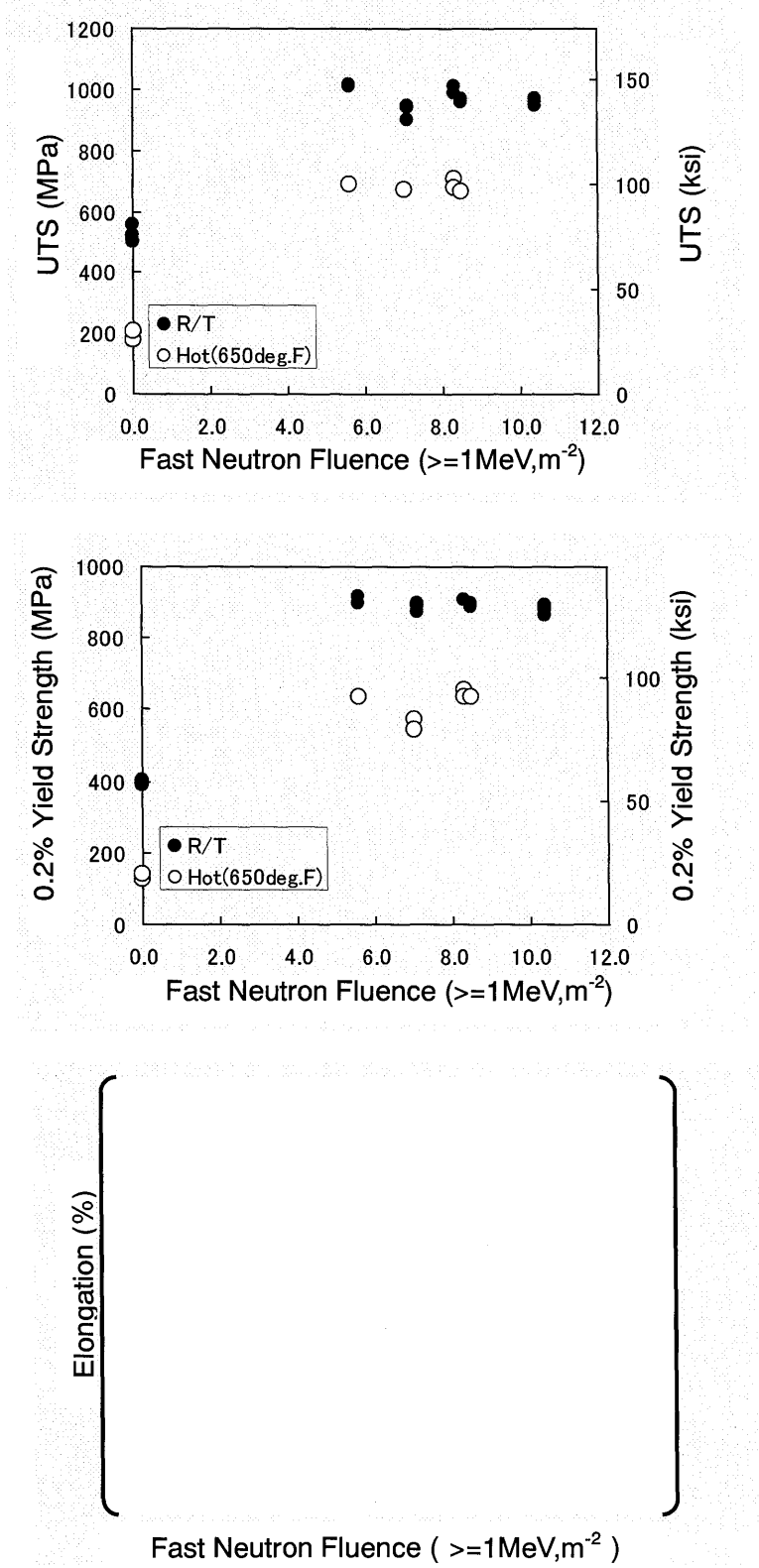


Figure B.1.3.6-1 Mechanical Properties of the Control Rod Guide Thimble

B.2.0 TYPE 304 STAINLESS STEEL

Annealed type 304 stainless steel (SUS 304) is used for the top and bottom nozzles, sleeves for Inconel 718 grid spacers, and insert tubes in the fuel assembly. Cold-worked SUS 304 steel is used for cladding material in ICCC rods. The material properties are described in the following sections.

B.2.1 Physical/Thermal Properties

B.2.1.1 Density

The density of SUS 304 steel at 80 deg.F (27 deg.C) is reported to be 0.2818 lb/in³ (B.2-1). The density 0.2865 lb/in³ (7.93 g/cm³) is conservatively used in weight calculation of the fuel assembly.

B.2.1.2 Melting Point

The melting point of SUS 304 steel is reported to be from 2548 to 2647 deg.F (1398 to 1453 deg.C) (B.2-1).

Conservatively, the recommended design value is 2548 deg.F.

B.2.1.3 Thermal Expansion

The following equation expresses the temperature dependence of the elongation of SUS 304 steel due to thermal expansion (B.2-1):

$$e = 1.57 \times 10^{-5} \times ((T-32) \times 5/9 + 273.15) + 1.69 \times 10^{-9} \times ((T-32) \times 5/9 + 273.15)^2 \quad (2)$$

$$(\text{application range: } 80 \leq T \leq 2548 \text{ deg.F (} 27 \leq T \leq 1398 \text{ deg.C)})$$

where

e: Thermal expansion elongation of SUS 304 steel (in/in)

T: Temperature (deg.F)

The elongation of SUS 304 steel due to thermal expansion is shown in Figure B.2.1.3-1.

The recommended design value is calculated by the equation (2).

B.2.1.4 Thermal Conductivity

Thermal conductivity is given by the following equation (B.2-3).

$$K = \left[\right]$$

where

K: Thermal conductivity (BTU/hr-ft-deg.F) , T: deg.F

B.2.2 Chemical Properties

B.2.2.1 Chemical Composition

Mitsubishi materials specifications give the following chemical composition for SUS 304 steel according to the JIS and/or ASTM standard^(B.2-4).

| | JIS G3463 (wt%) | ASTM A-276 (wt%) ^(B.2-4) |
|----|-----------------|-------------------------------------|
| Cr | 18.0 - 20.0 | same as left |
| Ni | 9.0-13.0 | 8.0 - 10.5 |
| Mn | ≤ 2.00 | same as left |
| C | ≤ 0.030 | ≤ 0.080 |
| Si | ≤ 1.00 | same as left |
| P | ≤ 0.040 | ≤ 0.045 |
| S | ≤ 0.030 | same as left |
| Fe | The remainder | same as left |

B.2.2.2 Chemical Compatibility

SUS 304 steel has extreme resistance to corrosion in high-temperature water. The results of corrosion tests for SUS 304 steel in water (572 deg.F) with boric acid added to control dissolved oxygen are shown in Figure B.2.2.2-1^(B.2-5). Regardless of the surface treatment of the steel, a strong and fine oxidation layer is formed on the surface in the initial 2,000 hrs, and the additional corrosion with longer exposures is small. The data for the mean corrosion rate, obtained from corrosion tests for SUS 304 steel in water with boric acid added to control dissolved oxygen, are shown in Figure B.2.2.2-2^(B.2-5). These data confirm that the corrosion rate decreases as the exposure time increases.

With respect to the stress corrosion cracking (SCC) characteristics of SUS 304 steel in the primary coolant, it is believed that SCC will not occur in SUS 304 steel under the water chemistry conditions of the PWR primary coolant, considering the relationship between chlorine ion concentration and dissolved oxygen concentration^(B.2-6).

B.2.3 Mechanical Properties

B.2.3.1 Young's Modulus (Coefficient of Elasticity)

(1) Annealed SUS 304 steel

The Young's modulus for annealed SUS 304 steel follows the values shown in ASME Sec II Part D Subpart 2 table TM-1.

The following temperature dependent equation for the Young's modulus of SUS 304 steel is used:

$$E = 28.3 \times 10^6 \quad (T = 70 \text{ deg.F})$$

$$E = ((25.3 - 25.9) / (600 - 500) \times (T - 500) + 25.9) \times 10^6 \quad (500 \leq T \leq 600 \text{ deg.F})$$

$$E = ((24.8 - 25.3) / (700 - 600) \times (T - 600) + 25.3) \times 10^6 \quad (600 \leq T \leq 700 \text{ deg.F})$$

where

E: Young's modulus of SUS 304 steel (psi)

T: Temperature (deg.F)

(2) Cold-worked SUS 304 steel

Since young's modulus for the cold-worked SUS 304 steel is not given in ASME Sec II Part D Subpart2 table TM-1, the design value for Young's modulus is ^(B.2-3):

$$E = 29.38 \times 10^6 - 6.63 \times 10^3 T$$

where

E: Young's modulus (psi)

T: Temperature (deg. F)

B.2.3.2 Poisson's Ratio

The following equation is used for the Poisson's ratio of SUS 304 steel ^(B.2-3):

$$\nu = 0.26 + 4.3 \times 10^{-5} T \text{ (deg.F)} \quad (0 \text{ deg.F} \leq T \leq 1500 \text{ deg.F})$$

where

T: Temperature (deg.F)

B.2.3.3 Modulus of Rigidity (Modulus of Transverse Elasticity)

The modulus of rigidity of SUS 304 steel is given by ^(B.2-3):

$$G = E / 2 (1 + \nu)$$

where

E: Young's modulus

ν : Poisson's ratio

B.2.3.4 Tensile Properties

(1) Annealed SUS 304 steel

The equation for the yield strength of annealed SUS 304 steel used in design is based on the values shown in ASME Sec II Part D Subpart1, Table Y-1. The following temperature dependent equation for the yield strength of annealed SUS 304 steel is used:

$$S_y = 30.0 \quad (T = 70 \text{ deg.F})$$

$$S_y = (18.4 - 19.4) / (600 - 500) \times (T - 500) + 19.4 \quad (500 \leq T \leq 600 \text{ deg.F})$$

$$S_y = (18.0 - 18.4) / (650 - 600) \times (T - 600) + 18.4 \quad (600 \leq T \leq 650 \text{ deg.F})$$

where

S_y : Yield strength of annealed SUS 304 steel (ksi)

T: Temperature (deg.F)

Yield strength at over 650 deg.F are determined from the Figure B.2.3.4-1^(B.2-3). The determined yield strength are shown in Table B.2.3.4-1 which is used for the stress evaluation of welding part between the ICCC rod cladding and the end plug.

The values for the ultimate tensile strength of annealed SUS 304 steel used in design are based on the values shown in ASME Sec II Part D Subpart1, Table U. The following temperature dependent values are used for the tensile strength of annealed SUS 304 steel:

$$S_u = 75.0 \quad (T = 70 \text{ deg.F})$$

$$S_u = 63.4 \quad (500 \leq T \leq 650 \text{ deg.F})$$

where

S_u : Ultimate tensile strength of annealed SUS 304 steel (ksi)

The equation for the design stress intensity of annealed SUS 304 steel is based on the values shown in ASME Sec II Part D Subpart1, Table 2A. The following temperature dependent equation is used for the design stress intensity of annealed SUS 304 steel:

$$S_m = 20.0 \quad (T = 70 \text{ deg.F})$$

$$S_m = (16.6 - 17.5) / (600 - 500) \times (T - 500) + 17.5 \quad (500 \leq T \leq 600 \text{ deg.F})$$

$$S_m = (16.2 - 16.6) / (650 - 600) \times (T - 600) + 16.6 \quad (600 \leq T \leq 650 \text{ deg.F})$$

where

S_m : Design stress intensity of annealed SUS 304 steel (ksi)

T: Temperature (deg.F)

(2) Cold-Worked SUS 304

The minimum yield strength of approximately 75,000 psi at room temperature is recommended for 10-15% cold worked stainless tubing, as is shown by curve B in Figure B.2.3.4-2^(B.2-3).

Table B.2.3.4-2 shows the yield strength values deduced from the curve at temperatures for which the stresses of the ICCC rod claddings are evaluated.

B.2.4 Irradiation Behavior

B.2.4.1 Swelling

Following equation is used for swelling evaluation of SUS 304 steel^(B.2-7):

$$\Delta V / V = \phi^{2.05-27 / \theta+78 / \theta^2} \times (T - 40) \times 10^{-10} \times \exp(32.6 - 0.015 T - 5100 / T)$$

where

$\Delta V / V$: Increased volume ratio (%)

θ : $T - 623.0$

T : Temperature (K)

ϕ : Fast neutron flux over 0.1 MeV ($\text{nvt} \cdot 10^{-22}$)

B.2.4.2 Creep

Following equation is used for creep evaluation of SUS 304 steel^(B.2-8):

$$\varepsilon_t = E \phi \sigma [C_1 \{ 1 - \exp(-E \phi t / C_2) \} + C_3 t]$$

where

ε_t : Total creep strain (in/in)

E : Average neutron energy

ϕ : Fast neutron flux over 0.1 MeV ($\text{n/cm}^2/\text{sec}$)

σ : Effective stress (psi)

t : time (hours)

C_1 : constant = $\left(\begin{array}{c} \\ \\ \\ \end{array} \right)$

C_2 : constant = $\left(\begin{array}{c} \\ \\ \\ \end{array} \right)$

C_3 : constant = $\left(\begin{array}{c} \\ \\ \\ \end{array} \right)$

B.2.5 References

- (B.2-1) NUREG/CR-6150, Vol. 4, Rev. 2, INEL-96/0422, SCDAP/RELAP5/MOD3.3 Code Manual, MATPRO-A Library of Materials Properties for LWR Accident Analysis. January 2001
- (B.2-2) M. Hasegawa, Ed. "Stainless Steel Handbook", 3rd Edition (Japan Stainless Steel Association) (1995), Nikkan Kogyo Shinbun, p.1428

- (B.2-3) P.J.Kuchirca, "Properties of Fuel and Core component Materials", WCAP-9179, revision 1 and WCAP-9224 (Non proprietary)
- (B.2-4) American Society for Testing and Materials (ASTM), B276,"Standard Specification for Stainless Steel Bars and Shapes"
- (B.2-5) Maekawa and M. Kagawa, "Corrosion of Stainless Steels in High-Temperature Boric acid Solutions", Corrosion Engineering, Vol. 17 No. 3 (1968)
- (B.2-6) A. John Sedriks, "Corrosion of Stainless Steels", John Wiley & Sons New York, 1979.
- (B.2-7) E.R.Gilbert, "In Reactor Creep of Reactor Materials", Reactor Technology, Vol.14, No.3, Fall, 1971
- (B.2-8) "Fuel Densification Supplemental Information San Onofre Nuclear Generating Station Unit 4, Cy 4", July, 1973, WCAP-8131 Addendum 1

Table B.2.3.4-1 Yield Strength at over 650 deg.F (Annealed SUS 304)

| Temperature | | Yield Strength | |
|-------------|-------|---------------------|-------|
| deg.F | deg.C | psi | MPa |
| 662 | 350 | 18.34×10^3 | 126.5 |
| 752 | 400 | 17.48×10^3 | 120.5 |
| 842 | 450 | 16.87×10^3 | 116.3 |

Table B.2.3.4-2 Yield Strength at over 650 deg.F (Cold-Worked SUS 304)

| Temperature | | Yield Strength | |
|-------------|-------|---------------------|-------|
| deg.F | deg.C | psi | MPa |
| 662 | 350 | 60.26×10^3 | 415.4 |
| 752 | 400 | 55.89×10^3 | 385.3 |
| 842 | 450 | 50.82×10^3 | 350.4 |

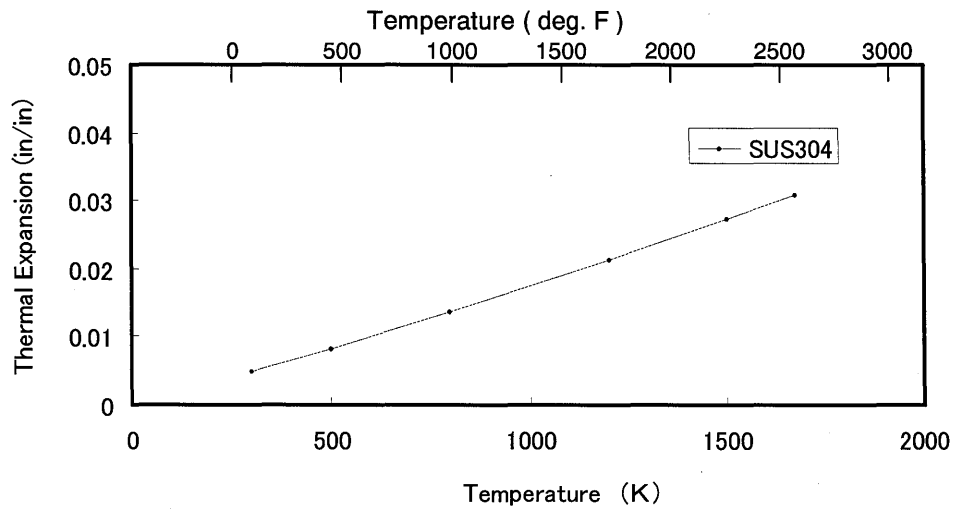


Figure B.2.1.3-1 Thermal Expansion of SUS 304

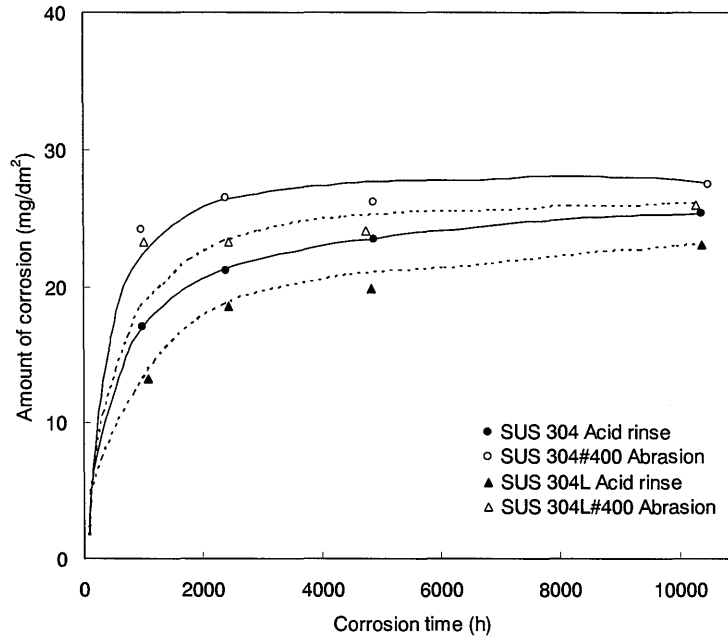


Figure B.2.2.2-1 Results of Corrosion Tests for SUS 304 in High-Temperature Water with Boric Acid Added to Eliminate Dissolved Oxygen (Test Temperature: 572 deg.F)

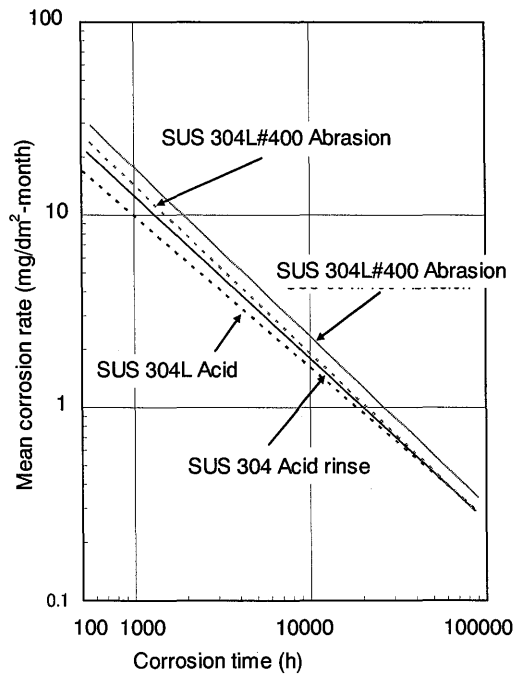


Figure B.2.2.2-2 Mean Corrosion Rates for SUS 304 in High-Temperature Water with Boric Acid Added to Eliminate Dissolved Oxygen (Test Temperature: 572 deg.F)

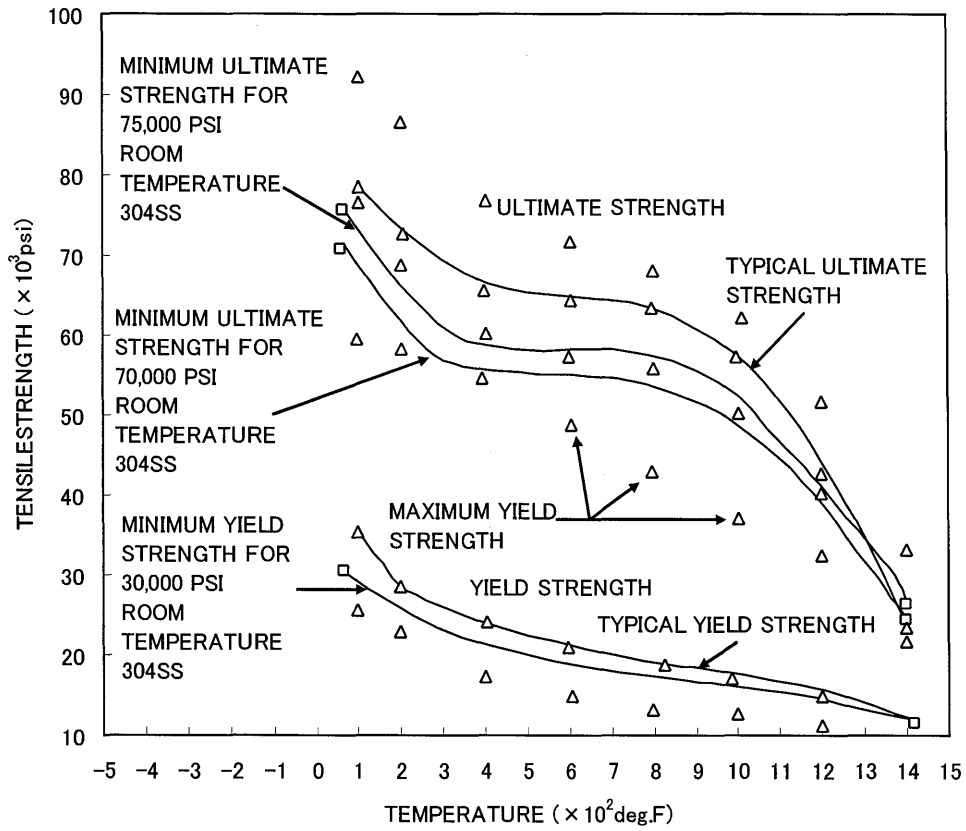


Figure B.2.3.4-1 Tensile Strength of 10-12% Cold Worked Type 304 Stainless Steel

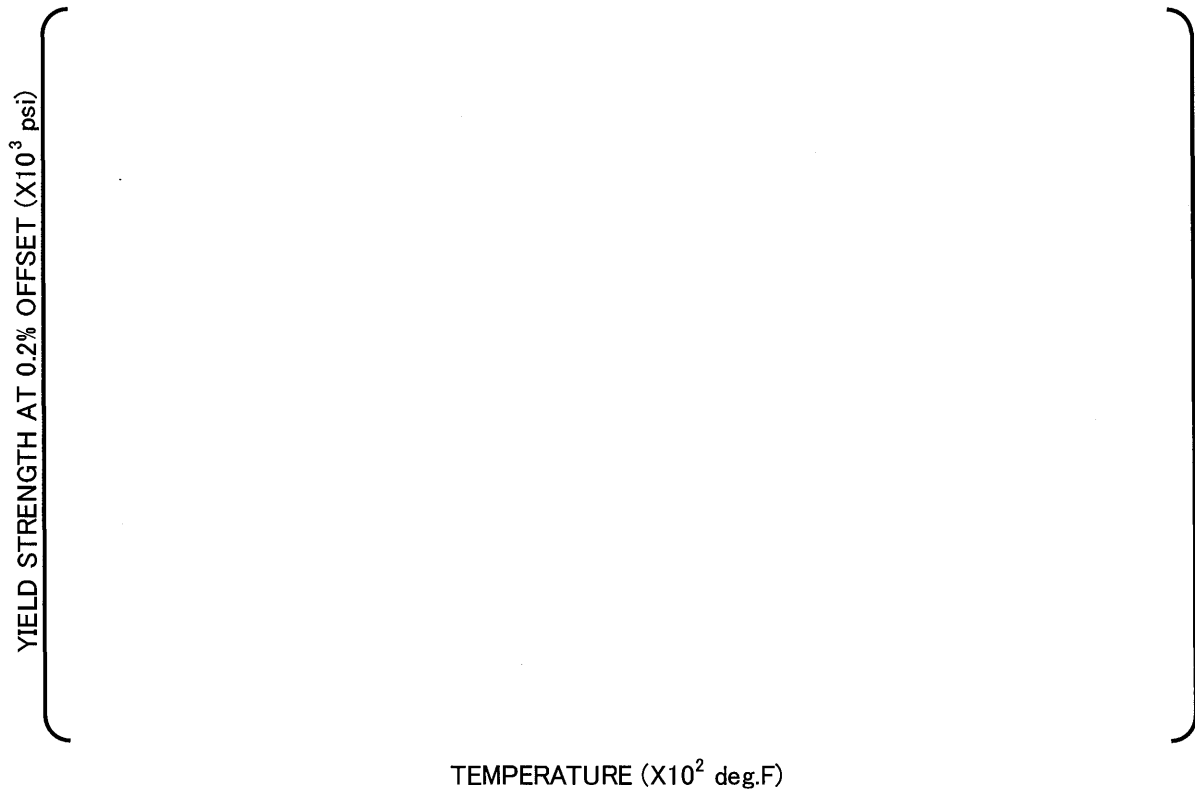


Figure B.2.3.4-2 Yield Strength of 10-12% Cold Worked Type 304 Stainless Steel

B.3.0 INCONEL-718

The precipitation-hardening nickel-based alloy Inconel-718 (ASTM B 670^(B.3-1)) is used for the top and bottom grid spacers, and the holddown spring with the top nozzle in the US-APWR fuel assembly. Inconel-718 material properties are described in the following sections.

B.3.1 Physical/Thermal Properties

B.3.1.1 Density

The measured density at room temperature is [] lb/in³ ([] g/cm³)^(B.3-2) which is used for fuel assembly weight calculation.

B.3.1.2 Melting Point

Melting point data of Inconel-718 exists in the range from 2300 to 2437 deg.F (1260 to 1336.1 deg.C)^(B.3-2).

Minimum melting temperature of 2300 deg.F (1260 deg.C) is used in design.

B.3.1.3 Thermal Expansion

The design curve of thermal expansion coefficient^(B.3-2) for the Inconel-718 is given by:

$$C = [] \quad (3)$$

where

$$\left[\begin{array}{l} \\ \\ \\ \\ \end{array} \right]$$

This design curve is shown in Figure B.3.1.3-1.

B.3.2 Chemical Properties

B.3.2.1 Chemical Composition

The chemical compositions of Inconel-718 are:

| | | |
|--------------------|-------------|-----|
| Nickel | 50.0 - 55.0 | wt% |
| Chromium | 17.0 - 21.0 | wt% |
| Niobium + tantalum | 4.75 - 5.50 | wt% |
| Molybdenum | 2.80 - 3.30 | wt% |
| Titanium | 0.65 - 1.15 | wt% |

| | | |
|------------|-------------|-----|
| Aluminum | 0.20 - 0.80 | wt% |
| Copper | 0 - 0.30 | wt% |
| Silicon | 0 - 0.35 | wt% |
| Manganese | 0 - 0.35 | wt% |
| Phosphorus | 0 - 0.015 | wt% |
| Sulfur | 0 - 0.015 | wt% |
| Cobalt | 0 - 0.10 | wt% |
| Carbon | 0 - 0.08 | wt% |
| Boron | 0 - 0.006 | wt% |
| Iron | balance | |

B.3.2.2 Corrosion

A fine oxide layer forms on the surface of nickel-based alloys such as Inconel-718 in high-temperature water. This oxide layer prevents any significant increase in the corrosion. Even when Inconel-718 is oxidized in a 1499 deg.F (815 deg.C) beryllium-steam mixed gas, the total increase in mass of the corrosion layer is no more than 0.4 mg/dm², and at 300 hours the Inconel-718 corrosion has effectively saturated as seen in Figure B.3.2.2-1^(B.3-3). In reactor, the Inconel-718 corrosion will be even less, since the temperatures of the bottom and top grid spacers will be significantly lower than this test temperature.

B.3.2.3 Chemical Compatibility

Extensive in-reactor experience has shown that the chemical reaction of Inconel-718 is negligible over its lifetime in fuel assembly components. However, an eutectic reaction of Nickel and Zirconium (and Iron and Zirconium also) occurs at high temperature about 1760 deg.F (960 deg.C). This eutectic reaction will be suppressed by the oxide layer formed between Nickel and Zirconium, and will occur only after a considerable increase in the temperature. Hence the oxide layer acts as a barrier even if the eutectic reaction is generated and the reaction is limited.

B.3.3 Mechanical Properties

B.3.3.1 Elastic Modulus

(1) Measured values

(a) Young's modulus

The Young's modulus is given by the following equation^(B.3-2):

$$E = AT^3 + BT^2 + CT + D \quad (4)$$

where

E = Young's modulus (psi)

T = Temperature (deg.F)

$$A = \left[\quad \right]$$

$$\begin{matrix} B = \\ C = \\ D = \end{matrix} \left[\begin{matrix} \\ \\ \end{matrix} \right]$$

The data on which equation (4) is based has been obtained for Inconel-718 solution treated for one hour at 1700 to 1850 deg.F (926.7 to 1010 deg.C), heat treated at 1325 deg.F (718.3 deg.C) for 8 hours and then furnace-cooled to 1150 deg.F (621.1 deg.C) for a total of 18 hours of heat treatment. The above equation is shown in Figure B.3.3.1-1.

The following data has been also reported ^(B.3-2):

$$\left[\begin{matrix} \\ \\ \end{matrix} \right]$$

These data are in good agreement with equation (4).

(b) Shear modulus

The shear modulus is given by the following equation ^(B.3-2):

$$S = AT^3 + BT^2 + CT + D \tag{5}$$

where

S = Shear modulus (psi)

T = Temperature (deg.F)

$$\begin{matrix} A = \\ B = \\ C = \\ D = \end{matrix} \left[\begin{matrix} \\ \\ \\ \end{matrix} \right]$$

The data on which equation (5) is based has been obtained from material subjected to the same heat treatment as described for the Young's modulus data. Equation (5) is plotted in Figure B.3.3.1-2.

(2) Design values

Equations (4) and (5) are the design equations used for the Young's modulus and shear modulus, respectively.

B.3.3.2 Poisson's Ratio

Temperature dependence of Poisson's ratio from room temperature to 1200 deg.F (648.9 deg.C) is given by the following equation ^(B.3-2,4):

$$\nu = AT^3 + BT^2 + CT + D \quad (6)$$

where

$$\begin{aligned} \nu &= \text{Poisson's ratio} \\ T &= \text{Temperature, deg.F (70 - 1200 deg.F (21.1 - 648.9 deg.C))} \\ A &= 2.473 \times 10^{-11} \\ B &= 1.262 \times 10^{-9} \\ C &= 4.940 \times 10^{-5} \\ D &= 0.2966 \end{aligned}$$

B.3.3.3 Ultimate Tensile Strength

(1) Measured values

(a) Unirradiated Inconel-718

The curve of ultimate tensile strength (UTS) based on data sources ^(B.3-4, 5) at room temperature is shown as in Figure B.3.3.3-1. The data are obtained from material that has been annealed for one hour at from 1700 to 1850 deg.F (926.7 to 1010 deg.C), subjected to standard two-stage aging at 1325 deg.F (718.3 deg.C) for 8 hours, and then furnace-cooled to 1150 deg.F (621.1 deg.C) for a total aging time of 18 hours.

(b) Irradiated Inconel-718

As shown in Figure B.3.3.3-2, UTS of Inconel-718 is slightly varied with irradiation ^(B.3-6).

(2) Design values

Ni-based alloys exhibit the same irradiation behavior as austenitic stainless steels. Accordingly, the strength is expected to increase for PWR operating conditions. The UTS for design is conservatively specified by that of unirradiated Inconel-718.

The design curve for solution treated hot-rolled, cold-rolled, and two-stage aged Inconel-718 is given by the curve as the minimum ultimate tensile strength in Figure B.3.3.3-3. The shape of this curve is based on the curve given in Figure B.3.3.3-1.

B.3.3.4 Yield Strength

(1) Measured values

(a) Unirradiated Inconel-718

The curve of 0.2% yield strength (YS) based on data sources ^(B.3-4, 5) at room temperature is shown in Figure B.3.3.4-1. The data are obtained from material that has been annealed for one hour at from 1700 to 1850 deg.F (926.7 to 1010 deg.C), subjected to standard two-stage aging

at 1325 deg.F (718.3 deg.C) for 8 hours, and then furnace-cooled to 1150 deg.F (621.1 deg.C) for a total aging time of 18 hours.

(b) Irradiated Inconel-718

Yield strength is slightly increased with irradiation as previously shown in Figure B.3.3.3-2^(B.3-6).

(2) Design values

Since the YS of Inconel-718 is expected to increase for PWR operating conditions, the YS for design is conservatively specified by that of unirradiated Inconel-718.

The design value for the minimum 0.2% YS for solution treated hot-rolled, cold-rolled and two-stage aged Inconel-718 is give by the curve as the minimum 0.2% YS in Figure B.3.3.4-1. The design value for the minimum room temperature YS is { } psi ({ } MPa) obtained from the curve.

B.3.4 References

- (B.3-1) American Society for Testing and Materials (ASTM), B670, "Standard Specification for Precipitation-Hardening Nickel Alloy (UNS N07718) Plate, Sheet, and Strip for High-Temperature Service"
- (B.3-2) P.J.Kuchirca, "Properties of Fuel and Core component Materials", WCAP-9179, revision 1 and WCAP-9224 (Non proprietary)
- (B.3-3) T.T. Claudson, R.E. Westerman, "An Evaluation of the Corrosion Resistance of Several High Temperature Alloys for Nuclear Applications", BNWL-155(1965)
- (B.3-4) TID-26666, "Nuclear Systems Materials Handbook", HEDL, 1975
- (B.3-5) GEMP-1004, "Advanced Pressure Vessel Materials", Seventh Annual Report - AEC Fuels and Materials Development Program
- (B.3-6) W.J.Mills, "Effect of irradiation on the fracture toughness of Alloy 718 plate and weld", Journal of Nuclear Materials 199 (1992), pp.68-78

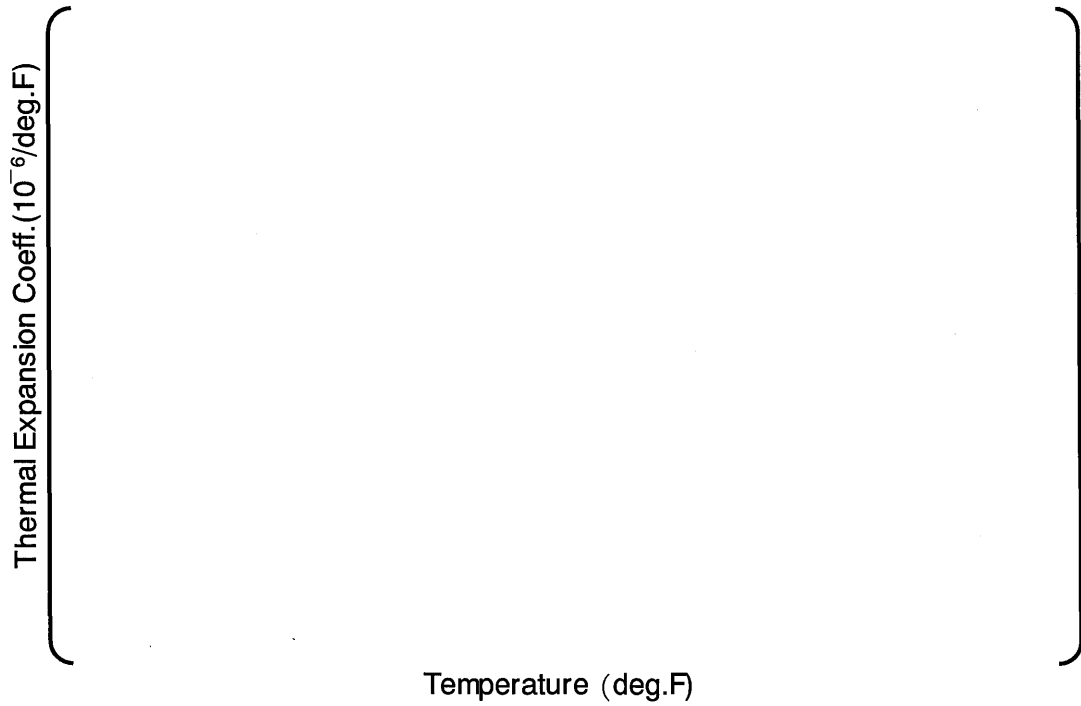


Figure B.3.1.3-1 Coefficient of Thermal Expansion for Inconel-718

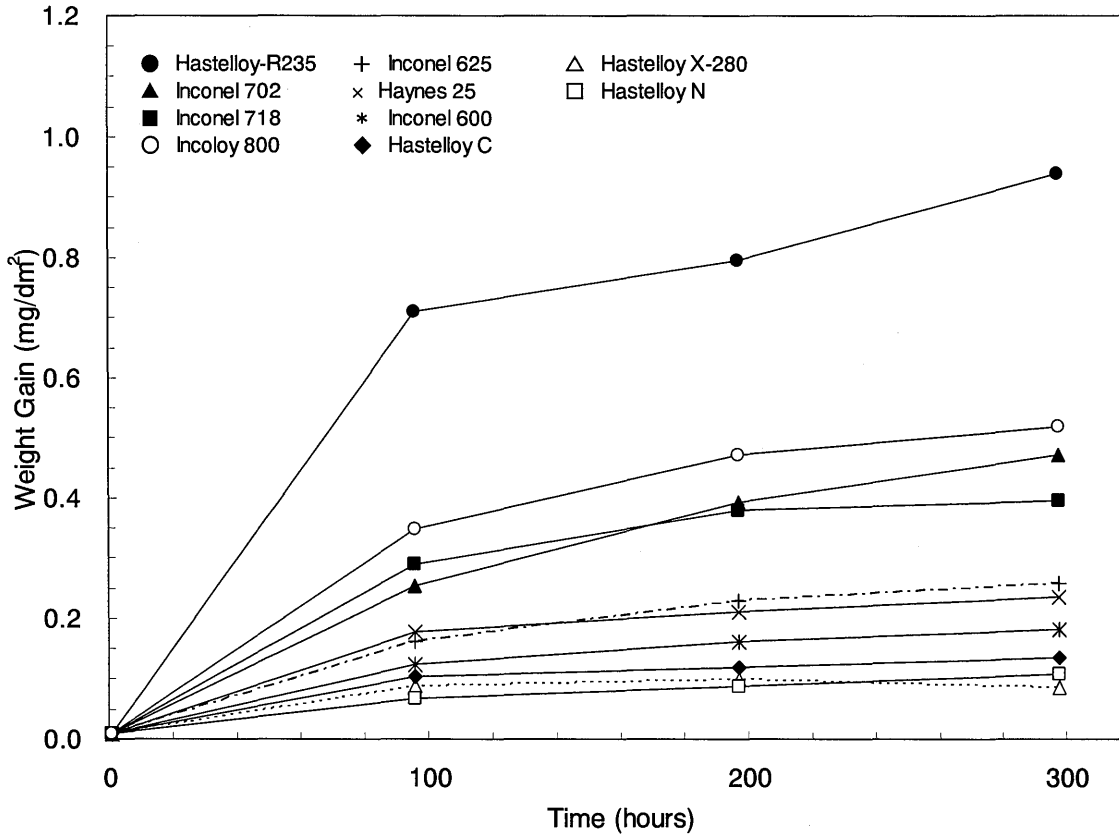


Figure B.3.2.2-1 Corrosion Weight Increase for Inconel-718 (1499 deg.F)

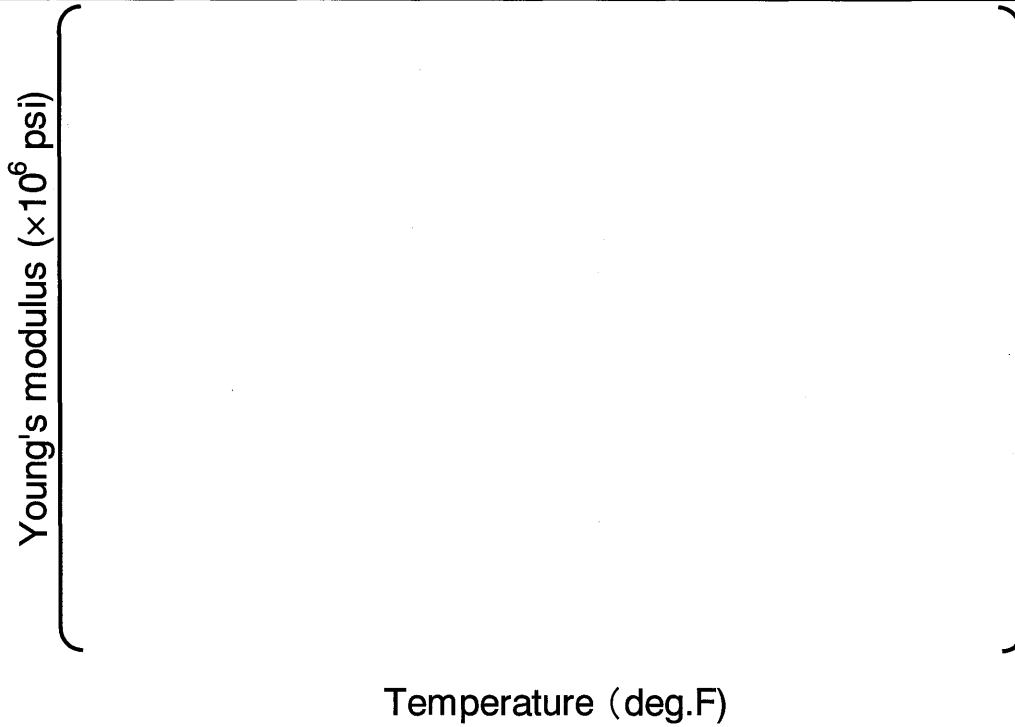


Figure B.3.3.1-1 Young's Modulus Design Curve for Inconel-718

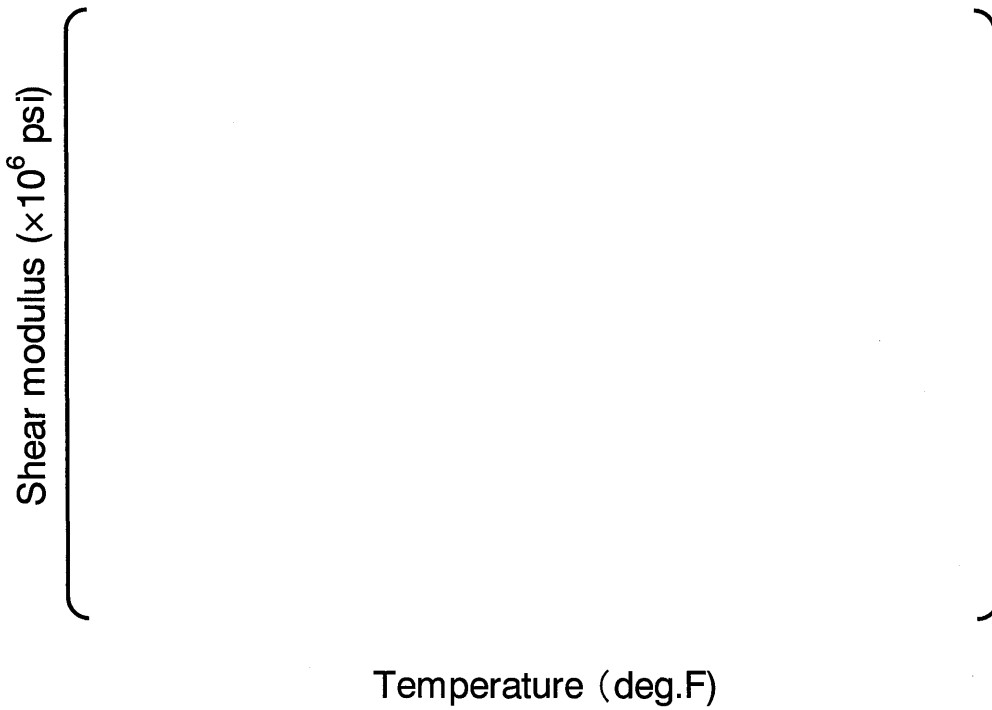


Figure B.3.3.1-2 Shear Modulus Design Curve for Inconel-718

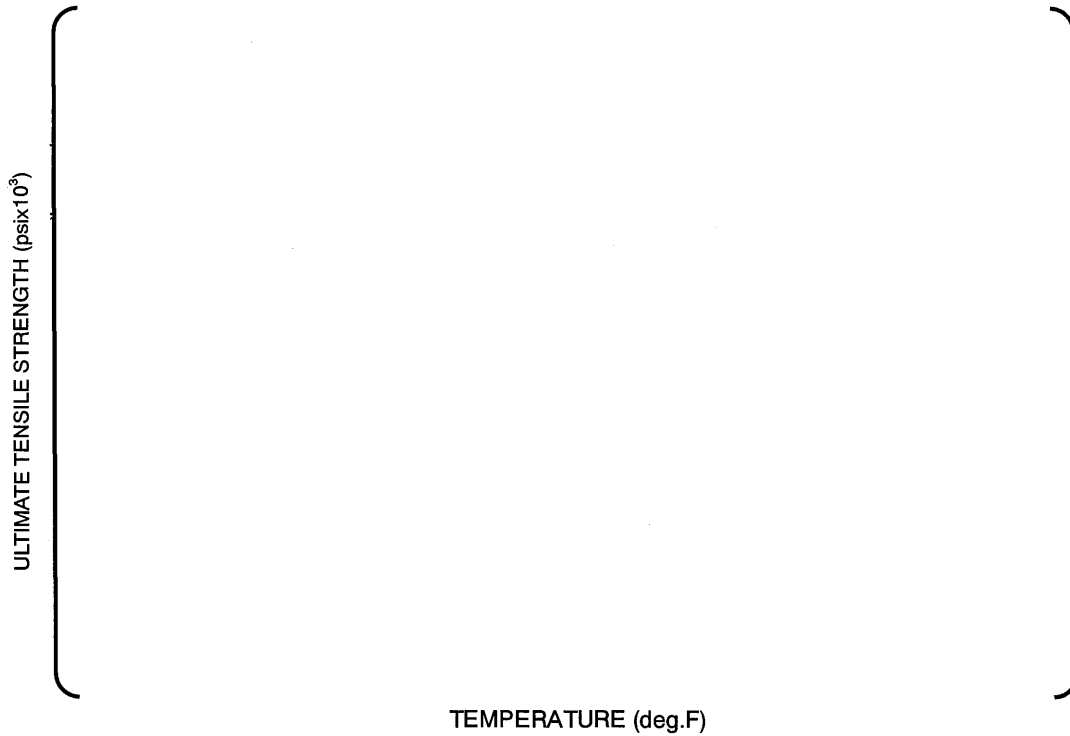


Figure B.3.3.3-1 Ultimate Tensile Strength for Unirradiated Inconel-718

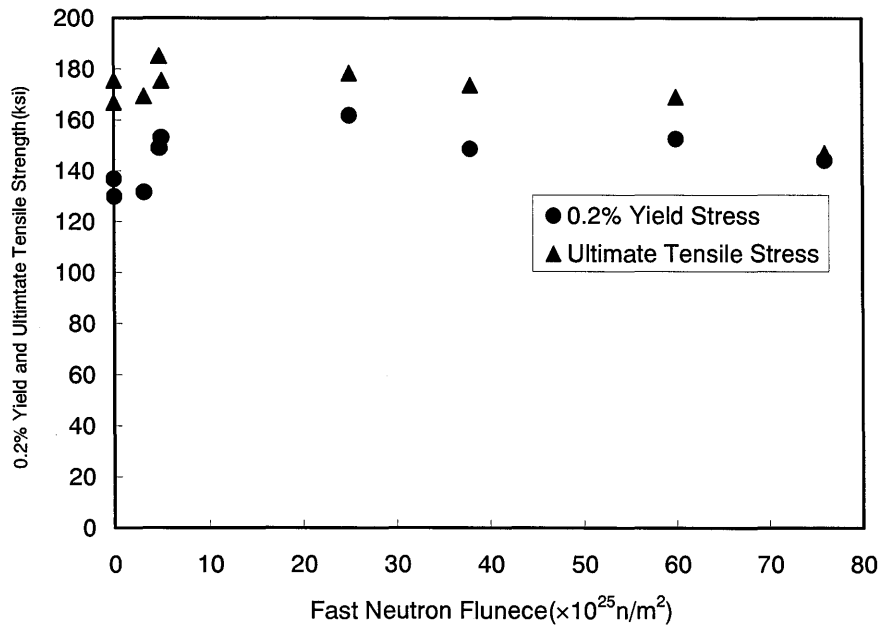


Figure B.3.3.3-2 Neutron Fluence Dependency of Tensile Strength in Inconel-718

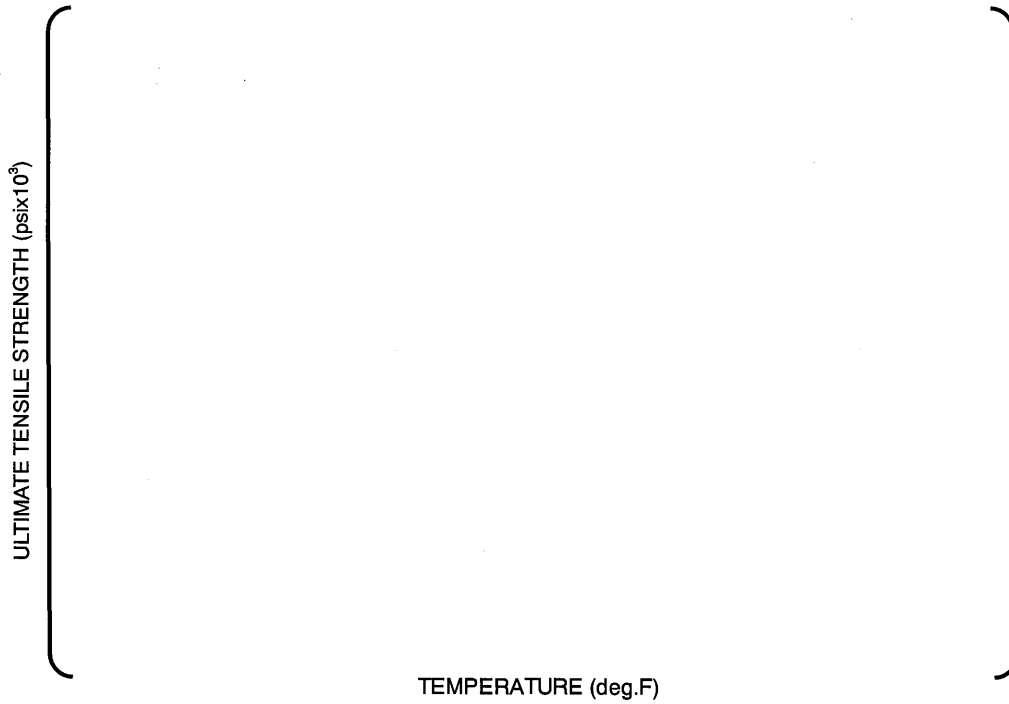


Figure B.3.3.3-3 Ultimate Tensile Strength Design Curve for Unirradiated Inconel-718

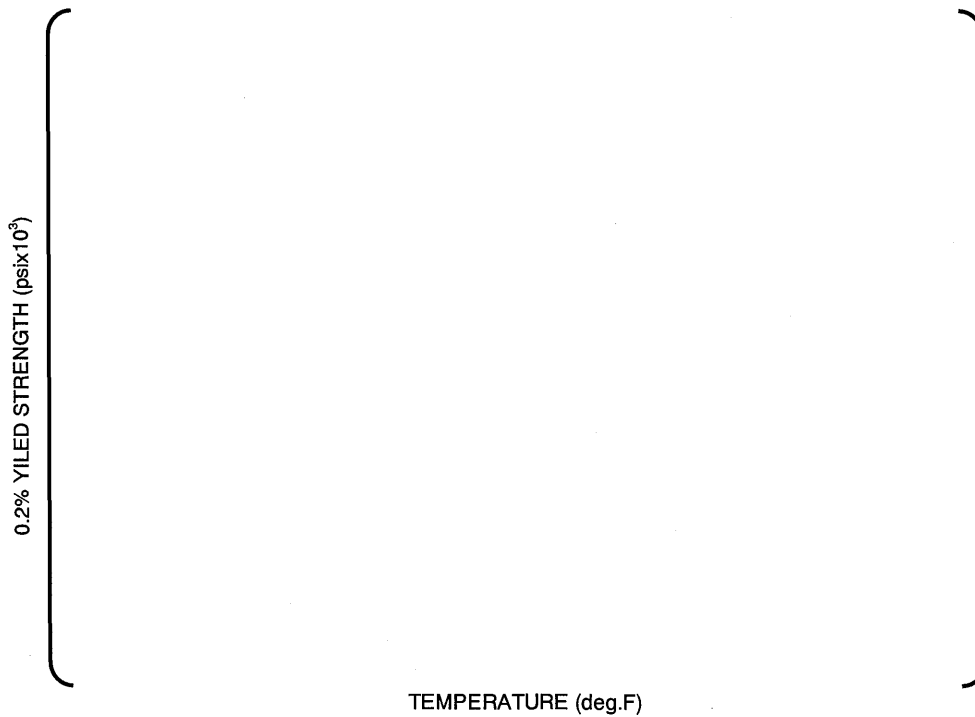


Figure B.3.3.4-1 0.2% Yield Strength for Unirradiated Inconel-718

B.4.0 SILVER-INDIUM-CADMIUM (Ag-In-Cd) ALLOY

The silver-indium-cadmium (Ag-In-Cd) alloy is used as a neutron absorbing material in control rods for light-water reactor. The composition of the Ag-In-Cd alloy used in Mitsubishi PWRs is 80 wt% Ag, 15 wt% In and 5 wt% Cd.

B.4.1 Physical/Thermal Properties

B.4.1.1 Density

Density measurements performed at the Bettis Laboratory ^(B.4-1,2,3) are reported to be 0.3674 lb/in³ (10.17 g/cm³) at 77 deg.F (25deg.C) for a nominal 80% Ag, 15% In, 5% Cd alloy. This density is used for weight calculation of the control rod.

B.4.1.2 Melting Point

Melting point measurements performed at the Bettis Laboratory ^(B.4-1,2,3) are reported to be 1472 ± 18 deg.F (800 ± 10 deg.C) for nominal 80% Ag, 15% In, 5% Cd alloy. Conservative value of 1454 deg.F (790 deg.C) is used in design.

B.4.1.3 Thermal Expansion

Thermal expansion measurements performed at the Bettis Laboratory ^(B.4-1,2,3) are reported to be 12.5 x 10⁻⁶ in/in/deg.F (22.5 x 10⁻⁶ in/in/deg.C) from 77 to 932 deg.F (25 to 500 deg.C) for a nominal 80% Ag, 15% In, 5% Cd alloy. These values are used in design.

B.4.1.4 Thermal Conductivity

Thermal conductivity in the range of temperature, 120 to 1112 deg.F (50 to 600 deg.C) are reported by the Battelle Memorial Institute ^(B.4-1,2,3) for a nominal 80% Ag, 15% In, 5% Cd Alloy. Results, which are used in design, are shown in Table B.4.1.4-1.

B.4.2 Chemical Properties

B.4.2.1 Chemical Composition

The Mitsubishi materials specifications specify the chemical composition as listed below for Ag-In-Cd alloy.

| Element | Composition by weight (%) |
|------------------|---------------------------|
| Ag | 79.5 - 80.5 |
| In | 14.75 - 15.25 |
| Cd | 4.75 - 5.25 |
| Bi | 0.030 or less |
| Pb | 0.030 or less |
| Total impurities | 0.250 or less |

B.4.2.2 Chemical Compatibility

Corrosion test result of the Ag-In-Cd alloy in still water at 600 deg.F (316 deg.C) is shown in Figure B.4.2.2-1^(B.4-1, 2). The figure shows that the corrosion rate for the Ag - 13.6 wt% In - 4.9 wt% Cd alloy is about 0.9 mg/dm²/day. Figure B.4.2.2-2 shows the corrosion characteristics of Ag - 12.1 wt% In - 9.4 wt% Cd - 2.0 wt% Sn (to simulate the composition resulting from elemental transformation by irradiation) alloy in simulated PWR primary coolant (water at 600 deg. F moving at 10 ft/sec, hydrogen added, pH: 9.5-10.5 with LiOH)^(B.4-2). There is little change in the alloy weight, even after 200 days, which shows good corrosion resistance.

There is a large change in weight when the dissolved oxygen concentration is high, several parts per million (note that dissolved oxygen in the PWR primary coolant is controlled to several parts per billion or less by adding hydrogen). The presence of dissolved oxygen in the primary coolant has a large effect of the corrosion resistance of Ag-In-Cd alloy^(B.4-1, 3). Since the Ag-In-Cd alloy is contained in SUS 304 cladding, there will be no contact with the primary coolant as far as the cladding is not failed.

With respect to the compatibility of the Ag-In-Cd alloy and the SUS 304 cladding, though no published data has been found, no problems with chemical compatibility at normal operating temperatures have been revealed from studies of two-element equilibrium state diagrams for Fe and Ni, the main constituents of SUS 304, and Ag-In-Cd-Sn^(B.4-4). In addition, Mitsubishi PWR operational experience has shown no issue with the compatibility of the Ag-In-Cd alloy and the SUS 304 cladding.

B.4.3 Mechanical Properties

B.4.3.1 Young's Modulus

Although Young's modulus is not used in the design of the control rod at present, the Young's modulus for the 80 wt% Ag - 15 wt% In - 5 wt% Cd alloy reported by C.R. Tipton, et. al.,^(B.4-5) are given in Table B.4.3.1-1.

B.4.3.2 Tensile Characteristics

Although tensile characteristics such as yield strength and ultimate tensile strength are not used in the design of the control rod, the tensile characteristics for the 80 wt% Ag - 15 wt% In - 5 wt% Cd alloy obtained by the Bettis Atomic Power Laboratory are presented in Table B.4.3.2-1^(B.4-1, 2). The post-irradiation mechanical characteristics for Ag - 15 wt% In - 4.8 wt% Cd alloy are shown in Table B.4.3.2-2^(B.4-4). The 0.2% yield strength and ultimate tensile strength of the irradiated material increase relative to the unirradiated material, and the total elongation decreased.

B.4.3.3 Radiation Swelling

The swelling behavior of the Ag-In-Cd alloy due to irradiation is considered to be caused by element transformation and second-phase separation. Figure B.4.3.3-1 shows the dimensional change (swelling) behavior of the Ag-In-Cd alloy due to irradiation. The swelling estimated from the data in Figure B.4.3.3-1 is about 0.5 Vol.% / 10²¹ n/cm² (E>0.6 eV)^(B.4-4).

B.4.4 References

- (B.4-1) P.J.Kuchirca, "Properties of Fuel and Core component Materials", WCAP-9179, revision 1 and WCAP-9224 (Non proprietary)
- (B.4-2) I. Cohen, "Development and Properties of Silver-Base Alloys as Control Rod Materials for Pressurized Water Reactors", US-AEC Report WAPD-214 (1959)
- (B.4-3) W.K. Anderson and J.S. Theilacker, "Neutron Absorber Materials for Reactor Control". US-AEC (1962)
- (B.4-4) A. Strasser and W. Yario, "Control Rod Materials and Burnable Poisons", EPRI-NP-1974 (1981)
- (B.4-5) C.R. Tipton et al., "Reactor Handbook", 2nd Edition, Vol. 1. Materials, US-AEC (1960)

Table B.4.1.4-1 Thermal Conductivity of 80 wt% Ag - 15 wt% In - 5 wt % Cd Alloy

| Temperature | | Thermal Conductivity | |
|-------------|----------|---------------------------|-------------------|
| (deg. F) | (deg. C) | (Btu/hr-ft ²) | (Watts/cm-deg. C) |
| 32 | 0* | 31.7 | 0.548 |
| 77 | 25* | 32.7 | 0.546 |
| 120 | 50 | 34.1 | 0.589 |
| 212 | 100 | 36.3 | 0.626 |
| 392 | 200 | 40.7 | 0.701 |
| 572 | 300 | 44.3 | 0.764 |
| 752 | 400 | 47.4 | 0.818 |
| 932 | 500 | 50.1 | 0.864 |
| 1112 | 600 | 52.3 | 0.902 |

Table B.4.3.1-1 Young's Modulus of 80 wt% Ag - 15 wt% In - 5 wt% Cd Alloy

| Temperature | | Young's modulus |
|-------------|----------|-----------------|
| (deg. C) | (deg. F) | (psi) |
| 25* | 77 | 11.52 |
| 100 | 212 | 11.13 |
| 200 | 392 | 10.62 |
| 300 | 572 | 9.86 |
| 316 | 1112 | 9.68 |

Table B.4.3.2-1 Tensile Characteristics of Un-irradiated Ag - In - Cd Alloy

| Alloy No. | Composition (w/o) | | | | Test Temp (°F) | 0.2% YS (psi) | UTS (psi) | Red. Of Area (%) | Elong in 2 in. (%) |
|-----------|-------------------|------|-----|----|----------------|---------------|-----------|------------------|--------------------|
| | Ag | In | Cd | Sn | | | | | |
| 2533 | 81.6 | 13.6 | 4.9 | - | 70 | 10,500 | 42,800 | 62 | 67 |
| | | | | | 600 | 9,600 | 17,600 | 50 | 54 |
| 2727 | 80.7 | 14.3 | 5.1 | - | 70 | 8,200 | 38,000 | 60 | 67 |
| | | | | | 600 | 7,800 | 25,500 | 57 | 54 |

Table B.4.3.2-2 Post-irradiation Mechanical Characteristics of Ag -15 wt% In - 4.8 wt% Cd Alloy

| Sample History | Irradiation Conditions | | Tensile Test Conditions and Data | | | | Creep Rupture Test | | | DPH Hardness |
|----------------|------------------------|--|----------------------------------|--------------------|-----------------------|--------------|--------------------|-----------------------|--------------|--------------------|
| | Temp. °C | Neutron Exposure Thermal nvt x10 ²¹ | Temp. °C | Yield Strength ksi | Ultimate Strength ksi | Elongation % | Temp. °C | Time to Failure Hours | Elongation % | |
| Control | — | — | 20 | 20 | 49.1 | 50 | 315 | 97.4 | 31 | |
| " | — | — | — | — | — | — | 315 | 97.3 | 15 | |
| Irradiated | 260 | 2.0 | 600 | 15.5 | 15.5 | 24 | 315 | 29 | 16 | |
| " | 260 | 2.0 | — | — | — | — | 315 | 37 | 24 | |
| " | 260 | 2.0 | — | — | — | — | 315 | 40 | 15 | |
| Control | — | — | 20 | 8.2 | 37.2 | 50 | | | | 87 |
| " | — | — | 20 | 8.2 | 39.4 | 52 | | | | 87 |
| " | — | — | 20 | 8.7 | 38.7 | 50 | | | | 56 |
| Irradiated | 200 | 1.4 | 20 | 13.6 | 41.4 | 44 | | | | 72 |
| " | 200 | 1.0 | 20 | 21.4 | 41.6 | 44 | | | | 94 |
| " | 200 | 0.3 | 20 | 27.9 | 4.4 | 44 | | | | 109 ^(a) |

(a) After 44 days anneal at 340°C hardness decreased to 53.

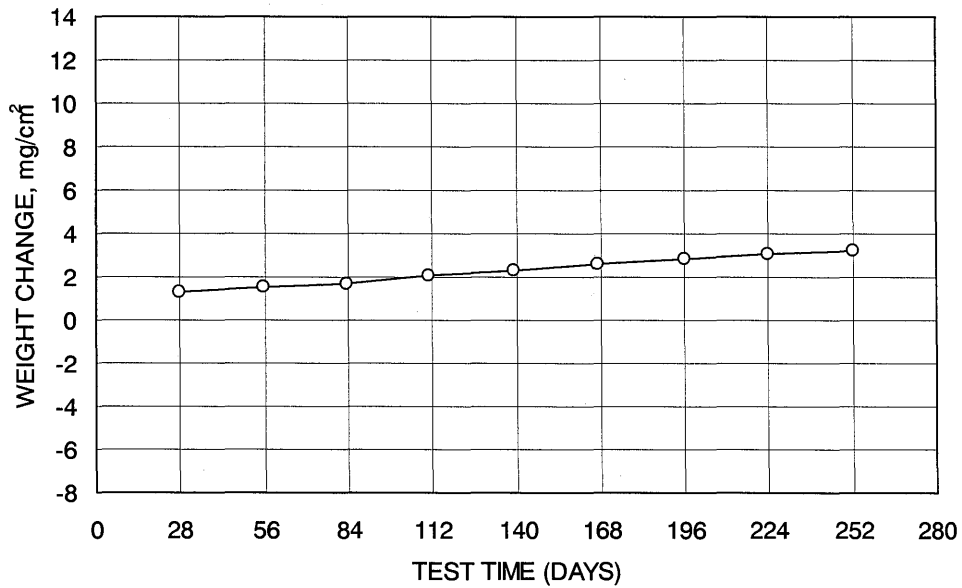


Figure B.4.2.2-1 Corrosion Test Result for Ag - In - Cd Alloy (600 deg.F in Still Water)

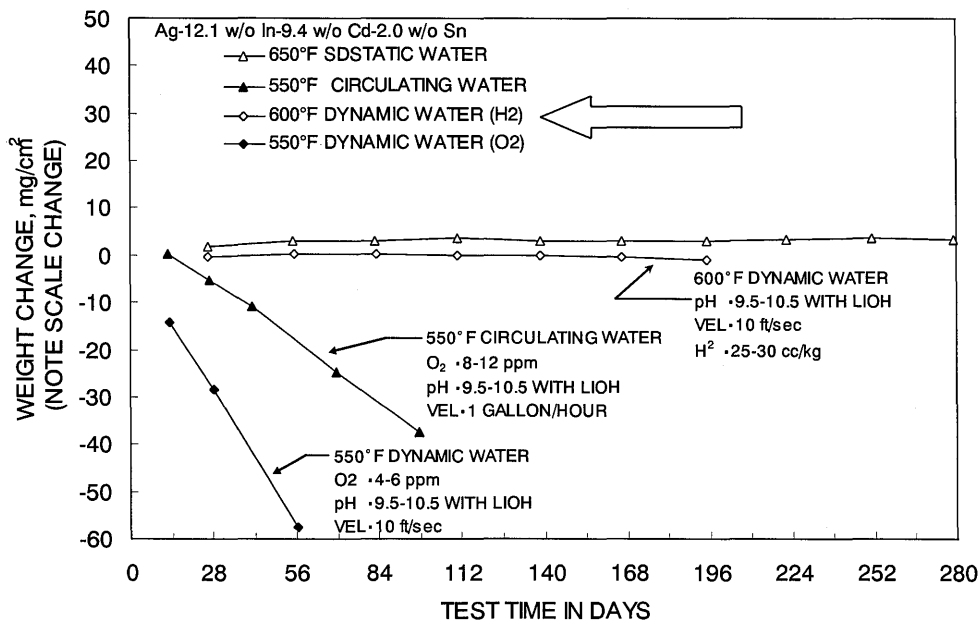


Figure B.4.2.2-2 Corrosion Test Results for Ag - In -Cd Alloy (600 deg.F, Simulated Primary Coolant Water Quality)

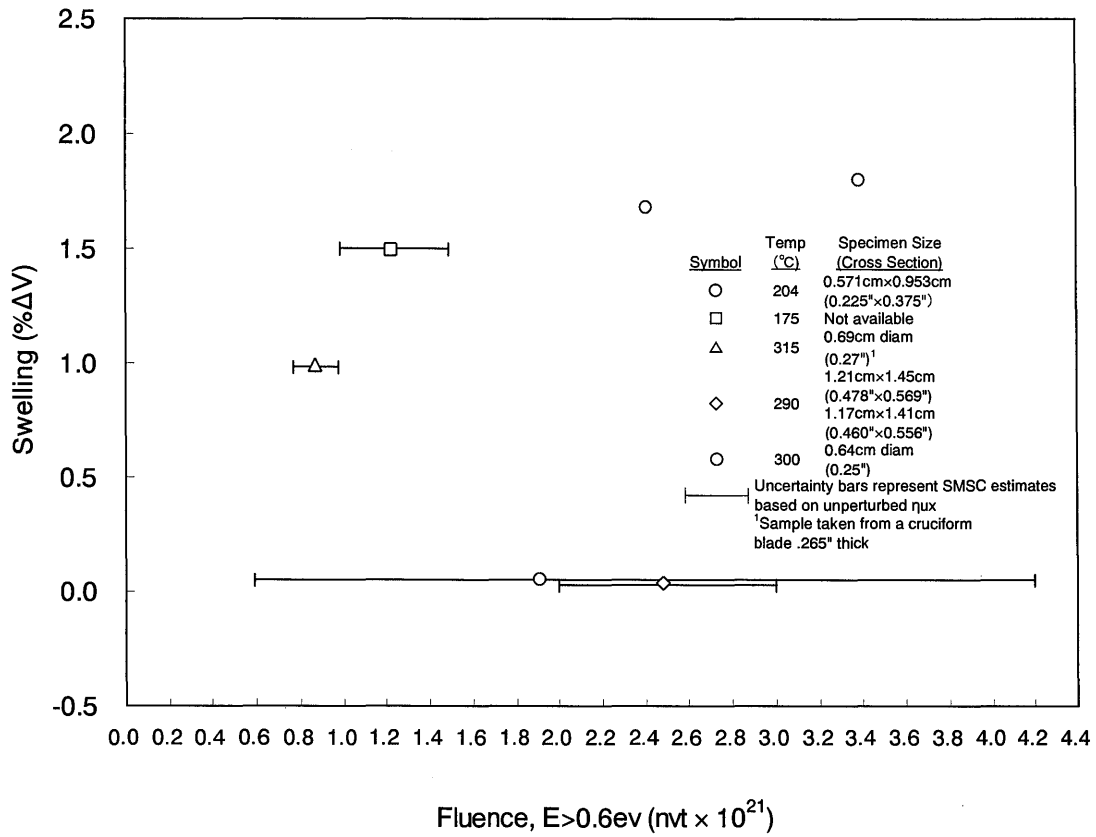


Figure B.4.3.3-1 Radiation Swelling Characteristics of Ag - In - Cd Alloy (Irradiation Temperature: 347 - 599 deg.F)

B.5.0 BOROSILICATE GLASS

The borosilicate glass, code 7740 is used as a neutron absorbing material in burnable absorber rods for light-water reactor.

B.5.1 Physical/Thermal Properties

B.5.1.1 Density

The density range of borosilicate glass at room temperature is given as 0.0802 to 0.0914 lb/in³ (2.22 to 2.53 g/cm³) with a most probable value of 0.0910 lb/in³ (2.52 g/cm³). For design purposes, density of borosilicate glass of 0.0806 lb/in³ at room temperature is used.

B.5.1.2 Softening Point

The borosilicate glass, code 7740, is [] deg.F ([] deg.C). For design purposes, the softening point of borosilicate glass is taken as [] deg.F ([] deg.C).

B.5.1.3 Thermal Expansion

The thermal expansion of borosilicate glass, code 7740 is [] in/in/deg.F ([] in/in/deg.C) from room temperature to 572 deg.F (300 deg.C).

B.5.1.4 Thermal Conductivity

References (B.5-1 and 2) show temperature dependence of thermal conductivity from 170 deg.F (350 K) to 936 deg.F (775 K) for borosilicate glass, code 7740. The dependence is expressed by the following equation:

$$C = 2.4 \times 10^{-6} T + 2.15 \times 10^{-3}$$

where

C: thermal conductivity (cal/sec-cm-K)

T: temperature (K)

This equation for the thermal conductivity of borosilicate glass is used in design.

B.5.2 Chemical Properties

B.5.2.1 Chemical Composition

The nominal composition of borosilicate glass, code 7740 ^(B.5-3) is:

| | |
|--------------------------------|----------|
| SiO ₂ | 80.9 w/o |
| Na ₂ O | 4.0 w/o |
| K ₂ O | 0.04 w/o |
| Al ₂ O ₃ | 2.3 w/o |
| B ₂ O ₃ | 12.7 w/o |
| Fe ₂ O ₃ | 0.03 w/o |

The B_2O_3 concentration range from [] to [] wt% and a natural boron oxide with a ^{10}B concentration of [] wt% is used. Impurity elements are as follows.

| |
|--|
| |
|--|

B.5.3 Chemical Compatibility

Under tensile loading in contact with water or steam for long time, stress corrosion cracking may reduce the strength of the material by a factor of 2 or more^(B.5-4).

Contact with water and liquids other than water (water-insoluble organic solvents, etc.) results in little effect including deterioration in strength.

Borosilicate glass has not reacted with the type 304 stainless steel.

B.5.4 Mechanical Properties

B.5.4.1 Young's Modulus

Although Young's modulus of borosilicate glass is not directly used in design, it is less than [] ksi ([] GPa) .

B.5.5 Irradiation Behavior

B.5.5.1 Radiation Swelling

Because glass has an irregular structure that results from the super-cooling of a molten material, it is generally less susceptible to damage from neutron radiation than are crystalline materials, and neutron radiation produces little change in its mechanical and thermal properties. Nevertheless, borosilicate glass is subject to swelling from the generation of He and Li by the $^{10}B(n, \alpha)^7Li$ reaction. The radiation swelling occurs mainly near the surface. Warping in the low-temperature region creates cracks, which in turn reduce the mechanical strength and thermal conductivity. Therefore, this material must be used in the cladding of metal or other such material when used in the reactor^(B.5-1,5).

B.5.5.2 Gas Release

The burnable absorber makes use of the neutron absorption of the ^{10}B in the borosilicate glass. The absorption is accompanied with helium generation. The release of the helium gas increases the internal pressure of the burnable absorber rod.

Internal pressure increase is calculated as follows.

(1) Mol number of ^{10}B in borosilicate glass per burnable absorber rod is calculated by following values.

- Density and volume of borosilicate glass
 - Weight percent of B_2O_3 in borosilicate glass, boron in B_2O_3 and ^{10}B in its isotopes
- (2) All of the calculated ^{10}B above is supposed to be supplied in (n,α) reaction, which releases same mol number of helium gas.
- (3) The mol number of the released helium gas is converted into Increase of internal pressure by ideal gas equation.

B.5.6 References

- (B.5-1) P.J.Kuchirca, "Properties of Fuel and Core component Materials", WCAP-9179, revision 1 and WCAP-9224 (Non proprietary)
- (B.5-2) "Handbook of Thermophysical Properties of Solid Materials", Vol. 3, 1961, Goldsmith, et al
- (B.5-3) Iwaki Glass Company Limited, "Speciality Glass for lightning and Industrial Applications", September, 1992
- (B.5-4) Yamane et al., "Glass Engineering Handbook", Asakura Publishing, July 1999
- (B.5-5) Materials Engineering/Materials Selector 73, Mid-September 1972, Vol.76, No. 4

B.6.0 ANTIMONY-BERYLLIUM

Antimony-Beryllium (Sb-Be) is used as secondary neutron radiation source. Currently, the Sb-Be used by Mitsubishi is in the form of sintered pellets obtained from mixture of Sb and Be powders.

B.6.1 Physical/Thermal Properties

B.6.1.1 Density

Since the Sb-Be pellets are a 50 percent volume mixture of Sb and Be powders, the 100 percent theoretical density is [] lb/in³ ([] g/cm³) based on densities of 0.241 lb/in³ (6.68 g/cm³) and 0.0668 lb/in³ (1.85 g/cm³) respectively for Sb and Be^(B.6-1, 2).

In materials specification, Mitsubishi requires a minimum density of [] lb/in³ ([] g/cm³) at room temperature. For design purpose such as weight calculation, 0.126 lb/in³ is used.

B.6.1.2 Melting Point

The melting point of the Sb-Be pellet is expected to be 1167 deg.F (630.5 deg.C)^(B.6-1, 2).

For design purposes, minimum melting point of [] deg.F ([] deg.C) is conservatively used for Sb-Be pellets.

B.6.1.3 Thermal Expansion

Temperature dependence of thermal expansion for the Sb-Be is shown in Figure B.6.1.3-1 up to 850 deg.F (454 deg.C) and are represented by the following equation which is used in design^(B.6-2):

$$C = []$$

where

C: mean coefficient of thermal expansion (10⁶ in/in/deg. F)

T: temperature (deg. F)

B.6.1.4 Thermal Conductivity

Thermal conductivity values^(B.6-2) from 150 deg.F to approximately 1000 deg. F is given by:

$$C = []$$

where

C: thermal conductivity (Btu-in/ft²-hr-deg.F)

T: temperature (deg.F)

B.6.2 Chemical Properties

B.6.2.1 Chemical Composition

The chemical composition of the Sb-Be pellet used as burnable absorber material is specified as follows:

| Element | Composition (wt %) |
|---------|--------------------|
| | |

B.6.2.2 Chemical Compatibility

Although there is no published data on the chemical compatibility of the Sb-Be pellets and the SUS 304, Van Engen, et al., have reported that no problems were seen in studies of binary state diagrams of Sb and Be and the main constituent elements of stainless steel at temperatures of 932 deg.F (500 deg.C) or less^(B.6-3).

B.6.3 Mechanical Properties

B.6.3.1 Compressive Strength

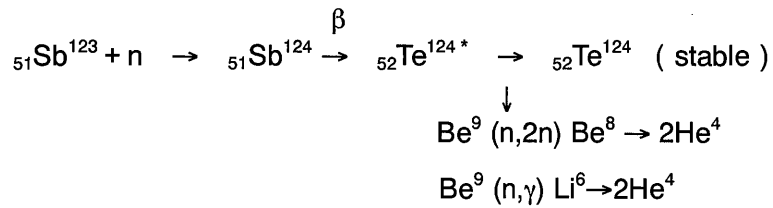
Compressive strength of Sb-Be pellet is reported as follows^(B.6-2). The strength is increased with the increase of density.

| <u>Density (%T.D.)</u> | <u>Compressive strength (psi)</u> |
|------------------------|-----------------------------------|
| | |

B.6.4 Irradiation Behavior

B.6.4.1 Gas Release

Sb-Be becomes radio-active by nuclear reaction shown below and release helium gas which brings internal pressure increase of the secondary neutron source rod.



Based on weight of beryllium in the secondary neutron source rod, the volume of the released helium is determined.

Volume of the helium released from beryllium of 0.0022 lb (1g) is calculated by using following values:

- The emission rate of helium from a gram of beryllium under design-based core power condition
- Power density for objective core design
- Mechanical lifetime for the secondary neutron source rod
- Capacity factor of the core

B.6.5 References

- (B.6-1) David R. Lide, Editor, "Handbook of Chemistry and Physics", 80th edition. the Chemical Rubber Co., 1999-2000
- (B.6-2) P.J.Kuchirca, "Properties of Fuel and Core component Materials WCAP-9179", revision 1 and WCAP-9224 (Non proprietary)
- (B.6-3) Van Engen W R, "Report on antimony-beryllium neutron sources examined after 7.45 effective full power years in the Dodewaard, Dimensional Stability and Mechanical Behavior of Irradiated Metals and Alloys Brighton", Vol. 2 (1983)

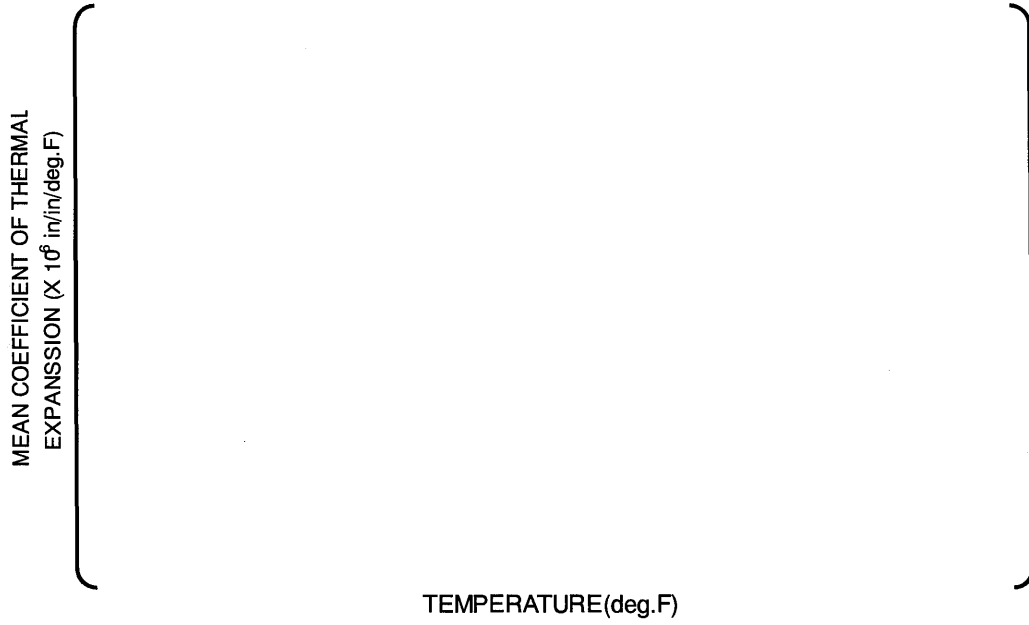


Figure B.6.1.3-1 Thermal Expansion of Sb-Be Pellets

Appendix C

**FUEL ROD FRETTING
EVALUATION METHODOLOGY**

February 2008

**© 2008 Mitsubishi Heavy Industries, Ltd.
All Rights Reserved**

Table of Contents

| | |
|--|------|
| List of Figures | C-3 |
| C.1.0 INTRODUCTION | C-4 |
| C.2.0 DESCRIPTION OF FRETTING WEAR CALCULATION | C-5 |
| C.2.1 Fuel Rod Model | C-5 |
| C.2.2 Vibration Amplitude Evaluation Model | C-9 |
| C.2.3 Wear Calculation Model | C-13 |
| C.2.4 Computational method for Fuel Rod Wear Evaluation During Irradiation | C-16 |
| C.3.0 FUNDAMENTAL TESTS AND ANALYSIS | C-18 |
| C.3.1 Frequency and Damping for Various Spring Forces | C-18 |
| C.3.2 Wear Constants Evaluation Test | C-21 |
| C.3.3 5x5 Bundle 500 Hours Hydraulic Test | C-24 |
| C.4.0 VERIFICATION | C-32 |
| C.4.1 Full-Scale Fuel Assembly Hydraulic Test | C-32 |
| C.5.0 SUMMARY AND CONCLUSIONS | C-36 |
| C.6.0 REFERENCES | C-37 |

List of Figures

| | | |
|----------------|---|------|
| Figure C.2.1-1 | Fuel Rod Model..... | C-7 |
| Figure C.2.1-2 | Sample Result of Modal Analysis (9-Grid Spacer Fuel Rod Vibration Mode)..... | C-8 |
| Figure C.2.3-1 | Schematic Wear Front | C-15 |
| Figure C.2.4-1 | Calculation Procedure for Fretting Wear | C-17 |
| Figure C.3.1-1 | Rod Vibration Test using a 6x6 3-span Rod Bundle | C-19 |
| Figure C.3.1-2 | Frequency Dependence on Cell Condition | C-20 |
| Figure C.3.1-3 | Damping Dependence on Cell Condition..... | C-20 |
| Figure C.3.2-1 | Wear Test Setup | C-22 |
| Figure C.3.2-2 | Wear Test Container Configuration | C-22 |
| Figure C.3.2-3 | Wear Sensitivity Dependence on the Grid Spacer Cell Condition..... | C-23 |
| Figure C.3.2-4 | Sliding Mode Wear Sensitivity - Dependence on Spring Force | C-23 |
| Figure C.3.3-1 | Test Bundle..... | C-26 |
| Figure C.3.3-2 | Hydraulic Test Loop | C-27 |
| Figure C.3.3-3 | Fuel Rod Typical Vibration Response | C-28 |
| Figure C.3.3-4 | Comparison of Measured and Calculated Peak Amplitude Frequency | C-29 |
| Figure C.3.3-5 | Comparison of Measured and Calculated Mean Amplitude | C-29 |
| Figure C.3.3-6 | Comparison of Measured and Calculated Wear Depths | C-30 |
| Figure C.3.3-7 | Comparison of the Measurements and Calculation for the Uneven Wear Depth Distribution in a Dimple Pair | C-31 |
| Figure C.4.1-1 | Span Amplitude Measured by Flow Test..... | C-34 |
| Figure C.4.1-2 | Comparison of Calculated Span Amplitude with Measurement | C-34 |
| Figure C.4.1-3 | Comparison of Calculated Wear Depth with Measurement | C-35 |

C.1.0 INTRODUCTION

Fretting wear is one of the most important concerns for fuel rod design. Since fretting wear is a complicated phenomenon depending on several mechanical and hydraulic mechanisms, it is usually evaluated by long-time hydraulic testing using prototype fuel assemblies. However, it is useful to develop analytical methods to evaluate fretting wear because such methods can be used to evaluate the effects of fuel assembly design changes. A well-tuned model that accounts for the contributions from the various mechanisms that affect vibration and wear has a valuable role in reducing the risk of fretting wear in the design of the fuel assembly structure.

Mitsubishi has developed a semi-empirical calculation method for evaluating fretting wear that consists of three main parts. The first is a modal analysis of the fuel rod, which includes the effects of spring force relaxation. The second is the calculation of the vibration amplitude of the rod in the span between grid spacers, which gives the slip displacements at the grid spacer supports. The third is a model for calculating the wear depth, taking into account the growth of the oxide layer on the cladding surface. These components of the Mitsubishi fretting model are used in succession to calculate the fretting wear through a fuel rod irradiation.

Rod vibration tests have been conducted, with the spring force level as a parameter, to verify the rod vibration model. The wear coefficient was measured in the configuration of the actual rod and grid spacer cell.

The Mitsubishi fretting wear model has been verified by a hydraulic test for 500 hours.

A description of the fretting wear model, fundamental tests to calibrate the model and the model verification results are also discussed in the following sections.

C.2.0 DESCRIPTION OF FRETTING WEAR CALCULATION

A computational calculation method for the fretting wear consists of three basic parts:

- the modal analysis of the fuel rod
- the flow-induced vibration analysis
- the wear depth calculation

These separate components are integrated for fretting wear evaluation of the fuel rod.

C.2.1 Fuel Rod Model

In the fuel assembly structure the fuel rods are held in a bundle by the grid spacers. Each fuel rod consists of a cladding tube, plugged at both ends, that contains the UO₂ fuel pellets and the plenum spring, and is supported by the springs and dimples at each grid spacer elevation. The fuel rod is modeled by the finite element method (FEM) technique, as shown in Figure C.2.1-1. The FEM model is generated using 2-dimensional beam elements that account for the moment of inertia of the cladding tube, including the contribution from the pellet stack and the weight of the fuel rod. Six linear-spring elements are used to model the rod support system at each grid spacer elevation: a set of one spring and two dimples for both the normal and the tangential direction.

It is important to carefully treat the effect of spring force relaxation due to irradiation in the evaluation of rod vibration characteristics, since the spring force relaxation significantly affects the frequency and amplitude of fuel rod vibration. In addition, the progress of the wear at the support positions is sensitive to the spring force relaxation. As described below, a semi-empirical equation developed by Reavis^(C-1) is used to calculate the rod vibration amplitude. The natural frequency of the fuel rod must be calculated to use the Reavis equation. The empirical treatment described below is used to simulate the change in the natural frequency due to the spring force relaxation.

- (a) For the as-built (BOL) cell condition, the normal and tangential stiffness for all spring/dimple supports are used. The normal stiffness of the spring or dimple can be measured by a fundamental test. On the other hand it is generally difficult to measure the tangential stiffness directly. The multiplicative factor to obtain the tangential stiffness from the normal stiffness is derived by the fuel rod modal analysis.
- (b) In the condition where the rod and the grid spacer springs and dimples are just in contact, after the spring force has fully relaxed, the tangential stiffness elements for both of the spring/dimple sets are eliminated from the model.
- (c) In the condition where there is a gap between the rod and the grid spacer springs and dimples, one of the normal-dimple stiffness is eliminated from the treatment simulating just contact condition. Hence only one dimple and the spring in the normal direction support the rod. This treatment is appropriate, from the following considerations of the situation of fuel rod in the flow field:

- In a grid spacer cell with a gap the fuel rod would lean against the dimple and/or spring due to the hydraulic force and misalignment of rod and grid spacer cell.
- Cross flow would be generated in the core by various mechanisms, such as the inlet flow distribution, uneven gap formation between adjacent fuel assemblies, mixing vanes, etc.
- The bowing or distortion of the fuel rod and/or assembly would cause this misalignment.
- In this situation of a grid spacer cell with a gap between the rod and the spring and dimples, there would be a high probability that the fuel rod vibration with the support of one dimple and the spring would occur.

(d) In conditions (a) and (b), a reduced effective stiffness is applied to the tangential spring/dimple elements to account for the spring force relaxation.

This treatment of the effects of spring relaxation makes it possible to express the various rod support conditions, including the grid spacer cell with the gap between the rod and the spring and dimples, using linear stiffness elements. Thus the modal analysis of the fuel rod can be used for all the different grid spacer support conditions.

Figure C.2.1-2 shows sample results from a modal analysis for a fuel rod supported by 9 grid spacers.

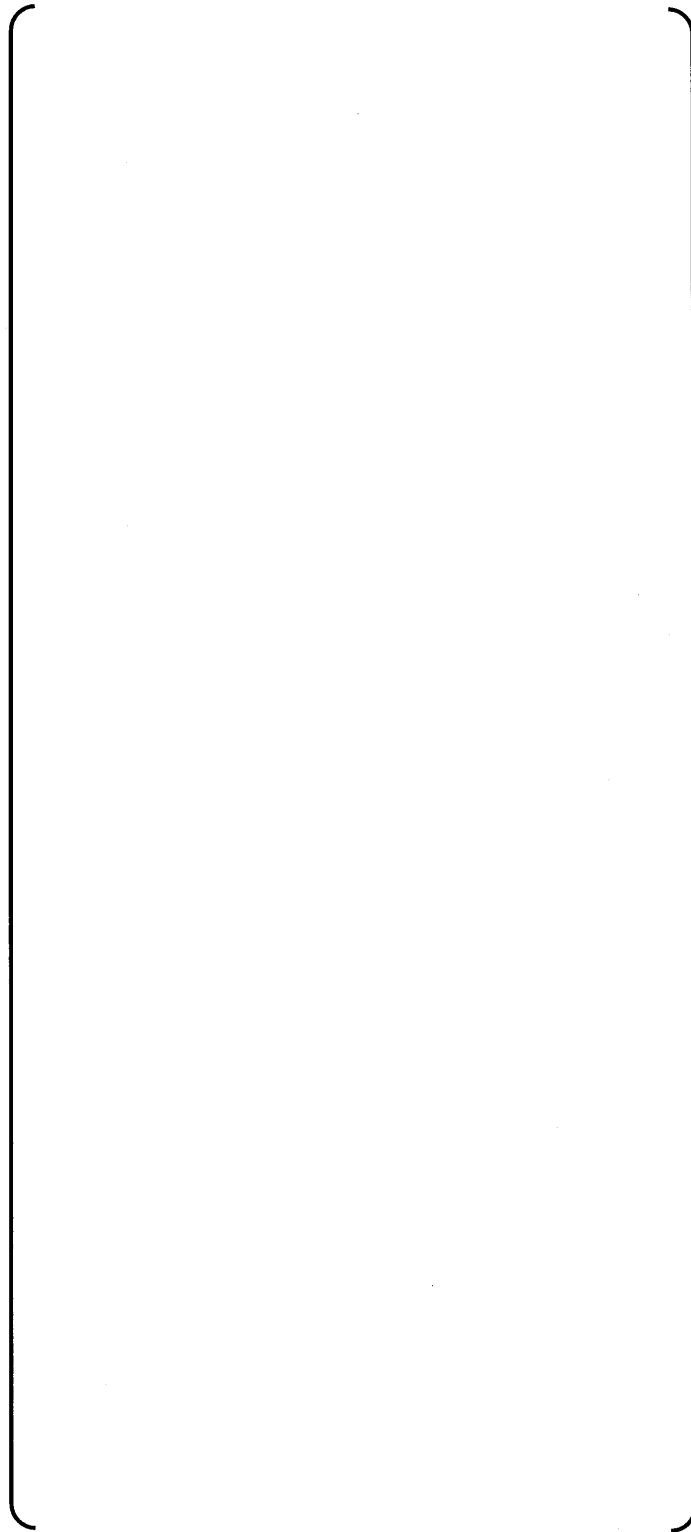
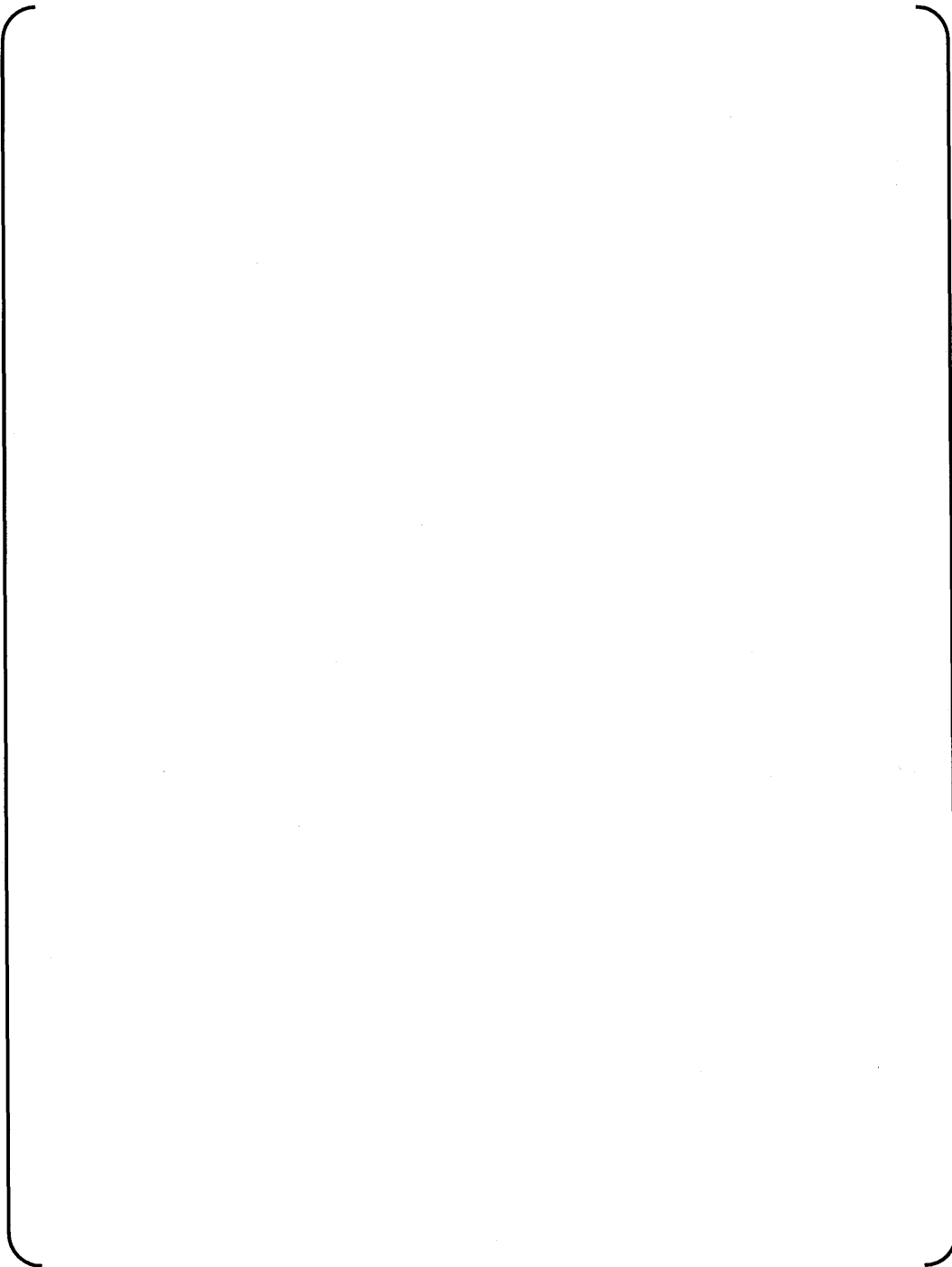


Figure C.2.1-1 Fuel Rod Model



**Figure C.2.1-2 Sample Result of Modal Analysis
(9-Grid Spacer Fuel Rod Vibration Mode)**

C.2.2 Vibration Amplitude Evaluation Model

Reavis^(C-1) gives the following semi-empirical equation to estimate the vibration amplitude of fuel rod span:

$$\delta_{rms} = C \eta_d \eta_D \eta_L \frac{dL}{W f_n^{1.5} \xi^{0.5}} U \rho \nu^{0.5} \quad (C.2.2-1)$$

where

| | |
|--------------------------|---|
| δ_{rms} | RMS amplitude |
| C | Adjusting coefficient |
| η_d, η_D, η_L | Scaling factors, $\eta_d = \text{func}\left(\frac{f_n d}{U}\right)$, $\eta_D = \text{func}\left(\frac{f_n D}{U}\right)$, $\eta_L = \text{func}\left(\frac{f_n L}{U}\right)$ |
| d | Rod diameter |
| D | Hydraulic diameter |
| L | Span Length |
| W | Span Weight |
| f_n | Frequency |
| ξ | Damping Ratio |
| U | Flow velocity |
| ρ | Density of water |
| ν | Kinetic viscosity of water |

Although this equation is well known, Mitsubishi has developed a modification to it in order to adequately evaluate the temperature dependence. The rationale for this modification is given by the following example:

Consider the following case:

| | |
|--------------------|------------|
| Rod diameter | : 9.5mm |
| Hydraulic diameter | : 11.8mm |
| Span length | : 500mm |
| Span weight | : 0.25 kgf |
| Frequency | : 65Hz |
| Damping factor | : 0.02 |
| Flow velocity | : 5m/s |

Using the room temperature values for density and viscosity, the root mean square (RMS) amplitude is calculated to be [] mil ([] μm). Taking the frequency and damping to be constant and using the 302 deg.F (150 deg.C) values for the water density and viscosity, the calculated RMS amplitude is [] mil ([] μm). Such strong temperature dependence, with a reduction of the amplitude at the higher temperature, is inconsistent with our experience. The most probable reason for this result is the assumption that the damping is constant. Although the fact that the frequency decreases at the higher temperature affects the calculated result, this effect is relatively small. Generally it is difficult to experimentally estimate the proper damping factor, especially for high temperature conditions.

The model for the temperature dependence of the vibration amplitude is based on the results obtained by Blevins^{(C-2),(C-3)} and Connors^(C-4). Blevins represented the RMS response of a fuel rod for fundamental mode as

$$\delta_{rms} = 0.036K(UD^2)^{1/2} \left(\frac{\rho D^2}{m}\right) \left(\frac{U}{f_n D}\right)^{1.5} \left(\frac{d}{D}\right)^{1.5} \left(\frac{D}{L}\right)^{0.5} \left(\frac{1}{\zeta}\right)^{0.5} \quad (\text{C.2.2-2})$$

K Constant

m Mass per unit length including added mass of fluid

Connors approximated the hydraulic damping as

$$\zeta = 0.052 \left(\frac{\rho D^2}{m}\right) \left(\frac{U}{f_n D}\right) \left(\frac{\nu}{DU}\right)^{0.22} \quad (\text{C.2.2-3})$$

D, m, f_n Diameter, weight per unit length and frequency of rod

ρ, ν, U Density, viscosity and velocity of water

Substituting equation C.2.2-3 into equation C.2.2-2 and neglecting mechanical damping yields

$$\delta_{rms} = 0.158K(UD^2)^{1/2} \left(\frac{\rho D^2}{m}\right) \left(\frac{U}{f_n D}\right) \left(\frac{d}{D}\right)^{1.5} \left(\frac{D}{L}\right)^{0.5} \left(\frac{\nu}{DU}\right)^{-0.11} \quad (\text{C.2.2-4})$$

Using equation C.2.2-4, the temperature correlation for the vibration amplitude becomes

$$\frac{\delta}{\delta_{ref}} = \left(\frac{\rho}{\rho_{ref}}\right)^{0.5} \left(\frac{\nu_{ref}}{\nu}\right)^{0.11} \left(\frac{f_{n,ref}}{f_n}\right) \quad (\text{C.2.2-5})$$

Using the room temperature values of the example problem as the reference values in equation C.2.2-5, the ratio of amplitude at 302 deg.F (150 deg.C) to the amplitude at room temperature becomes about [], which is consistent with our test experience.

On the other hand, substituting equation C.2.2-3 into the Reavis equation C.2.2-1 gives a temperature correlation for the vibration amplitude as

$$\frac{\delta}{\delta_{ref}} = \left(\frac{\rho}{\rho_{ref}}\right)^{0.5} \left(\frac{\nu_{ref}}{\nu}\right)^{-0.39} \left(\frac{f_{n,ref}}{f_n}\right) \quad (\text{C.2.2-6})$$

The difference in the viscosity dependence of equations C.2.2-5 and C.2.2-6 suggests that a modification of viscosity term in equation C.2.2-1 will improve the results for the temperature dependence of the rod vibration amplitude. The following procedure allows using equation C.2.2-1 to estimate the vibration amplitude at any temperature:

- Calculate the natural frequency of the rod considering hot material properties
- Use the room temperature viscosity in the last term of equation C.2.2-1

- Use vibration damping given by equation C.2.2-3 to account for the temperature dependence of the viscosity
- Adjust the coefficient C in equation C.2.2-1 to meet the results obtained by the flow induced vibration test at room temperature

This procedure gives the vibration amplitude for a single span.

Applied procedure to extend the procedure for the single span rod to the fuel rod with multi spans is:

- (1) Modal analysis of fuel rod (described in Section C.2.1)
 - (2) Span-amplitude estimation for each vibration mode using the above equations
 - (3) Maximum amplitude span and extension to all spans based on the results of the modal analysis
- SRSS (Square root of the sum of the squares) summation of amplitudes
 - Estimation of the amplitude at the grid spacer support position according to the mode shape
 - Estimation of slip displacement at the grid spacer support position considering the slip limit related to the spring force relaxation

Several options can be used for the SRSS summation of the amplitudes. The typical calculation process using the simplest option is:

$$w_m = \frac{\delta_{rms,m}}{MAX(\delta_{rms,m})} \quad (C.2.2-7)$$

$$x_m(y) = w_m \cdot \delta_{rms,m} \phi(y) \quad (C.2.2-8)$$

$$x(y) = \left(\sum x_m(y)^2 \right)^{1/2} \quad (C.2.2-9)$$

$$x(y) = C \cdot x(y) \quad (C.2.2-10)$$

Where

- m : m-th mode
- x : amplitude
- y : axial coordinate
- C: Coefficient
- ϕ : normalized mode shape

where the weight coefficients for the SRSS summation are determined from the magnitude of each modal amplitude, equation C.2.2-7, and the amplitude distribution for each mode along the length of fuel rod is calculated using these weights and summed, equations C.2.2-8 and C.2.2-9, with the resulting SRSS amplitude adjusted by the coefficient C, equation C.2.2-10. The coefficient C is experimentally determined.

The other options that can be used adjust the weight coefficients using equation C.2.2-7a or C.2.2-7b to emphasize the lower mode responses, which are the general feature of the observed behavior, are:

$$w_m = \frac{\delta_{rms,m} / f_m}{MAX(\delta_{rms,m} / f_m)} \quad (C.2.2-7a)$$

$$w_m = \frac{\delta_{rms,m} / f_m^2}{MAX(\delta_{rms,m} / f_m^2)} \quad (C.2.2-7b)$$

The vibration amplitudes at the grid spacer positions are obtained from the above procedure for the span amplitudes. Moreover, the slip displacements for the wear calculation is also needed, which are estimated using:

$$x_{m,g} = w_m \cdot \delta_{rms,m} \phi_g(y) \quad (C.2.2-11)$$

$$s_{m,g} = x_{m,g} - \frac{F\mu}{k_g} \quad (C.2.2-12)$$

$$l_g = (\sum (s_{m,g} f_m 4)^2)^{1/2} \quad (C.2.2-13)$$

$$L_g = s_g t \quad (C.2.2-14)$$

In the above equation, the subscript "g" indicates the grid spacer spring or dimple at the grid spacer support location. Here k_g is the spring or dimple stiffness and is used to obtain the amount that the slip amplitude exceeds the slip limit, equation C.2.2-12, where F is the spring force. For the dimple location $F/2$ is used instead of F . The slip displacement per unit time is evaluated by the alternative SRSS form given by equation C.2.2-13, and equation C.2.2-14 gives the total slip displacement through the time of operation t .

More exactly, equation C.2.2-11 is modified by a multiplying factor C_m :

$$x_{m,g} = C_m w_m \cdot \delta_{rms,m} \phi_g(y) \quad (C.2.2-11')$$

$$C_m \cong 1.2$$

Where

C_m : Amplitude conversion factor from RMS amplitude to averaged peak amplitude.

This factor converts the RMS amplitude to the averaged peak amplitude. From the definition of slip displacement by equation C.2.2-13, it is proper to use this type of the peak amplitude rather than the RMS amplitude. The value for C_m is calculated as follows.

Assuming Gaussian distribution in the rod vibration, the probability, $\varphi(a)$ in which the peak amplitude would be less than the value a is given by

$$\varphi(a) = 1 - \exp(-a^2 / (2\sigma^2)) \quad (C.2.2-15)$$

σ RMS amplitude

a Amplitude

Introducing the ratio of the amplitude to its RMS value, equation C.2.2-15 can be written as

$$\begin{aligned} \varphi(a) &= 1 - \exp(-x^2 / 2) \\ x &= |a| / \sigma \end{aligned} \quad (\text{C.2.2-16})$$

The averaged peak amplitude is obtained by substituting $\varphi(a) = 0.5$ into equation C.2.2-16, assuming that it appears with a 50% probability in a random process. The ratio of the averaged peak amplitude to the RMS amplitude is then given by

$$x = [2 \ln(2)]^{1/2} = 1.177$$

which gives the value for the C_m factor in equation C.2.2-11'.

C.2.3 Wear Calculation Model

The fretting wear volume calculation is based on the Archard equation^(C-5)

$$V = SFL \quad (\text{C.2.3-1})$$

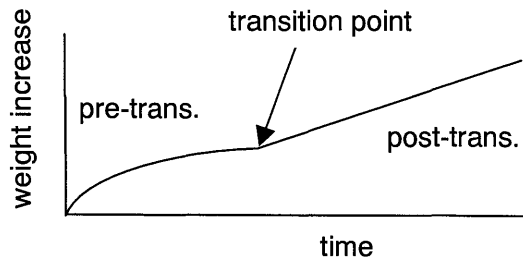
where S is the specific wear ratio, L is the value of the total slip displacement as given by equation C.2.2-14 and F is the spring force. $F/2$ is used instead of F when equation C.2.3-1 is applied at a dimple location. Although the Archard equation is very simple and comprehensive for the sliding wear mechanism, a modification of F is used to apply C.2.3-1 to the fuel rod wear process, in particular just after spring force relaxation. The modified force F^* given below is based on the Mitsubishi experience.

$$F^* = F + F_d \quad (\text{C.2.3-2})$$

$$F_d = k_g x_g \quad (\text{C.2.3-3})$$

In contrast to the static spring force F , F_d is the dynamic component calculated from the vibration amplitude, x_g at the grid spacer and the stiffness of the grid spacer spring or the dimple, k_g . In the actual situation the fuel rod would vibrate randomly, following an oval trajectory in the grid spacer cell, and its vibration would not result in pure sliding between the fuel rod and the spring or the dimple. The above modification to the spring force makes it possible to calculate the wear process sequentially from the regime of a high spring force to the stage just after the spring force has relaxed.

The oxide layer on the surface of cladding tube significantly affects the wear process. The specific wear coefficient S in equation C.2.3-1 is determined accounting for the growth of the oxide layer and the progression of the wear depth. The growth of the oxide layer is estimated using empirical models. Hilner^(C-6) has described the corrosion process for Zircaloy cladding in terms of pre- and post-transition phases:



Schematic corrosion model

$$\text{pre-transition: } \Delta W^3 = K_C \exp(-Q_C / RT) t \cdot C_w \quad (\text{C.2.3-4})$$

$$\text{post-transition: } \Delta W = \Delta W + K_L \exp(-Q_C / RT) (t - t_t) \cdot C_w \quad (\text{C.2.3-5})$$

$$\text{weight increment at transition point: } \Delta W_t = W_0 \exp(-A / RT) \quad (\text{C.2.3-6})$$

where K_C , K_L , Q_C , Q_L , A , W_0 and t_t are determined from out-of-pile tests by Hilner, and a multiplicative fitting factor C_w is used to apply these equations to the Mitsubishi irradiation data base. The oxide layer thickness is obtained from a standard conversion from the above equations for the weight gain by corrosion.

After obtaining the wear volume, the depth of the wear scar is calculated from the geometric shape of the cladding tube and the spring or the dimple as shown in Figure C.2.3-1. Simple geometric considerations provide the relation between the increment in the wear volume and wear depth:

$$\Delta V = \left[\sqrt{A h_0} + \sqrt{A (h_0 + \Delta h) \left(1 - \frac{\Delta h}{2A} \right)} \right] \Delta h B \quad (\text{C.2.3-7})$$

$$A = D - h_0$$

where

- V = Wear Volume
- ΔV = Increment of Wear Volume
- Δh = Increment of Wear Depth
- h_0 = Wear Depth
- D = Diameter of Cladding Tube
- B = Width of Contact Area

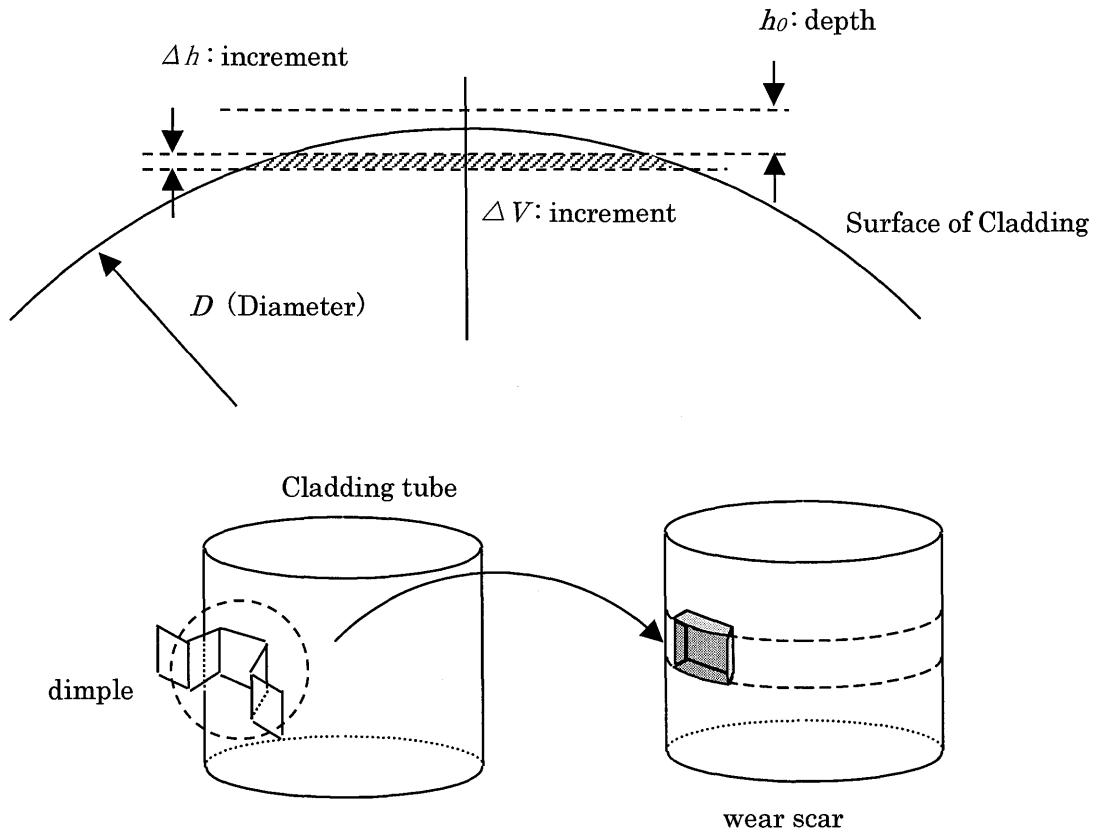


Figure C.2.3-1 Schematic Wear Front

C.2.4 Computational method for Fuel Rod Wear Evaluation During Irradiation

The computational method has been developed by Mitsubishi to evaluate the progress of the fretting wear as a fuel rod is irradiated. For this purpose, the calculation procedure has been designed to consider the changing behavior of the irradiation-related characteristics such as the spring force relaxation and the oxidization of cladding surface. The calculation flow is summarized in Figure C.2.4-1.

Initially the rod specification data and some fundamental data are read from the database file "proj.db". The fuel rod FEM model is generated in the computational method from these data.

There are three kinds of time loops in the calculation procedure. The first one, identified as "cycle" in Figure C.2.4-1, represents the irradiation cycle. In the beginning of the calculation for this loop, cycle-related information, such as the flow velocity for the prescribed fuel location in the core, are read from the "proj.in" file. The second loop is identified as "term" in Figure C.2.4-1. The time length of a "cycle" is divided into several time intervals to properly treat the change of some of the fuel rod and grid spacer cell mechanical characteristics, such as the relaxation of spring force by creep and the oxide layer growth on surface of cladding. The necessary modifications are added to the FEM model of the fuel rod at the start of each time increment in the "term" loop. The fuel rod modal analysis, the calculation of the vibration amplitude and the slip displacement, and the calculation of wear increment are performed in turn in each of the "term" time increments. The last time loop is the one for the wear calculation. A finer time increment is needed in this loop to properly calculate the evolution of the wear, taking into account the effects of the oxide layer and the geometric effect of the conversion of the wear volume to the wear depth.

Several options can be used for the calculation of the spring force relaxation. Since the neutron fluence at each spacer elevation is calculated, the spring force level at any time can be roughly estimated using a relation between the spring force and the fluence. When a more precise evaluation is required, the spring force relaxation process can be directly given in a time-dependent form. In this case, another evaluation tool provides the spring force relaxation data, taking into account the diameter change of the cladding due to creep-down, the pellet/clad interaction, etc.

The calculated results are output to two kinds of files. The results concerning the modal analysis and the vibration amplitudes are written to the output file "proj_00x.fout". The suffix "00x" means the output for x-th "term" loop. All the wear results for the rod's complete irradiation history are written to the "proj.out" file.

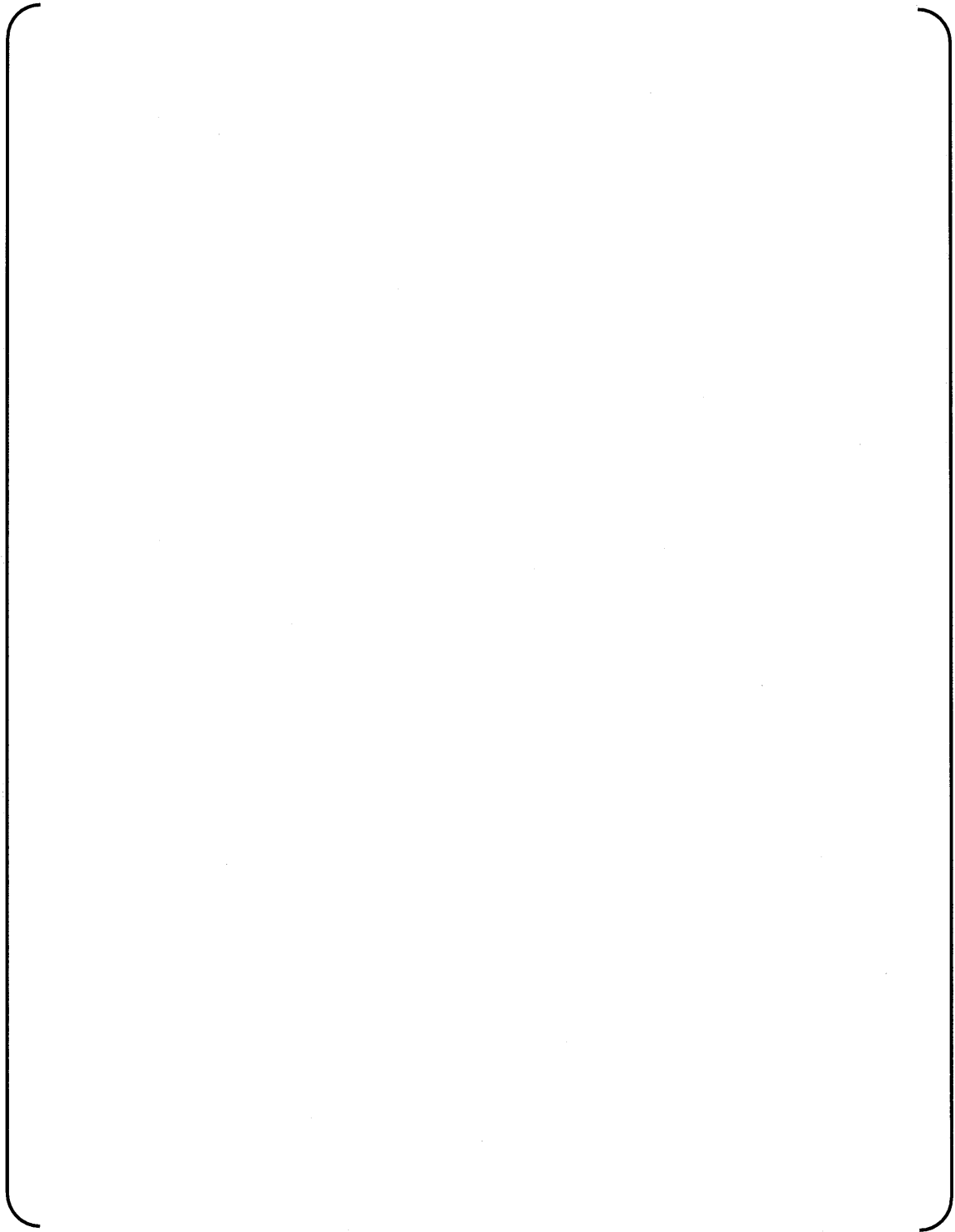


Figure C.2.4-1 Calculation Procedure for Fretting Wear

C.3.0 FUNDAMENTAL TESTS AND ANALYSIS

Several fundamental tests were conducted to calibrate the empirical models in the computational method and to confirm the validity of the modeling.

C.3.1 Frequency and Damping for Various Spring Forces

To confirm the method for modeling the spring force relaxation, a vibration test of a 3-span rod bundle was conducted as shown in Figure C.3.1-1. The vibration response at middle of the span was measured by the displacement detector for the four kinds of cell conditions: as-built, EOL (5% spring force level), just-contact (zero force) and existence of gap between the fuel rod and the grid spacer spring.

The frequencies calculated by the model (see section C.2.1) are compared with the measured data in Figure C.3.1-2. The frequency decreases as the spring force decreases. The calculation results are in good agreement with measurements.

The spring force level of the rod support also affects the magnitude of the damping. In these tests the damping characteristics were evaluated experimentally. The measured damping data are summarized in Figure C.3.1-3. This result represents the fact that the vibration damping is very low at a high spring force level (as-built), it rapidly increases with the relaxation of the spring force, and, after loss of spring force (just contacting condition) the damping decreases. This behavior suggests that the friction loss due to slippage between rod and the support causes the damping. This is responsible for the peak in the damping at the low spring forces just before the complete loss of spring force. This observation may also correspond to the high wear rate when there is high damping. Hence it is important to properly account for the vibration damping in the wear analysis. The damping described here is the "structural" damping. An empirical model for this structural damping, dependent on spring force level, is used in the computational calculation.

The sum of the mechanical and hydraulic components of the damping is used in the fretting wear calculation. The Connors expression given above (equation C.2.2-3) is used to calculate the hydraulic damping factor.

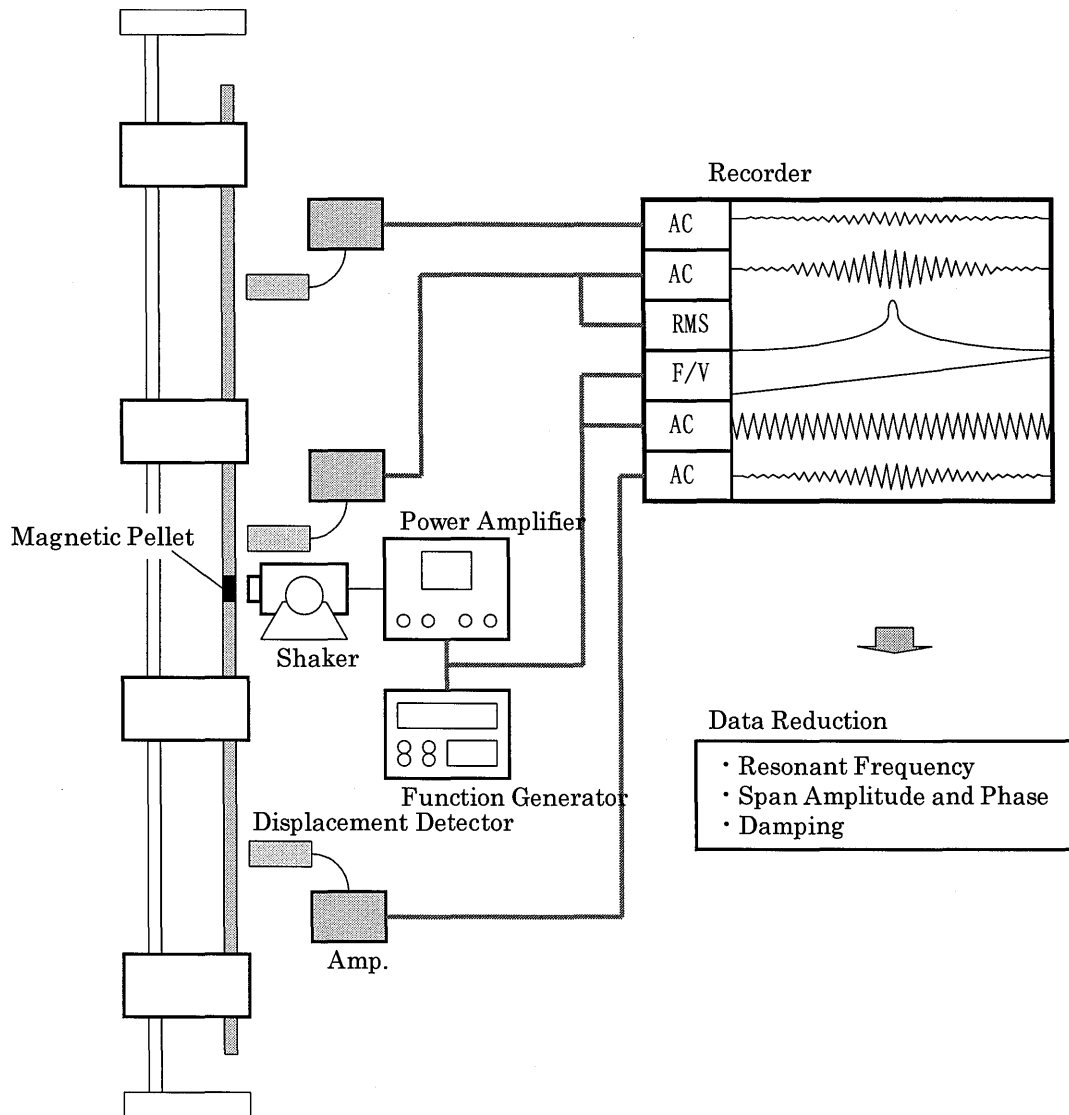


Figure C.3.1-1 Rod Vibration Test using a 6x6 3-span Rod Bundle

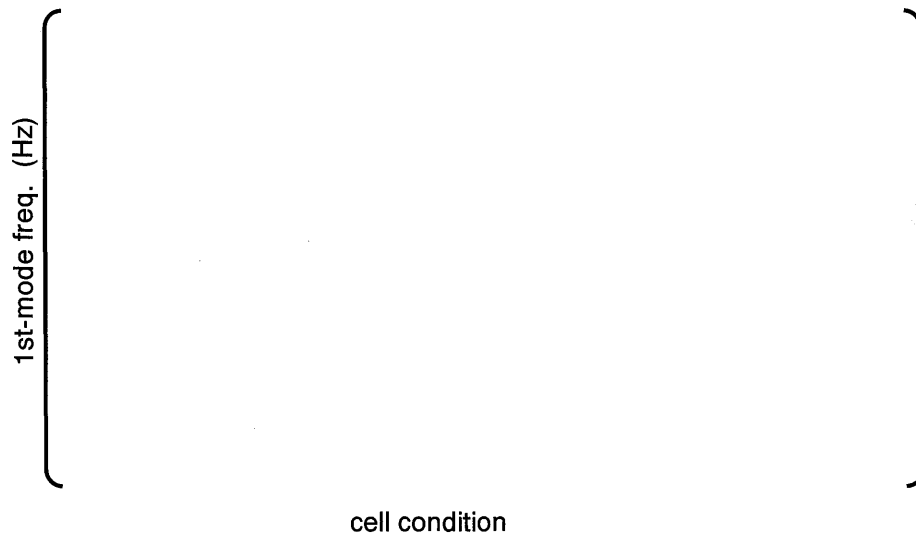


Figure C.3.1-2 Frequency Dependence on Cell Condition

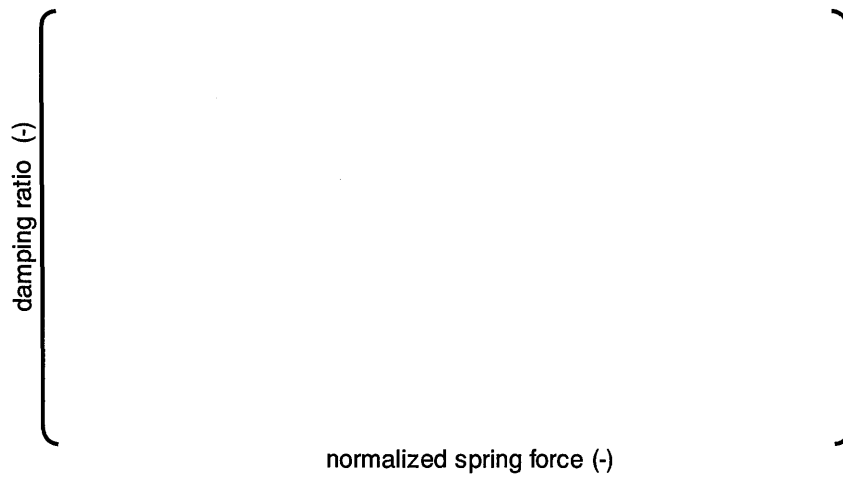


Figure C.3.1-3 Damping Dependence on Cell Condition

C.3.2 Wear Constants Evaluation Test

The wear coefficient is very sensitive to the system to be evaluated. Test equipment in a special configuration was developed to obtain the wear coefficient for the rod and grid spacer configuration. Figures C.3.2-1 and C.3.2-2 show the test equipment. The test piece consists of a short length of cladding tubing and the tube holder, which is mounted in the test container with support by the grid spacer springs and the dimples. The test can be conducted with different testing atmospheres inside the container, such as air or steam. The vibration of the test piece is amplified when shaking the container due to the inertia force exerted by the weights attached at both ends of test piece. The small amplitude vibration can be controlled with this test apparatus, enabling the wear tests to be conducted in the range of actual rod vibrations.

Figure C.3.2-3 shows the typical result of a series of tests in air at 590 deg.F (310 deg.C). This Figure shows the wear sensitivity normalized to the as-built (BOL) cell condition where the exciting force is kept constant. The wear sensitivity remains low as long as there is a high spring force, but it increases rapidly and peaks with the low spring force for the near EOL condition. The wear sensitivity decreases in the still lower spring force regimes, such as the just contacting condition. This result can be explained by the decrease in the friction work due to the loss of the spring force, even though the slippage increases. In the gapped cell the wear sensitivity increases again, because the wear mechanism shifts from a sliding mode to an impact mode.

The spring force dependence of the wear sensitivity in the sliding mode, shown in Figure C.3.2-4, is very similar to the structural damping characteristics shown in Figure C.3.1-3. The effective wear coefficient in the sliding mode has been obtained by data reduction using the vibration amplitude of test piece and the spring force.

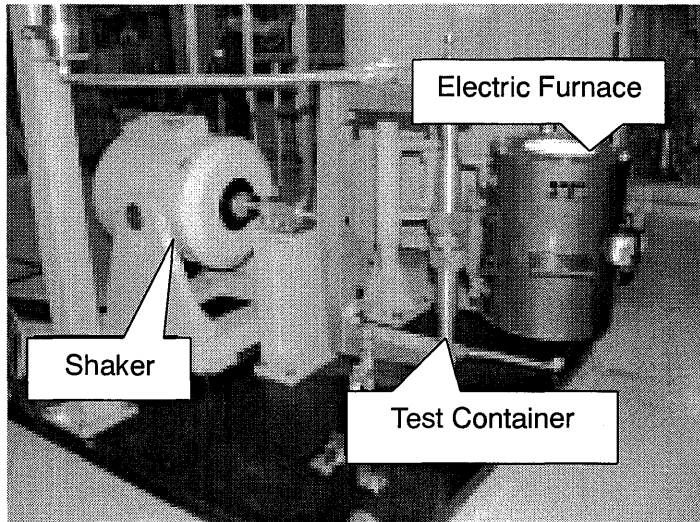


Figure C.3.2-1 Wear Test Setup

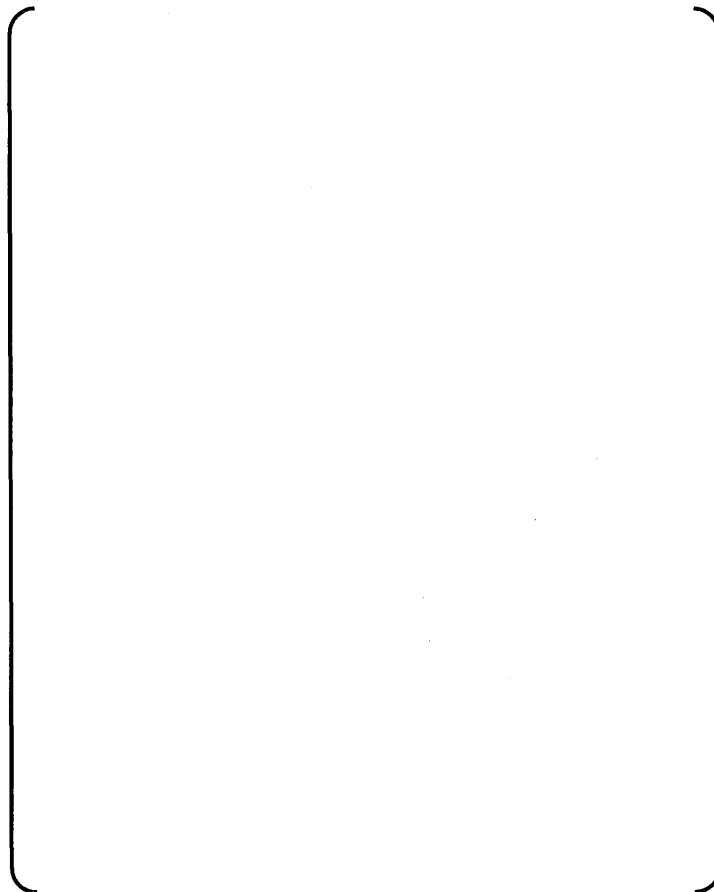


Figure C.3.2-2 Wear Test Container Configuration

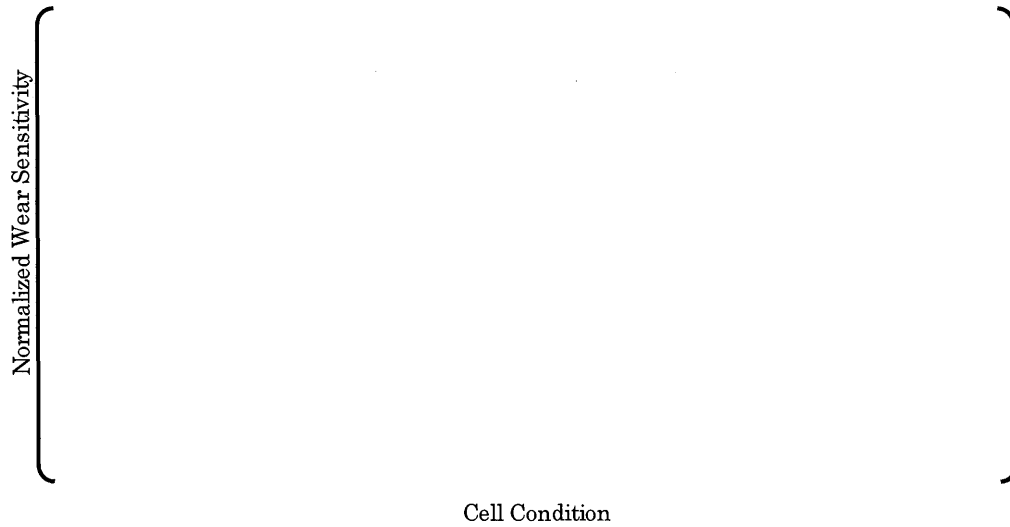
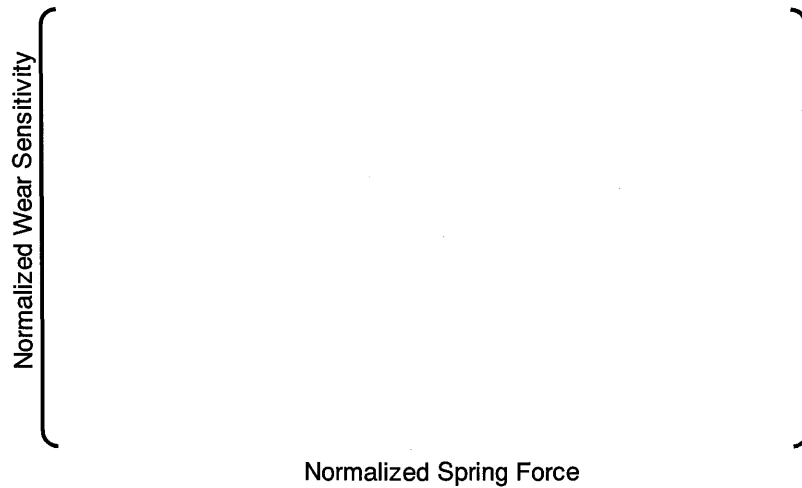


Figure C.3.2-3 Wear Sensitivity Dependence on the Grid Spacer Cell Condition



**Figure C.3.2-4 Sliding Mode Wear Sensitivity
- Dependence on Spring Force -**

C.3.3 5x5 Bundle 500 Hours Hydraulic Test

Hydraulic test for 500 hours at room temperature was conducted to verify the computational models for flow induced vibration and fretting wear progress. The vibration amplitude and frequency were measured during the test and the wear scars were measured after the flow test. A analysis was done for these test conditions and its results were compared with the measurements to verify the models.

Test Description

Two test bundles with 5x5 grid spacers and 4-span configuration were used in the flow test. Figure C.3.3-1 shows the structure of the test bundle. The lower three spans of Mitsubishi 17x17 conventional fuel assembly with 9-grid spacers were used for this test, with a short top span. Several 5x5 grid spacers were prepared by cutting them from full-sized 17x17 Zircaloy-4 grid spacers. Thus the natural frequency of the rod in this test bundle for lower mode is the same as for a full length rod. The cell conditions in the bottom four grid spacers were adjusted to give several spring force levels: as-built (BOL), EOL ([] % spring force) and gap, [] mil ([] μm). The cells in the top grid spacer were all set to BOL spring force levels to prevent the rod from moving up due to the hydraulic forces, or dropping. Accelerometers were attached to some of the rods at the mid-span elevation. The third span from the bottom, where the modal analysis predicted a large response, was selected for measuring the response of each rod. The vibration responses were measured and analyzed to obtain the amplitudes and frequencies during the flow test. The flow rate was kept at 18.0 ft/s (5.5 m/s), to simulate the upper limit of the mechanical design flow rate.

The flow test was conducted shown in Figure C.3.3-2. This facility has a flexible capability to conduct flow tests for both full-sized fuel assemblies and small-scale test bundles such as the one used in this test.

Test Results – Fuel Rod Frequency and Amplitude

Typical rod vibration responses are shown in Figure C.3.3-3. These Figures show the spectrum of the measured rod mid-span acceleration for BOL, EOL or gapped cells. The accelerometer signals were monitored throughout the test. The frequencies for the peak accelerations in the spectrums measured at approximately 250 hours into the test and at the end of the test are shown in Figure C.3.3-4. The change in the peak acceleration frequency with time is small, as can be seen from the small bands on the data shown in this Figure.

The measured acceleration signals were double integrated with respect to time with a low frequency cut-off. Since the rod vibration is basically random, these measured data were reduced to the mean value and standard deviation. Figure C.3.3-5 shows the mean amplitude with 1s (one sigma) bands for the different cell conditions. Only calculated results are shown for the just contacting cell. The difference in the mean amplitude is relatively small for the BOL and EOL cell conditions, but it increases significantly for the gapped cell. The calculation results are acceptable for each cell condition. The factor C in equation C.2.2-1 is adjusted for these calculations. Using a larger value for C will give conservative results, i.e., larger amplitudes with appropriate consideration for the spring force. The results of this test provide the basis for the use of the vibration model for design analyses as described in Section C.2.1.

Test Results – Fretting Wear

The fuel rods were visually observed and the depth of wear scars at the grid spacer supports was measured at the completion of the hydraulic test for 500 hours. No wear scar was observed for the rods supported by the BOL cells. Wear marks were observed in the rods supported by the EOL cells, but the depth of these wear marks was less than the [] mil ([] μm) measurement detection limit. Measurable wear scars found at both the dimple and spring positions in the rods in the gapped cells. The measured wear depth results (maximum value for each scar) are summarized in Figure C.3.3-6. The largest wear depths were measured at the lower grid spacer position.

The wear calculation was performed for each case of a BOL, EOL and gapped cell rod, and the additional case of a just contacting cell (not tested). No wear was calculated for the BOL and EOL cells, consistent with the test data. The calculated values for the gapped cell and the just contacting cell are compared with gapped cell wear depth data in Figure C.3.3-6. In the measured wear data there was a trend for an uneven distribution for a pair of dimples in one grid spacer support. If a relatively large wear was observed at any dimple, only a very small wear was observed at the other dimple. The differences in the wear depth when this occurs are shown in Figure C.3.3-7. The calculated results show a similar trend, as is shown in this Figure. This feature is typical behavior for the rods with gapped cells, which vibrate with one dimple support, and confirms the modeling for the rod support in gapped cell.

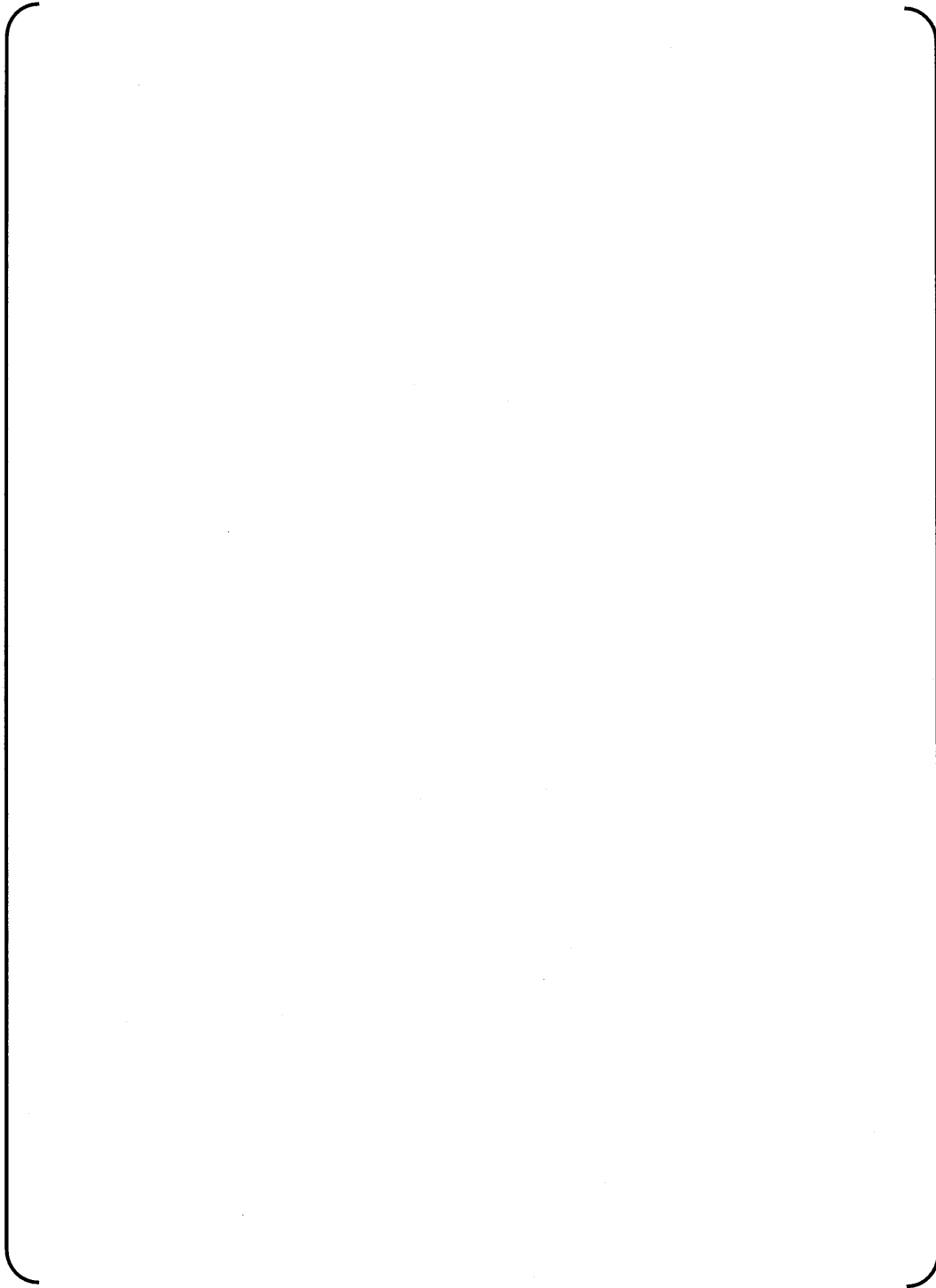


Figure C.3.3-1 Test Bundle

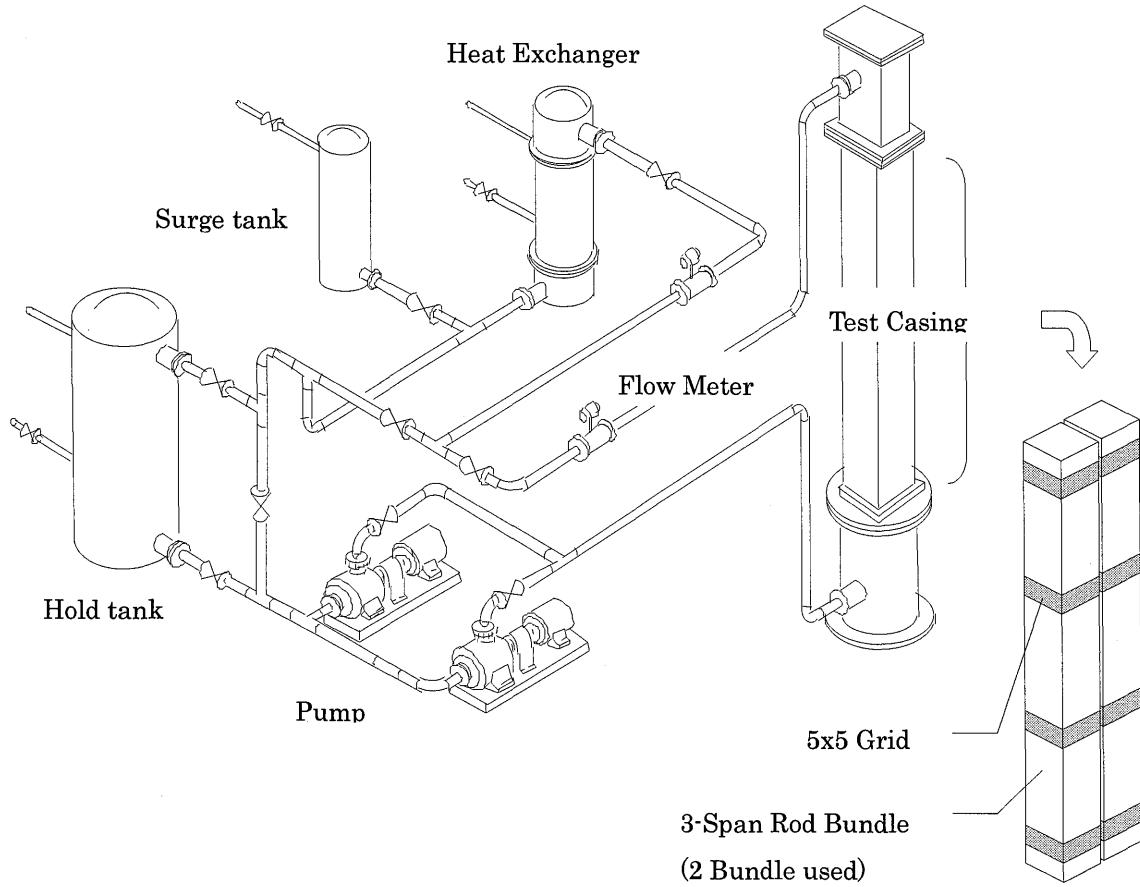


Figure C.3.3-2 Hydraulic Test Loop

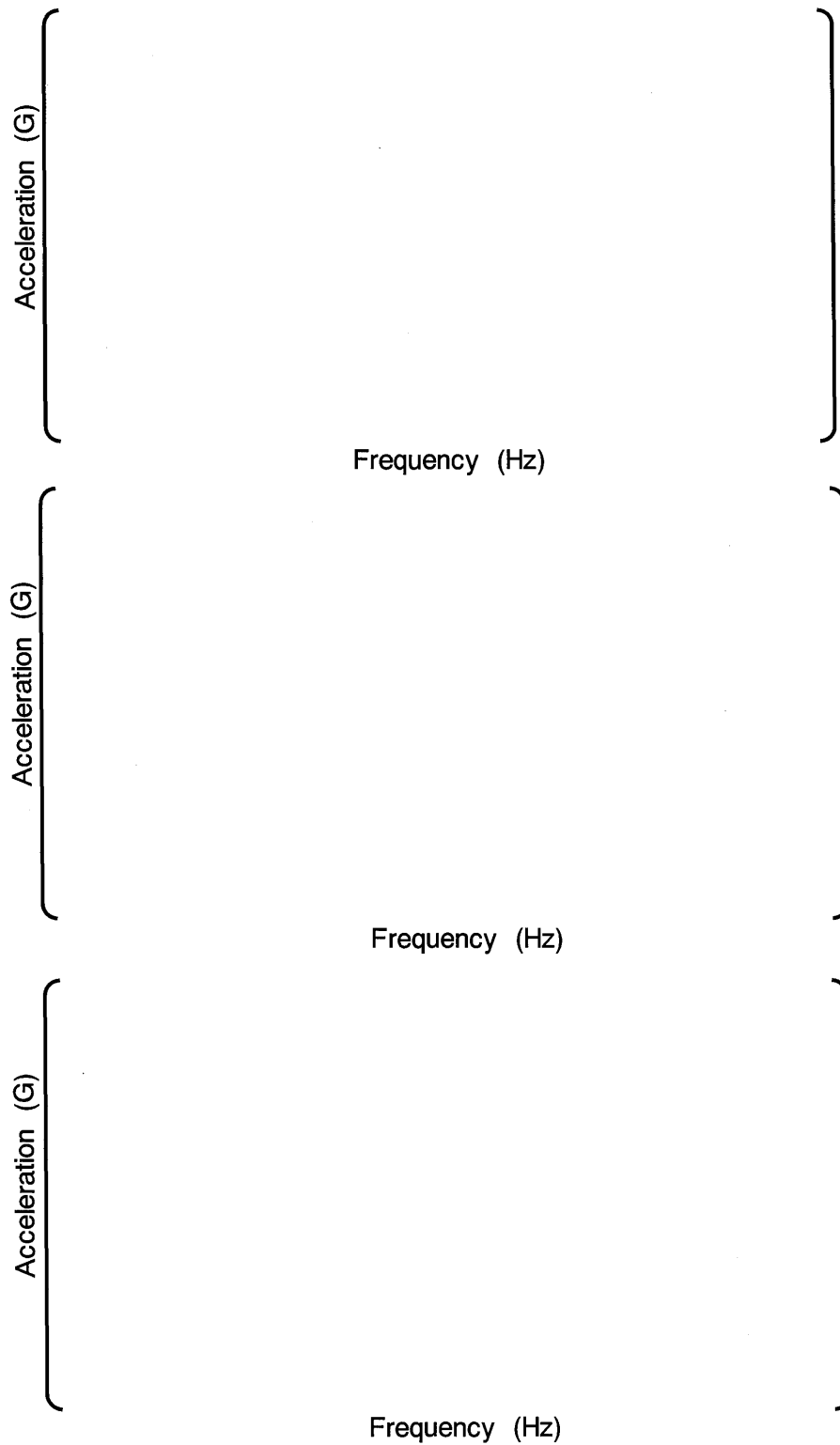


Figure C.3.3-3 Fuel Rod Typical Vibration Response

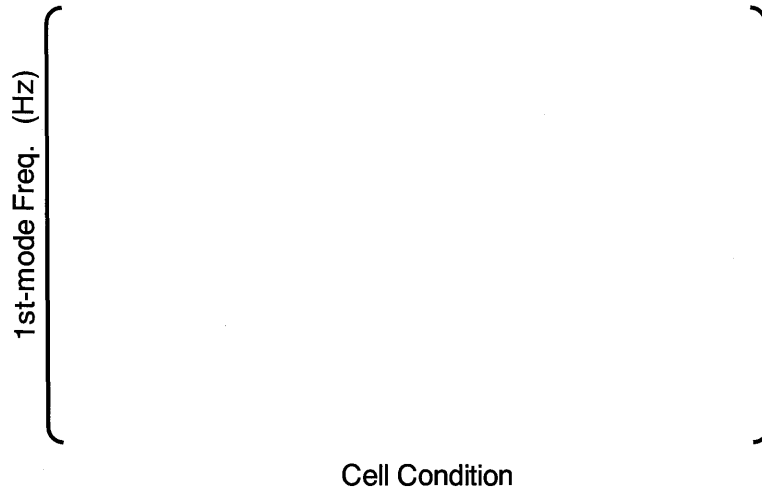


Figure C.3.3-4 Comparison of Measured and Calculated Peak Amplitude Frequency

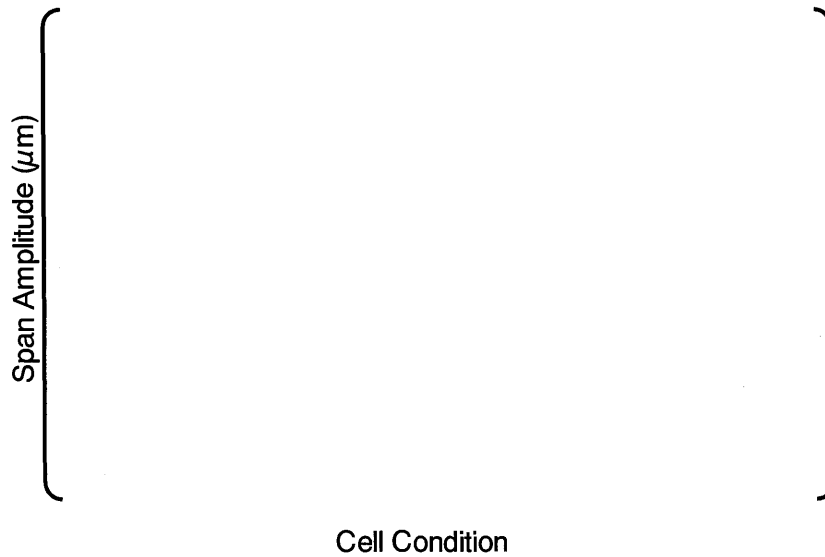


Figure C.3.3-5 Comparison of Measured and Calculated Mean Amplitude

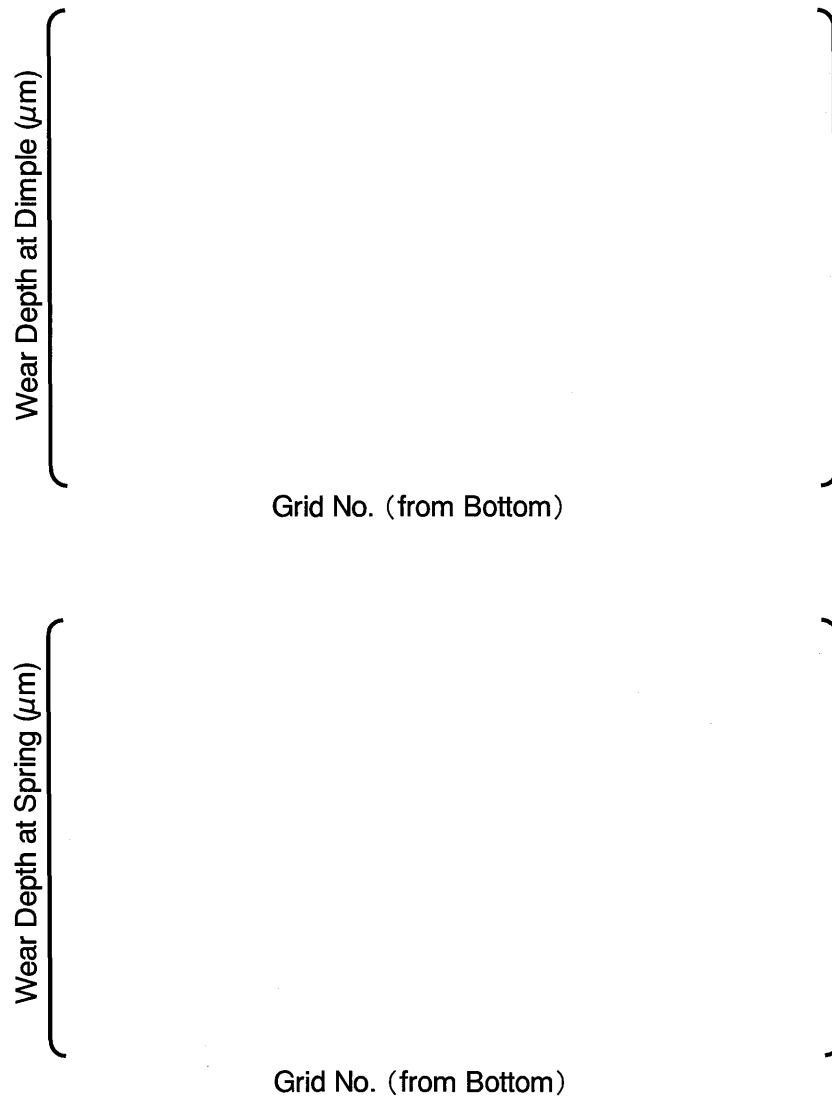


Figure C.3.3-6 Comparison of Measured and Calculated Wear Depths

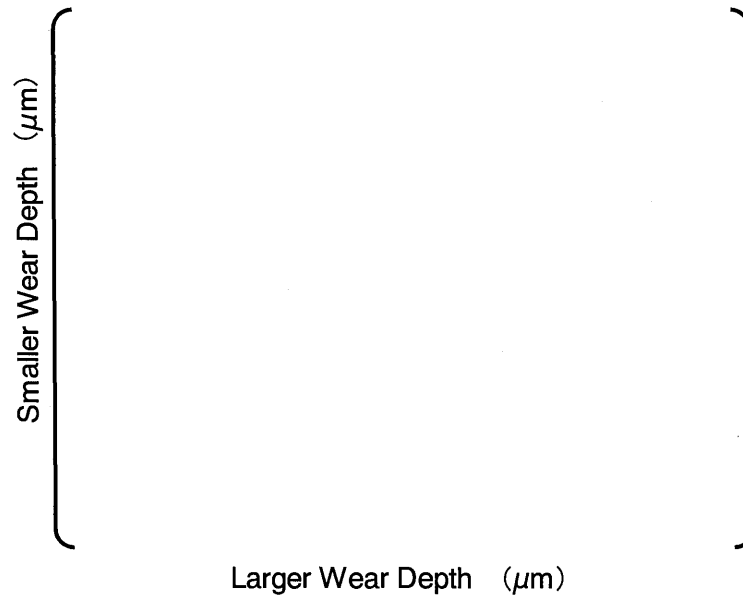


Figure C.3.3-7 Comparison of the Measurements and Calculation for the Uneven Wear Depth Distribution in a Dimple Pair

C.4.0 VERIFICATION

The simulation analysis was done to verify the flow-induced vibration models for a full-scale fuel assembly. The calculated span amplitude and wear depth were compared with the measurements.

C.4.1 Full-Scale Fuel Assembly Hydraulic Test

In order to verify the models for flow induced vibration and fretting wear, the flow test of 14x14 fuel assembly with 7 Inconel grid spacers, which was conventional for 2-loop PWR plant in Japan, was conducted by the similar configuration of test loop of Figure C.3.3-2. In the test, the rod vibration responses in EOL, just-contact (JC) and gapped (GAP) cells were measured and the wear scars were observed after 500 hours operation of 18.0 ft/s (5.5m/s) flow at room temperature. The adjustment of cell conditions for JC (zero spring force) and GAP, [] mil ([] μm) were conducted for all grid spacers except the top. For the EOL rod, the spring forces at intermediate grid spacers were adjusted to 20% level of BOL. The span amplitudes were measured using the accelerometer instrumented in the rods at the first and fourth span from the bottom.

The measured span-amplitudes are plotted in Figure 4.1-1. The differences of span amplitude between GAP and JC or EOL rod are relatively small. This unexpected result may be caused by the rod bowing and/or distortion of skeleton, which resulted in the rod contact to dimples at gapped cell and formed similar situation with JC at intermediate grid spacers. This explanation is supported by the fact that the very small wear scars were observed at intermediate grid spacers although their cell sizes had been adjusted as GAP before the test.

Based on the above interpretation, the calculated model was prepared including additional case for the gapped cell as follows.

- EOL, JC, GAP : same cell conditions with test rod
- GAP* : gapped cell for only bottom grid spacer and just contact for intermediate grid spacers

The calculated span-amplitude distributions are shown in Figure 4.1-2 with measured data. Although the measured data are restricted, the magnitudes of calculated amplitudes are reasonable compared with measurements. In addition the calculated amplitude distribution by GAP* agrees with measured data rather than GAP model.

Figure 4.1-3 shows the comparison of calculated and measured wear depth. Almost all of wear scars were observed at lower grid spacer positions of GAP rods and the maximum wear depth reached more than [] mil ([] μm) . Only small wear scar (less than [] mil ([] μm)) was observed at JC rod. No wear scar was observed at EOL rods. In the calculation, no wear for EOL rod and wear up to [] mil ([] μm) for JC rod were obtained. GAP rod model calculated about [] mil ([] μm) wear. The flat distribution of wear depth calculated by GAP rod model is different from the measured one. Preferably, the result by GAP* rod model shows the same profile with measured wear distribution. These results suggest that the treatment of GAP rod model gives the conservative wear evaluation although the additional treatment needs in order to express more actual behavior at gapped cell. On the whole, it was confirmed that the vibration and wear calculation model proved to be useful in evaluating the

fretting wear of fuel rod.



Figure C.4.1-1 Span Amplitude Measured by Flow Test



Figure C.4.1-2 Comparison of Calculated Span Amplitude with Measurement

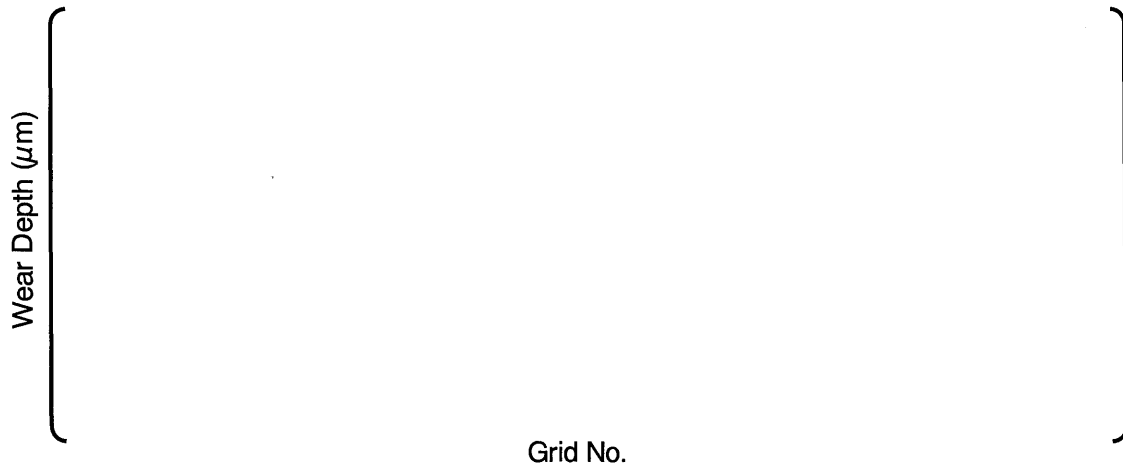


Figure C.4.1-3 Comparison of Calculated Wear Depth with Measurement

C.5.0 SUMMARY AND CONCLUSIONS

The computational method for fretting wear of the fuel rod has been developed. It calculates span-wise vibration amplitudes using the Reavis equation and reduced slip displacements at the grid spacers. The effect of spring force relaxation is included in the model. After calculation of the vibration amplitudes, the evolution of the wear volume is calculated using the Archard equation and accounting for the oxide layer growth on the cladding surface.

The applicability of the computational method has been verified by comparing the calculated results with results obtained from hydraulic tests, including the hydraulic test for 500 hours. The developed method has enabled the calculation of the fuel rod fretting wear during irradiation, while accounting for in-reactor behavior, such as creep relaxation of spring force and growth of the oxide layer on the cladding. This method is used to evaluate fuel assembly design changes to reduce the risk of fretting wear of the fuel cladding.

C.6.0 REFERENCES

- (C-1) J. R. Reavis, "Vibration Correlation for Maximum Fuel-Element Displacement in Parallel Turbulent Flow", Nucl. Sci. Eng. 38, 63-69 (1969)
- (C-2) R. D. Blevins, "Flow-Induced Vibration in Nuclear Reactors : A Review", Progress in Nuclear Energy, vol 4, p.42
- (C-3) R. D. Blevins, "Flow Induced Vibration", Van Nostrand Reinhold, New York, 1977, p.163
- (C-4) H. J. Connors, S. J. Savolelli and F. A. Kramer, "Hydrodynamic Damping of Rod Bundles in Axial Flow", PVP-Vol.63 (ASME), pp.122-124
- (C-5) J. F. Archard, "Contact and Rubbing of Flat Surfaces", J. Applied Physics 24, p981, (1953)
- (C-6) E. Hillner, "Corrosion Zirconium-Base Alloys An Overview", ASTM STP 633 (1977), p.211

Appendix D

FUEL CLADDING COLLAPSE EVALUATION

February 2008

**© 2008 Mitsubishi Heavy Industries, Ltd.
All Rights Reserved**

Abstract

Long circular tubes such as nuclear fuel cladding, have the potential for the occurrence of creep collapse due to the effect of an external pressure. For a nuclear fuel rod, where axial gaps (or interpellet gaps) can form in the fuel pellet column, the section of cladding tube having lost the support effect of the pellets may collapse due to long-term creep deformation under external coolant pressure during the operation in reactor. This report presents a description for method for evaluating fuel rod creep collapse of PWR fuel rods.

A statistical model is used to calculate the fraction of fuel rods that have collapsed, i.e. the collapsed rod frequency as a function of time for a given fuel region. The primary factors affecting collapse behavior process and thus determining collapse time for a single fuel rod are the rod internal pressure (or differential pressure), cladding temperature, fast neutron flux, initial cladding tube ovality, axial gap length size in the fuel column, etc. Correlation functions relating these factors, including axial gap length, to the collapse time are used in the collapsed rod frequency calculation. These correlation functions have been derived from parametric analyses using a mechanistic model of creep collapse physics and from the out-of-pile test data. Each factor is treated as a variable with probability distribution, which can be assigned from reactor core and fuel characteristics (rod power, axial power profile, cladding initial ovality, axial gaps formed).

The mechanistic model fundamentally uses the creep buckling analysis method developed by W. K. Wilson for long circular and hollow tubes to evaluate the creep collapse of fuel rod cladding with an infinite axial gap length. The model analyzes the evolution with time of the stress and deformation distributions in the radial and tangential directions on a two-dimensional horizontal cross section of cladding tube and hence the time dependent change in the ovality of cladding tube. For finite gap length, the support effect due to both end pellets are accounted for by introducing an empirical derived axial finite gap effect model for the tube displacement which is dependent on axial gap length.

The evaluation methodology (mechanistic model and statistical model) was originally developed for Zircaloy-4 (Zr-4) cladding PWR fuel (14×14, 15×15, and 17×17 fuel types of rods array). The mechanistic model has been confirmed by data from out-of-pile creep collapse test conducted using autoclave equipment: it gives almost good agreement with data for the evolution of the ovality as a function of time. The statistical model has been verified by comparison with data from early Zir-4 cladding fuel that experienced creep collapse fuel failures. This verification confirms that the methodology gives appropriately conservative predictions for creep collapse: It gives overall good trace for the observed trend and gives moderately larger creep collapse fractions than were observed for those early fuels.

The creep collapse problem has subsequently been eliminated by changes in the fuel design and fabrication techniques: the introduction of fuel rod pre-pressurization and higher density fuel pellets. They counter the external pressure and significantly reduce the possible gap size formed in the fuel pellet column respectively. No creep collapse rod failures have been observed following the implementation of these fuel fabrication improvements.

The Mitsubishi creep collapse evaluation methodology is now applicable to fuel designs with new cladding alloys, such as ZIRLO, by adding their cladding creep properties. The aspects other than the creep properties, such as model structure, remain the same as Zr-4 cladding fuel, which have been adequately verified for Zr-4 cladding PWR fuel.

Table of Contents

| | |
|--|------|
| List of Tables..... | D-5 |
| List of Figures | D-6 |
| D.1.0 INTRODUCTION | D-7 |
| D.2.0 BACKGROUND AND MECHANISM | D-8 |
| D.2.1 Background | D-8 |
| D.2.2 Mechanistic Model for Fuel Rod Creep Collapse | D-11 |
| D.3.0 COLLAPSE FREQUENCY EVALUATION..... | D-27 |
| D.3.1 Factors Affecting the Collapse Mechanism and Generic Methodology | D-27 |
| D.3.2 Collapse Frequency Calculation Theory and Formulation | D-31 |
| D.3.3 Calculation Method for Collapse Frequencies..... | D-48 |
| D.3.4 Validation and Verification..... | D-50 |
| D.4.0 EVALUATION OF US-APWR FUEL..... | D-54 |
| D.5.0 CONCLUSION | D-58 |
| D.6.0 REFERENCES | D-59 |

List of Tables

| | | |
|---------------|--|------|
| Table D.2.2-1 | Basic Assumptions in the Analytic Mechanical Model | D-14 |
| Table D.2.2-2 | Basic Relations and Equations (1/2) | D-15 |
| Table D.2.2-2 | Basic Relations and Equations (2/2) | D-16 |
| Table D.2.2-3 | Creep Theory and the Equations | D-17 |
| Table D.2.2-4 | Zircaloy-4 Cladding Creep Model Equations | D-18 |
| Table D.2.2-5 | ZIRLO Cladding Creep Model Equations | D-19 |
| Table D.3.2-1 | Equation for the Ovality-Quadrupled Uniform Creep Strain ϵ_{uc4} | D-40 |
| Table D.3.2-2 | Equation for the Relation between the Ovality-Quadruple Time (t_{uc4}) and the Collapse Time (t_{col}) (1/2) | D-41 |
| Table D.3.2-2 | Equation for the Relation between the Ovality-Quadruple Time (t_{uc4}) and the Collapse Time (t_{col}) (2/2) | D-42 |
| Table D.4-1 | Core and Fuel Design Summary of US-APWR | D-56 |
| Table D.4-2 | Fuel Loading Scheme Planned for US-APWR | D-56 |

List of Figures

| | | |
|----------------|--|------|
| Figure D.2.1-1 | Schematic of Creep Collapse Phenomenon of a Fuel Rod in Nuclear Reactor Operation | D-9 |
| Figure D.2.1-2 | Forces Exerted on Cross Section of Initially Oval-shaped Tube under External Pressure | D-10 |
| Figure D.2.2-1 | Geometry and Coordinate System for Mechanics Analysis of Initial Oval Tube under External Pressure | D-20 |
| Figure D.2.2-2 | Creep-induced Ovalization Process of Initially Oval Tube under External Pressure | D-20 |
| Figure D.2.2-3 | Development of Stress and Creep Due to Bending for Initial out-of-round Tube under External Pressure | D-21 |
| Figure D.2.2-4 | Schematic Flow Diagram of Analysis for Creep Collapse Process for Fuel Rod Cladding Tube..... | D-22 |
| Figure D.2.2-5 | Comparison of Calculated and Measured Ovality for Out of Pile Test.. | D-23 |
| Figure D.2.2-6 | Comparison of Calculated and Measured Ovality for Out of Pile Test.. | D-24 |
| Figure D.2.2-7 | Comparison of Calculated and Measured Ovality for Out of Pile Test.. | D-25 |
| Figure D.2.2-8 | Comparison of Calculated and Measured Ovality for Out of Pile Test.. | D-26 |
| Figure D.3.1-1 | Illustration of Fuel Rods, Reactor Core and Distributions of the Several Factors that Contribute to Creep Collapse | D-29 |
| Figure D.3.1-2 | Schematic of the Generic Procedure to Calculate a Collapse Frequency from the Distribution of the Factors Determining Collapse | D-30 |
| Figure D.3.2-1 | Key Concepts for Providing the Linkages between the Significant Factors, the Collapse Time, and the Collapse Frequency..... | D-43 |
| Figure D.3.2-2 | Finite Gap Effect Correction Factor versus Gap Length..... | D-44 |
| Figure D.3.2-3 | Typical Time Averaged Relative Rod Power Census | D-45 |
| Figure D.3.2-4 | Typical Initial Ovality Distribution | D-45 |
| Figure D.3.2-5 | Relative Gap Length Size Distribution | D-46 |
| Figure D.3.2-6 | Gap Occurrence Frequency Distribution | D-47 |
| Figure D.3.3-1 | Schematic Flow Diagram of Analysis for the Cladding Collapse Frequency | D-49 |
| Figure D.3.4-1 | Comparison of Observed and Predicted Frequency of Fuel Rod Collapse for Plant A Region 1 fuel..... | D-51 |
| Figure D.3.4-2 | Comparison of Observed and Predicted Frequency of Fuel Rod Collapse for Plant B Region 2 fuel..... | D-52 |
| Figure D.3.4-3 | Comparison of Observed and Predicted Frequency of Fuel Rod Collapse for Plant C Region 1 fuel..... | D-53 |
| Figure D.4-1 | Collapsed Rod Frequency versus Time for U-Rods in US-APWR..... | D-57 |
| Figure D.4-2 | Collapsed Rod Frequency versus Time for G-Rods in US-APWR..... | D-57 |

D.1.0 INTRODUCTION

Cladding flattening and collapse failures of nuclear fuel rods were observed worldwide in some PWR plants in the early 1970's. These early designed PWR fuels used lower density fuel pellets and fuel rods internally unpressurized or low pressurized; in contrast to the current fuels. Lower density fuel pellets like the earlier fuels tends to have a larger densification than current higher density fuel. In the present, it is understood that the principal reasons of the collapse failure are larger densification with lower density fuel pellets and non-or-low pressurized rods.

Densification occurrence will contract fuel pellet volume, resulting in the shrinkage of fuel pellet column length (i.e., fuel stack length) and possibility of axial gap (i.e. empty section or inter-pellet gap) formations in the fuel pellet column. Axial gap forms unsupported section in the cladding tube. When significantly large axial gaps form, the cladding tube sections at the axial gaps may deform flat due to cladding creep mainly dependent on differential pressure across the cladding wall. If the deformations proceed further and reach the mechanical instability, the cladding tube sections eventually collapse into the gaps. ^(D-1,2,3)

As the above, the unsupported sections of the cladding tube can collapse due to plastic instability resulting from long-term cladding creep processes in the PWR environment: operating coolant water pressure, temperature and neutron irradiation. Precluding this cladding creep collapse phenomenon is one of the basic design requirements for maintaining fuel rod integrity. This requirement is satisfied by proper design and fabrication of the fuel rods, and assured by analytic evaluation of the creep collapse phenomenon for the fuel in the PWR plant core loading.

The Mitsubishi has developed a statistical model to evaluate the collapsed rod frequency as a function of time, i.e., the fraction of the rods in a given fuel region that have collapsed through the time less than or equal to a given time. Correlation functions have been developed to relate the collapse time to the fuel fabrication characteristics, the fuel in-reactor performance and the operating conditions that determines the collapse time.

These correlations have been derived from parametric analyses of the collapse time predictions obtained by using a mechanistic model for the creep collapse. Correlation relating the axial gap length to collapse time has been especially based on the out-of-pile collapse test data. A description of this mechanistic model is also given in this Appendix.

The statistical method is used to combine the frequency distributions for the values of each of the factors determining the collapse time, such as rod internal pressure, fast neutron flux, cladding tubing initial ovality, etc. This method provides collapse time predictions to determine the collapsed rod frequency. The collapsed rod frequency at a given time is evaluated as a fractional rate of the combined frequency of the factors that result in cladding creep collapse by that time, relative to the total combined frequency of the full range of the factors. To assure that creep collapse does not occur, the product of collapsed rod frequency and the total number of fuel rods in the region of concern is required to be less than 1.0 during the region's projected exposure life.

It should be noted that cladding flattening and creep collapse have not occurred for current fuel rod designs that adopt higher density fuel pellets and higher internal pressurization at fabrication.

D.2.0 BACKGROUND AND MECHANISM

D.2.1 Background

Creep collapse of a fuel rod is a phenomenon that can occur when axial gaps appear in the fuel pellet column. The unsupported cladding tube sections at these axial gaps deform more flatly under the compressive condition. Thus the ovality of the cladding tube increases with time and it could eventually cause collapse into the axial gap.

The axial gaps form due to the fuel pellet densification with irradiation exposure. The fuel densification behavior leads to shrinkage of the pellet in both the axial and radial directions. The reduction in the fuel pellet length causes axial settlement of the fuel pellet column and if the pellets hang up at some point in the fuel column, due to pellet and cladding interaction, an axially inter-pellet gap will occur.

The fuel rod cladding tube experiences compressive forces due to the pressure differential across the tube wall when the (hot) rod internal pressure is less than the outer coolant pressure at power operating condition. Under these conditions a cylindrical tube with an initial out-of-roundness (ovality) undergoes a bending component in addition to compressive component of the tube stresses, with the bending component increased proportional to an extent of the deflection from a perfect circle. The bending moments and thus the local stresses increase where the tube wall is more largely deformed both inward and outward. On the other hand, they decrease where the tube wall is less deformed.

The imbalance in the stress distribution leads to a non-uniform creep strain distribution through the tube wall cross section. The larger creep strain leads to a larger deflection of the tube, and the local stress increases still further. In this way the imbalance in the distribution of the creep deformation and stress in the tube wall increases progressively with time. As a consequence, where there are inter-pellet gaps (i.e., axial gaps) a fuel cladding tube with a slight initial ovality will deform into a more oval shape with increasing irradiation exposure. When the deformation from a perfect circular tube eventually becomes so large that the cladding tube experiences a mechanical instability, the tube completely collapses into the axial gap.

Figure D.2.1-1 shows a schematic depiction of processes of creep collapse of a fuel rod during nuclear reactor core operation. Figure D.2.1-2 shows the forces and bending moments acting on the initially oval-shaped tube under the influence of an uniform external pressure.

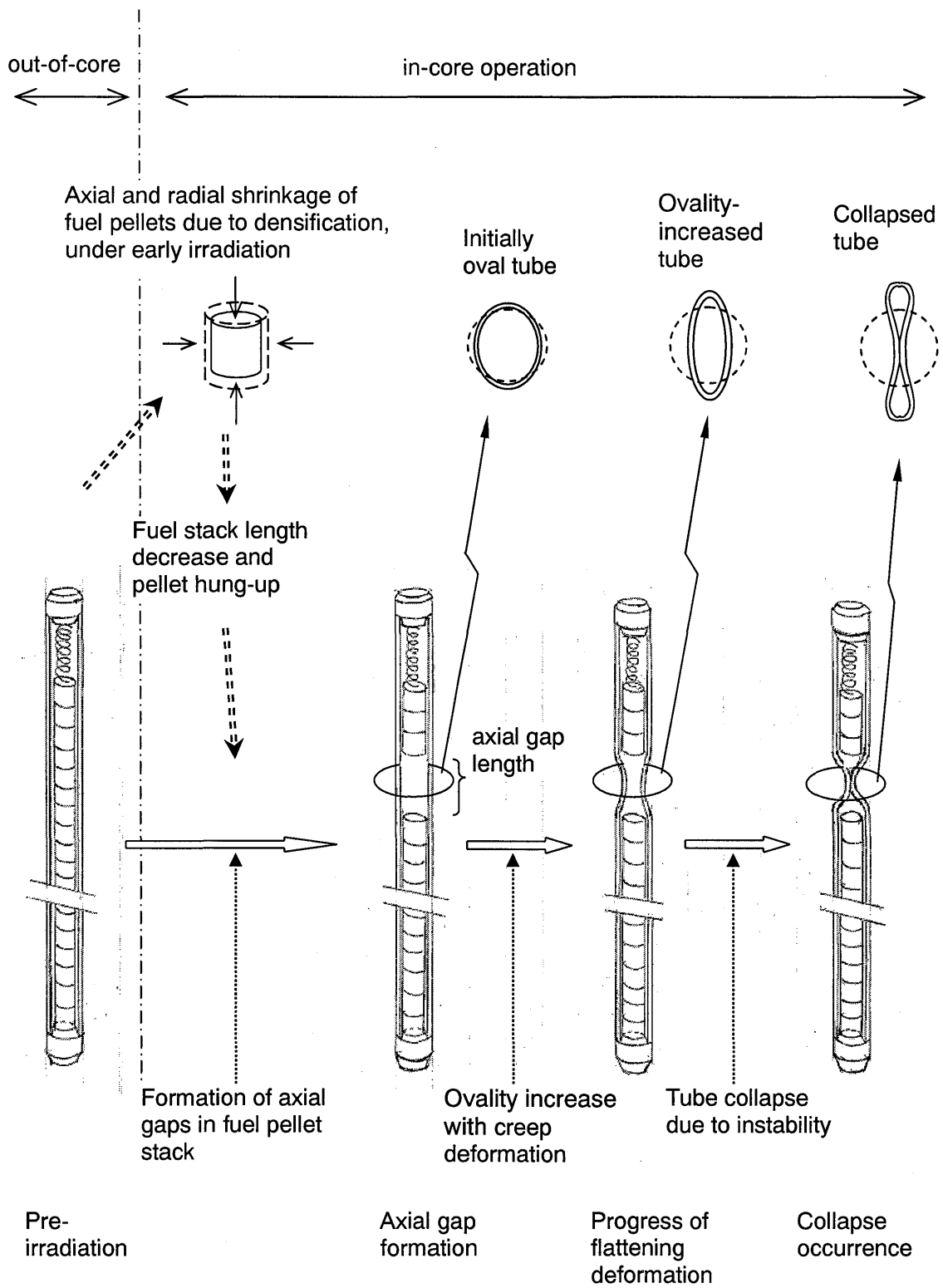


Figure D.2.1-1 Schematic of Creep Collapse Phenomenon of a Fuel Rod in Nuclear Reactor Operation

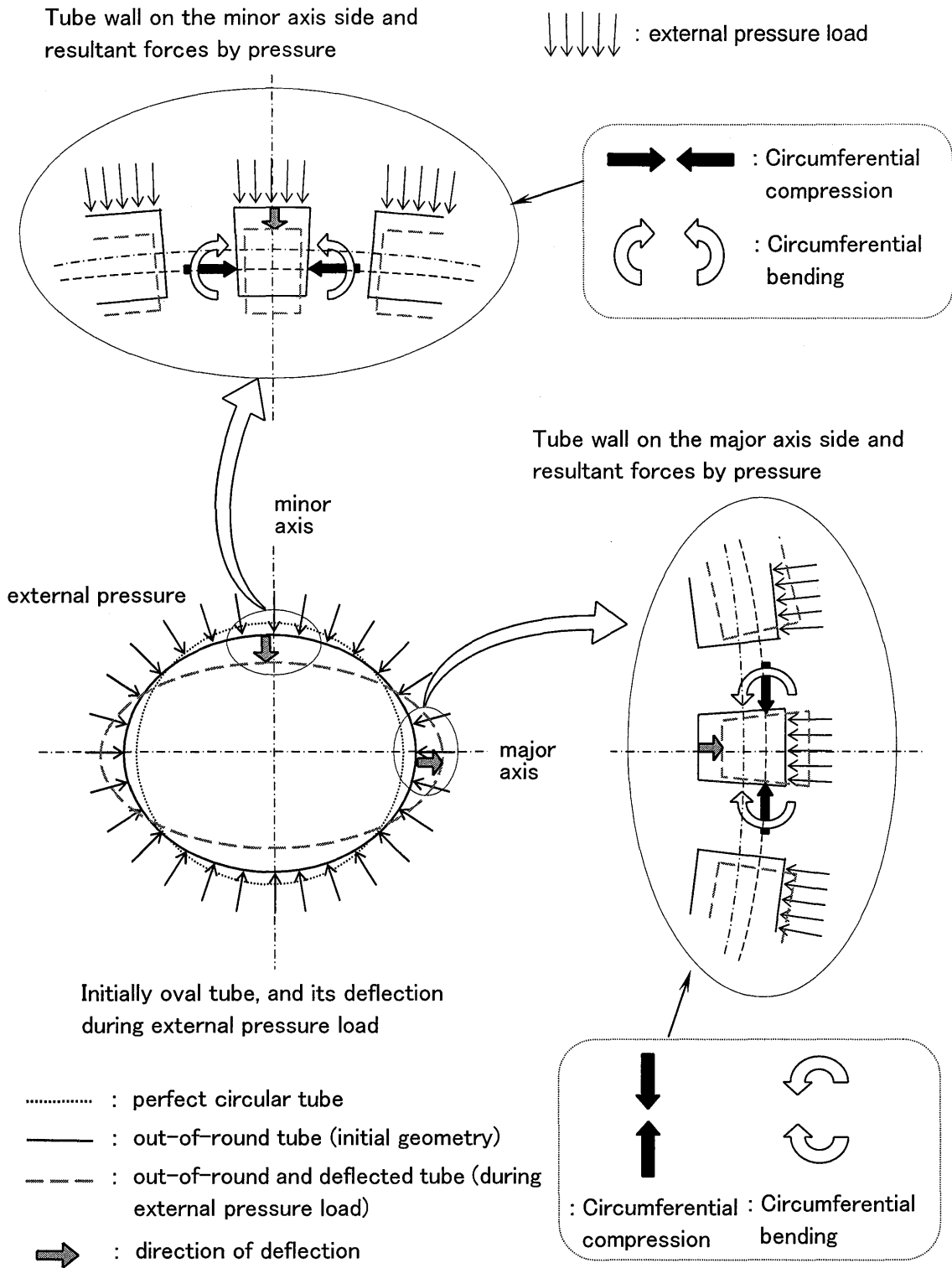


Figure D.2.1-2 Forces Exerted on Cross Section of Initially Oval-shaped Tube under External Pressure

D.2.2 Mechanistic Model for Fuel Rod Creep Collapse

The mechanistic model for cladding creep collapse is based on the method developed by W. K. Wilson^(D-4), which uses an analytical mechanical model to calculate the creep buckling of a long circular tube (a thin-walled cylinder) which initially has an out-of-round, oval, cross sectional shape and is subjected to uniform external pressure.

If the tube is perfectly round, it experiences only compressive forces and deforms uniformly under the external pressure. An initially oval tube experiences both a compressive force and bending moments that simultaneously act on the tube wall. These produce an imbalance in the stress, creep strain and deformation distributions through the tube wall cross section. As a consequence, the tube will deform into a more oval shape due to long-term creep of the cladding. The model analytically calculates the distributions of the stresses, strains, and deformations and their evolution due to creep under the action of compression and bending, in the cross-sectional plane of tube wall. The geometric model of the tube wall used is a quarter symmetric portion of the tube in a two-dimensional plane in the R- θ coordinate system.

The geometric model and the coordinate system of the mechanical analysis are shown in Figure D.2.2-1. The initial deflection curve in terms of the initial ovality is given by cosine function of 2θ to represent circumferential distribution of the deflection from a perfect circle^(D-4). The fundamental assumptions used in this analytical mechanical model are shown in Table D.2.2-1.

This model treats the tube as a long enough and hollow cylinder so that the physical behavior is independent of the axial (i.e. longitudinal) position. This model therefore corresponds to the case of an infinitely long gap.

Figure D.2.2-2 shows a schematic of the evolution of the tube cross sectional shape change due to non-uniform creep through the flattening process. Figure D.2.2-3 outlines the mechanisms through which the stress, bending moment and creep change with time. The bending moment acts positively at $\theta = \pi/2$ and negatively at $\theta = 0$, producing outward cladding creep at $\theta = 0$ and inward cladding creep at $\theta = \pi/2$. Hence the key mechanisms for the creep-induced increase in ovality are:

The initial elastic deformation is directly proportional to the initial ovality (that is, the as-fabricated deviation from an exactly circular cross section). Following the initial elastic strains of the tube, under the external pressure and the irradiation at elevated temperature of operational condition, creep deformation occurs tending to enlarge the initial deformed shape. The action of bending stresses, which also depend on the initial ovality, causes some elements in the cladding tube wall cross section to have a creep rate in excess of the creep rate corresponding to the mean hoop stress.

Hence more inward creep occurs where the cladding wall is initially deformed inwards and more outward creep occurs where the cladding wall is initially deformed outwards. This gives a non-uniform creep deformation which enhances the initial ovality, and the ovality increases, eventually resulting in cladding collapse.

The mechanistic model is based on the mechanical equations for the interrelationship between the stresses, strains (elastic, creep, and total strains), deflections and deformations. These equations are derived from the following basic mechanical relations^(D-4) :

- equilibrium conditions for the axial force, tangential force, and tangential moment
- compatibility conditions for the strain
 - linear relation of total tangential strain in the tube wall
 - curvature-deflection relationship in the tube wall
- elastic stress-strain relationship
- incompressibility of creep strains

The basic mechanical relations and the model equations derived from these basic equations and used in the mechanistic creep collapse analysis are given in Table D.2.2-2.

The analysis method of W. K. Wilson^(D-4) considers both the von Mises and Tresca rules as the plastic flow rule for the triaxial creep rate calculation, and both the strain hardening and time hardening laws as the mechanical equation of state form for the creep rate calculation for time-dependent temperatures and stresses. The Mitsubishi mechanistic model described here uses the von Mises flow rule and the strain hardening law because they are considered to be more common physical expressions. The equations used to calculate the creep strain changes in a given time increment are shown in Table D.2.2-3.

It is necessary to give an explicit creep model describing the creep behavior of cladding tube material to obtain creep strain rates used in this mechanistic analysis. The Mitsubishi mechanistic model uses the cladding creep models for either Zircaloy-4 (Zr-4) or ZIRLO™, which are given in Tables D.2.2-4 and D.2.2-5, respectively. They are the same cladding creep models as are used in the fuel rod design analysis^(D-5). These creep models have been developed and fully verified from in-reactor fuel rod creep data.

The model developed by W. K. Wilson^(D-4) is applicable to the case of an infinitely long gap. In reality, the axial gaps in the fuel column will have a finite length and the cladding tube inner surface will come into contact with the pellets just above and below the gap as the non-uniform creep deformation proceeds in the axial gap region. Once this contact occurs, further increases in the creep deformation are suppressed due to the support effect from the pellet-cladding contact. This support effect retards the creep deformation rate and leads to increased collapse times, or, for small enough gaps, gives sufficient support to completely preclude collapse occurrence.





These figures show that mechanistic model in general gives accurate or conservative predictions for the evolution of the ovality as a function of time over a wide range of internal pressure and tube initial ovality.

Table D.2.2-1 Basic Assumptions in the Analytic Mechanical Model



Table D.2.2-2 Basic Relations and Equations (1/2) ^(D-4)



Table D.2.2-2 Basic Relations and Equations (2/2)^(D-4)

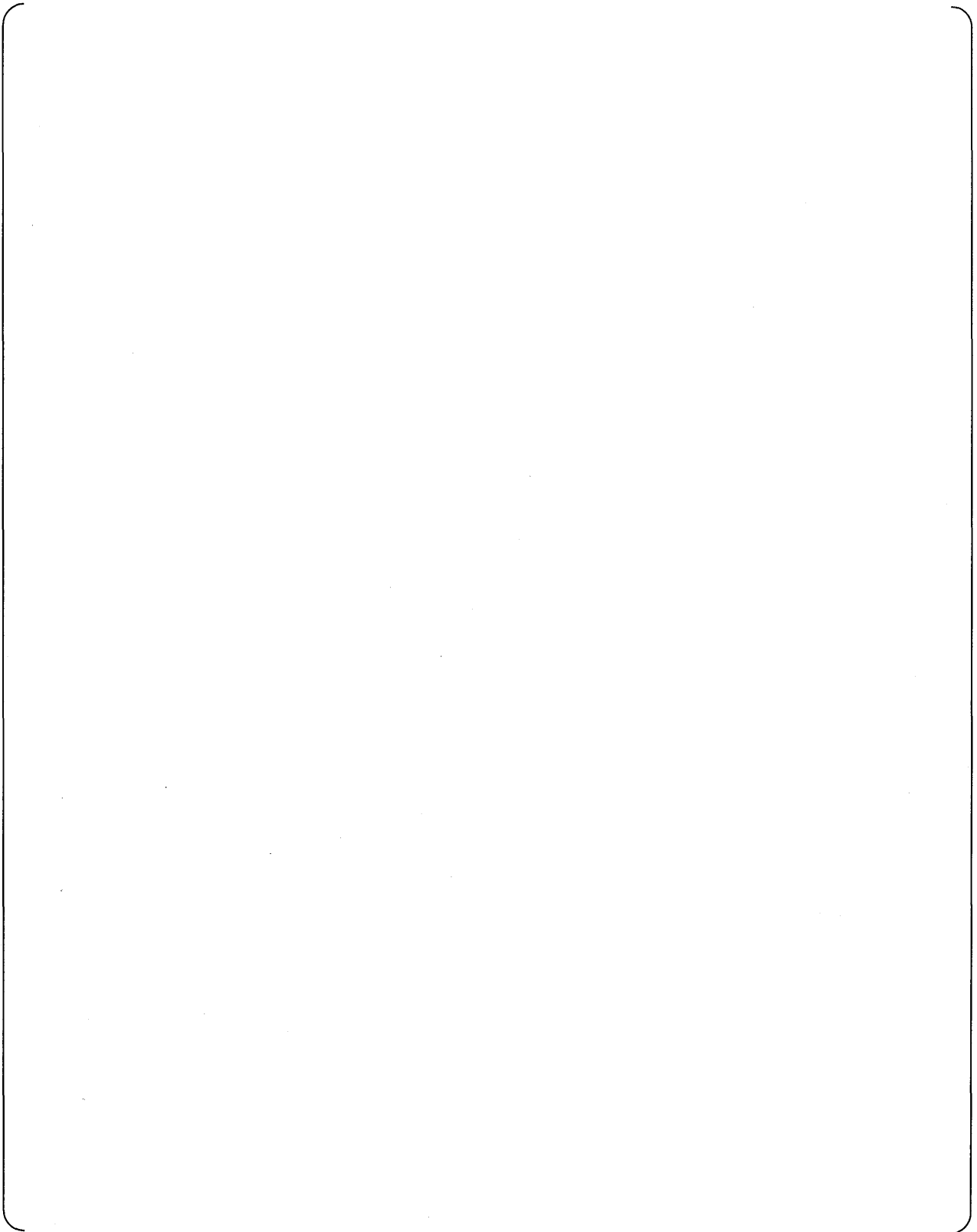


Table D.2.2-3 Creep Theory and the Equations ^(D-4)

Flow rule : von Mises theory

$$\dot{\varepsilon}_c^\theta = \frac{\dot{\varepsilon}_c^{eff}}{\sigma_{eff}} \left(\sigma_\theta - \frac{\sigma_z}{2} - \frac{\sigma_r}{2} \right)$$

$$\dot{\varepsilon}_c^z = \frac{\dot{\varepsilon}_c^{eff}}{\sigma_{eff}} \left(\sigma_z - \frac{\sigma_\theta}{2} - \frac{\sigma_r}{2} \right)$$

$$\dot{\varepsilon}_c^r = \dot{\varepsilon}_c^\theta - \dot{\varepsilon}_c^z$$

Hardening law : strain hardening theory

$$\dot{\varepsilon}_c^{eff} = F \left(\sigma_{eff}, \varepsilon_c^{eff} \right)$$

where,

$\dot{\varepsilon}_c^\theta, \dot{\varepsilon}_c^z, \dot{\varepsilon}_c^r$: tangential, axial, and radial creep strain rates at any point of tube wall effective stress

$\dot{\varepsilon}_c^{eff}$: effective creep strain rates at any point of tube wall

ε_c^{eff} : effective creep strain at any point of tube wall

σ_{eff} : effective stress strain at any point of tube wall

$\sigma_\theta, \sigma_z, \sigma_r$: tangential, axial, and radial stress at any point of tube wall effective stress

F : creep model equation

$$\sigma_e = (1/\sqrt{2}) \cdot [(\sigma_\theta - \sigma_r)^2 + (\sigma_z - \sigma_r)^2 + (\sigma_\theta - \sigma_z)^2]^{1/2}$$

$$\varepsilon_c^{eff} = \sqrt{2/3} \cdot [(\varepsilon_c^r)^2 + (\varepsilon_c^\theta)^2 + (\varepsilon_c^z)^2]^{1/2}$$

Table D.2.2-4 Zircaloy-4 Cladding Creep Model Equations^(D-5)

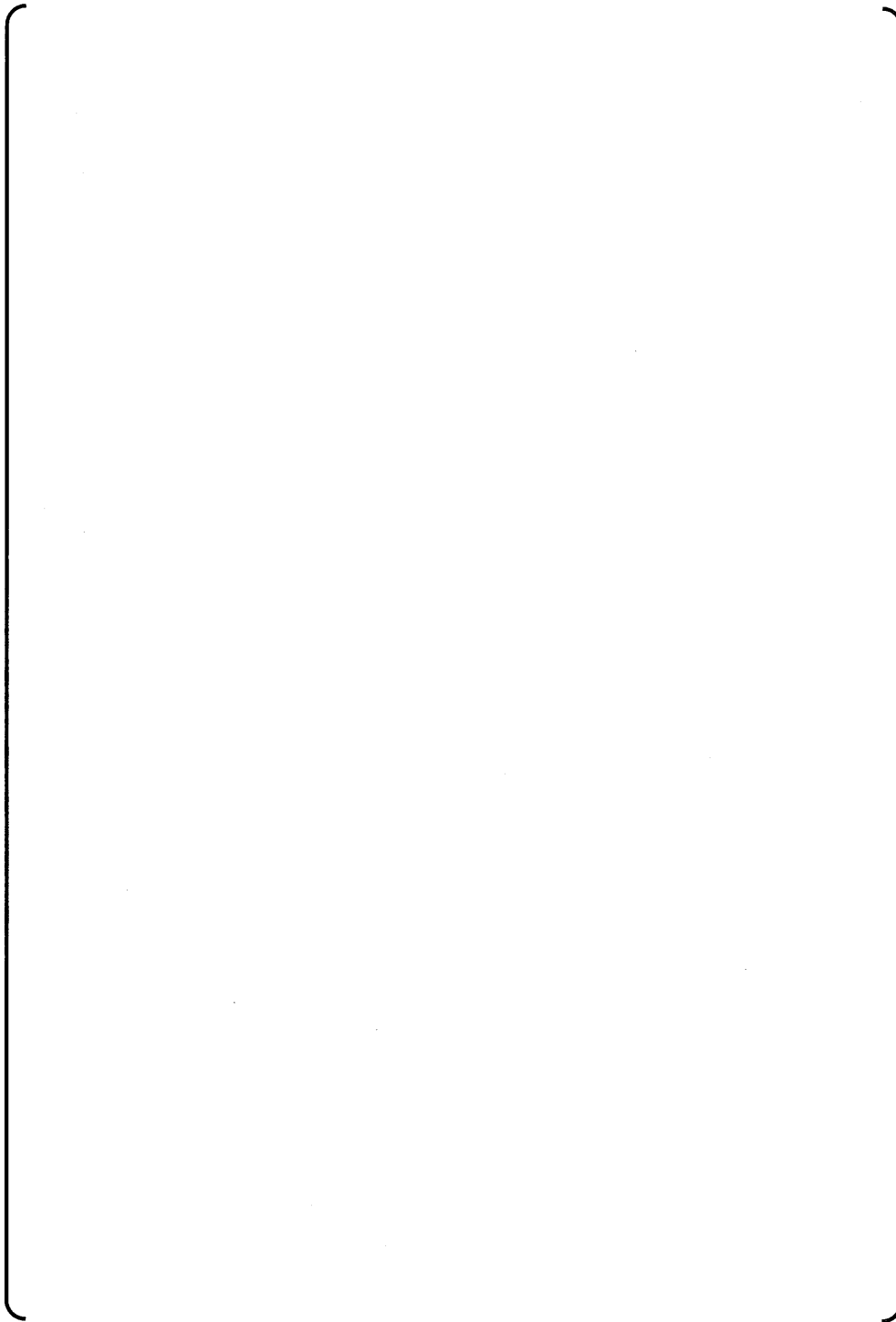
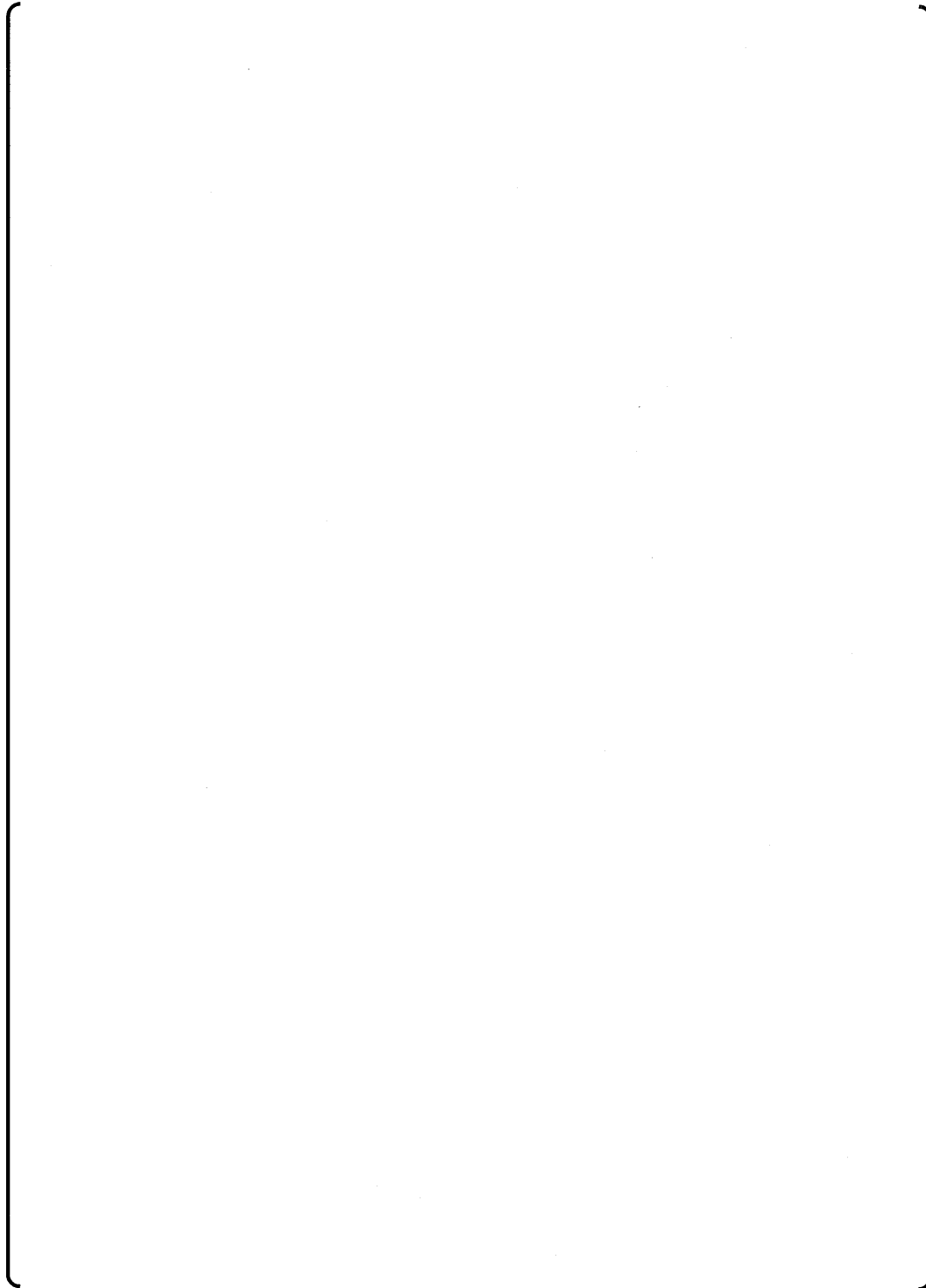


Table D.2.2-5 ZIRLO Cladding Creep Model Equations^(D-5)



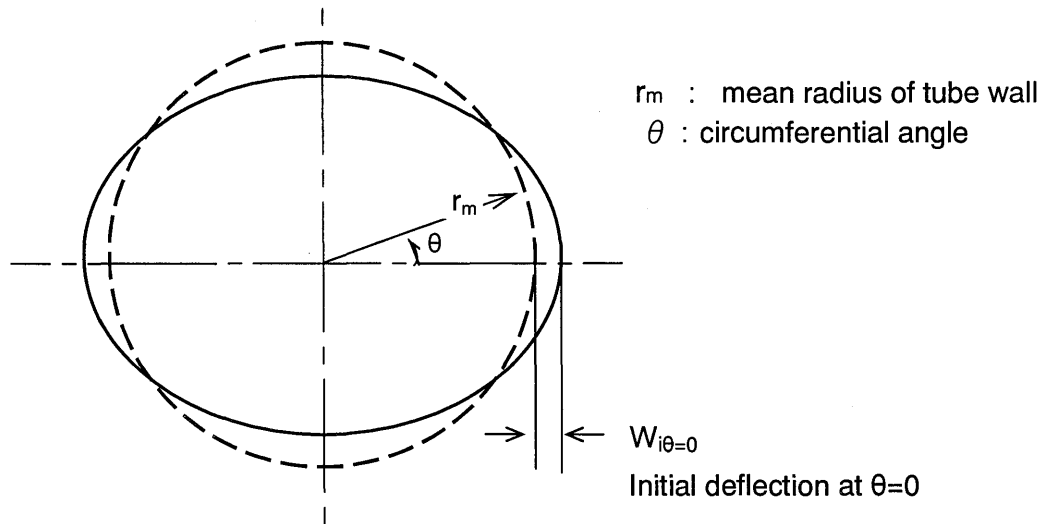


Figure D.2.2-1 Geometry and Coordinate System for Mechanics Analysis of Initial Oval Tube under External Pressure

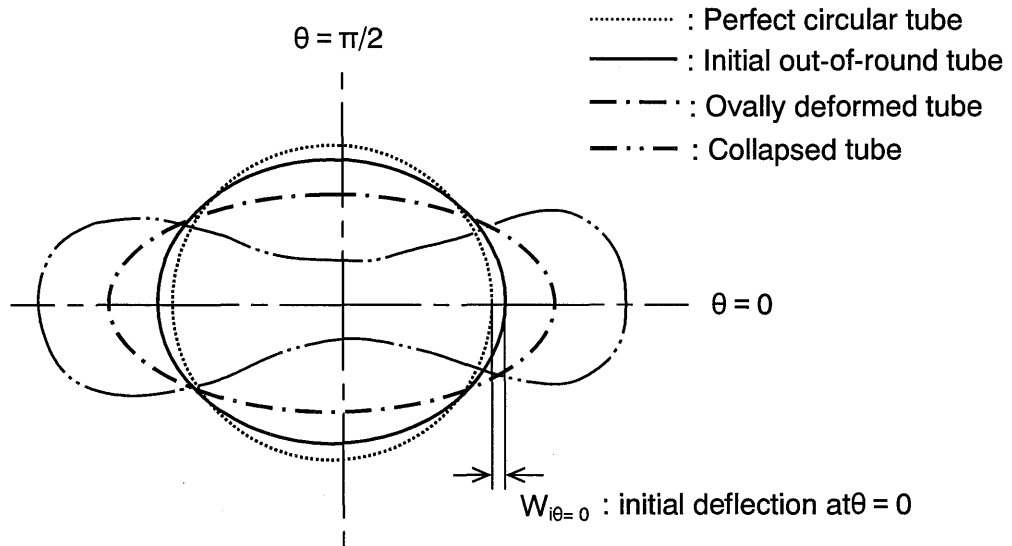


Figure D.2.2-2 Creep-induced Ovalization Process of Initially Oval Tube under External Pressure

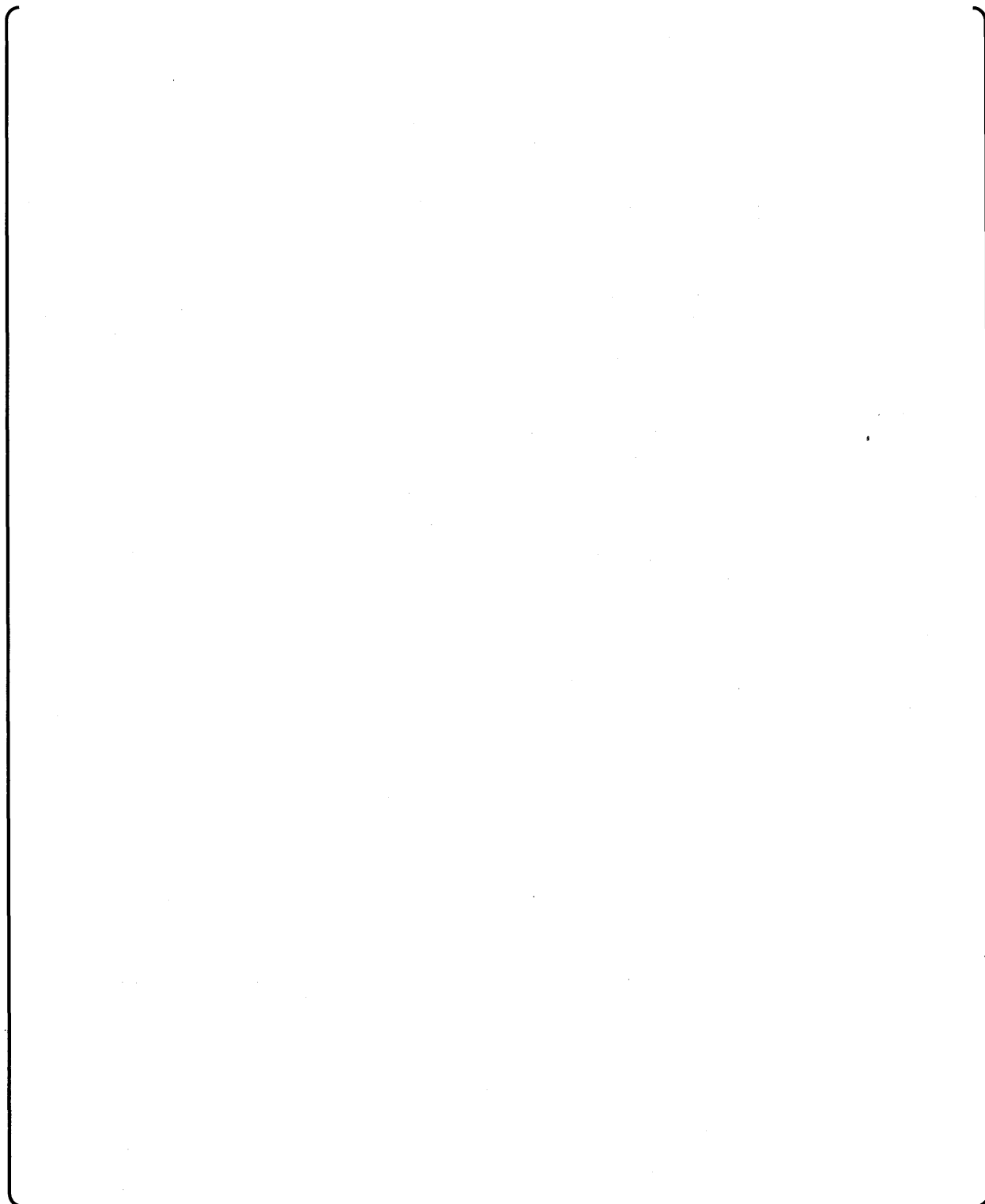


Figure D.2.2-3 Development of Stress and Creep Due to Bending for Initial out-of-round Tube under External Pressure

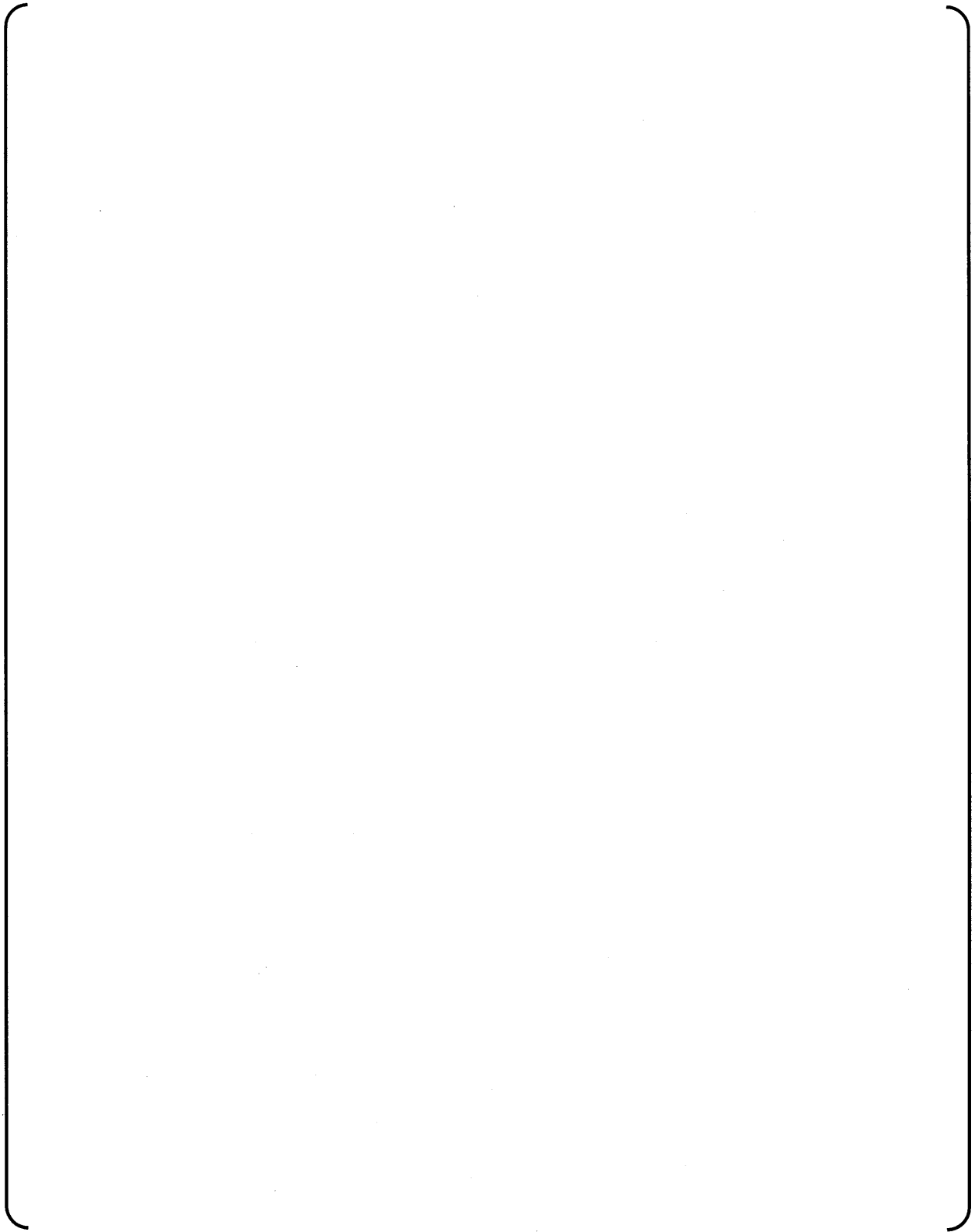


Figure D.2.2-4 Schematic Flow Diagram of Analysis for Creep Collapse Process for Fuel Rod Cladding Tube

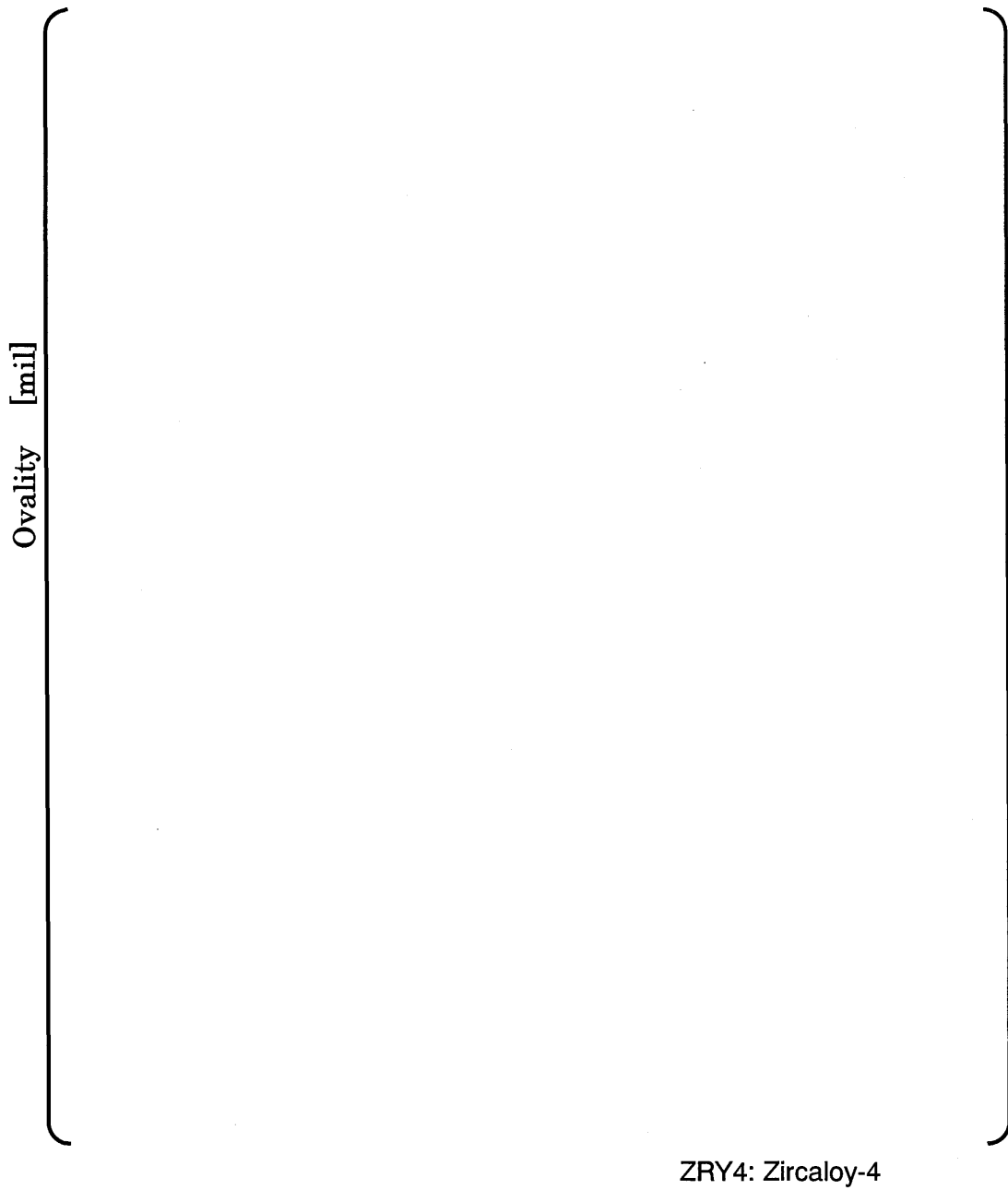
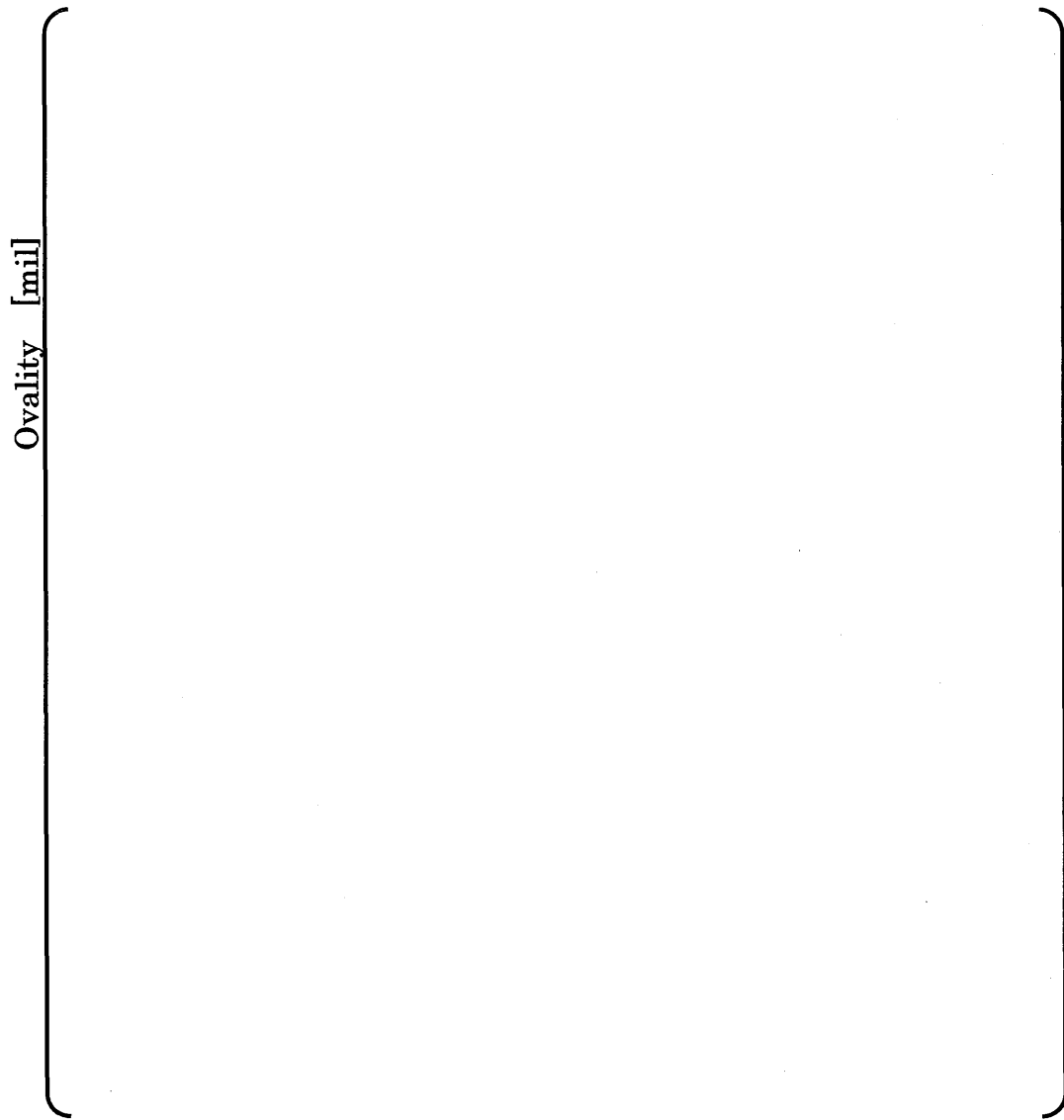
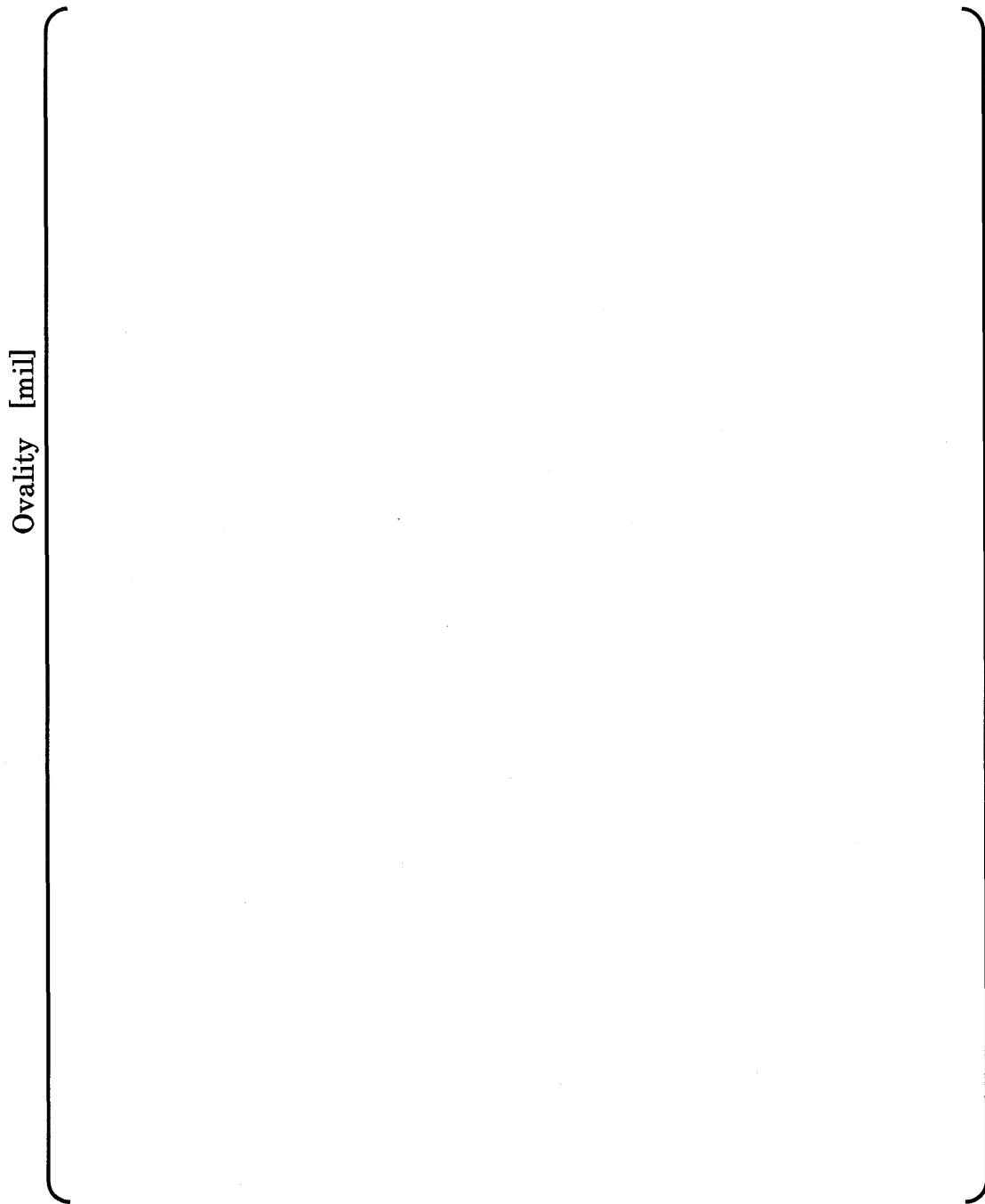


Figure D.2.2-5 Comparison of Calculated and Measured Ovality for Out of Pile Test



ZRY4: Zircaloy-4

Figure D.2.2-6 Comparison of Calculated and Measured Ovality for Out of Pile Test



ZRY4: Zircaloy-4

Figure D.2.2-7 Comparison of Calculated and Measured Ovality for Out of Pile Test

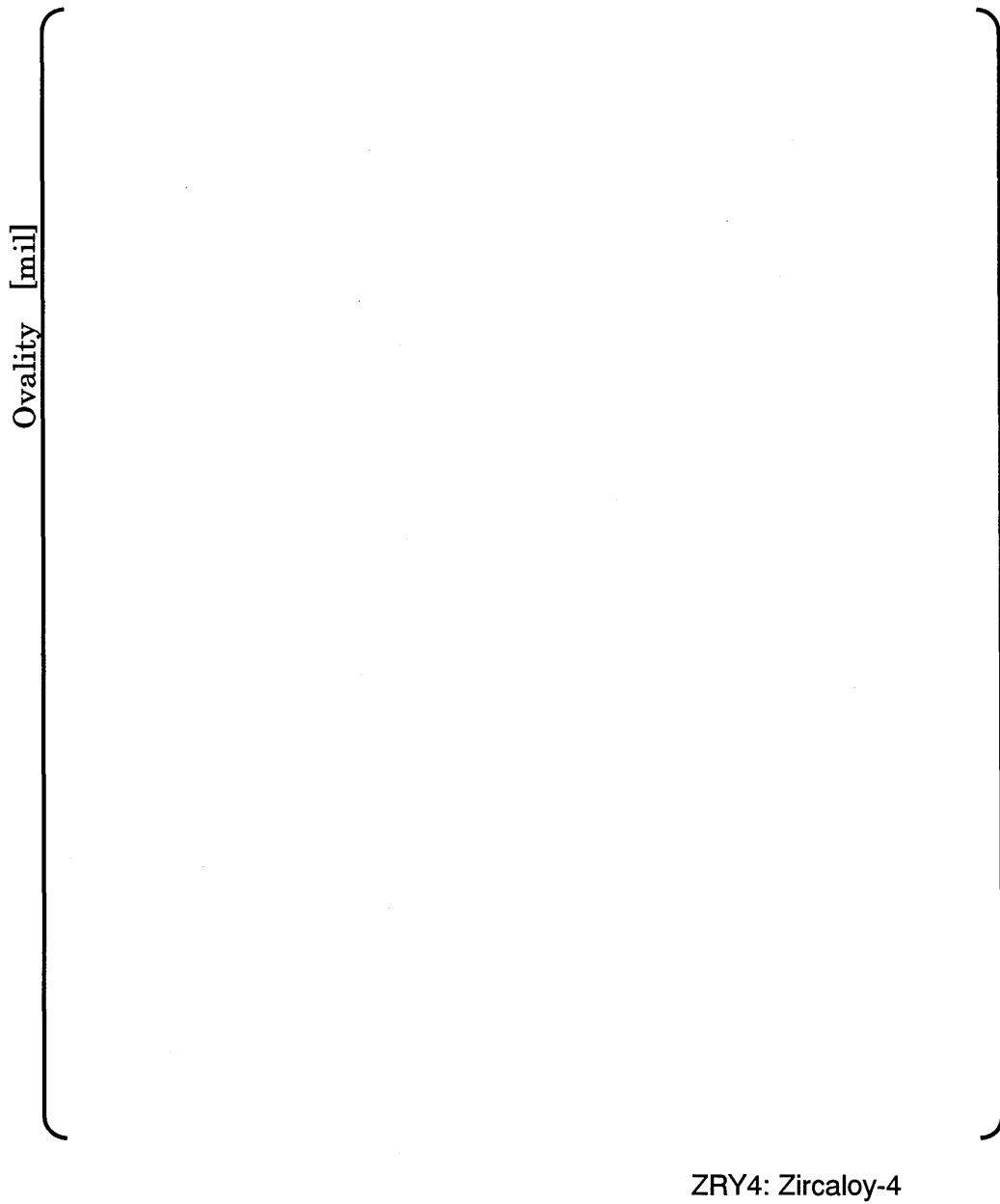


Figure D.2.2-8 Comparison of Calculated and Measured Ovality for Out of Pile Test

D.3.0 COLLAPSE FREQUENCY EVALUATION

D.3.1 Factors Affecting the Collapse Mechanism and Generic Methodology

Processes of In-pile fuel rod creep flattening and collapse are affected by fuel rod design and reactor core design and operating parameters. The key design parameters that characterize the generic fuel behavior and reactor operation are:

- Cladding tube geometry : radius, thickness
- Cladding material : Zr-4 or advanced cladding (ZIRLO)
- Core average linear power
- Core inlet temperature and coolant temperature rise

The cladding tube design geometry governs the stress and strain response to the pressure loads. The cladding material determines the cladding tube creep rate. The core average linear power determines the local fast neutron flux, which determines the magnitude of the irradiation creep component of the total cladding creep on the reason that fast neutron flux is proportional to the product of the core average linear power, the rod relative power and the axial power distribution. The core inlet temperature and coolant temperature rise determines the local cladding temperature, which determines the magnitude of the thermal creep component of the total cladding creep.

Given those key design parameters (i.e. cladding geometry, cladding material, and reactor operating conditions), the creep-induced ovalization and creep collapse phenomena of the fuel rods depends on the following factors:

- (1) The differential pressure across the cladding wall (i.e. the internal pressure, because generally the external pressure is constant, from the prospective of design sensitivity)
- (2) Cladding temperature
- (3) Fast neutron flux
- (4) Gap length size
- (5) Cladding initial ovality (i.e. out-of-roundness of tube)

Factors (1) to (3) are the source of the cladding creep and determine the magnitude of the cladding creep rate. Factor (4) determines the pellet-contact-induced support effect that suppresses the cladding deformation for gap lengths less than an effectively infinite gap. Factor (5) is the source of the cladding tube wall bending and deflection from a circular cross section.

Those factors vary in their values from rod to rod in the core, due to differences in the fuel rod irradiation conditions, the nuclear and thermal-hydraulic characteristics of the reactor core (power distribution etc.), and fuel fabrication variability. Therefore the cladding collapse time varies from rod to rod throughout the reactor core. The collapsed rod frequency at any time is defined as a fractional ratio of fuel rods that have collapsed by that time, for all the fuel rods being irradiated simultaneously in a given fuel region.

of the collapse time. Each of these factors is considered to be statistically independent of each other.

$$t_{\text{COL}} = h(X) = h(X_1, X_2, \dots, X_Q) \quad (1)$$

t_{COL} : collapse time for a combination of the factors given values

$$X = (X_1, X_2, \dots, X_Q)$$

: factors that determine t_{COL} and are independent from other, where Q

is number of the factors ($Q = 4$ for the presented method)

$h(X)$: function that relates the factors to collapse time

then

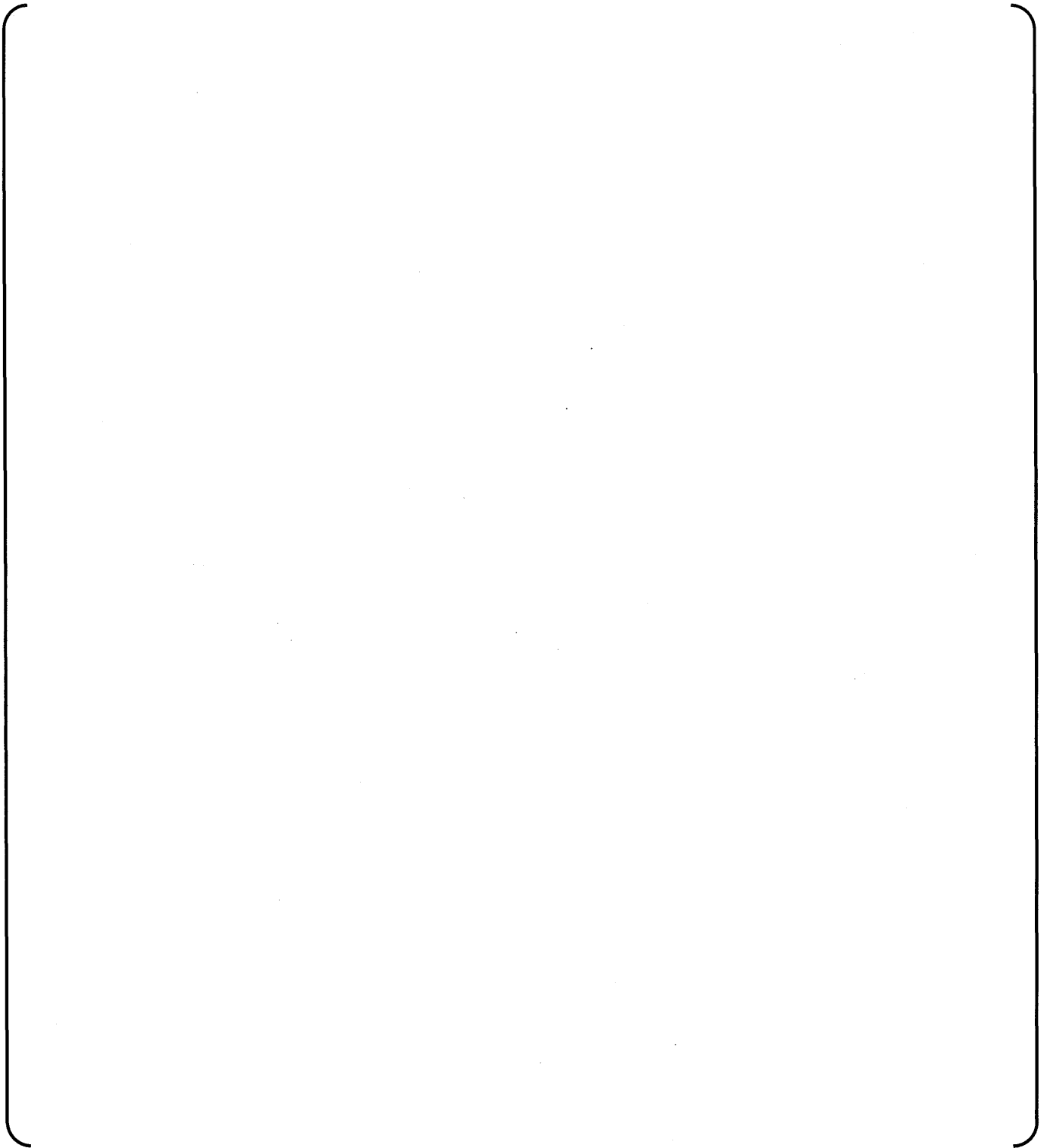


Figure D.3.1-1 Illustration of Fuel Rods, Reactor Core and Distributions of the Several Factors that Contribute to Creep Collapse



Figure D.3.1-2 Schematic of the Generic Procedure to Calculate a Collapse Frequency from the Distribution of the Factors Determining Collapse

D.3.2 Collapse Frequency Calculation Theory and Formulation

This section deals with the functional models for the collapse time, the frequency distributions for the factors that determine the collapse time, and the way in which these are combined to obtain the collapsed rod frequency as a function of time.

The key concepts for linking the significant factors that determine the collapse time to calculate the collapse fraction are shown in Figure D.3.2-1. The notation of *dis.* in this Figure refers to the factors that are given by a distribution of values, so that they may be treated as random variables.

D.3.2.1 Functional Models on Collapse Time for An Infinite Gap

As described in section D.3.1, the infinite-gap collapse time of cladding at any axial position is directly dependent on the following physical quantities and their distributions:

- Rod internal pressure
- Cladding local temperature
- Cladding local fast neutron flux
- Initial ovality

These quantities furthermore depend on the factors which are fuel designs and reactor conditions as follows:

Therefore the collapse time can be linked to these factors through functional representations by using appropriate parameters as variables of the functions.

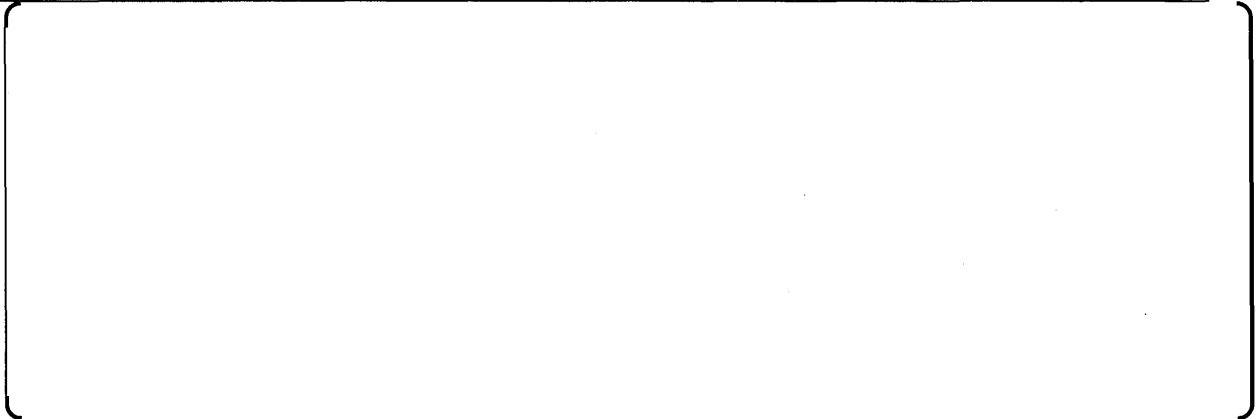
The collapse time functional models have been derived from the results obtained from a parametric evaluation of the dependence of the creep collapse time on these parameters using the mechanistic model described and validated in section D.2.2. In addition to the assumption used in this mechanistic model, the following additional assumptions have been used in the parametric evaluations:

From the parametric evaluations, the interrelationships between the collapse time and significant parameters can be characterized by two functional relations:

(1) "ovality-quadrupled uniform creep strain ϵ_{uc}^4 "

Table D.3.2-1 gives the equations for the ovality-quadrupled uniform creep strain.

(2) collapse time t_{col} versus "ovality-quadruple time t_{uc}^4 "

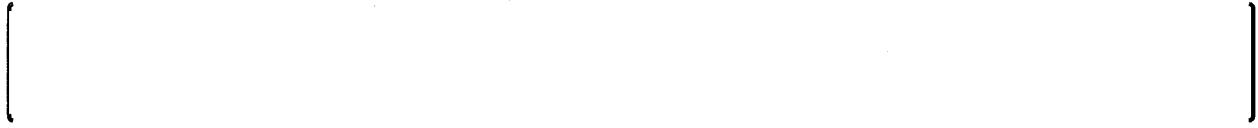


Using these functional relationships, the collapse time for an infinitely long gap is obtained by :

(a) Calculating the strain ϵ_{uc4} at the ovality-quadruple time {
{

(b) Calculating the ovality-quadruple time t_{uc4} corresponding to ϵ_{uc4} by inverting the
cladding creep model equation{
{

(c) Calculating the collapse time{
{



D.3.2.2 Gap Length Effect Model for Finite Gap Collapse Time

$$\left[\begin{array}{l} \left[\begin{array}{l} t_{col}(L_{gap}) = \left[\begin{array}{l} \begin{array}{l} (7-1) \\ (7-2) \end{array} \end{array} \right] \end{array} \right] \end{array} \right]$$

D.3.2.3 Integration Procedure for the Collapse Frequency



The collapse time is then determined by the following functional dependencies :

$$t_{col} = \left[\begin{array}{l} \text{---} \\ \text{---} \end{array} \right] \begin{array}{l} (8-1) \\ (8-2) \end{array}$$

where,

$$\left[\begin{array}{l} \text{---} \\ \text{---} \\ \text{---} \end{array} \right]$$

Hence at the j-th axial position, for a combination of the i-th rod power F_{PW}^i , the k-th initial ovality Wio^k , and the m-th gap size Lg^{mj} , the expression for the collapse time is :

$$\left[\begin{array}{l} \text{---} \\ \text{---} \\ \text{---} \end{array} \right] \begin{array}{l} (9-1) \\ (9-2) \\ (9-3) \end{array}$$

where,

$$\left[\begin{array}{c} \left[\phantom{f_{ijkm}} \right] \\ \phantom{f_{ijkm}} \end{array} \right]$$

$$f_{ijkm} = \left[\phantom{f_{ijkm}} \right] \tag{10}$$

where,

$$\left[\phantom{f_{ijkm}} \right]$$

The collapse frequency $f_{RC}(t)$ at any time t is obtained by summing all combinations of the frequencies f_{ijkm} for which the collapse time t_{col}^{ijkm} is less than t :

$$f_{RC}(t) = \left[\phantom{f_{RC}(t)} \right] \tag{11}$$

D.3.2.4 Interrelationships and Frequency Distributions

The interrelationships between the factors used in the collapse time calculation, and their frequency distributions, are needed to calculate the collapse time distribution and the collapse frequency.

Interrelationships for Collapse Time Factors

(1) rod internal pressure

$$\left[\begin{matrix} \left[\text{rod internal pressure} \right] \\ \left[\text{cladding temperature} \right] \\ \left[\text{fast neutron flux} \right] \end{matrix} \right] \quad (12)$$

(2) cladding temperature

Cladding temperature T_c^{ij} at any axial position is related to the rod relative power and relative axial elevation by the following formula.

$$\left[\text{Cladding temperature } T_c^{ij} \text{ relationship formula} \right] \quad (13)$$

(3) fast neutron flux

The fast neutron flux ϕ^{ij} at any axial elevation is related to the rod relative power and the axial local relative power by the following formula.

$$\left[\text{fast neutron flux } \phi^{ij} \text{ relationship formula} \right] \quad (14)$$

(4) axial gap length size

$$\left[\text{axial gap length size relationship formula} \right]$$

$$\left[\left(\right) \right] \quad (15)$$

where,

$$\left[\right]$$

(6) initial ovality

Initial ovality W_{io}^k is determined from cladding tube fabrication data.

Frequency Distributions for Collapse Fraction Factors

(1) rod power census (F_{PW}^i, f_{PW}^i)

$$\left[\right]$$

(2) initial ovality distribution ($W_{io}^k, f_{W_{io}^k}$)

$$\left[\right]$$

(3) relative gap size distribution (F_{GS}^m, f_{GS}^m)

[]

(4) gap occurrence distribution (f_{GP}^j)

[]

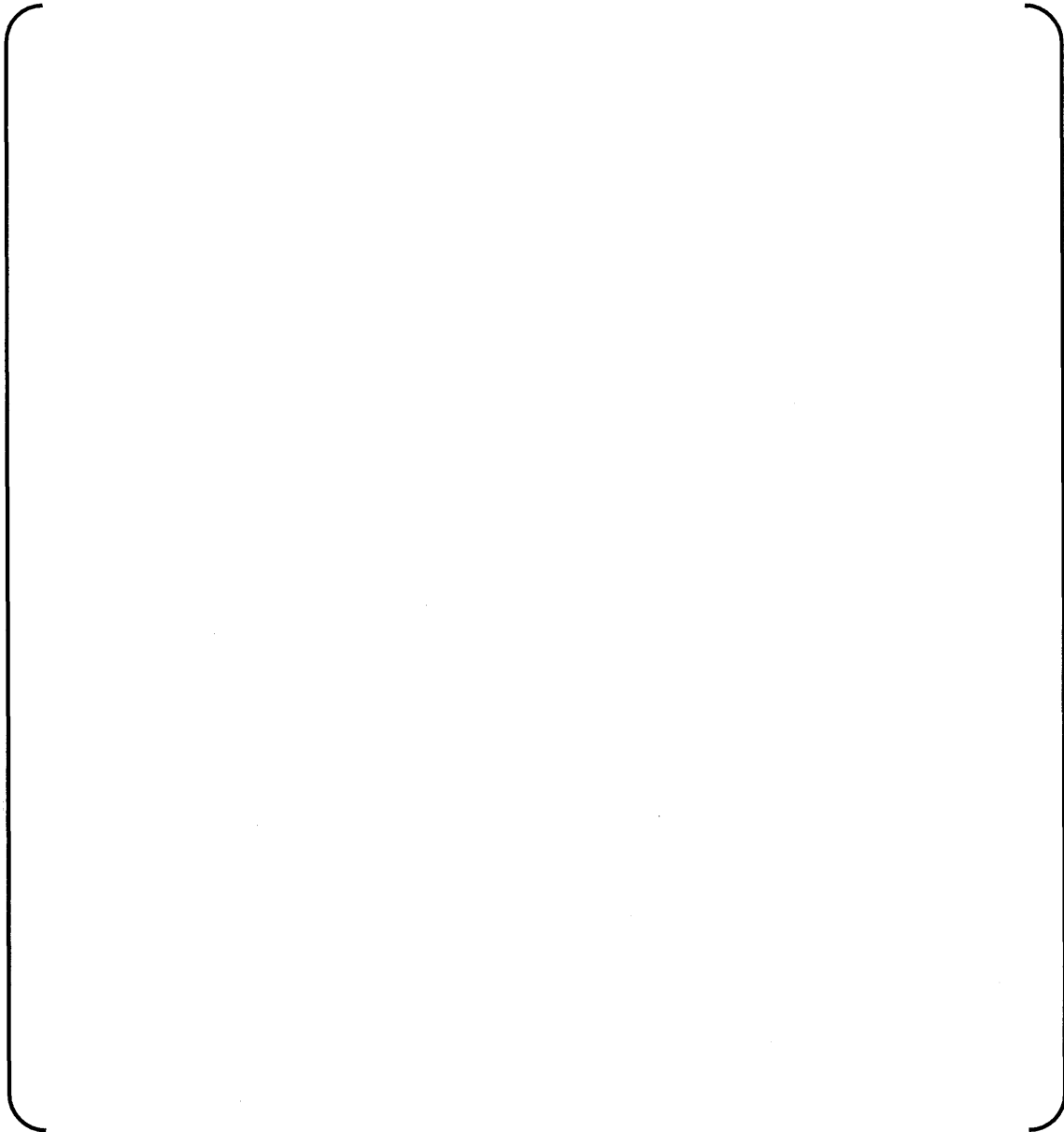
Table D.3.2-1 Equation for the Ovality-Quadrupled Uniform Creep Strain ϵ_{uc4} 

Table D.3.2-2 Equation for the Relation between the Ovality-Quadruple Time (t_{uc4}) and the Collapse Time (t_{col}) (1/2)

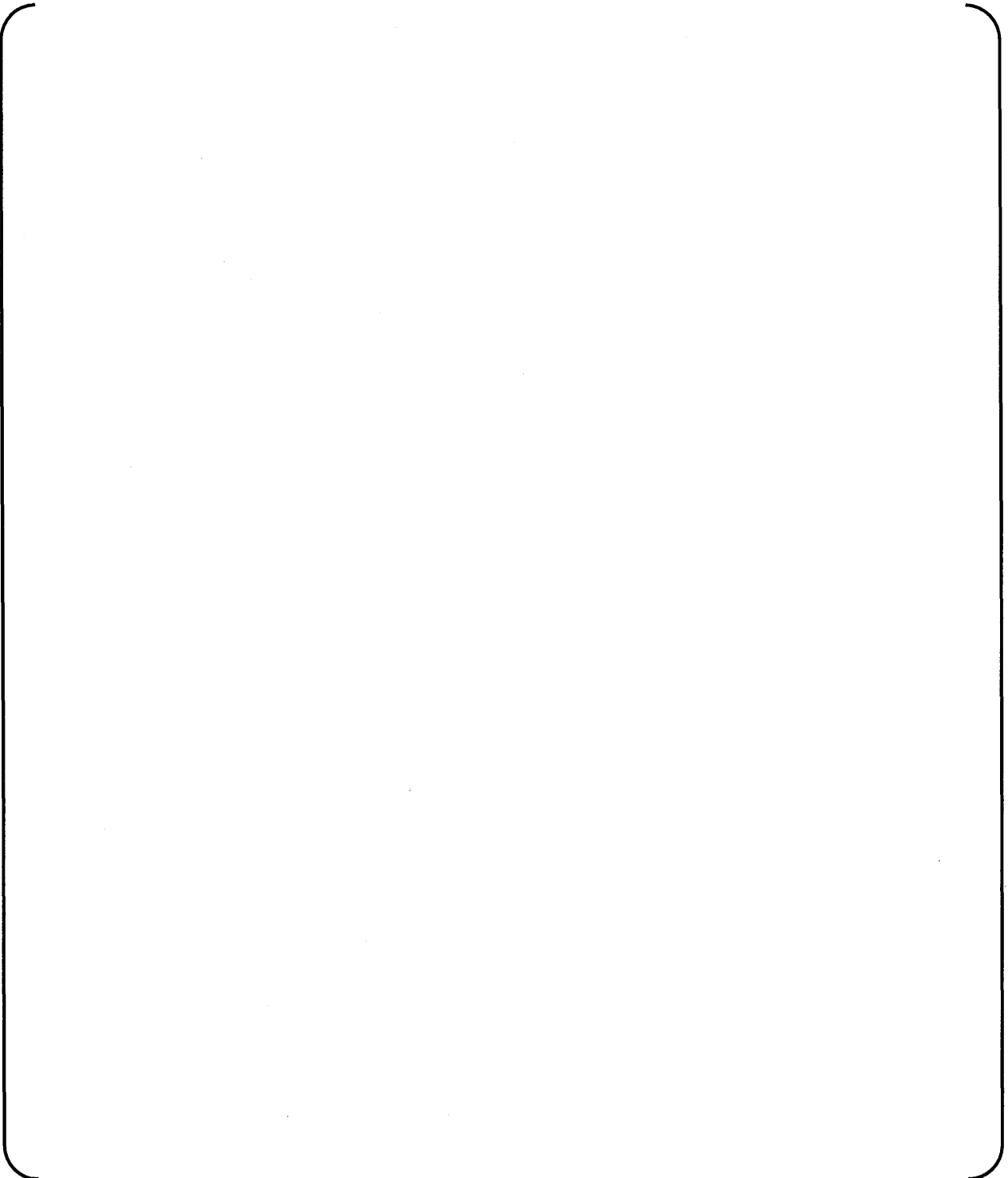
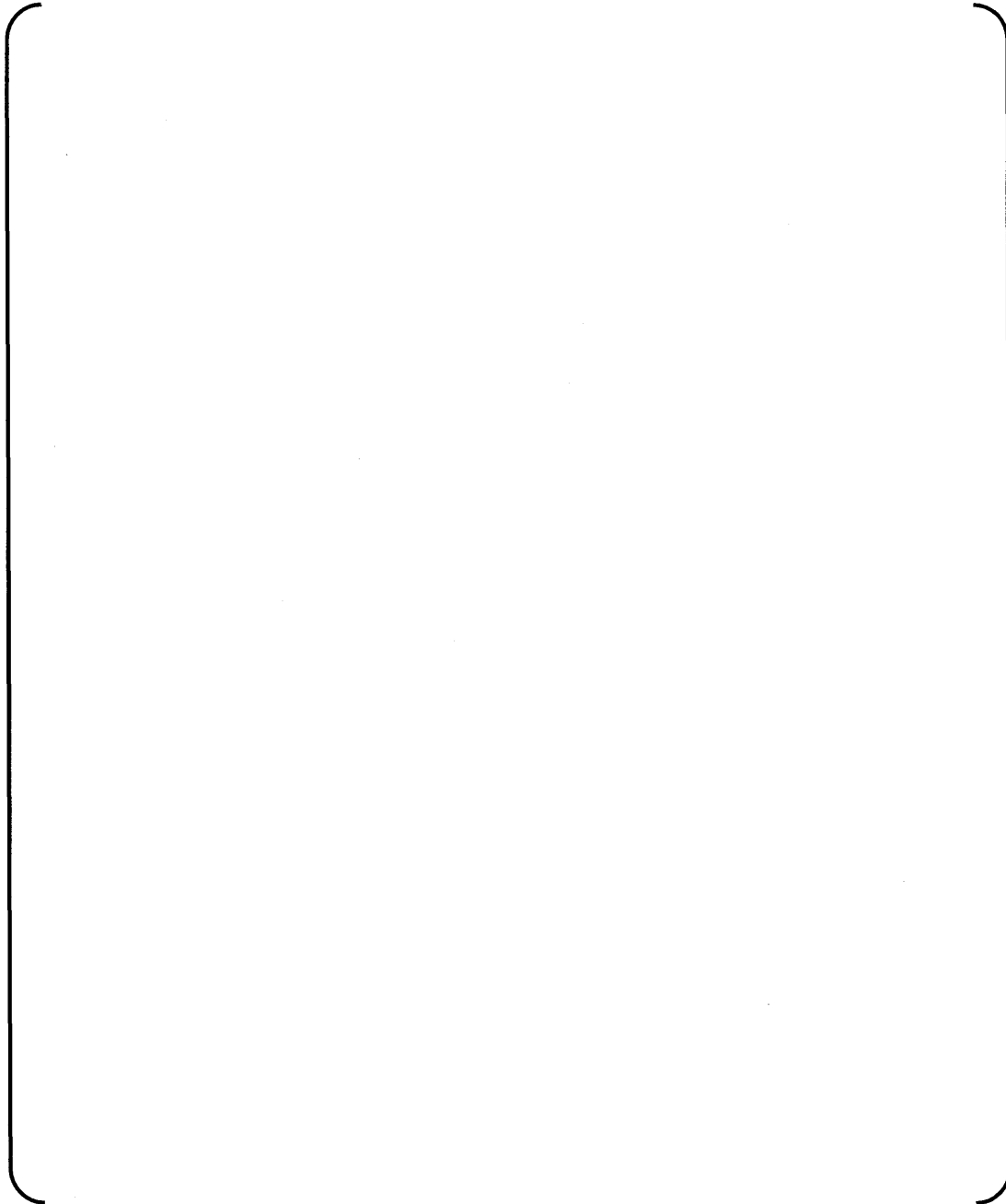


Table D.3.2-2 Equation for the Relation between the Ovality-Quadruple Time (t_{uc4}) and the Collapse Time (t_{col}) (2/2)

A large, empty rounded rectangular frame with a thin black border, intended for the equation described in the caption above. The frame is centered on the page and occupies most of the vertical space between the caption and the footer.

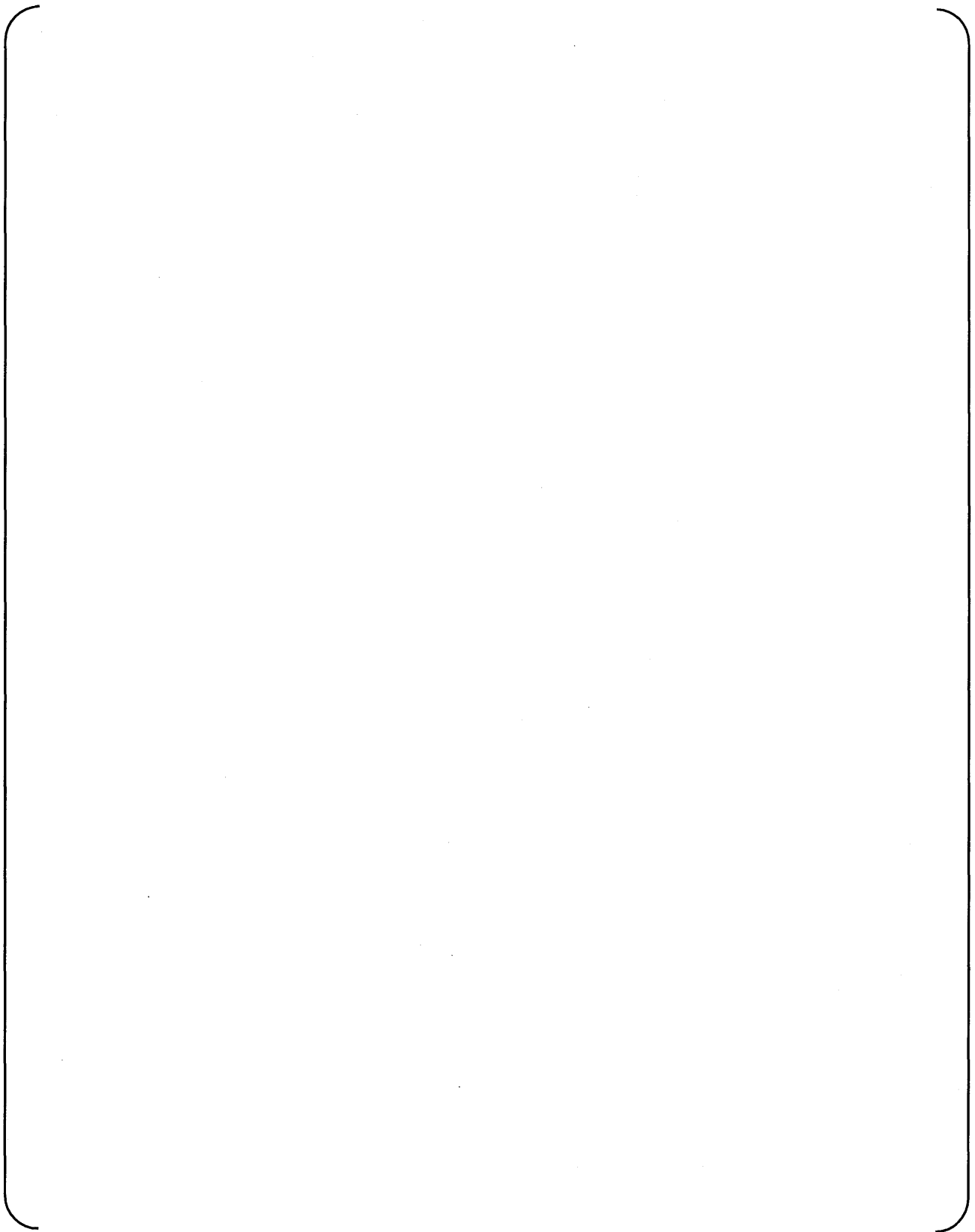


Figure D.3.2-1 Key Concepts for Providing the Linkages between the Significant Factors, the Collapse Time, and the Collapse Frequency

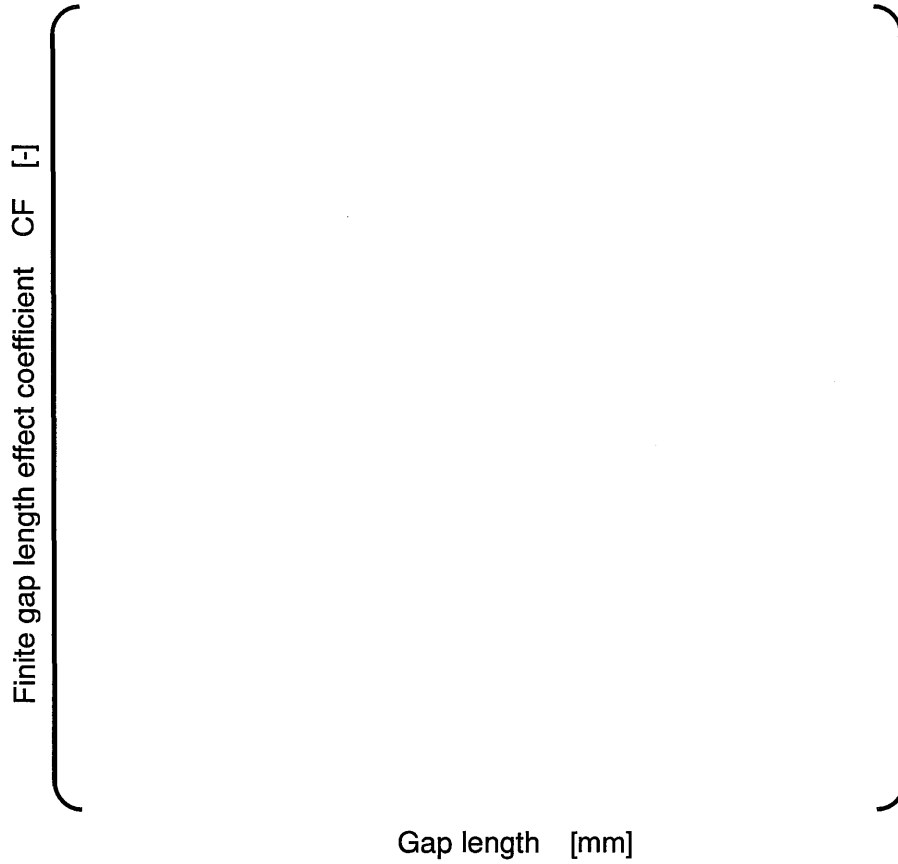


Figure D.3.2-2 Finite Gap Effect Correction Factor versus Gap Length

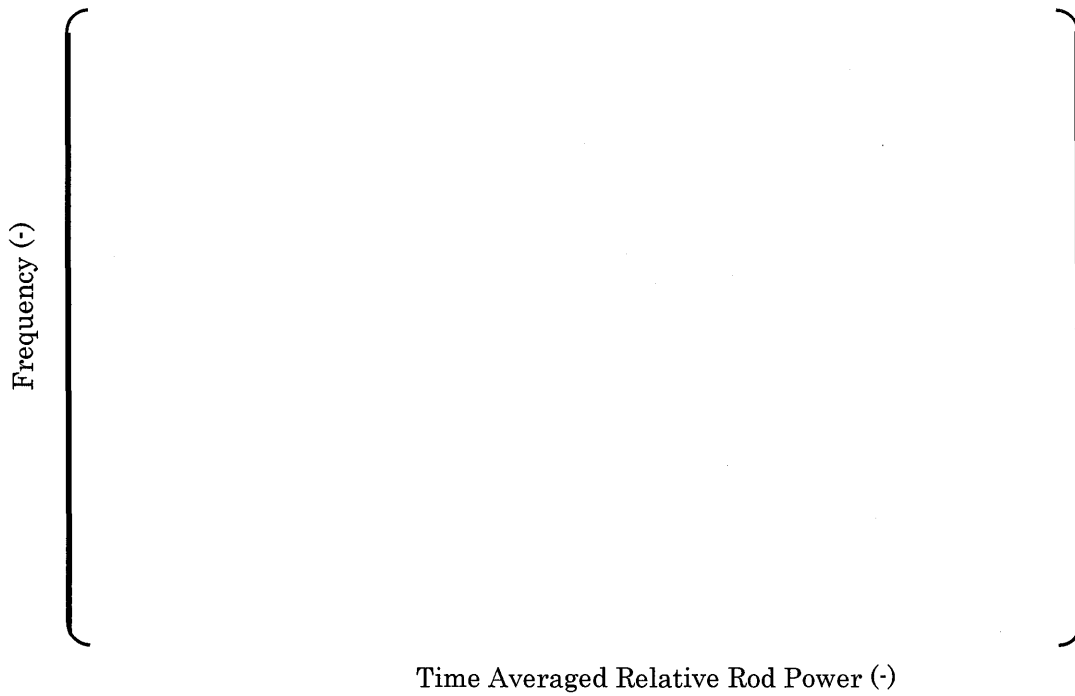


Figure D.3.2-3 Typical Time Averaged Relative Rod Power Census

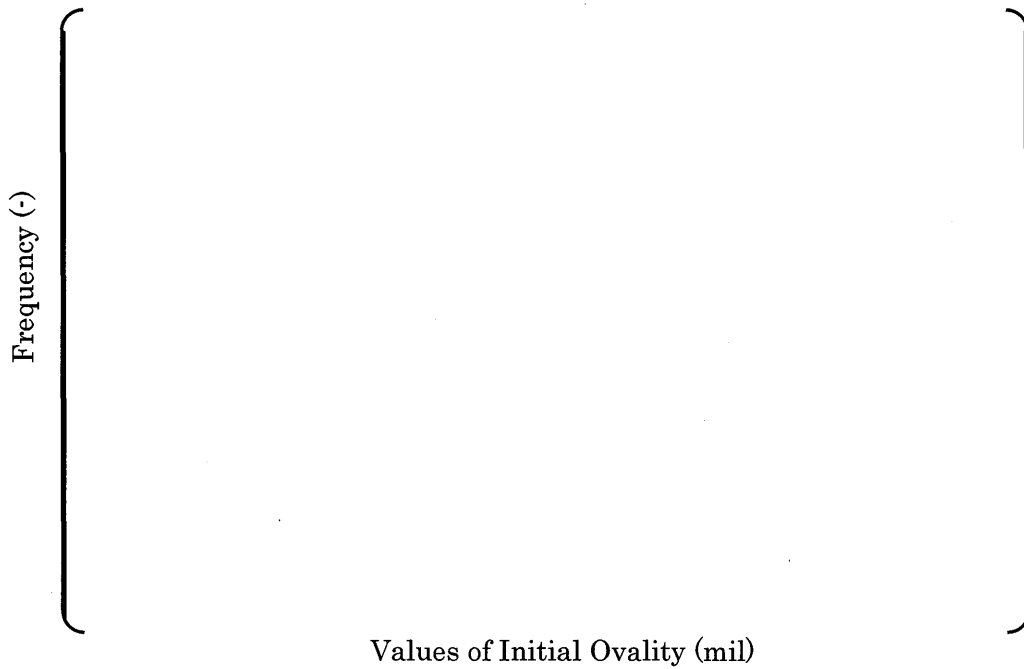


Figure D.3.2-4 Typical Initial Ovality Distribution

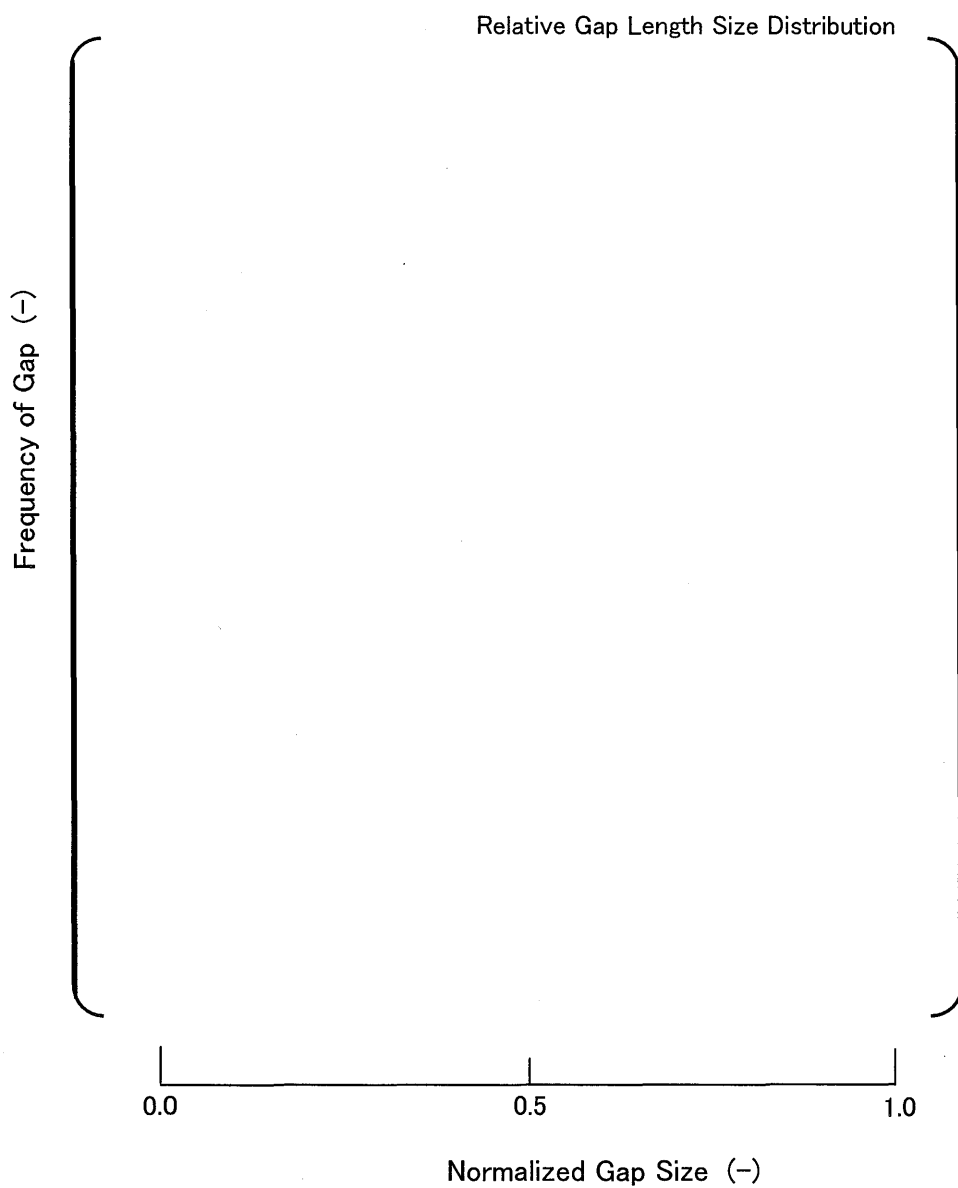


Figure D.3.2-5 Relative Gap Length Size Distribution

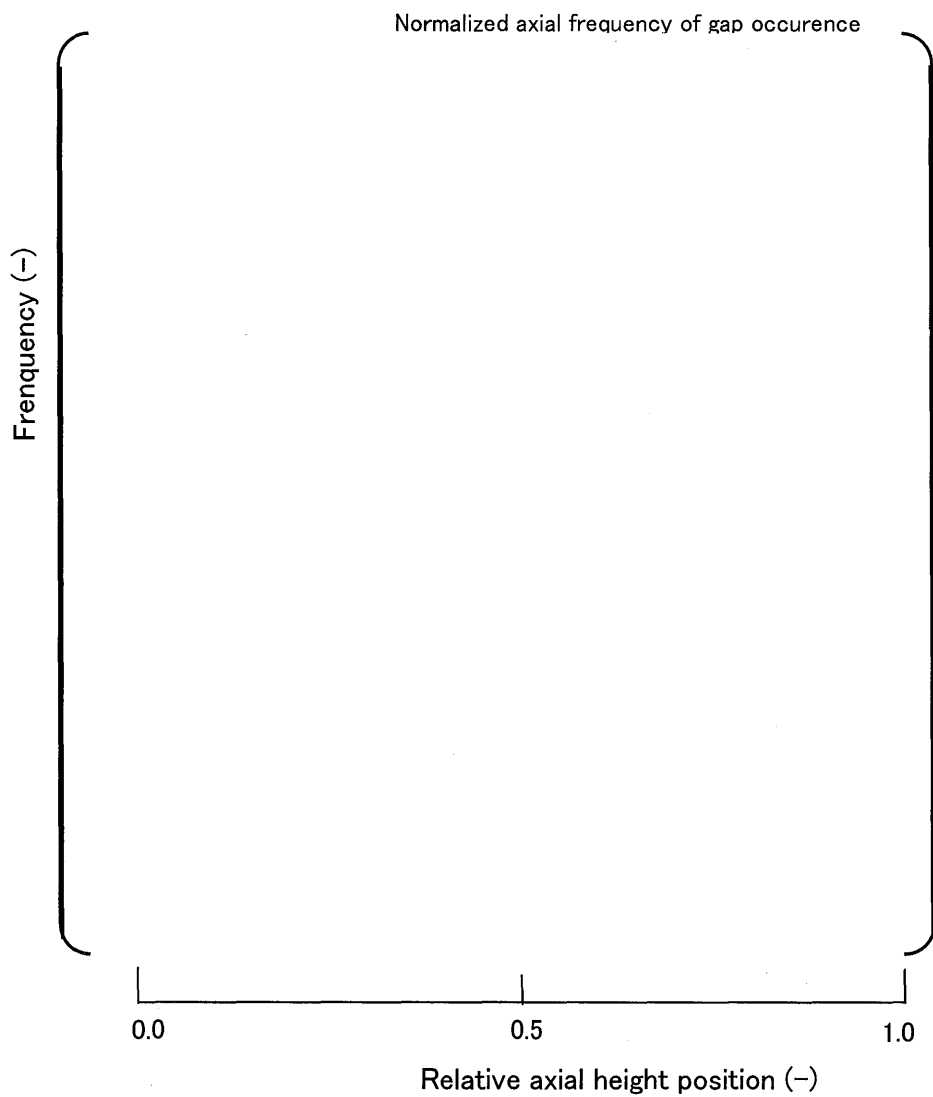


Figure D.3.2-6 Gap Occurrence Frequency Distribution

D.3.3 Calculation Method for Collapse Frequencies

The Mitsubishi has developed the statistical model to evaluate cladding collapse frequency for PWR type fuel. The model is described by the generic methodology (section D.3.1), and formulation and assumptions for the quantitative calculation of the cladding collapse times and frequencies (section D.3.2). Figure D.3.3-1 shows the schematic flow chart of analysis for fuel cladding collapse frequency. The structure has four iteration loops on rod power, axial nodes, ovality, and gap size, and a time iteration loop. This loop structure enables collapse times to be calculated over the full range of the significant variable collapsing factors and then the synthesis of these collapse time results to obtain the collapse frequency at any time.

The major inputs for the calculation are as follows.

- specification of fuel rod design and cladding material (ZIRLO, Zr-4)
- reactor conditions (inlet temperature and temperature rise, core averaged fast neutron flux, internal pressure change rate)
- maximum total gap length size

The maximum total gap size is determined from the maximum fuel stack length shrinkage during the life due to in-core fuel pellet densification. It is calculated using the fuel densification model used in the fuel rod design and performance analysis.

- relative rod power census
- axial power distribution
- initial ovality size distribution (typical inputs are predefined in the program)

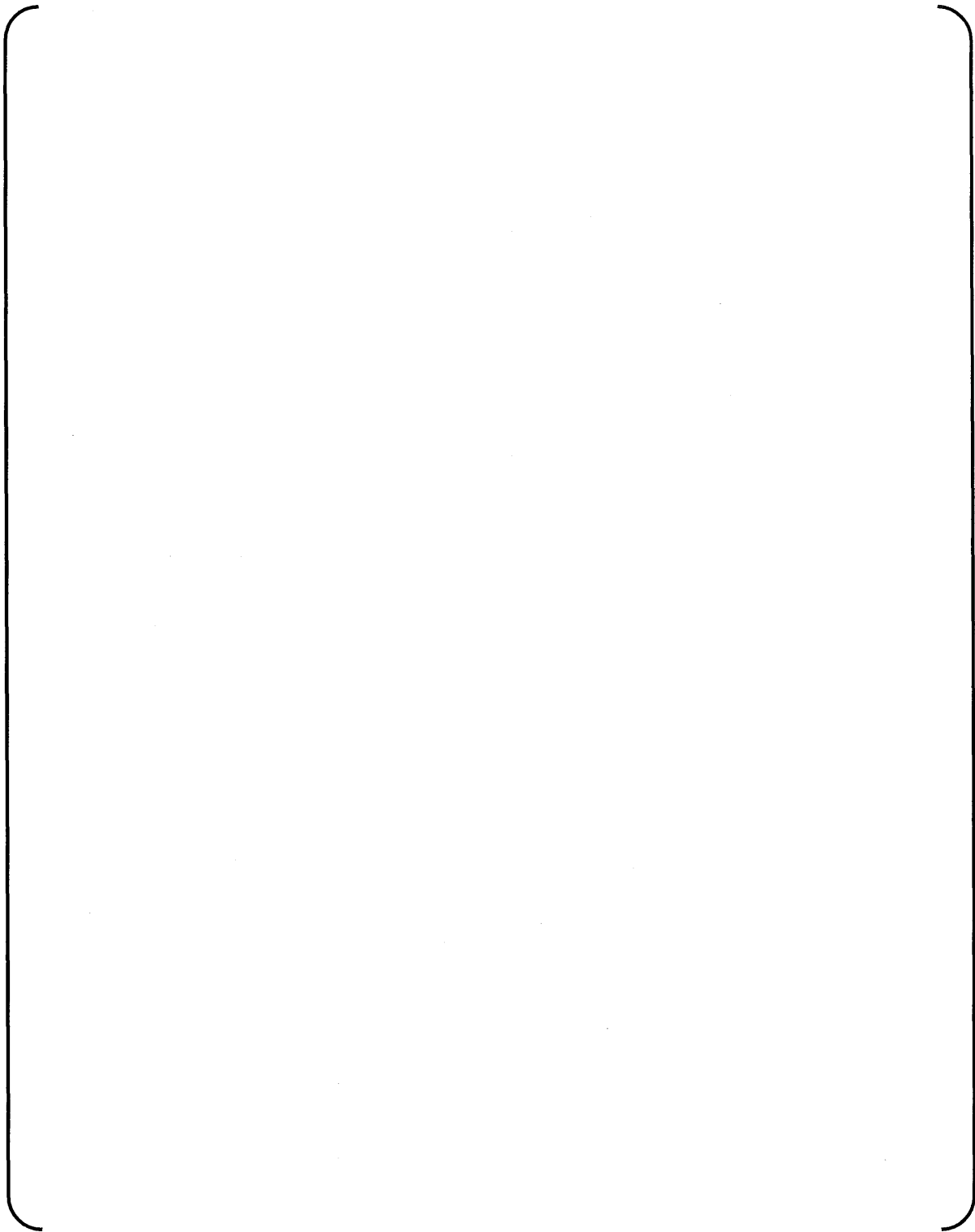


Figure D.3.3-1 Schematic Flow Diagram of Analysis for the Cladding Collapse Frequency

D.3.4 VALIDATION AND VERIFICATION

The statistical collapse model is based on the following technical approach for the calculation of the cladding collapse frequency (or collapse fraction).

The statistical model uses mathematical expressions for the mechanical correlations, the findings derived from fuel rod irradiation experience, and the results obtained from parametric studies using the mechanistic model for cladding creep collapse. The statistical model provides the collapse frequency as a function of time for PWR fuel from the values and/or distributions of

Validation and verification of the statistical model have been performed by comparing the predictions by the model with creep collapse data for several fuel regions with earlier designed Zr-4 cladding fuel, which experienced creep collapse failures in the commercial reactor.

These results confirm that the Mitsubishi statistical model is applicable to the cladding creep collapse evaluation for PWR fuel adequately and conservatively.

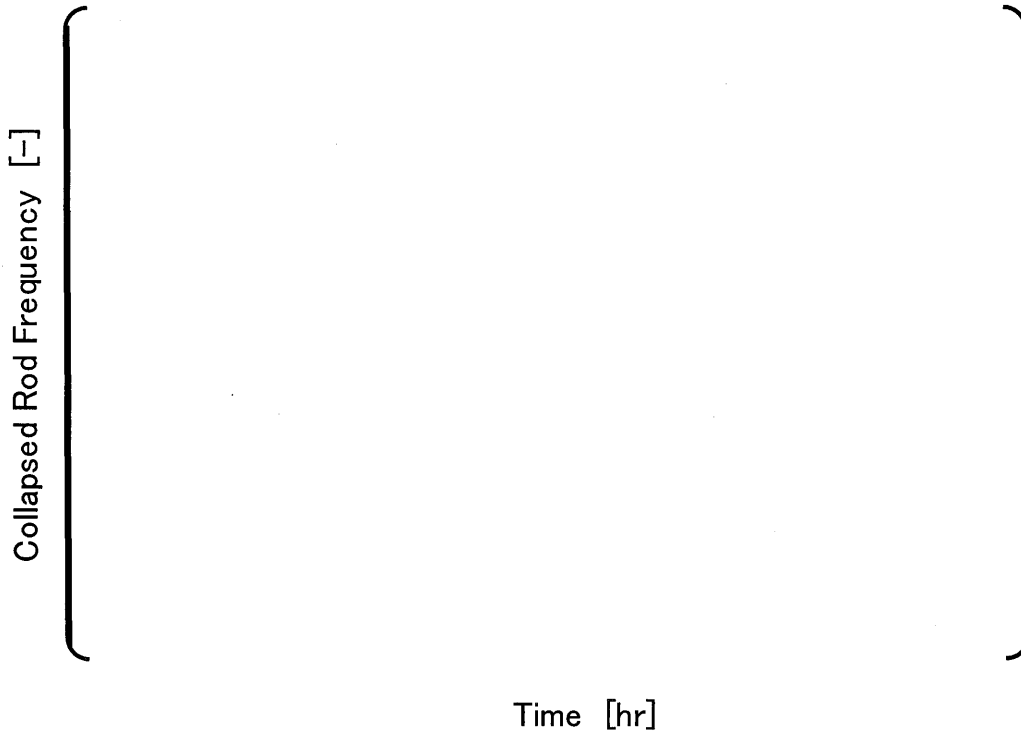


Figure D.3.4-1 Comparison of Observed and Predicted Frequency of Fuel Rod Collapse for Plant A Region 1 fuel

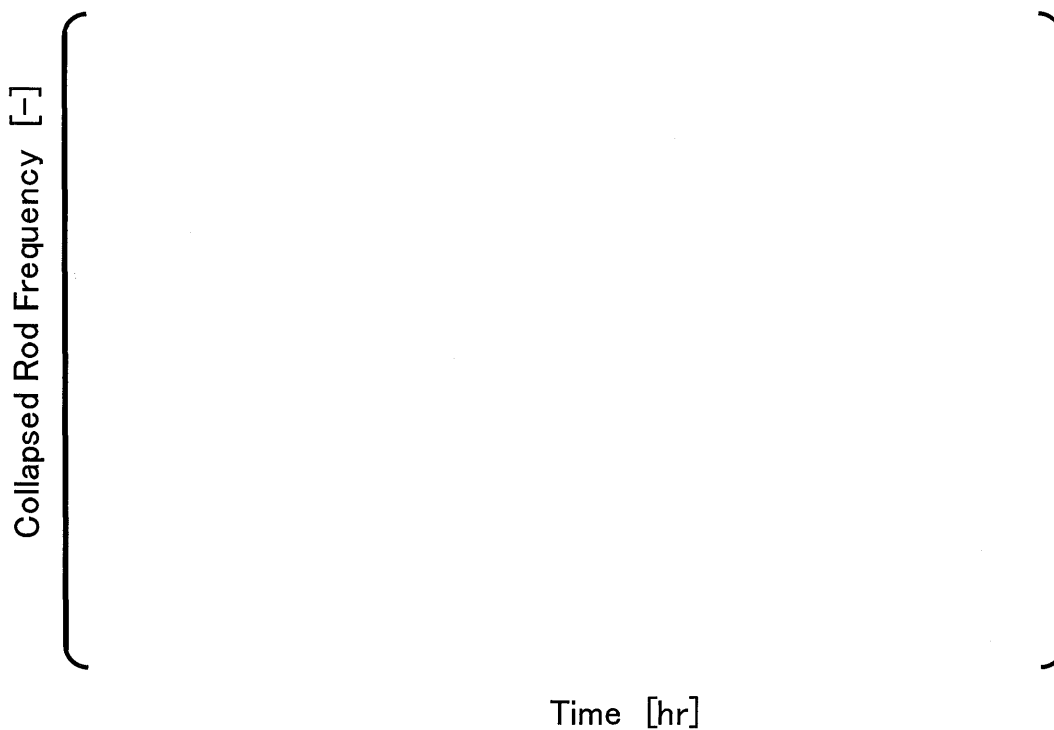


Figure D.3.4-2 Comparison of Observed and Predicted Frequency of Fuel Rod Collapse for Plant B Region 2 fuel

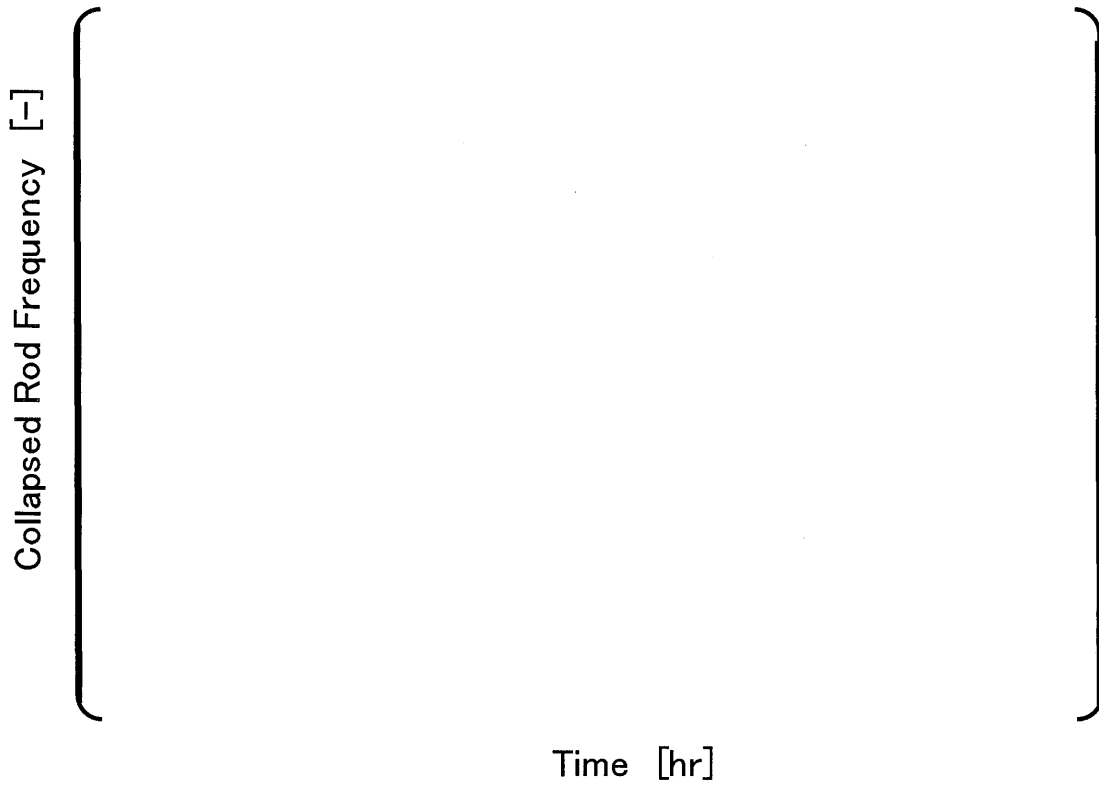


Figure D.3.4-3 Comparison of Observed and Predicted Frequency of Fuel Rod Collapse for Plant C Region 1 fuel

D.4.0 EVALUATION OF US-APWR FUEL

Evaluation of fuel rod creep collapse for ZIRLO cladding applied to US-APWR fuel has been performed using the statistical model. The collapsed rod frequency as a function of time for a given fuel region is evaluated.

(1) Characteristics of Reactor Core and Fuel of Concern

US-APWR fuel design parameters are described in Section 2 of this report. The fuel rod uses higher density fuel pellets and internally initial pressurization. The nuclear design accommodates 24 month equilibrium cycle operation with fuel maximum burnup below the design rod burnup of 62GWD/MTU as described in Appendix A of this report.

Table D.4-1 and D.4-2 present core and fuel design summary, and fuel loading scheme for the equilibrium cycle core as described in Appendix A. The reactor core uses two types of fuel rod: UO_2 rod and $(\text{U,Gd})\text{O}_2$ rod. UO_2 rod includes UO_2 pellets over the entire fuel length, whereas $(\text{U,Gd})\text{O}_2$ rod mostly includes Gd_2O_3 contained UO_2 pellets, which are denoted as $(\text{U,Gd})\text{O}_2$ pellets, and partially UO_2 pellets.

Creep collapse frequencies have been evaluated for a UO_2 rod group and a $(\text{U,Gd})\text{O}_2$ rod group separately.

(2) Design Criterion

Fuel rod design shall preclude cladding creep collapse during the projected fuel lifetime.

When a calculation is required, it should be confirmed that the predicted collapsed rod frequency be well below the frequency level corresponding to one rod collapse failure.

(3) Assumptions and Basic Conditions

Main assumption and considerations are as follows:



(4) Results

Figure D.4-1 and D.4-2 show the calculated collapse frequencies versus time and the frequency levels corresponding to one rod collapse failure for UO_2 rod group and $(\text{U,Gd})\text{O}_2$ rod group respectively. The predicted collapse rod frequencies are lower than one rod collapse failure frequency for both UO_2 rods and $(\text{U,Gd})\text{O}_2$ rods for largely over the projected fuel lifetime. Therefore, it is assured that fuel rod creep collapse is precluded for more than the fuel operating time or fuel design burnup of US-APWR fuel.

Table D.4-1 Core and Fuel Design Summary of US-APWR

| Items | Design or Values | Remarks |
|--|-------------------------------|---|
| Cycle Time | 23.5EFPM | |
| Cycle Burnup | 23,000MWD/MTU | |
| Fuel Enrichment | 4.55wt%U235 | for UO ₂ pellet |
| | 2.95wt%U235 | for (U,Gd)O ₂ pellet and UO ₂ pellet loaded in (U,Gd)O ₂ rod |
| Fuel Density | 97%TD. | for both UO ₂ pellet and (U,Gd)O ₂ pellet |
| Coe Average LHGR (Linear Heat Generation Rate) | 4.6kw/ft | |
| Coolant Pressure | 15.5MPa[a] (2250psi[a]) | |
| Fuel Stack Length (Active Fuel Height) | 13.8ft (420cm) | for both UO ₂ pellet and (U,Gd)O ₂ pellet |
| Initial Backfill Pressure | () | |
| Fuel Assembly | | |
| Asy type | Rod type | Number of rods Pellets contained |
| U | UO ₂ rod | 264 all UO ₂ pellets |
| | UO ₂ rod | 248 all UO ₂ pellets |
| U-Ga | (U,6wt%Gd)O ₂ rod | 16 (U,6wt%Gd)O ₂ pellets and partially UO ₂ pellets |
| | UO ₂ rod | 240 all UO ₂ pellets |
| U-Gb | (U,10wt%Gd)O ₂ rod | 24 (U,10wt%Gd)O ₂ pellets and partially UO ₂ pellets |

**Table D.4-2 Fuel Loading Scheme Planned for US-APWR
24 month Equilibrium Cycle Core**

| Reactor Core | Cycle Number | ... | N-2 th Cy | N-1 th Cy | N th Cy | N+1 th Cy | ... |
|--------------------------------|------------------------|----------------------------------|----------------------|----------------------|--------------------|----------------------|-----|
| | Cycle Burnup (MWD/MTU) | ... | 23,000 | 23,000 | 23,000 | 23,000 | ... |
| | Cycle Time (EFPH) | ... | 17,167 | 17,167 | 17,167 | 17,167 | ... |
| Fuel Region | Fuel Assembly Type | Number of Fuel Assemblies Loaded | | | | | |
| ... | ... | ... | ... | ... | ... | ... | ... |
| Region N-1 | U-Gb | 64 | 64 | 1 | | | |
| | U | | 12 | 12 | | | |
| | U-Ga | | 52 | 52 | | | |
| Region N | U-Gb | | 64 | 64 | 1 | | |
| | U | | | 12 | 12 | | |
| | U-Ga | | | 52 | 52 | | |
| Region N+1 | U-Gb | | | 64 | 64 | 1 | |
| | U | | | | 12 | 12 | |
| | U-Ga | | | | 52 | 52 | |
| ... | U-Gb | | | | 64 | 64 | 1 |
| | U | | | | | 12 | 12 |
| ... | ... | ... | ... | ... | ... | ... | ... |
| Total Fuel Assemblies per Core | | ... | 257 | 257 | 257 | ... | ... |



**Figure D.4-1 Collapsed Rod Frequency versus Time for UO₂ Rods
in US-APWR
24 month Equilibrium Core Reloading Fuel**



**Figure D.4-2 Collapsed Rod Frequency versus Time for (U,Gd)O₂ Rods
in US-APWR
24 month Equilibrium Core Reloading Fuel**

D.5.0 CONCLUSION

The Mitsubishi collapse evaluation methodology has a capability to evaluate the mechanical creep collapse process and to calculate the fraction (frequency) of cladding creep collapse for PWR nuclear fuel rods. The validity and verification of the model has been demonstrated through the comparison with out-of pile experimental data on Zircaloy-4 cladding tubes and with creep collapse data for early-designed Zircaloy-4 cladding fuel regions where creep collapse occurred in PWR nuclear power plants.

The Mitsubishi collapse evaluation methodology is applicable to ZIRLO cladding in the same manner as Zircaloy-4 by applying cladding creep model which is well verified by the in-reactor creep data.

Evaluation performed using the statistical evaluation method shows that the fuel rod design of US-APWR conforms to the cladding collapse criterion.

D.6.0 REFERENCES

- (D-1) G.Roberts et al., "An Investigation of the Cladding Collapse Phenomenon in Beznau IPWR", ANS Topical Meeting, Water Reactor Fuel Performance, May 1977
- (D-2) F.Garzarolli et al., "The Main Causes of Fuel Element Failure in Water-Cooled Power Reactors", Atomic Energy Review 17 1, 1979
- (D-3) Frost, Brian R. T., "Nuclear Fuel Elements", Pergamon Press, New York, 1982
- (D-4) W.K.Wilson, "A Method of Analysis for the Creep Buckling of Tubes under External Pressure", WAPD-TM-956, October 1970
- (D-5) "Mitsubishi Fuel Design Criteria and Methodology", MUAP-07008-P (Proprietary) and MUAP-07008-NP (Non-Proprietary), May 2007